UNIVERSITY OF OKLAHOMA

GRADUATE COLLEGE

EVALUATING THE EFFECTS OF VEGETATION COVER AND PHENOLOGY ON THE COMPONENTS OF THE SURFACE ENERGY FLUXES, SOIL TEMPERATURE AND ITS DAMPING DEPTH, SOIL MOISTURE AND THE PARTITIONING OF THE EVAPOTRANSPIRATION ACROSS FOREST, GRASSLAND AND DESERT ECOSYSTEMS

A THESIS

SUBMITTED TO THE GRADUATE FACULTY

In partial fulfillment of the requirements for the

Degree of

MASTER OF SCIENCE

By

TRI G. PHAM
Norman, Oklahoma
2020

EVALUATING THE EFFECTS OF VEGETATION COVER AND PHENOLOGY ON THE COMPONENTS OF THE SURFACE ENERGY FLUXES, SOIL TEMPERATURE AND ITS DAMPING DEPTH, SOIL MOISTURE AND THE PARTITIONING OF THE EVAPOTRANSPIRATION ACROSS FOREST, GRASSLAND AND DESERT ECOSYSTEMS

A THESIS APPROVED FOR THE

SCHOOL OF CIVIL ENGINEERING AND ENVIRONMENTAL SCIENCE

BY THE COMMITTEE CONSISTING OF

Dr. Jason R. Vogel, Chair

Dr. Hernan A. Moreno, Co-Chair

Dr. Jeffrey B. Basara, Committee Member

Acknowledgements

This thesis is dedicated to my parents, my sister Tu Pham, and my brother-in-law Dachuan Shi for their support and encouragement to pursue my professional goals.

I would like to express my sincere gratitude to my advisors, Dr. Jason R. Vogel and Dr. Hernan A. Moreno as well as the committee member, Dr. Jeffrey B. Basara, for their invaluable guidance, advice, and constructive feedback on my research studies. Without their support, I could not complete my Master's studies. Also, I would like to acknowledge the Oklahoma Water Survey and the United States Army Research, Development and Engineering Command Army Research Office (ARO) for the funding of the project (W911NF-18-1-0007).

Finally, I would like to thank my friends Bonheur, M'Kenzie, Jorge, Saliou, Walter, Dr. Laura Alvarez, and all professors and department staff at the School of Civil Engineering and Environmental Science for their teachings and support during my studies.

Table of Contents

List of Tables

List of Figures

List of Acronyms

CC: Correlation Coefficient

ECT: Eddy Covariance Tower

EOSDIS: Earth Observing System Data and Information System

ET: Evapotranspiration

G: Ground heat flux

H: Sensible heat flux

LAI: Leaf Area Index

LE: Latent heat flux

MODIS: Moderate Resolution Imaging Spectroradiometer

NSE: Nash-Sutcliffe Efficiency Coefficient

RMSE: Root Mean Square Error

TIN: Triangulated Irregular Network

tRIBS: TIN-based Real Time Integrated Basin Simulator

Abstract

The understanding and modeling of the effects of land-cover change on the behaviors of evapotranspiration flux and its partitioning, soil moisture, soil temperature, and surface energy fluxes which include ground heat flux, sensible heat flux, and latent heat flux (evapotranspiration) is an active research field with applications to hydrologic engineering. Knowledge of these shifts could improve our estimations of precipitation, heat waves, drought mechanisms, soil moisture and flood forecasting. This study utilized long-term eddy covariance measurements and remote sensing data to investigate the effects of both vegetation cover disturbance and vegetation phenology on key hydrologic variables at seven research sites in Oklahoma and Arizona. The study focused on: (1) the use of eddy covariance measurements and remote sensing data for comparison of surface energy fluxes, soil moisture, and soil temperatures, (2) the calibration and validation of the TIN-based Real-time Integrated Basin Simulator (tRIBS) hydrological model to simulate surface energy and water balance variables and to assess its ability to predict short- and long-term time series at hourly time steps, (3) the partitioning of the evapotranspiration into three components: transpiration from vegetation, wet canopy evaporation from intercepted precipitation on leaves and soil evaporation and the identification of the roles of vegetation and precipitation on the partitioning, (4) the calculation of the daily temperature damping depths at the research sites quantification of roles of vegetation and soil moisture and, (5) the development of a toolkit to automate and visualize tRIBS simulations and reduce human errors.

This study found that:

(1) tRIBS demonstrated its capability to conduct footprint type of simulations at an hourly time step by using process-based conceptualizations and remote sensing with high correlation and Nash-Sutcliffe model efficiency coefficients between simulations and observations. The model also captured the diurnal variability of the simulated variables, which potentially can be used to fill the gap in the missing eddy covariance measurements.

(2) Across simulations sites, responses of simulated ground heat flux, sensible heat flux, and soil temperatures depended on soil heat conductivity and heat capacity parameters. Additionally, latent heat flux seemed to depend on both soil thermal properties but also on the stress thresholds for transpiration and evaporation, in addition to the hydraulic conductivity, air entry bubbling pressure, and pore distribution index. Soil moisture was more complex and sensitive to the saturated hydraulic conductivity and stress threshold.

(3) In arid environments (i.e. Santa Rita, AZ), differences in vegetation cover represented differences in the distribution of the surface energy balance components. For example, latent heat flux was always higher for grassland than creosote or mesquite cover. Also, at the grassland location, both sensible heat flux and soil temperature were lower due to higher ground coverage percentage. Ground heat flux was similar between the three cover types with slightly higher rates from March to June at the herbaceous cover and lower rates at the mesquite site. For soil moisture, mesquite experienced the lowest average values both at near surface and deeper soil layers.

(4) In forested sites, thinning of tall vegetation due prescribed fire (i.e. Flagstaff, AZ) reduced the amount of latent heat flux, sensible heat flux and the total net radiation

while increased the ground heat flux and soil temperature which led to reductions in soil moisture. The severity of the thinning was the main indicator on the subsequent responses of the surface-energy fluxes, soil moisture, and soil temperature.

(5) The damping depth in forest ecosystem and desert ecosystem exhibited seasonal variations and the partitioning of evapotranspiration showed the highest contribution came from soil evaporation for both ecosystems. Furthermore, the partitioning of evapotranspiration from the simulation outputs and the high agreement with actual sap flow measurements at US-SRC showed its potential to be used in future study to estimate the partitioning of ET without the need for expensive equipment and fieldwork.

(6) VisualtRIBS was developed to visualize the spatial outputs of the simulations and a collection of scripts were compiled into in R language to process MODIS satellite data and set up the tRIBS simulation folder. The calibration was also improved to simultaneously calibrate 26 parameters.

Results from this study can be used for providing new insights into the physics that drive the shifts in the land-atmosphere interactions due to vegetation phenology and abrupt changes in the land cover. All outcomes of this research will assist the U.S. Army Research Office through conceptualizations on the shifts in the land surface conditions for decision making on deployment and terrain operability as well as the Oklahoma Water Survey in assessing the relationship between vegetation and hydrologic cycle components.

Chapter 1: Introduction

Vegetation cover provides multiple benefits to both rural and urban ecosystems. Within the hydrologic cycle, vegetation helps preventing erosion (Duran et al., 2006; Feagin et al., 2009; Tiegang et al., 2013), promote soil layer development and facilitates water infiltration (Thompson et al., 2010; Abella et al., 2013; Frouz, 2017). In addition, vegetation converts solar radiation and atmospheric CO_2 into biomass, releasing oxygen and water (Panferov et al., 2001; Algimantas etal., 2010). Vegetation also provides shading to the soil and thus participates in the water and energy balances below canopy (Duveiller et al., 2018). In scenarios of abrupt or gradual land cover change, the status of vegetation will significantly alter both the energy and radiation aftermath locally and perhaps regionally. The ability of plants to intercept water and provide radiation sheltering affects the soil water content, while plant photosynthetic activity drives the movement of water from the soil to the plant stomata to determine evapotranspiration (expressed as latent heat flux). In addition, canopy cover regulates the partitioning of net radiation through reducing sensible and ground heat fluxes (Guillevic et al., 2002; Timouk et al., 2009). Soil moisture limits actual evapotranspiration when the available energy is not limited. Dryer soil also means higher temperature gradients between the surface and the atmosphere, which leads to higher flux of sensible and ground heats.

There have been studies on the effects of vegetation disturbance as well as vegetation phenology on the partitioning of surface energy fluxes, soil moisture and soil temperature. Duveiller et al. (2018) found that vegetation replacement due to agricultural expansion in the tropic regions led to an increase in surface temperature and a decrease in net radiation and evapotranspiration. Montes-Helu et al. (2009) found that the conversion

of ponderosa pines to grassland decreased the overall net radiation, latent heat, and sensible heat but increased the soil heat flux. In addition, latent heat flux became the dominant component of the surface energy balance during warm and wet seasons but sensible heat flux dominated the energy budget during cold and dry seasons. The shift from forest to grassland also caused the surface temperature to increase in the summer. Dore et al. (2010) reached the same conclusion where evapotranspiration was smaller post-thinning after ponderosa pine forest disturbance. The effect of reduced evapotranspiration due to forest disturbance also led to larger soil water storage and increased the magnitude as well as temporal variability of soil moisture (He et al., 2013).

For semiarid environments (Sanchez-Mejia et al., 2014), there is a significant relationship between deep soil moisture and land-atmospheric interactions that are modulated through surface vegetation. Lu et al. (2011) found that volumetric soil water content is the restriction on evapotranspiration rate and the top 50 centimeters contributed the most to the moisture loss in soil. In addition, according to the authors, detailed soil layer characteristics are essential in quantifying the interactions between evapotranspiration and vegetation root distributions. Kurc and Small (2004) conducted an analysis of in-situ measurements and their results highlighted the direct relationship between surface soil water storage and evaporation rate which accounted for a large fraction of the total evapotranspiration. Furthermore, they also found that utilizing only root-zone soil moisture to predict the evapotranspiration rate was inappropriate in the semiarid desert environment. A study by Gomez-Plaza et al. in 2001 compared the temporal changes in soil moisture controlling factors between an unburnt (abundant vegetation cover) and burnt (less vegetation) area in a semi-arid region. The authors found

that during wet conditions, soil moisture behavior at the unburned site was controlled by solar radiation and the physiology of vegetation cover whereas during dry periods, soil moisture at the area depended significantly on the amount of water drained to it from the contributing area at higher elevations. On the contrary, the main control factors at the burned site that regulated soil moisture were directly connected to the soil texture and the topographic slope of the study area that did not vary seasonally.

Vegetation phenology also played an important role in the partitioning of the surface energy balance. Schwartz and Crawford (2013) observed that the change in latent and sensible heats at the onset of spring season in Oklahoma was characterized by an abrupt change rather than a gradual one. The effect of inter-annual variations in vegetation on evapotranspiration was observed to be weaker at the regional scale due to a larger impact from atmospheric variations according to Guillevic et al. (2002). Dan and Jinjun found a high correlation between the seasonal variations of surface energy fluxes and LAI in northern mid-latitudes in their 2007 research and the importance of dynamic LAI on the partitioning of the surface energy fluxes was confirmed by Blyth et al. in 2010. The increase in LAI led to an increase in sensible heat flux in both shrubs and forest. However, the relationship between LAI and sensible heat flux was not linear as the changes of vegetation height from tundra to tall shrubs to forest which correspond to the increase in LAI are not at the similar rate as sensible heat flux, this suggests other physiological and structural parameters may control the sensible heat flux (Beringer et al., 2005). On the contrary, changes in surface temperature and latent heat flux were proportional to the changes in LAI (Lawrence and Slingo, 2004). Even though the mentioned studies have examined the effects of vegetation phenology on the partitioning of surface energy fluxes,

soil temperature, and soil moisture time series, the lack of long term measurements at the time of these studies through eddy covariance methods prevented further understanding into the long-term effects of vegetation shifts and the variables of interest.

Friedl demonstrated the viability of utilizing thermal remote sensing data in modeling the surface energy balance in his 2002 research study. Despite the shown viability, there is a lack of models that can incorporate both physical characteristics of soil and vegetation and remote sensing data to simulate all components of the surface energy balance, soil moisture, and surface temperature as well as their diurnal behaviors. The Mapping Evapotranspiration with Internalized Calibration (METRIC) model by Allen et al. (2007) relied on satellite data to estimate the evapotranspiration as the residual of the surface energy balance with high accuracy. However, it is only applicable for ET and the simulations can only be conducted for smaller regions and requires high-resolution weather data to make predictions. Furthermore, it also requires highly-trained experts with strong background in physics to operate the models, which makes METRIC inaccessible to the public and military personnel.

Regarding physically-based modeling, Kahan et al. (2006) found the importance of LAI, stomatal resistance, and hydraulic conductivity on the accuracy of computing sensible and latent heat fluxes while thermal diffusivity appeared to affect the diurnal variation in surface temperature. Overall, there is a shortage of research studies that tackle the understanding of the controlling factors, (i.e. soil properties and dynamic vegetation characteristics) on the soil thermal and hydraulic characteriscs and the surface energy budget components through the use of distributed hydrological model. The tin-based Real-time Integrated Basin Simulator (tRIBS) has the capability to both accept multi-parameters

from multiple sources (field observations and remote sensing data) and produce reliable predictions for all component of the surface energy fluxes, surface and root-zone temperatures, and soil moisture at sub-hourly time steps and over a prolonged periods of simulation. In addition to being a physically-based and distributed, this model has the capability to continuously ingest the spatially-varied terrain data and, through physics-based equations, represent the dynamic relationships between partially saturated vadose zone and land surface response to intra- and inter-storm events. tRIBS's efficient computational architecture and utilization of dynamic remote sensing data make it appropriate to utilize in this study. Previous studies have shown that tRIBS has the capability to perform quality simulations in a wide range of climatic conditions and complex terrains such as semiarid with ponderosa pine (Mahmood and Vivoni, 2011), mixture of pasture, agricultural grassland, and deciduous as well as evergreen forest (Kim et al. 2012), and Sinaloan thornscrubs and Madrean woodlands (Barroso et al., 2014). Simulations of evapotranspiration and soil moisture conducted with tRIBS also showed its reliability and consistency in estimating these variables over a long period of time at multi-scale from individual pixel to the whole catchment (Liuzzo et al., 2010; Vivoni et al., 2010). Using tRIBS, Ivanov et al. (2004) and Vivoni et al. (2010) found that the spatio-temporal variability of surface soil moisture within an area can be attributed to the variability of both precipitation and potential evapotranspiration, while at the root-zone level, the subsurface soil structure and texture play a major role. Also the authors found that landscape characteristics control the variability of soil moisture during prolonged dry periods. Ivanov et al. (2004) discussed the relationship between hydrological processes and land surface characteristics, and the links between surface water – groundwater dynamics using a

spatially distributed approach with tRIBS. The test simulations provided satisfactory results in deploying the model to different watersheds. In addition to adequately simulate surface runoff (Vivoni et al. 2008; Macaro et al. 2010; Moreno et al., 2012, 2013, 2014, Pierini et al. 2014; Robles-Morua et al. 2012), evapotranspiration (Mendez-Barroso et al. 2014; Moreno et al. 2016) and soil moisture (Ivanov et al., 2004, Vivoni at al. 2010; Mascaro and Vivoni, 2012; Mendez-Barroso et al., 2014, Mahmood and Vivoni, 2011; 2014; Mascaro et al. 2015), the tRIBS model can also be used to simulate land surface temperature (Xiang et al. 2014) with reliable results at high temporal resolution, despite sparse ground observation data. Its performance on simulating heat fluxes (latent, sensible and ground) was investigated by Mendez-Barroso et al. (2014) and was shown to produce reasonable results; however, underestimation of latent heat flux may occur in summer due to the model inability to account for deep soil layer (> 1 m) uptake of water.

The goals of this Master's thesis are to: (1) Compare the temporal variability of ground-surface and root-zone soil temperature and soil moisture and the components of the surface-energy budget across three contrasting environments (i.e. desert, grass, forest) and their responses to abrupt (i.e. precipitation, fire and thinning) and gradual (i.e. phenology) vegetation change; (2) Calibrate and validate a process-based, fully distributed hydrological model to facilitate simulation of synthetic vegetation scenarios and subsequent responses; (3) Estimate the partitioning of evapotranspiration and the soil temperature damping depth through the use of the calibrated model and evaluate the effects of vegetation and soil moisture; and (4) Create a visualization tool and automatic processing scripts to facilitate the collection and readiness of data inputs, simulations and output visualization in tRIBS.

The results from this study not only will contribute to the existing knowledge base of ecohydrology, hydrometeorology, hydrological modeling and vadose zone hydrology, but also to other disciplines such as meteorology in predicting changes in atmospheric fluxes at vegetation-disrupted areas, agriculture in determining the water budget and surface temperatures, and public policy for adapting to the long-term effects of vegetation disruption (e.g. thinning or burning), replacement (in cultivated areas) or substitution (in developed lands). The knowledge of the effects of the vegetation change on the surface energy fluxes, evapotranspiration partitioning, soil temperature profile, damping depth and surface and root-zone soil moisture will contribute to the enhance the state of the art in process-based modeling at gauged and ungauged regions. It will also provide researchers, scientists, and engineers tools to facilitate the simulation process and an integrated simulation platform from data processing to model setup and output visualization and analyses, which will further decrease the required time to process large amounts of data and potential errors. Furthermore, this research will provide a huge advantage to military operations as high-resolution distributed hydrological modeling can be applied to determine the soil moisture and fluxes at similar regions of interest as well as to pinpoint anomalies on the ground resulting from abrupt vegetation changes.

Chapter 2: Objectives and Goals

The overall objective of this study was to utilize observed time series from micro-meteorological observations sites and a physically-based model to investigate the effects of gradual and abrupt changes in vegetation cover on surface and root-zone soil moisture and temperatures, and surface energy fluxes at three different-ecosystem sites: (1)

Grassland in Marena OK, (2) Forest in Flagstaff AZ, and (3) Desert in Santa Rita AZ. The second objective of this study was to calibrate and validate a process-based, fully distributed hydrological model to facilitate the simulation of the study variables and the creation of synthetic vegetation scenarios and subsequent responses. The third objective was to assess the behavior of the soil temperature and its damping depth at these sites as well as the partitioning of evapotranspiration into three components: Evaporation from bare soil, evaporation from wet canopy, and transpiration. The damping depth will also be evaluated in terms of the vegetation cover and average soil moisture across ecosystems. The final objective was to produce and publish a number of scripts for data extraction, model setup, and visualization to help engineers and scientists perform this type of model simulations and to reduce errors from manual data processing. In particular, the visualization tool is expected to researchers and decision makers on the potential effects of land cover changes on the water and energy budgets. Down the road, the model will be used to help forecast the combined effects of severe drought and vegetation change on the overall water cycle at the regional scale.

Chapter 3: Study Sites, Data and Methods

4.1. Study Sites

This Master's thesis focused on three ecosystems each with different meteorological and soil-monitoring stations located within the states of Arizona and Oklahoma, United States of America. Detailed information about each site is presented in sections 4.1.1 to 4.1.3.

4.1.1. Forest Ecosystem

This ecosystem is located near Flagstaff, Arizona within the Northern Arizona Centennial Forest. The measurement sites are featured by three eddy covariance flux towers: US-FUF, US-FMF, and US-FWF. All three towers are surrounded by ponderosa pine forest. Figure 1 presents the locations of the three ECT at Flagstaff, AZ.

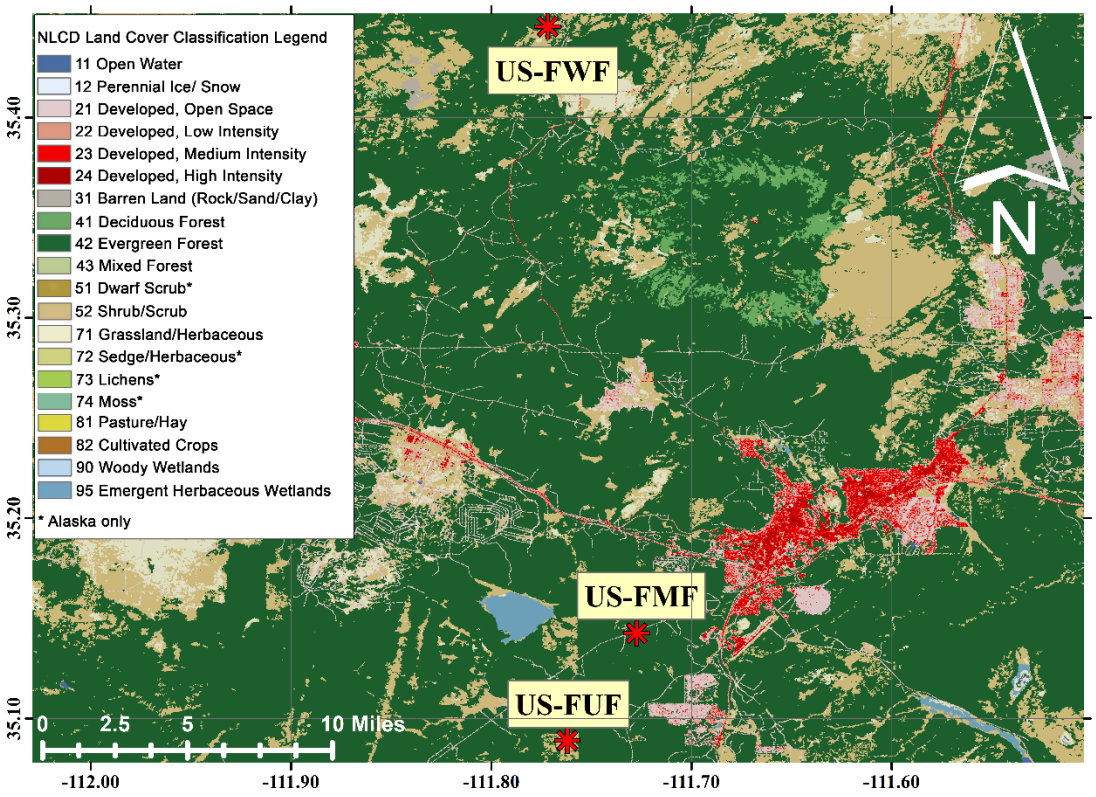

Figure 1: Regional locations of US-FUF (Control Station), US-FMF (2006 Thinning), and US-FWF (1996 Wildfire), the three forest eddy covariance systems, on a land cover map near Flagstaff, AZ.

US-FUF: The US-FUF Flagstaff Unmanaged Forest is the forest ecosystem control site, located in a public land, at an elevation of 2180 meters above the sea level where no historic disturbance has happened to vegetation (Dor et al. 2016). The soil composition is of fine montmorillonitic complex of frigid Typic Argiborolls and Mollic Eutroboralfs with

a gentle slope of less than 2% (Dor et. al, 2016). The A horizon consists of 37% sand, 39% silt and 24% clay while the B horizon has a textural combination of 31%, 34%, and 35%, respectively. The average canopy height of the ponderosa pine is 18 meters (Roman et al. 2009).

US-FMF: The US-FMF Flagstaff Managed Forest site was subjected to thinning and pruning of ponderosa pines, in September 2006 (Dor et al. 2006), but without surface vegetation replacement. Soil composition of the A horizon is 27% sand, 60% silt, and 12 % clay while for the B horizon 13% is sand, 46% is silt, and clay is 40%. The site elevation is 2160 meters above the sea level.

US-FWF: The US-FWF Flagstaff Wildfire site experienced a severe wildfire known as the Hochderffer Fire in June 1996. Due to this, the ponderosa pine was naturally replaced with grasses and early successional shrubs and forbs that occupy a flat area (Dor et al. 2016). Soil composition post-fire consists of 30% sand, 57% silt, and 13% clay for the A horizon and 20% sand, 55% silt, and 25% clay for the B horizon. The site elevation is 2270 meters above the sea level.

Figure 2 illustrates the two-dimensional flux footprint for each of the simulation sites, utilizing the Kljun's footprint prediction model (Kljun et al., 2015). The flux footprint is an important areal index in determining location and extent of the surface source areas. Compared to other flux footprint models such as the Large Eddy Simulation (LES; Luhar and Rao, 1994; Leclerc et al., 1997) or Eulerian models of higher-order turbulence closure (Sogachev and Lloyd, 2004), Kljun's model offers estimations of the fetch's width and shape as well as the effects of surface roughness on the contributing areas. In addition, the model can be estimated directly using measurements from the ECT

which makes it the suitable for the type of information available. It is observed from Figure 2 that less vegetation cover led to a larger footprint area. Thus, US-FWF has the largest contributing area which extended nearly 200 meters from the ECT while at US-FMF, the source area extended to only 60 m from the ECT.

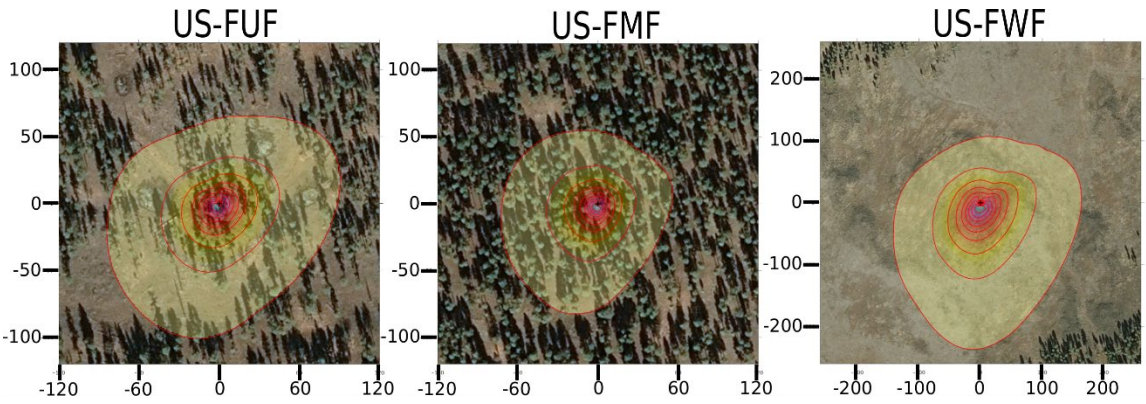

Figure 2: Climatological flux footprint at each of the ECTs within the forest ecosystem, based on the model developed by Kljun et. al (2015). Each contour line represents 10% increment inward, starting with 10% for the most external contour level. According to data availability, the periods of time used for each footprint are: US-FUF from 2006 to 2007, US-FMF from 2009 to 2010, and US-FWF from 2007 to 2008.

4.1.2. Desert Ecosystem

This ecosystem is part of the Santa Rita Experimental Range in southern Arizona, since 1911. It was founded in 1903 with oversight by the United States Forest Service with purposes of advancing research on ecology and desert rangelands. The research range holds a long-term collection of photographs of land cover changes since 1953, livestock grazing history since 1908, and monthly time series of precipitation since 1922. Location of the three ECTs of interest is presented in Figure 3 on a land cover type map.

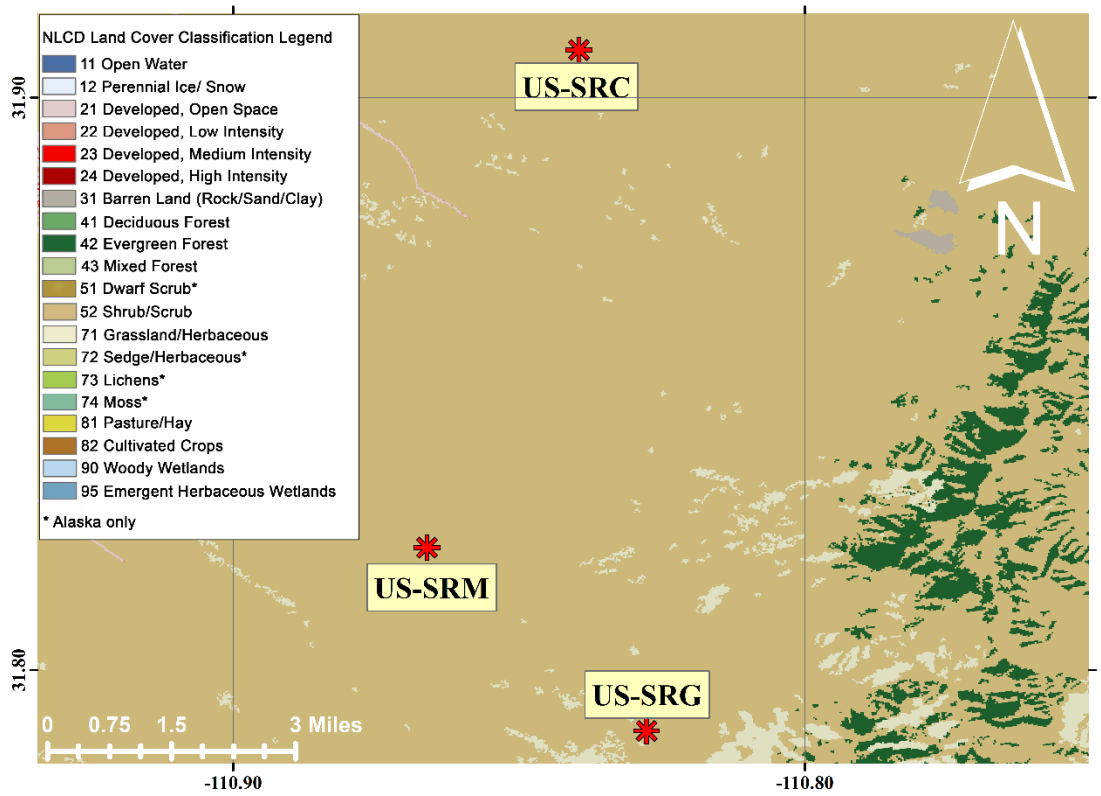

Figure 3: Regional location of US-SRC (Creosote-Dominated), US-SRM (Mesquite-Dominated), and US-SRG (Herbaceous Plants and Trees), the three desert eddy covariance systems within the Santa Rita experimental range on a land cover type map.

US-SRC: US-SRC Santa Rita Creosote is dominated by creosote bush (Kurc 2016) with an average canopy height of 1.7 m (Canavaugh et al. 2011). The site is located at an elevation of 991 m.a.s.l. in an area with a topographic slope between 5 and 10%. This site was commissioned in 2008. The soil at this site is classified as Sandy Loam, however, detailed information about each soil horizon is not available. The site elevation is 950 meters above the sea level.

US-SRM: US-SRM Santa Rita Mesquite is a semidesert grassland with dominant vegetation of mesquite trees and typical canopy height of 2.5 m in average (Kurc 2016). Mesquite has been the dominant vegetation at the area for the last 100 years with little

disturbance. The soil is characterized as sandy loam with 74% sand, 10% silt, and 15% clay. The site elevation is 1120 meters above the sea level.

US-SRG: Santa Rita Grassland is similar to US-SRM but with near 90% coverage of C4 perennial grass (Kurc 2016). The average canopy height at the site is 2.5 m (Canavaugh et al. 2011). The soil is characterized as deep loamy sands, however, similar to US-SRC, detailed information regarding each soil horizon is not available. The site elevation is 1291 meters above the sea level.

Contrastingly to the forest ecosystem, the three desert research sites do not experience any abrupt vegetation modification by thinning or fire. However, the sudden water and energy changes induced by the intermittent North American Monsoon showers are a significant driver of the vegetation, soil thermal and hydraulic conditions and of the partitioning of the surface energy budget. Flux footprints for each of the three ECTs are illustrated in Figure 4. It is observed that the contributing source area for creosote-dominated ECT (US-SRC) is the smallest with the 10% contributing contour approximately 80 m from the US-SRC ECT while the mesquite site (US-SRM) has the largest contributing source area with the 10% contribution contour extending more than 200 m from the ECT.

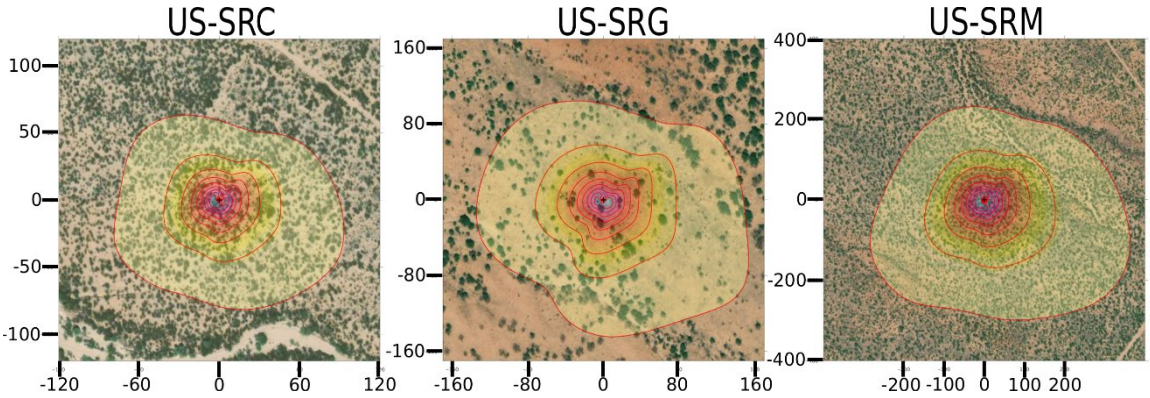

Figure 4: Climatological flux footprint contribution at each of the eddy covariance systems based on the model developed by Kljun et al. (2015). Each of the contour lines represent an increment of 10% of the frequency contribution to the fluxes observed at each ECTs starting from 10% at the most external contour. The following study periods were used to compute these footprints: US-SRC from 2009 to 2010, US-SRG from 2009 to 2010, and US-SRM from 2009 to 2010.

4.1.3. Grassland Ecosystem

The Marena, Oklahoma In Situ Soil Testbed (MOISST) is a research site in Marena, OK with focus on monitoring and comparisons between in-situ and remote sensing technologies for soil moisture. It was established in 2010 and led by Prof. Tyson Ochsner at Oklahoma State University and Dr. Michael Cosh at the United States Department of Agriculture. The site is characterized by its low topographic relief, well-drained silty clay loam soil with tallgrass prairie as the dominant vegetation. The ecological integrity of this research site is maintained by periodical burning every three years to remove red cedar encroachment and maintain the tallgrass prairie cover (Cosh et al. 2016). The exact dates of the most recent vegetation thinning are April 25th 2012, April 20th 2015 and April 10th 2018. The locations of the four soil moisture testbed locations and the MARE Mesonet tower are illustrated in Figure 5. For this study, data from MARE Mesonet tower and SMAP ISST Site A were used for tRIBS simulations and output validation due to the

incompleteness of the measurements at the eddy covariance tower. The MARE Oklahoma Mesonet station was included in this thesis due to the unreliable weather forcing measurements as reported by Celis (2019) within the eddy covariance measurements. Such variables are incoming shortwave radiation, wind speed, air temperature, atmospheric pressure, relative humidity, and precipitation. The climatological flux footprint at the single MOISST ECT in Figure 6 shows a total extension of the contributing area (up to the 10% contour line) of approximately 50 m in the East, West, and North directions and 100 m to the south.

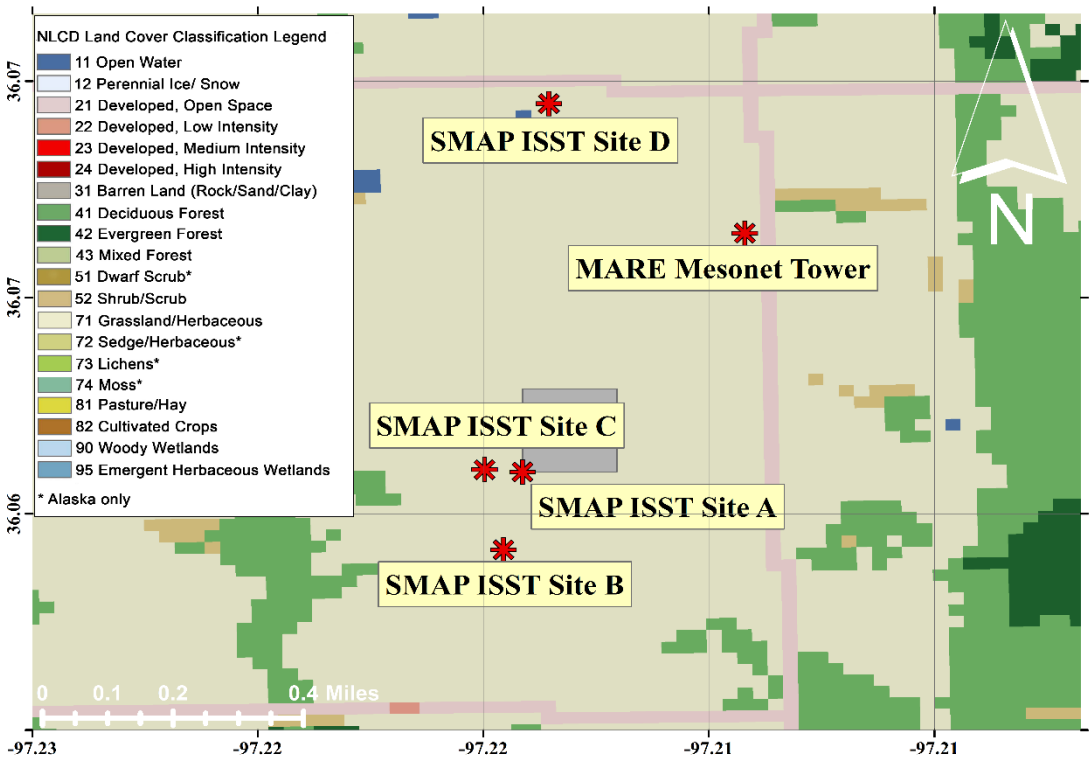

Figure 5: Regional locations of the Oklahoma MOISST research sites on a map of land cover types. Soil moisture data for the analysis and simulations pertain to site SMAP ISST Site A. The eddy covariance tower is also installed at the SMAP ISST Site A and the MARE Mesonet tower is shown in the eastern area. The grey rectangle denotes the northeastern patch where the controlled burning occurred.

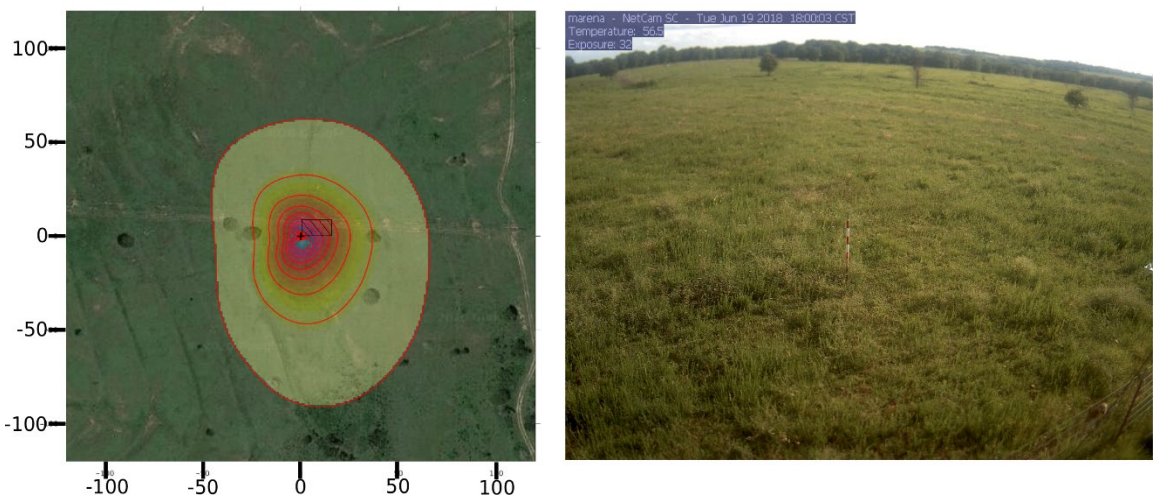

Figure 6: Climatological flux footprint contribution at the eddy covariance system (left) based on the model developed by Kljun et al. (2015). Each of the contour lines represent an increment of 10% of the frequency contribution to the fluxes observed at the ECT starting from 10% at the most external contour. The study period that was used to compute such a footprint was from 01/01/2016 to 12/31/2017. Phenocam image of surface vegetation cover at the ECT site (right). The shaded rectangle denotes the northeastern patch where the controlled burning occurred.

4.2. Data

4.2.1. In situ Micrometeorological, Vapor, Heat Flux and Soil Moisture Data

The data used for the numerical simulations of this study were collected from micrometeorological and soil measurements at eddy covariance towers (ECTs) located at each of the study ecosystems from both the AmeriFlux and FLUXNET networks. The measurements are stored at 30-minute temporal resolution. Weather forcing variables include incoming shortwave radiation (IS; $W.m^{-2}$), air temperature (Ta; °C), relative humidity (HR; %), wind speed (WS; $m.s^{-1}$) and atmospheric pressure (Pa; mbar) that are averaged to 1-hour temporal resolution. Precipitation (P; mm), is accumulated at 1-hour temporal resolution. In addition, the following measurements are also utilized for comparison, calibration, and validation purposes: Latent heat flux (λE; $W.m^{-2}$), sensible

heat flux (H; $W.m^{-2}$), net radiation (R_n; $W.m^{-2}$), surface temperature (T_s; °C), surface soil water content (SWC; degree of saturation) at 10 cm below the surface, and rootzone soil water content (RWC; degree of saturation) at 1 m below the surface, where applicable. The instruments at the sites are standardized and regularly calibrated and the measurements quality controlled

4.2.2. Satellite Data

The satellite information used in deriving the vegetation parameters for the numerical simulations was downloaded from the EOSDIS platform (https://earthdata.nasa.gov/eosdis). Such satellite products are summarized in Table 1.

Table 1: Remote sensing products utilized to capture terrain properties and dynamic vegetation. Product name, source, obatained parameters, spatial resolution, and temporal resolution, are included.

Product Name	Source	tRIBS Parameters Obtained	Spatial Resolution (meters)	Temporal Resolution (days)
Landcover	USGS	Landcover Type	30	N/A
Digital Elevation	USGS	Elevation	30	N/A
MCD43A	MODIS	Albedo	500	1
MCD15A3H	MODIS	LAI/fPAR	500	4
MOD13Q1	MODIS	NDVI	250	16

The land cover type determines vegetation and aerodynamic characteristics such as height, roughness and zero-displacement height. Albedo controls the amount of reflected incoming shortwave radiation. LAI, NDVI and fPAR play a critical role in describing vegetation cover and activity into the calibrated model. Leaf Area Index (LAI) has been used in many land-surface and climate models as it directly influences the passage of sunlight trough vegetation (Liang et al. 2012) and the interception of water (Rutter, 1965). LAI is obtained from NASA MODIS products (see Table 1) and is an important component

within the tRIBS equations used to estimate several vegetation parameters. According to Carlyle-Moses and Price (2007), the canopy field capacity (S, mm) can be calculated as (1):

$$S = 0.5LAI \tag{1}$$

Pitman (1989) introduced an exponential relationship to estimate the throughfall coefficient (p, unitless), also using LAI as (2):

$$p = e^{-1.5LAI} \tag{2}$$

The optical transmission (k_t, unitless) coefficient is also estimated using LAI (Xiang et al. 2014) with the relationship as (3):

$$k_t = e^{-0.61LAI} \tag{3}$$

The Fraction of Photosynthetically Active Radiation (fPAR, unitless) is another important parameter that indicates the portion of photosynthetically active radiation used by plants. fPAR is obtained from the same MODIS product as LAI (see Table 1). The absorbed photosynthetically active radiation can be estimated as (4):

$$Q = 0.45I_s fPAR \tag{4}$$

Where I_s is the incoming solar radiation, which is obtained directly from the eddy covariance tower measurements. The canopy stomatal resistance term (r_s, s/m) is estimated using an equation developed by Schulze et al. in 1995, shown as (5):

$$r_s = \left(\frac{1}{LAI}\right)\left[\frac{Q_{50}+Q}{g_{max}Q}\right] \tag{5}$$

Where g_{max} is the maximum stomatal conductance, Q is the value of the absorbed photosynthetically active radiation, and Q_{50} is the value of Q when g_{max} is half of its value. In 1999, Carlson and Ripley derived an equation using NDVI to estimate the vegetation

fraction (v_f, unitless), expressed as (6). V_f varies between zero (0) meaning no vegetation to one (1) meaning full vegetation cover at a particular modeling element:

$$v_f = \left[\frac{NDVI - NDVI_{min}}{NDVI_{max} - NDVI_{min}}\right]^2 \quad (6)$$

4.3 Process-based, Numerical Model

The tin-based Real-time Integrated Basin Simulator, tRIBS, is a physically-based, distributed model that utilizes spatially-varied atmospheric, soil and land cover parameters to simulate the hydrologic response and energy distribution within an area of study (Ivanov et al. 2004; Vivoni et al. 2005). The conceptualization of all processes linking hydrological processes and surface energy flux balance based on physical quantities, in addition to the model's resolution only constrained by the resolution of input data, allows tRIBS to be an appropriate tool for this research. Forcing variables used for the model simulations include precipitation (P), atmospheric pressure (PA), wind speed (WS), relative humidity (RH), and the incoming shortwave radiation (IS). All inputs are averaged from half-hourly to hourly time steps except for precipitation, which is accumulated into hourly intervals. Table 2 and Table 3 describe the tRIBS model inputs and the associated units for soil and vegetation parameters, respectively.

Table 2: Soil parameters and their units in tRIBS

Parameter	Description	Unit
Ks	Saturated Hydraulic Conductivity	mm/hr
Θs	Soil Moisture at Saturation	
Θr	Residual Soil Moisture	
m	Pore Distribution Index	
ψ_B	Air Entry Bubbling Pressure	mm
f	Decay Parameter	mm^{-1}
As	Saturated Anisotropy Ratio	
Au	Unsaturated Anisotropy Ratio	
n	Porosity	
ks	Volumetric Heat Conductivity	J/msK

Cs	Soil Heat Capacity	J/m^3K

Table 3: Vegetation parameters and their units in tRIBS.

Parameter	Description	Unit
a	Canopy Storage	mm
b1	Interception Coefficient	
P	Free Throughfall Coefficient	
S	Canopy Field Capacity	mm
K	Drainage Coefficient	mm/hr
b2	Drainage Exponential Parameter	mm^{-1}
Al	Albedo	
h	Vegetation Height	m
Kt	Optical Transmission Coefficient	
Rs	Canopy-Average Stomatal Resistance	s/m
V	Vegetation Fraction	
LAI	Canopy Leaf Area Index	
Θ^*_s	Stress Threshold for Soil Evaporation	
Θ^*_t	Stress Threshold for Plant Transpiration	

In tRIBS, soil moisture is computed based on coupled surface and subsurface processes (Vivoni et. al 2005, 2007). The unsaturated soil moisture profile is based on Brook and Corey equilibrium formula (1964) whereas the residual and the saturation soil moisture is acquired from the input parameters for each soil type (Ivanov et. al, 2004). Lateral soil moisture re-distribution is driven by the topographic gradient, groundwater topography and subsurface fluxes which include vertical recharge and exfiltration as well as horizontal fluxes from subsurface water flow.

4.4. Methodology

4.4.1. Surface Energy Fluxes, Soil Moisture and Soil Temperatures and Their and Vegetation/Precipitation-Induced Shifts

Comparison of surface energy fluxes, soil moisture, and surface temperatures among each set of ECTs at the Forest, Desert and Grassland ecosystems is conducted through statistical metrics and time series plots. For the MOISST site, 20 days of pre- and post-thinning measurements are separated and compared to determine the changes in magnitude of the variables of interests.

4.4.2. Damping Depth and its Vegetation and Soil Moisture-Induced Shifts

Damping depth characterizes the penetration of the daily thermal wave into the subsurface soil profile (Roxy et. al, 2014) in which the flux variation in the subsurface decreases with depth relative to that of the land surface variation. Specifically, it refers to the depth at which the amplitude of the thermal wave decreases to 1/e of the amplitude of the thermal wave observed at the surface. The expression for this characterization, i.e. the range of the soil temperature variation as a function of depth and time, is expressed through equation 7:

$$T(z,t) = T_{ave} + A_0 \exp\left(-\frac{z}{D}\right)\left[\sin(t-8) - \frac{z}{D}\right] \quad (7)$$

Where T(z,t) is the soil temperature at depth z at time t, T_{ave} is the average temperature over the period of interest, A_0 denotes the amplitude of the wave at the surface, and D is the damping depth. The minus eight (-8) in the equation denotes the typical lag time for heat to transfer downward to the subsurface medium. With measurements from two different depths, the damping depth is estimated using equation 8:

$$D = \frac{z_1 - z_2}{\ln(A_2) - \ln(A_1)} \quad (8)$$

Where D is the damping depth in meters, z_1 and z_2 are the depths at which the measurements are recorded. A_1 and A_2 are the differences between daily temperature and the monthly average surface temperature at depths z_1 and z_2 as expressed by equation 9:

$$A_i = T_{ave} - T(z_i) \quad (9)$$

These calculations are performed at eddy covariance research sites where there are at least two measurements of soil temperature at different depths, e.g. 2- and 10-cm or 10- and 100-cm. The damping depth is then calculated at hourly temporal scale based on the daily average temperature (T_{avg}) and hourly soil temperature measurements ($T(z_i)$) at the site. The resulting hourly damping depths are averaged to daily values due to the less representativeness of the soil temperature as a sinusoidal wave day to day (Jury et. al, 1991). Comparisons of the damping depths are conducted across stations within the same ecosystem (e.g desert and forest) and their changes after abrupt changes in vegetation (e.g. forest and grasses) and under pulses of precipitation (e.g. desert). For Santa Rita, the calculations of damping depth and its variability are performed for US-SRM and US-SRG using the soil temperature measurements at 5- and 10-cm due to the completeness in measurements and being the closest to the available depths at Flagstaff, AZ. The 5- and 10-cm depth of soil temperature measurements are also chosen so that the seasonal oscillations can potentially be observed in damping depths (Holmes et al., 2008). For Flagstaff, the calculations are performed for US-FUF and US-FWF using the soil temperatures at 2- and 10-cm as these are the only available soil temperature measurements. Finally, for MOISST site at Marena, OK, the damping depth was calculated

using the 2.5- and 10-cm depth soil temperature. For all ecosystems, the comparisons are conducted with daily damping depths over one-year period.

4.4.3. tRIBS Model Setup

tRIBS will be used to simulate (i.e. calibrate and validate) six variables at the voronoi element scale: net radiation, ground heat flux, sensible heat flux, latent heat flux, surface and root-zone temperature, and surface and root-zone soil moisture (as soil water content) during one-year long simulations to capture their diurnal and seasonal variability. LAI, NDVI and Normalized Burn Ratio (NBR), calculated from surface reflectance, are used to determine the vegetation phenology and sudden changes. Initial soil parameters such as hydraulic conductivity and porosity will be based on typical values from other studies at similar soil types while vegetation parameters such as vegetation height will be based on the site descriptions to provide the model with reasonable values.

4.4.4. tRIBS Model Calibration

After verifying that a spin-up simulation had successfully run without any errors, the Shuffled Complex Evolution (SCE) algorithm (Duan, 1993) was used as the calibration master. SCE partitions the solution space (soil and vegetation input parameters) into local communities (small groups of input parameters) and search for the best combinations based on the upper and lower limits of the input parameters as well as the optimization criteria. The calibration is performed at the control towers (at the Forest ecosystem) or for years previous to the historic abrupt changes (at the Grassland and Desert ecosystems) to find the parameter combination that minimizes the Root Mean Square Error (RMSE) between observed and simulated time series of the study variables. The calibration procedure is

expected to produce results similar to those observed at the eddy covariance systems. The Table 4 presents the calibration periods for the seven study stations.

Table 4: Selected periods for model parameter calibration previous to any abrupt changes with start and end date for each of the seven ECTs

Station	Calibration Start	Calibration End
US-FUF	01/01/2006 00:00	12/31/2006 23:00
US-FWF	01/01/2007 00:00	12/31/2007 23:00
US-FMF	01/01/2009 00:00	12/31/2009 23:00
US-SRC	01/01/2009 00:00	12/31/2009 23:00
US-SRM	01/01/2009 00:00	12/31/2009 23:00
US-SRG	01/01/2009 00:00	12/31/2009 23:00
MOISST	01/01/2016 00:00	12/31/2016 23:00

Due to the similarity in vegetation and soil types at the three research locations within the forest ecosystem and the lack of data before the wildfire in 1996 at US-FWF, the calibration performed at the control tower (US-FUF) becomes the benchmark for the other two towers. However, at the grass ecosystem, the lack of a control site obliged to the calibration of the model for periods previous to the vegetation disturbance and then after such events with the purpose of quantifying the changes in parameter values pre and post-fire.

4.4.5. tRIBS Model Validation

Model validation is performed for a time period different than the calibration with the purpose of assessing the temporal transferability of the calibrated parameters. The simulation results are then assessed by computing RMSE, CC, NSE, and Bias to determine if the calibrated parameters are adequate. The Table 5 describes the periods of model validation for all seven stations.

Table 5: Selected periods for model validation start and end dates for each of the seven ETCs

Station	Validation Start	Validation End
US-FUF	01/01/2007 00:00	12/31/2007 23:00
US-FWF	01/01/2008 00:00	12/31/2008 23:00
US-FMF	01/01/2010 00:00	12/31/2010 23:00
US-SRC	01/01/2010 00:00	12/31/2010 23:00
US-SRM	01/01/2010 00:00	12/31/2010 23:00
US-SRG	01/01/2010 00:00	12/31/2010 23:00
MOISST	01/01/2017 00:00	12/31/2017 23:00

Observed values of the six variables of interest (ground heat flux, latent heat flux, sensible heat flux, net radiation, soil moisture and soil temperature) are plotted and compared against each other to determine the difference in their magnitude before and after the abrupt changes (at the Forest and Grassland ecosystems) and seasonally to determine the effect of vegetation phenology (at the Desert ecosystem).

4.4.6. Evapotranspiration Partitioning and its Vegetation/Precipitation-Induced Shifts

The partitioning of ET into transpiration, evaporation from bare soil, and evaporation from wet canopy is conducted through the built-in tRIBS's partitioning module. This partitioning is only verified for the Santa Rita, AZ sites due to the presence of model validation data. Such an assessment is performed for year 2009 at monthly scale aiming to reduce noise and diurnal fluctuations. Absolute and percent differences in the rate of evapotranspiration components among the three sites were computed to provide insights into the main contributors to the total ET. Partitioning results from tRIBS were compared to a machine learning-based method developed by Moreno et al. (2020) to evaluate the agreements between the two. At Flagstaff, AZ, the partitioning was performed

for US-FUF and US-FWF for year 2007. However, due to the absence of observed or modeled data on the ET partitioning there was not verification of the partitioning at these sites.

4.4.7. Soil Temperature Damping Depth and its Relation to Vegetation and Soil Moisture.

Daily tRIBS simulated soil temperature at the surface and root-zones were used to estimate damping depths across all ecosystems and create scatterplots relating damping depth versus daily average soil moisture (at the surface and root-zone). In order to elucidate the relations between damping depth and vegetation, simulated tRIBS outputs were also plotted against LAI.

4.4.8. Partitioning of ET and Site Inter-comparison

Partitioning of evapotranspiration was conducted through the built-in tRIBS's partitioning module. The corresponding partitions were visualized and compared using three different figures for each of the seven stations across Oklahoma and Arizona. The first comparison was made with the monthly average rate of ET and its components: transpiration, soil evaporation, and wet canopy evaporation. The second comparison was made utilizing similar monthly average rates of ET but in relative term as the percentage of contribution of ET partitions on the total evapotranspiration rate. The third comparison was carried with the hourly rates of ET and its components for the months of June, July, and August to assess the change during the transition from dry season to wet season at the desert and forest ecosystems.

4.4.9. Comparison of the Soil Temperature Damping Depths Pre- and Post-Disturbance

The comparison of damping depths pre- and post-disturbance was conducted between US-FUF and US-FWF through the use of daily time series of tRIBS-modeled damping depths for a whole year from January 1st to December 31st, 2007. In addition, time series of soil temperature at all available depths were also utilized to visualize the changes in amplitude of soil temperature.

Chapter 5: Results and Discussion

5.1. Effects of Abrupt and Gradual Vegetation Change on Surface Energy Fluxes, Shallow and Root-Zone Soil Moisture and Temperature and Soil Temperature Damping Depth.

5.1.1. Forest Ecosystem

Figures 7 and 8 illustrate inter- and intra-annual comparisons between the control (US-FUF), burned (US-FWF) and thinned (US-FMF) sites at the forest ecosystem of all variables of interest. The following lines summarize the observations per variable:

Precipitation: Figure 7 (last panel) illustrates the time series of monthly precipitation from 2006 to 2011 at each of the three stations in Flagstaff, AZ. At the control site, US-FUF, received the highest amount of precipitation in summer 2006 while US-FWF received the highest amount of precipitation in summer 2007 and summer 2009. Overall, with the exception of some months in 2006 and 2007, the precipitation time series showed similar patterns in magnitude and phase between the three sites in Flagstaff, AZ.

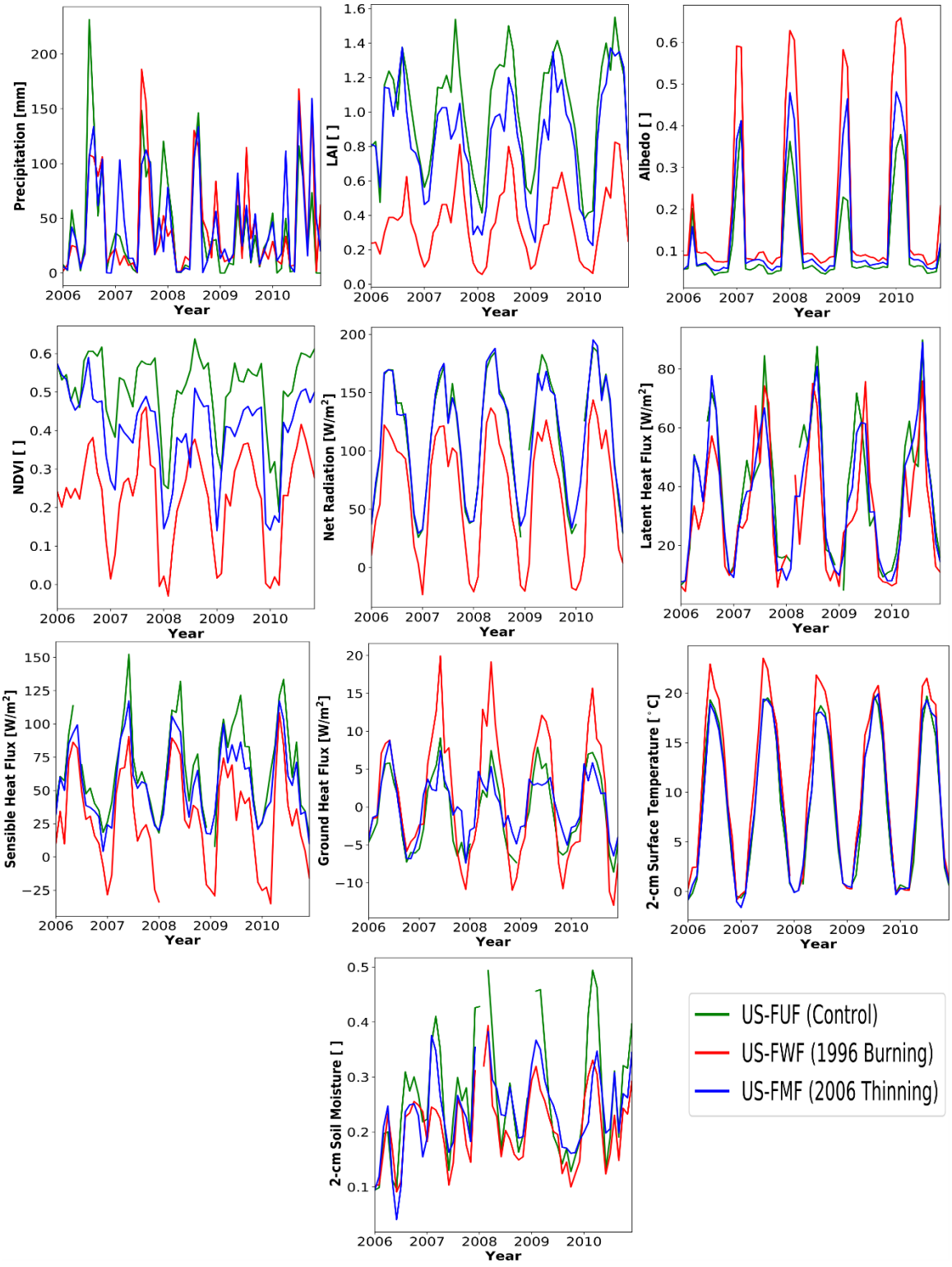

Figure 7: Time series comparison of LAI, NDVI, albedo, net radiation, latent heat flux, sensible heat flux, ground heat flux, soil temperature at 2cm, soil moisture at 2 cm and precipitation at the control (US-FUF), burned (US-FWF) and thinned (US-FMF) sites.

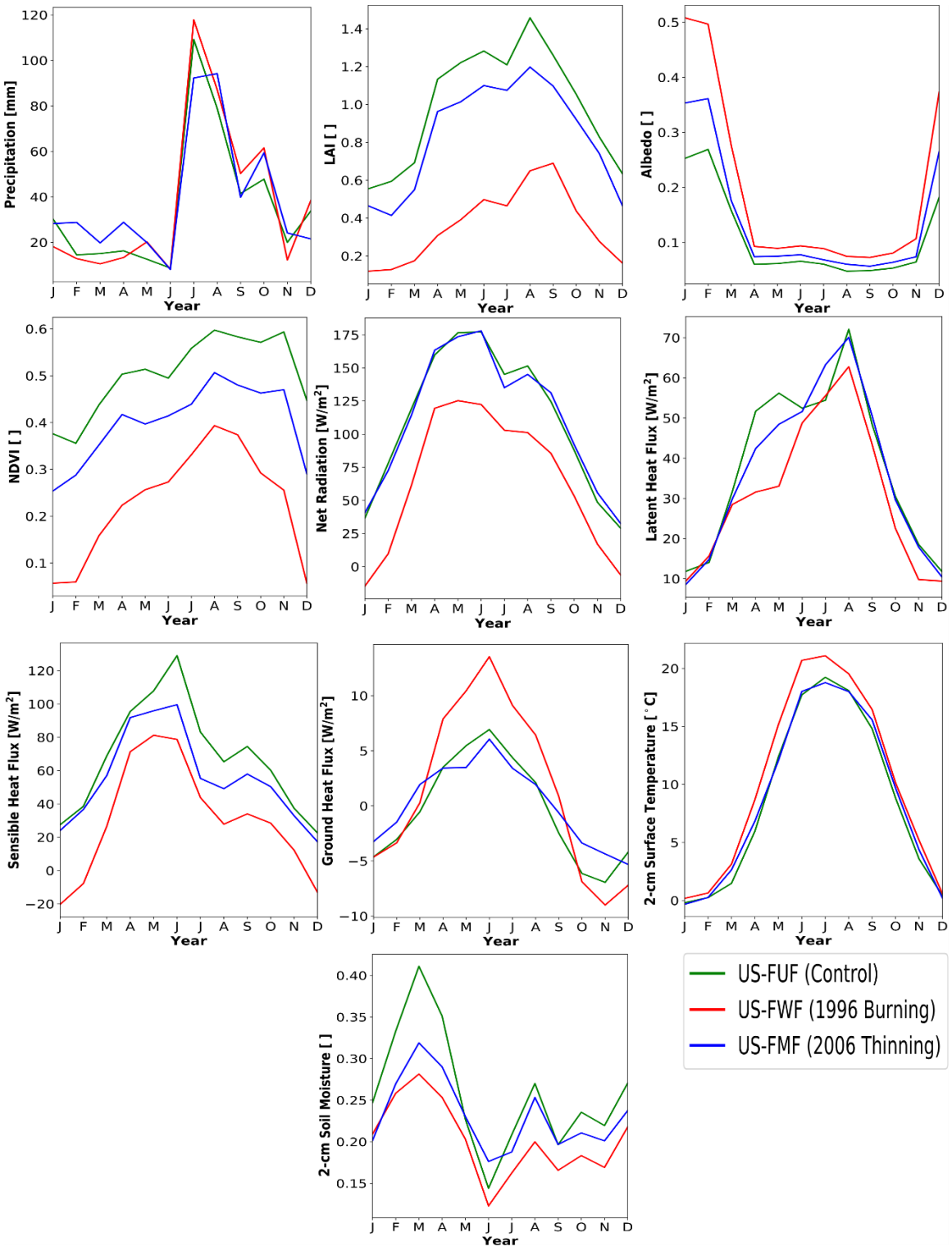

Figure 8: Monthly average values of (from left to right, and top down) precipitation, LAI, NDVI, albedo, net radiation, latent heat flux, sensible heat flux, ground heat flux and soil temperature at 2 cm, soil moisture at 2 cm at the control (US-FUF, green line), thinned (US-FMF; blue line) and burned (US-FWF, red line) sites over the period of 2006 to 2010.

Figure 8, complementarily, illustrates the average monthly precipitation over the period of 2006 to 2010. Precipitation is unimodal across all three stations with a peak in July and August forced by the Monson system.

LAI: Time series of monthly averaged LAI values in Figure 7 illustrate similar time phasing but magnitude differences between the three stations. In order of magnitudes, US-FUF was always higher than US-FMF and this one higher than US-FWF. At US-FUF values ranged between 1.2 and 1.6 in summer and between 0.5 and 0.8 during winter for most of the period between 2006 and 2010 with an exception in early 2006 where observed LAI at US-FMF was higher. At US-FMF summer time values typically ranged from 1.0 to nearly 1.4 and winter time values from 0.3 to 0.6. The effects of thinning at US-FMF can be seen clearly with significantly lower LAI values in summer 2007 months. In addition, its recovery or replacement of shrubs and grasslands can also be seen from 2007 onward with LAI gradually increased year over that year. Understandably, LAI values at US-FWF with severe disturbance from wildfire in 1996 were the lowest both in winter and summer. Furthermore, it also had the largest differences in LAI compared to the other two stations, ranging only from less than 0.1 to 0.8 annually. The time series of LAI in figure 7 also shows the long-term consequences of wildfire where the effects of thinning can be observed a decade later. The monthly-averaged LAI values over the period of 2006 to 2010 (Figure 8) also presents a similar picture with US-FUF's LAI being the highest, followed by US-FMF's LAI and US-FWF's LAI. Additionally, the seasonal variations of LAI are easily observed in Figure 8 where lowest LAI were observed in January while highest LAI occurred in September. Another interesting observation was the slope of LAI transitioning

from winter to summer time. At US-FWF such a slope was milder than the slopes of LAI at US-FUF and US-FMF which were observed to be steeper.

Albedo: Time series of albedo at US-FWF were the highest, followed by US-FMF and US-FUF. This is reasonable as undisturbed ponderosa pine forest with high LAI values at US-FUF would absorb more incoming radiation while at the human-induced thinning at US-FMF and the wildfire disturbed US-FWF, bare surface and replaced grass and shrubs would reflect more incoming radiation back to the atmosphere. From Figure 7, it is also observed that there was sudden increase in albedo values at the three sites in December and January, this can be explained by the presence of snow on the surface and the needle shredding by the ponderosa pines which enhanced the reflection of solar radiation during winter months. Generally, the time series of albedo were consistent between the three stations over the year. However, there was an outlier in early 2006 where albedo was significantly lower possibly by the relatively dry winter and low snow accumulation (see Figure 7 precipitation time series). From Figure 8, most of the differences in albedo were concentrated during the winter months, as opposed to summer months where albedo remained similar with smaller variations between the three stations.

NDVI: From both Figure 7 and Figure 8, it is observed that time series of NDVI mimic the observed patterns and differences in LAI with highest NDVI observed at US-FUF, followed by US-FMF and US-FWF with lowest NDVI. The highest values of NDVI at US-FUF occurred during summer months and ranged from 0.5 to 0.6 indicating undisturbed, extensive coverage of ponderosa pine forest. The effects of human-induced thinning at US-FMF in Fall 2006 can also be observed with the sudden drop in NDVI values during summer 2007 onward. At this site, NDVI ranged from 0.5 to 0.6 in summer 2006 to 0.4 to

0.5 indicating loss of some ponderosa pines as well as the replacement of shrub and grass at the disturbed area. For the winter months, NDVI at both US-FUF and US-FMF displayed smaller differences between 0.15 to 0.3. Similar to the observations of LAI, the effects of the 1996 wildfire remained visible at US-FUF a decade later with a summer NDVI of 0.3 to 0.4 which indicated extensive loss of ponderosa pine forest, increase in amount of bare soil and replaced shrubs and grassland. The extensive vegetative loss was further amplified during the winter months with NDVI below zero during some periods. Average monthly NDVI over the 5-year period from 2006 to 2010 in Figure 8 displays peak NDVI in August, matching the observed peak LAI in August. The extensive loss of vegetation at US-FWF was clearly visible in the same Figure 8 with significantly lower monthly NDVI compared to US-FUF and US-FMF.

Net Radiation: Figures 7 and 8 illustrate the inter- and intra-annual time series of monthly averaged net radiation from 2006 to 2010, respectively. Mean monthly net radiation values showed little difference across the control and thinned sites despite clear difference in LAI, Albedo and NDVI between them. Specifically, net radiation at the thinned site ranged from 0.98 to 1.08 times that at the control site or a difference of just 0–|10| $W.m^2$ (see Tables 6 and 7). On the other hand, net radiation values at the burned site were considerably smaller, ranging from -1.5 to -2.0 times those at the control site, or a difference of 35 to 60 $W.m^{-2}$ below the values reported at the control station. The reason for such a drastic change in net radiation between the burned and control as well as human-induced thinning sites could be attributed to increased outgoing (i.e. upward) terms of the radiation balance as a result of both increased albedo and upward long-wave radiation due to a reduced vegetation fraction, which could be seen through the lower LAI and NDVI values at US-FWF. These

reasons led to a clearer surface that created a more reflective and hotter ground (see Figure 7) post-fire, thereby increasing the radiative heat loss at US-FWF.

Latent Heat Flux: Similar to net radiation, latent heat flux was higher for the control and thinned sites but slightly lower for the burned site. It can be observed that latent heat flux is low during the winter months due to lower net radiation and LAI values and increased throughout the summer period as a result of higher net radiation and vegetation cover for all three stations. Surface energy balance-wise, latent heat flux was the second largest component. US-FMF experienced a reduced latent heat flux in 2007 as a result of the human-controlled thinning which was also observed through reduced LAI and NDVI values during the same period. The two seasonal peaks in the time series of LE every year in April and August obeyed to increases in net radiation and vegetation activity (i.e. LAI and NDVI) respectively. Compared to US-FUF, latent heat flux at US-FWF had noticeably lower overall values by the reduced vegetation fraction (Figure 7) and the low latent heat flux during the winter was observed to be similar to that of US-FMF. From Figure 8, the months from March to May were characterized by significantly lower LE at US-FWF at about 30 $W.m^{-2}$, compared to 50 to 60 $W.m^{-2}$ at US-FUF. August to November saw sharp decreases in latent heat flux, similar to US-FUF and US-FMF while LE remained nearly constant at 10 $W.m^{-2}$ in November and December. Despite having the highest amount of monthly average precipitation accumulation in July and overall lower LAI and NDVI, latent heat flux in July at US-FWF was only slightly higher than that at US-FUF, suggesting that even though bare soil would enhance the evaporation, transpiration had more significant role in the forest ecosystem. Comparatively, it seems like the effects fire affected more clearly the evapotranspiration rate by reducing it more drastically than the

thinning event even though this wildfire event occurred in 1996 and the controlled thinning 10 years later in 2006.

Sensible Heat Flux: Mimicking the patterns of net radiation, sensible heat flux was always lower at the US-FWF. Being the largest component of the surface energy budget for US-FUF and US-FMF, differences between post-thinning sensible heat flux at US-FUF and US-FMF sites were more evident during the summer months, as seen in Figure 7, with the control site showing higher values in excess of 15 to 30 $W.m^2$. Sensible heat flux at the burned site was considerably smaller than at the control site with differences ranging from 25 to 50 $W.m^{-2}$. In addition, during the winter months, sensible heat flux at the wildfire site was negative, meaning that surface soil was extremely cold and heat was instead transferred downwards from the atmosphere to the surface. From the same Figure, low winter NDVI and high albedo values at US-FWF indicated the presence of snow which explained the observed downward sensible heat flux. Another interesting observation is that even though US-FMF experienced a disturbance to its vegetation cover recently, its sensible heat flux direction was never downward to the surface, this leading to the conclusion that the extent of disturbance (through LAI and NDVI) highly influenced sensible heat behaviors. From Figure 8, it can be observed that sensible heat flux has a major peak in May-June and a second one in September. LAI and latent heat flux show an inverse relation with sensible heat flux as high LAI values occur simultaneously with low H values and vice versa. As high LAI values decrease the amount of radiation reaching the surface, and high latent heat flux would slower the rate of temperature increase, the two reasons make sensible heat flux decrease. Sensible heat flux was also observed to be related

to the occurrence of dry spells. This can be seen in Figure 8 where the highest sensible heat flux value was synchronous with the lowest accumulation of the precipitation in June.

Ground Heat Flux: The smallest component of the surface energy budget at Flagstaff, AZ is ground heat flux. The three stations reported similar patterns in ground heat flux with the highest annual variability (i.e. highest summer and lowest winter values) at US-FWF. Ground heat flux displayed unique behaviors in 2006 with almost no difference between the three stations. This outlier of ground heat flux also corresponded to the abnormally low albedo observed in 2006. The inter-annual variations in albedo can explain the variations in ground heat flux where high albedo in winter reflects more radiation back into the atmosphere which would lower the amount of heating the surface received. This also explains why ground heat flux was negative, i.e. heat was transferred upward, during the winter months at all three stations. On the other hand, low albedo during the summer months allowed more radiation to reach and heat the surface, causing the downward direction and increasing the rate of heat transfer. From 2007 until 2010, ground heat flux at US-FMF varied slightly compared to that of US-FUF with most of the differences happening during the late summer months. In addition, fluctuations in ground heat flux at US-FMF between its winter low and its summer high were less extreme than those observed at US-FWF. Obviously, the extreme of ground heat flux at US-FWF was due to having barer ground, and as a result, allowed more radiation to heat the surface during the summer and vice versa during the winter. Averaged ground heat flux over six years, as shown in Figure 8, showed another interesting observation, the ground heat flux in January and February was almost identical between US-FUF and US-FWF while G at US-FMF was noticeably higher despite the disturbance at both US-FMF and US-FWF. From the

same Figure, it is also observed that the peak of ground heat flux for the three stations matched the peak of sensible heat flux in the month of June and also corresponded to the month with lowest precipitation. Furthermore, even with the human-induced disturbance at US-FMF, its average monthly ground heat flux during summer was just slightly lower than at US-FUF. On the other hand, ground heat flux at US-FWF was almost three times higher than the other two stations, reaching almost 20 $W.m^{-2}$ in June. One possible explanation is that the disturbance at US-FWF was more extensive which created barer surface and the replaced vegetation did not fully cover the bare surface, making the fluctuations of with modified soil properties ground heat flux more extreme. In the case of US-FMF, the human-induced thinning was less severe, the loss of ponderosa pines was not as extensive and the disturbance did not alter the soil properties as much.

Surface Soil Temperature: The time series of surface temperature in Figure 7 show that US-FWF consistently had the highest values particularly during summer months compared to the two other sites. This was also consistent with higher ground heat flux observed at US-FWF. Clearly the peak of insolaton determines the phase of the annual cycle of soil temperature. In addition, it was observed that temperature at US-FMF was slightly higher than at US-FUF which the explanation is similar to that of US-FWF.

Surface Soil Moisture: The time series of soil moisture show that the soil at US-FUF could retain more water compared to the soils at US-FWF and US-FMF (See Figure 7). This could be explained by the loss of the litter layers due to disturbance at US-FWF and US-FMF which provides more capability to store water at US-FUF. In addition, vegetation disturbance produced hydrophobic conditions in the soil that increased the amount of runoff after each precipitation event, leaving less water to infiltrate into the soil and

therefore producing drier soil. This was reinforced from the recorded precipitation which was generally higher for most of the year at US-FWF than at US-FUF. Despite the variability in magnitude, monthly values of soil water content illustrate a typical annual cycle with a major peak in spring (March to April), possibly due to snowmelt, and a minor peak in August due to summer precipitation.

Annually, the mean values evidence that the US-FMF site showed the largest changes in soil moisture from 0.17 in 2006 pre-thinning to 0.24, or a 41.18% increase post-thinning from 2007 to 2010. The change in surface soil moisture can be seen from Figure 8 even though the seasonal precipitation depths remain relatively similar. Similar to US-FWF, the thinning at US-FMF caused the runoff to increase which decreased the amount of infiltrated water. From Figure 8, the precipitation accumulation was higher from January to June at US-FMF but the its soil moisture remained well below the soil moisture at US-FUF.

In order to gain a closer look to the response of soil moisture to precipitation and seasonality, time series of soil moisture at different depths (2- and 10-cm) for both US-FUF and US-FWF are shown in Figure 9 for a typical year 2007. Soil moisture at such two depths was consistently higher at US-FUF from March to December. On the other hand, despite precipitation is lower from February to April, the higher soil moisture values are a result of the lower net radiation and snowmelt processes in the region. It can also be seen that despite the month of September, the surface soil moisture at 2 cm is always higher than the value at 10 cm depth.

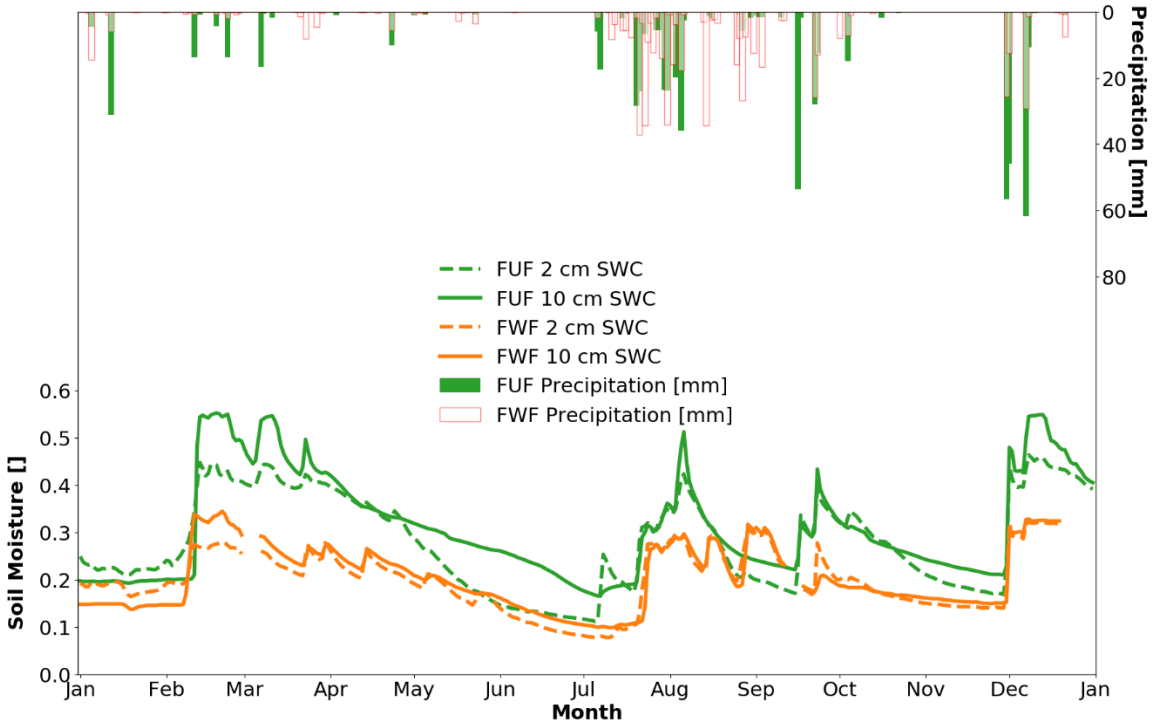

Figure 9: Time series of surface soil moisture at 2 cm and 10 cm depth at US-FWF (solid lines) and US-FUF (dashed lines) in 2007. The total precipitation at US-FUF was 636.6 mm and the total precipitation at US-FWF was 559.8 mm.

Soil Temperature Damping Depth: Figures 10 and 11 illustrate the time series of soil temperature at 2 and 10-cm depths at US-FUF and US-FWF for an example year (i.e. 2007). The comparison was performed only between US-FUF and US-FWF due to the soil temperature at 10-cm depth malfunctioned for the whole period of measurement at US-FMF. At US-FUF and US-FWF, both soil temperatures had similar variability year-long following the annual cycle of isolation. Between January and March and from September to December, soil temperature at both stations remained near or below zero at both depths. However, the soil temperature at 10 cm depth was higher than the surface temperature, indicating warmer sub-surface conditions. This was also observed by negative ground heat flux at both sites during the same time period. The soil temperature also exhibited a sharp

decrease in mid-September for both soil depths which also matched the higher precipitation accumulation of the same period that cooled the surface. At the same depth (i.e. 2-cm and 10-cm), soil temperatures at the control tower were lower than US-FWF, particularly from June to September. The observed differences between US-FUF and US-FWF could obey to the fact that for ponderosa pine forest the higher shading provided by higher LAI, NDVI values make the atmospheric temperature, instead of the incoming solar radiation, the controlling factor of the soil temperature. This is particularly evident during the summer months. The sinusoidal cycles in soil temperature at both sites also showed that the shallower depth was more susceptible to atmospheric forcing as illustrated in Figures 10 and 11 with increased temporal variability as indicated by the sharper rises and declines in the 2-cm soil temperature layer. Figures 12 and 13 illustrate the time series of the estimated damping depth at US-FUF and US-FWF for year 2007.

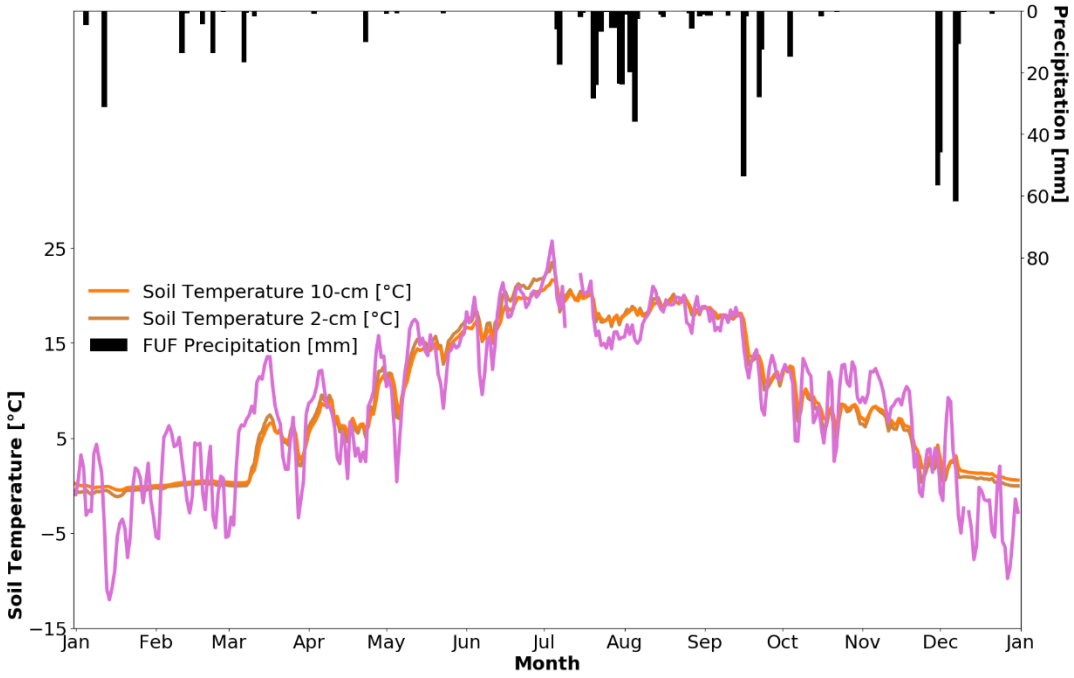

Figure 10: Time series of soil temperature at 2- and 10-cm depth at US-FUF during 2007.

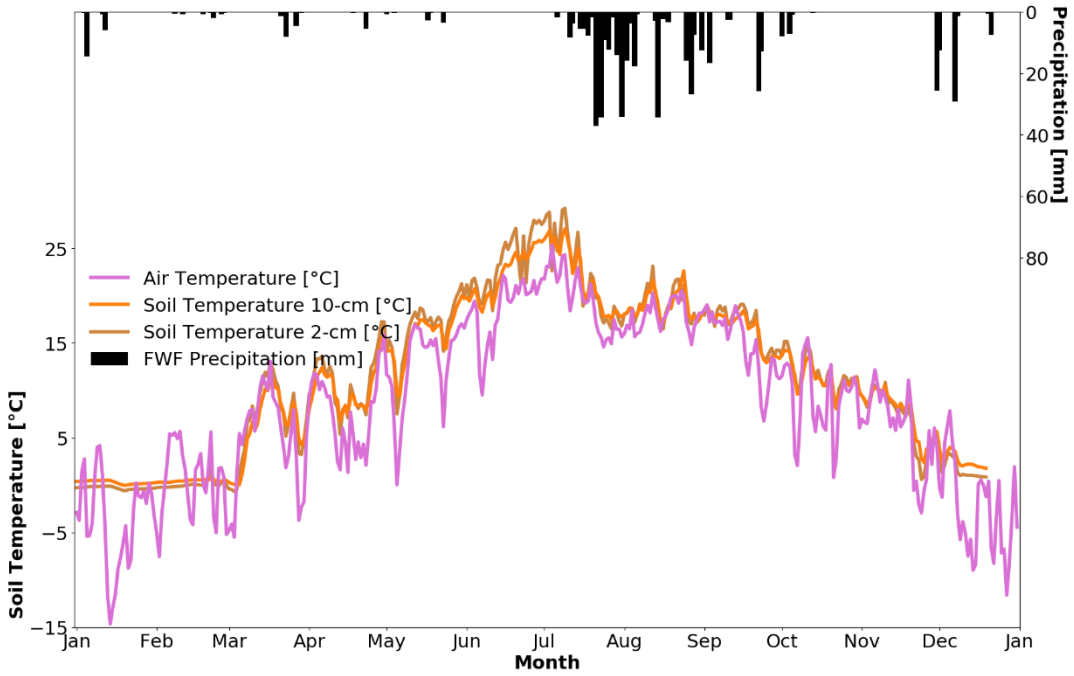

Figure 11: Time series of soil temperature at 2- and 10-cm depth at US-FWF during 2007.

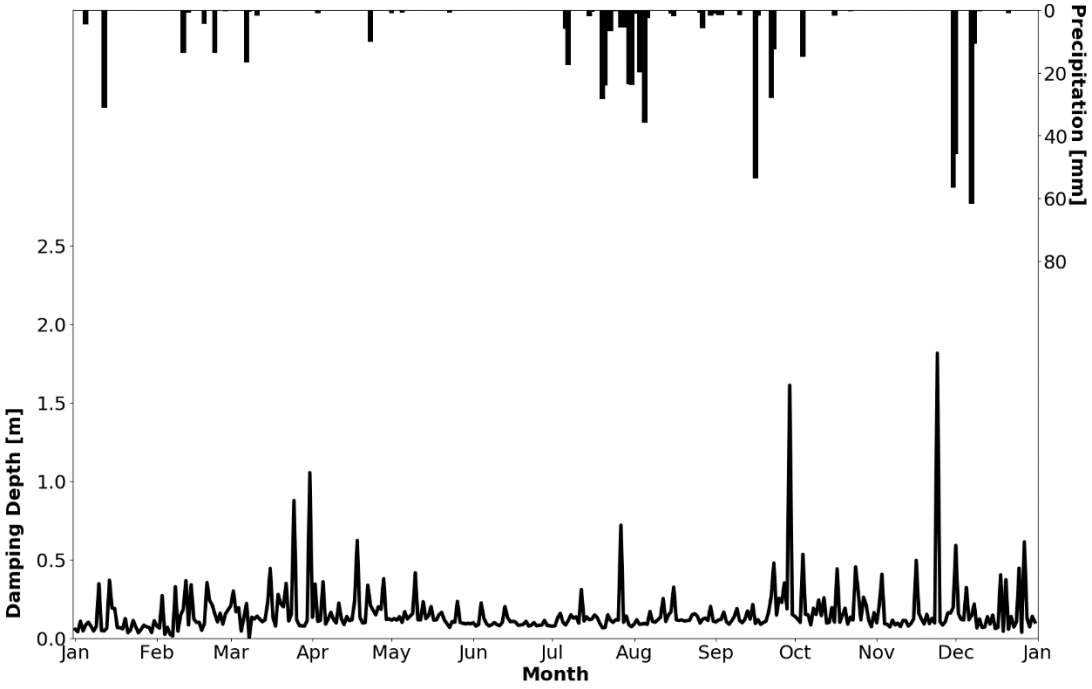

Figure 12: Time series of computed damping depths at US-FUF for year 2007. The depths that are used to compute damping depth are 2 and 10 cm.

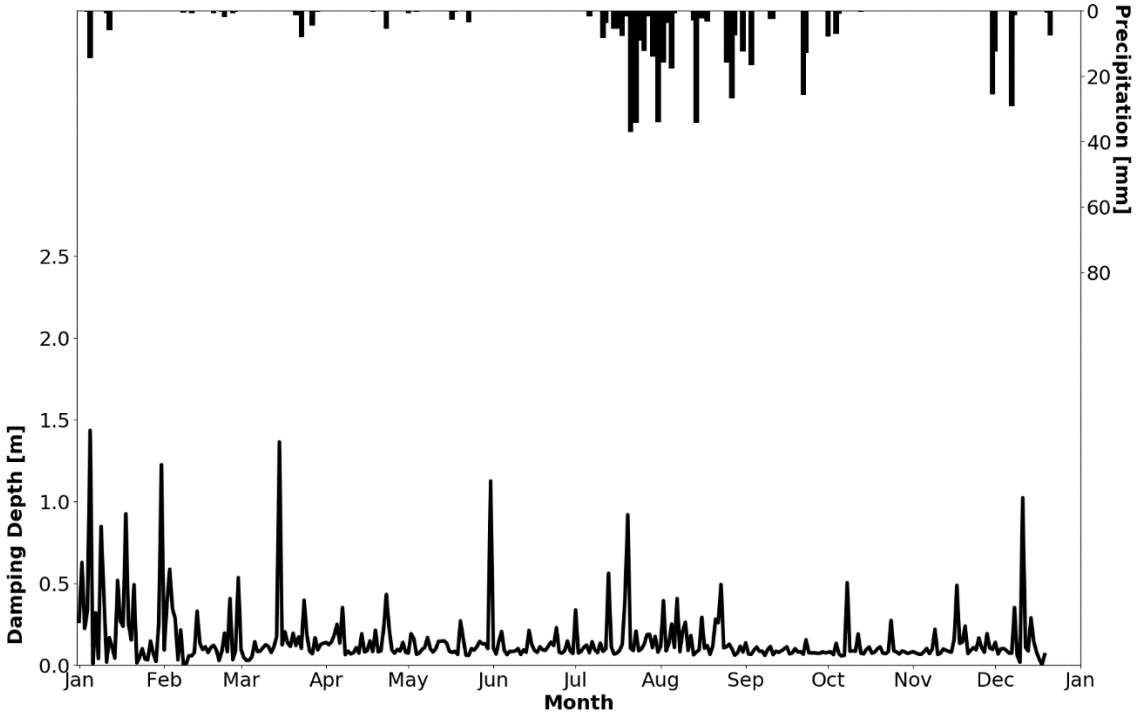

Figure 13: Time series of calculated damping depths at US-FWF for year 2007. The depths that are used to compute damping depth are 2 and 10 cm.

Figures 12 and 13 illustrate that, at US-FUF and US-FWF the soil temperature damping depth can have significant fluctuations from one day to another. Possible reasons for the fluctuations could be attributed to the amount of precipitation accumulation as soil moisture influences the thermal properties of soil (thermal conductance and specific heat) as well as the variability in air temperatures seen in Figures 10 and 11. Nevertheless, the two stations hold similarities and differences. At US-FUF the damping depth varies within 0.1 m to 2 m depth with shallower (between 0.1 m and 0.5 m) depths concentrated during the summer period from mid-May to mid-September. Precipitation had less effect on the damping depth at US-FUF due to high LAI which intercepted more rainfall, thereby reducing its cooling effect on the surface but also providing sheltering for insolation. The shallower damping depths at US-FUF during the summer months could also be explained

by the cooler temperatures at 10-cm at US-FUF due to the higher coverage of vegetation that reduced the income of solar radiation below canopy making the temperature gradient between 2- and 10-cm depths larger in the summer and resulting in shallower damping depths. At US-FWF, with the exception of January to March and mid-December, the calculated damping depths were relatively less variable with fluctuations between 0.1 and 0.3 m depth. Contrastingly, the damping depths were significantly higher from January to March with its maximum ranging from 2 to 3 m. Less vegetation cover at US-FWF allowed the subsurface temperature to be higher and retain more heat during winter which made damping depths of the same period higher. During the summer months, more radiation could reach deeper soil layers due to the lack of vegetation cover (as seen with low LAI and low albedo). Furthermore, due to the vegetation disturbance, more precipitation could be transformed into runoff instead of infiltrated water to cool off the deeper soil layer. The two reasons caused the summer damping depths to increase at US-FWF.

5.1.2. Desert Ecosystem

Figures 14 and 15 show the inter- and intra-annual variability of precipitation, LAI, NDVI, albedo, net radiation, surface energy balance components, surface and root-zone soil temperature and moisture for each of the three different vegetation study sites at Santa Rita, AZ with Mesquite (US-SRM), Creosote Bush (US-SRC) and Grassland (US-SRG) vegetation within the desert environment, from 2008 through 2014.

Precipitation: The interannual time series of precipitation illustrate similar patterns across sites with highest values with 2008 and 2010 being the wettest years. Furthermore, US-SRG appear to have the highest precipitation values among the three sites, followed by US-SRM and US-SRC.

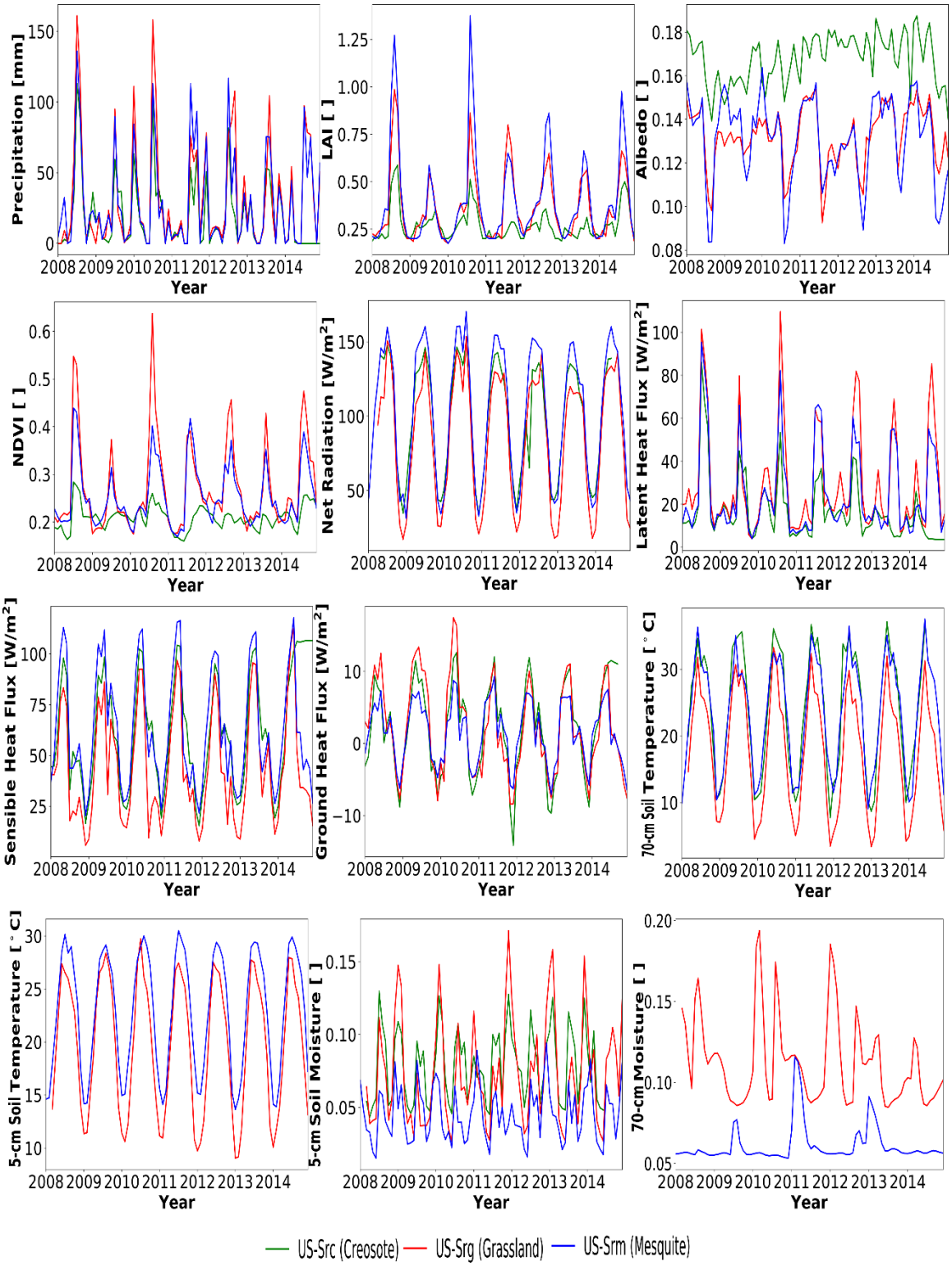

Figure 14: Time series comparison of precipitation, LAI, NDVI, albedo, net radiation, surface energy balance components, soil temperature and moisture at the surface (at 2 cm) and root-zone (70 cm for US-SRM and US-SRG) within the desert study sites in Santa Rita, AZ over the period from 2008 to 2014.

From Figure 15, US-SRC was observed to have significantly lower amount of precipitation compared to the other two sites particularly during the Summer Monsoon period. July was the month with the highest precipitation values across sites. The average precipitation in July at US-SRC was only 65 mm compared to 100 mm at both US-SRG and US-SRM. The months from January to June were characterized by similar precipitation values between the three sites with average rainfall between 20 mm in January and near zero in May. From October to December, precipitation at US-SRC once again was noticeably lower, at 10 to 30 mm, compared to 15 to 40 mm at US-SRG and US-SRM. Rainfall at US-SRG also decreased more gradually from July to September compared to US-SRC and US-SRM where precipitation decreased significantly from July to August.

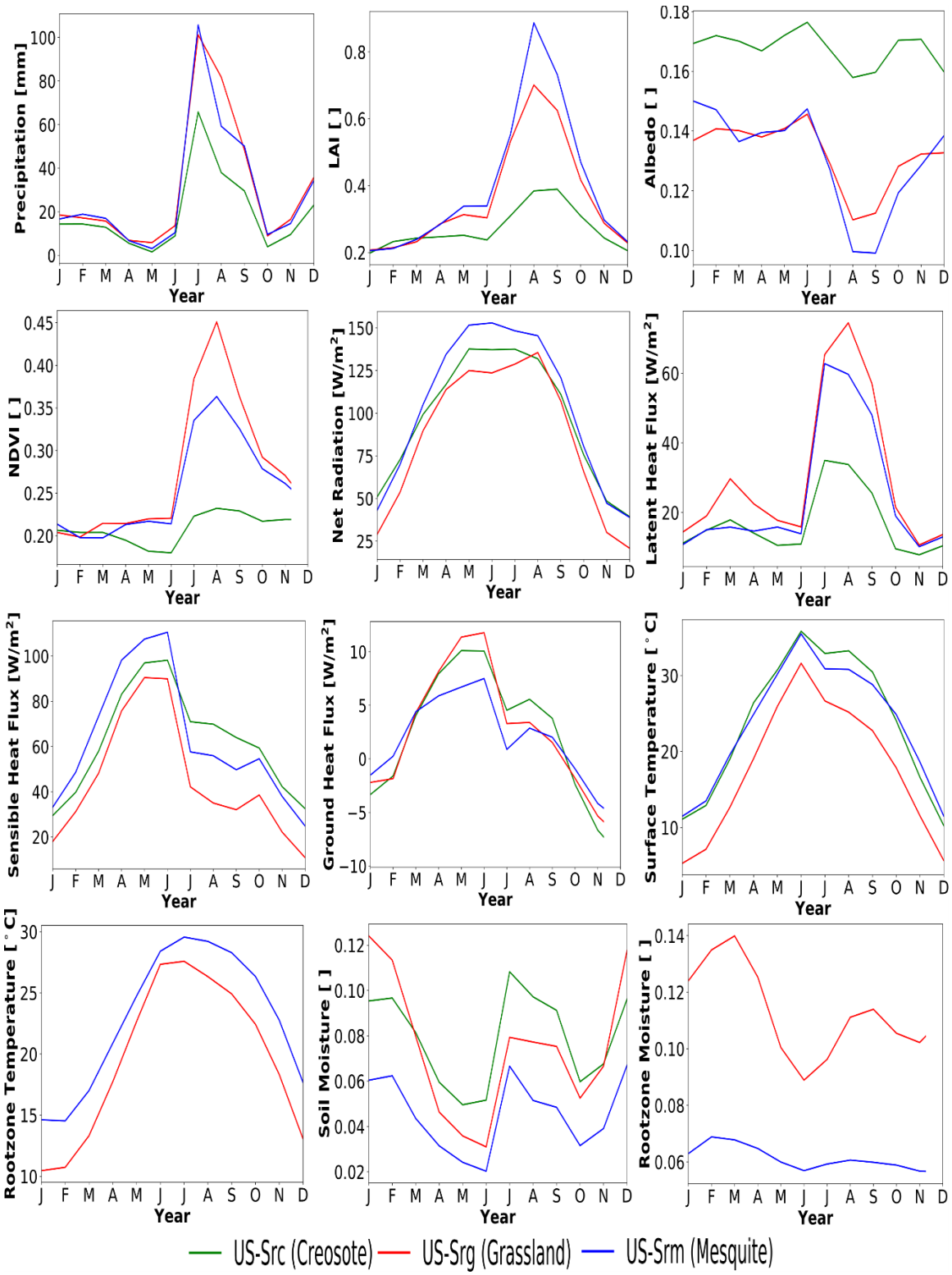

Figure 15: Monthly averages of precipitation , LAI, NDVI, albedo, net radiation, surface energy balance components, soil temperature and moisture at the surface (at 5 cm) and root-zone (70 cm for US-SRM and US-SRG) within the desert study sites in Santa Rita, AZ over the period from 2008 to 2014.

LAI: The three desert stations show similar patterns of vegetation cover and density fluctuations across years. Higher LAI values across all three stations occur in summer 2008 and 2010 simultaneously with the higher precipitation values during the same period at 1.25, 1.0, and 0.55 for US-SRM, US-SRG, and US-SRC, respectively. US-SRC had the lowest LAI while US-SRM has the highest LAI for most of the years between 2008 and 2014. The only exception was 2011 where LAI at US-SRG was the highest during the summer months. Similar to the three stations in Flagstaff, AZ, LAI values at Santa Rita were low in the winter months and sharply increased during summer with a peak in either August or September. Despite the substantial difference in summer months, winter LAI between the three stations was relatively similar at about 0.2.

Albedo: Albedo at US-SRC was the highest with monthly average values over the seven years' period between 0.16 and 0.18. December 2014 was characterized by abnormally low albedo at US-SRC which was not seen at either US-SRG or US-SRM. US-SRM and US-SRG had similar albedo values during the time period (see Figure 14). At the interannual scale, (Figure 15) it is seen that the lowest albedo values occurred in August and September of each year which correspond with the highest LAI in summer. The drastic reduction in albedo, is particularly evident at US-SRG and US-SRM. On average, the period from January to March was characterized by higher albedo at US-SRM. March to June was characterized by similar albedo between the two sites, ranging from 0.14 to 0.15. Both stations experienced a sharper drop in August and September compared to US-SRC with lowest albedo at US-SRG and US-SRM at 0.11 and 0.10, respectively. Overall, the range

of albedo values at the three stations suggested high percentage of highly reflective, bare ground with low vegetation cover.

NDVI: Despite the similarities between the time series of LAI and NDVI across the desert sites, US-SRG showed the highest values along the time series, despite US-SRM showed the highest LAI. This might mean that US-SRM with higher vegetation cover and denser architecture still showed less greening than the grasses at US-SRG. This might be related to potentially higher photosynthetic activity at US-SRG. Similar to LAI, the exceptionally higher NDVI in 2008 and 2010 was also observed in tandem with the high precipitation values of the same period, especially at US-SRG but not that marked at US-SRC. Furthermore, similar to LAI, NDVI was observed to be the lowest at US-SRC across the years with monthly average values between 0.15 and 0.22 over the period of 2008 to 2014 (see Figure 15). The highest monthly average NDVI was observed at US-SRG at 0.45, followed by US-SRM at 0.37 occurring in August for all three stations.

Net radiation: There are not significant differences in net radiation among the three desert sites, except by a pattern of higher summer values in US-SRM (Figure 14). As observed on Figure 14, mesquite-covered environment (US-SRM) presented the highest values of net radiation, followed by Creosote bush (US-SRC) and C4 Grassland (US-SRG). The highest net radiation at US-SRM is explained by its lowest albedo values which allow more radiation to be absorbed by the ground surface. US-SRC had the second highest net radiation despite its albedo values being the highest. The reason for this could be due to the lowest precipitation measured at US-SRC where the heat dissipation effects from rainfall was reduced, thus allowed more radiation to reach the surface. Net radiation at US-SRG peaked in August compared to the June peak at US-SRC and US-SRM. The lowest

albedo in August at US-SRG could be the reason for its peak in net radiation while the lowest measured precipitation in June could be the reason for the earlier peaks in June for US-SRC and US-SRM.

Latent Heat Flux: The two exceptionally high periods of precipitation, LAI and NDVI and low albedo in 2008 and 2010 are also observed through the time series of latent heat flux (Figure 14). The lowest values of latent heat flux were always observed at US-SRC as explained by both by its lower measured precipitation and LAI values. Combined with the highest albedo at US-SRC, it is safe to conclude that evaporation from bare soil was the main contributor to the total latent heat flux. This was consistent with the physiology of creosote that fold their leaves to reduce transpiration during the summer months. On average, the maximum rates of latent heat flux occurred in July for US-SRC and US-SRM according to the peak in precipitation during the same month (Figure 15). On the other hand, the peak LE at US-SRG was observed in August which matched the highest LAI and lowest albedo values at this site. The difference in peak occurrence of latent heat flux at US-SRG could further be explained by a milder decrease in precipitation at the site from July to August compared to shaper decrease observed at the other two stations. Latent heat flux was the largest component of the surface energy balance from July to September, and the second largest component during the remaining months at US-SRG and US-SRM. For US-SRC, latent heat flux was the second largest component year-round. The magnitude of latent heat at US-SRC was 1.8 times lower than that of US-SRG and US-SRM, annually-averaged with the highest difference in August at 2.2 times lower and lowest difference in January at 1.3 times lower, compared to US-SRG. In addition, there was a sharp decrease between March and August for both US-SRC and US-SRG which corresponded to the

substantially smaller amount of precipitation accumulation at the area during this time period at about 2 to 8 mm.

Sensible Heat Flux: Sensible heat flux at all three stations showed similar patterns with no sudden changes from 2008 to 2014 (Figure 14). Mesquite (US-SRM) had the highest sensible heat flux during the first semester of the year while Creosote (US-SRC) raised to the highest in the latter half of the year (Figure 15). Grassland (US-SRG) remained with the lowest values year-round. The highest values of sensible heat flux occurred in the month of June across sites. High values of sensible heat occur when low LAI are observed. Lower LAI allow more incoming radiation to heat the surface and increase the temperature gradient between the surface and the atmosphere. In addition, the maximum sensible heat flux coincided with high albedo values when more incoming radiation was reflected back to the atmosphere thus increasing sensible heat. Furthermore, the low precipitation values in the first six months of the year favored higher values of sensible heat flux. Sensible heat flux increased quickly from its low in January to the peak in June before sharply decreasing for the remaining months of the year. From Figure 15 it is also observed that the monthly average sensible heat flux had a slight increase in October at US-SRG and US-SRM.

Ground Heat Flux: As seen in Figure 14, the time series of ground heat flux showed similar patterns from 2008 to 2014 with slightly higher ground heat flux values at US-SRG. This component was the smallest flux among the energy budget components with values ranging from -10 $W.m^{-2}$ to 15 $W.m^{-2}$ at three stations. Negative values from October to March indicated a warmer sub-surface that conditioned an upward heat direction. The monthly average of ground heat flux, in Figure 15, shows maximum values in May and June, coincided with peak of sensible heat flux and minimum precipitation. Winter was

characterized by negative ground heat flux values, indicating upward direction of heat energy and warmer subsurface. Despite the high average albedo in the first six months of the year, ground heat flux was at the highest during this period. One possible explanation is that both LAI and NDVI were both also low during the same period so even though the surface reflected more radiation back to the atmosphere, the amount that reached the surface was high enough to increase the temperature gradient between the surface and subsurface layer. Due to high LAI and high precipitation accumulation, ground heat flux remained low at US-SRM and the subsurface temperature was not as warm. Overall, Mesquite-dominated vegetation (US-SRM) had the lowest seasonal variability in monthly average ground heat flux from 7.5 $W.m^{-2}$ in June to -5.8 $W.m^{-2}$ in December, compared to grassland- (US-SRG) and creosote-dominated (US-SRC) areas from 11.8 $W.m^{-2}$ in June to -7.3 $W.m^{-2}$ in December and from 10.1 $W.m^{-2}$ in June to -9.1 $W.m^{-2}$ in December, respectively.

Surface Temperature: Time series of surface temperature in Figure 14 show similar patterns among stations with slightly higher values in US-SRM and US-SRC. Overall, surface soil (at 2cm) temperature did not decrease below zero for the entire duration of 7 years of analysis. Similar to sensible and ground heat flux, surface temperature at Santa Rita was low during winter months and rapidly increased during summer months with peaks in June, matching the peak of sensible heat flux and ground heat flux as well as the low precipitation period. The surface temperature at US-SRG was noticeably lower than at US-SRC and US-SRM station. This is explained by higher albedo values at US-SRG that reflected more shortwave radiation back to the atmosphere, thus lowering the surface temperature. In addition, soil moisture at both surface and rootzone were higher at US-

SRG which helped dissipating the heat better. On the contrary, despite large differences in precipitation, LAI, and albedo between US-SRC and US-SRM, their surface temperatures were almost identical. A potential explanation is that the lower soil moisture at US-SRM reduced the soil ability to dissipate heat and in turn increased the surface temperature. For US-SRC, its high albedo reflected more radiation back to the atmosphere and less amount of radiation reached the surface; this combined with its high soil moisture prevented the surface from getting hotter.

Rootzone Temperature: Due to the instrument malfunction, there was no recorded deeper soil temperature at US-SRC. Figure 14 and Figure 15 shows that the soil temperature at US-SRG was 2 to 5°C cooler than at US-SRM. The higher NDVI at grassland environment could explain the cooler temperature where the dense vegetation cover provided cooling effects that reduced the amount of radiation penetrating the bare soil. Furthermore, the higher soil moisture and higher latent heat flux also helped dissipating the heat which in turn, lower the deeper layer soil temperature. On the contrary, lower latent heat flux, soil moisture at US-SRM, combined with higher water demand by mesquite as well as the lower vegetation coverage reduced the cooling effect of the canopy and water, allowing more radiation to penetrate deeper into the soil and increased the soil temperature.

Surface Soil Moisture: Soil moisture at 2 cm depth appeared to be higher at both US-SRM and US-SRG (Figure 14). It's evident that precipitation has a primary influence on surface soil moisture, particularly during July to September, November, December, and January to March (See Figure 15). Compared to the soil moisture observed in the forest ecosystem at Flagstaff, AZ, Santa Rita had significantly lower moisture across three sites with maximum measurements slightly above 0.15. The lowest surface soil moisture was observed at US-

SRM while there was more variability in moisture at US-SRG and US-SRC. Another observation made from the time series of soil moisture is that the seasonal variability at US-SRG was the largest. The larger seasonal difference at the grassland station could be attributed to higher variability in NDVI and related evapotranspiration. With the deeper and more interconnected root systems, of the grasses, more water could infiltrate the soil during the wetter months and vice versa. Therefore, more water could evaporate or transpire during drier months. The lowest soil moisture observed at US-SRM was explained by the fact that mesquites consumed two to three times more water (Klemmedson, 1977) than grassland which depleted the infiltrated water quickly despite similar amounts of precipitation occurred in both sites. US-SRM had the lowest monthly-averaged soil moisture from 0.06 in January and July to 0.02 in June. Similarly, surface soil moisture at US-SRC had its lowest value in May at 0.055 to its highest of 0.11 in July. US-SRG had the steepest drop in surface soil moisture from its highest in January of 0.12 to its lowest of 0.03 in June. In order to have a closer look Figures 16, 17 and 18 illustrate the time series of soil moisture at US-SRG, US-SRM and US-SRC at the levels for which data are avaible for an example year of 2009.

Rootzone Moisture: Similar to the rootzone soil temperature, the soil moisture measurements for US-SRC was not available at the 70-cm depth. From both Figure 14 and Figure 15, it is seen that the soil moisture at 70-cm depth was constantly lower at US-SRM than at US-SRG. The lower rootzone soil moisture in the mesquite-dominated area corresponded to the larger water consumption by mesquite, as mentioned in the surface soil moisture section. The higher demand by mesquite led to the withdrawal of water from

the deeper soil layer by its roots, resulting in significantly lower rootzone soil moisture with moisture remained near 0.06 for most of the period between 2008 and 2014.

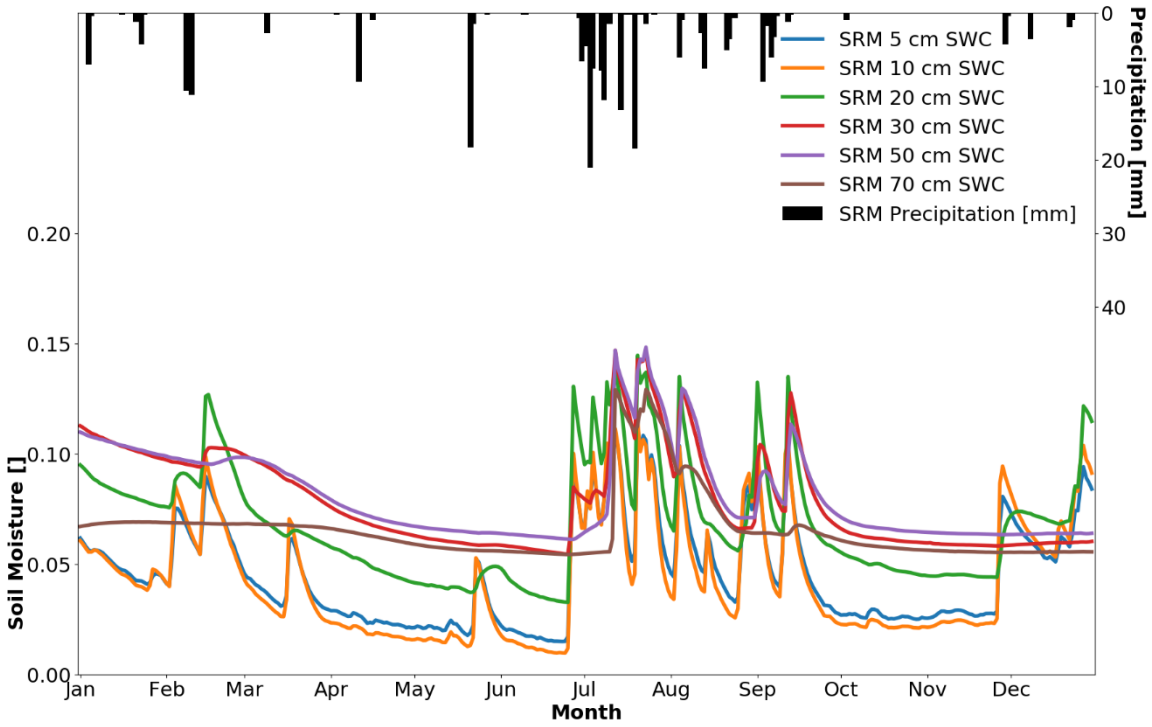

Figure 16: Time series of soil moisture at 5, 10, 20, 30, 50, 70-cm depth at US-SRM in 2009

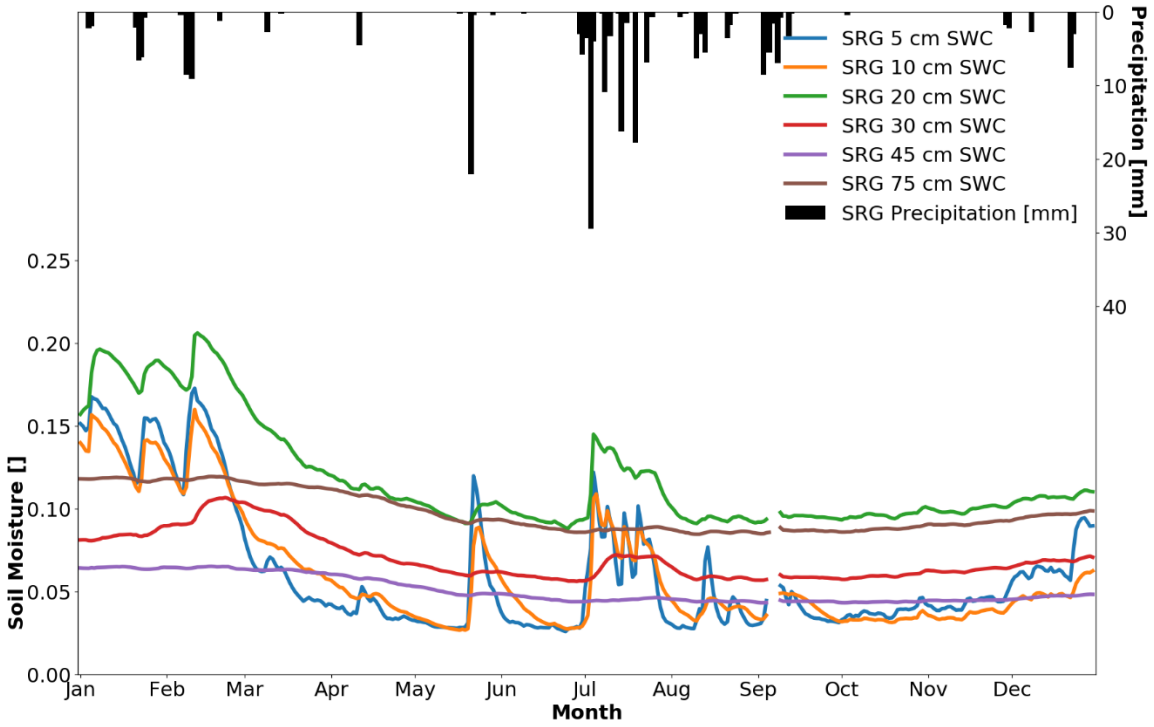

Figure 17: Time series of soil moisture at 5, 10, 20, 30, 45, 75-cm depth at US-SRG in 2009

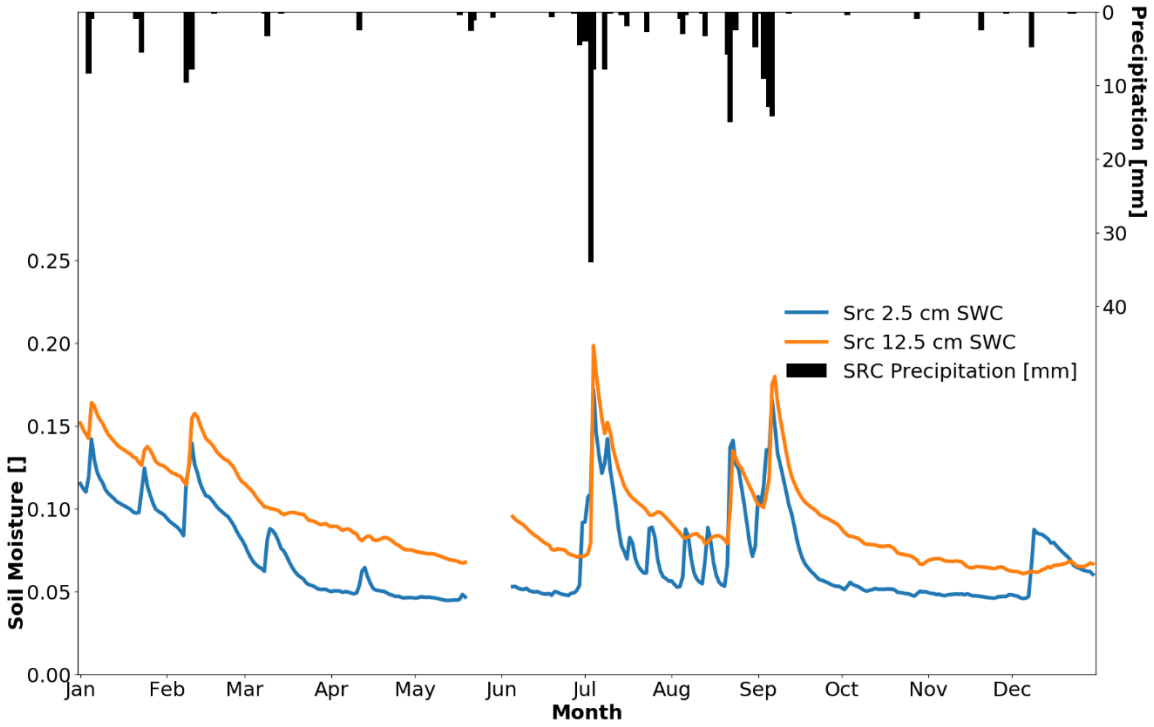

Figure 18: Time series of soil moisture at 2.5, 12.5-cm depth at US-SRC in 2019

It is clear that the soil moisture observations at US-SRG were higher than those at US-SRM during the first six months of 2009 and from October to November. July and August were characterized by similar soil moisture between two sites while September was marked with significantly lower soil moisture at US-SRG. The increase in thermal conductivity at US-SRM due to sharp increase in soil moisture allowed the shortwave radiation to heat the surface quicker and transferred down the deeper layer easier. In addition, both the vegetation fraction and the LAI were lower at US-SRM which increased the actual amount of radiation heating the surface after intercepted by the canopy. Furthermore, soil thermal capacity also increased which allowed heat to retain longer in the subsurface soil. These conditions explained why the damping depth at US-SRM was higher than at US-SRG.

Soil Temperature Damping Depth: The time series of soil temperature at different depths are illustrated in Figures 19 and 20 for US-SRM, US-SRG and US-SRC for an example year (2009). Due to a subsurface temperature sensor malfunction at US-SRC, the calculation of soil damping depth was not possible at the site. At US-SRM (Figure 19), soil temperatures shallower than 50 cm show higher temporal variability, while soil temperature at deeper depths (i.e. 70, 100, 130 cm) did not exhibit strong variations, especially from October to December. In addition, it is observed that the daily range of the soil temperature as well as the monthly fluctuations varied within a wide limit. Subsurface soil temperature generally decreased with depth with 100- and 130-cm temperatures almost identical from April to September. On the other hand, below 50-cm, soil temperatures were warmer than those shallower than 50 cm from January to mid-February and from November to December with higher temperatures in deeper layers. The time series of soil temperature at six different depths at US-SRG are illustrated in Figure 19. Compared to

soil temperature deeper than 50 cm at US-SRM, the 75-cm soil temperature at US-SRG still displays large temporal variability. Temperature at 28-, 45-, and 75-cm depths were warmer than the surface temperature from January to March and again from October to December. Similar to US-SRM, the soil temperature sharply dropped in June and July in response to the increase in precipitation accumulation after an extended period of no rainfall, similar to the observation made at Flagstaff, AZ.

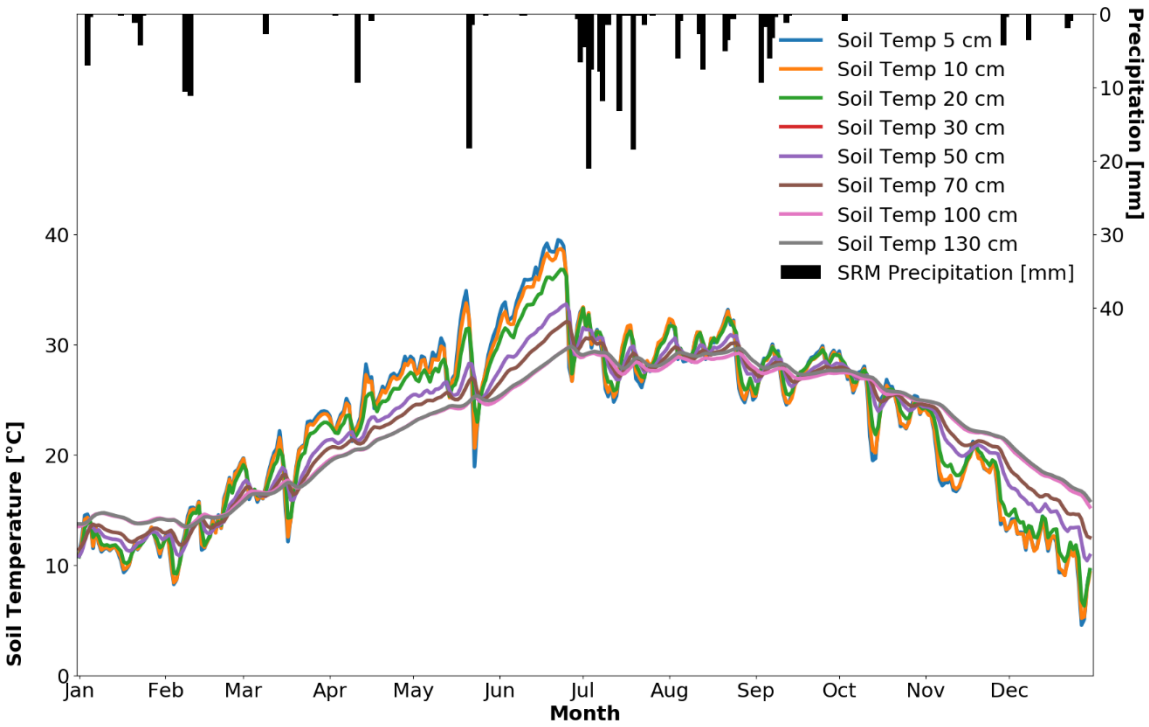

Figure 19: Time series of soil temperature at 5,10, 20, 50, 70, 100, and 130 cm depth at US-SRM in 2009.

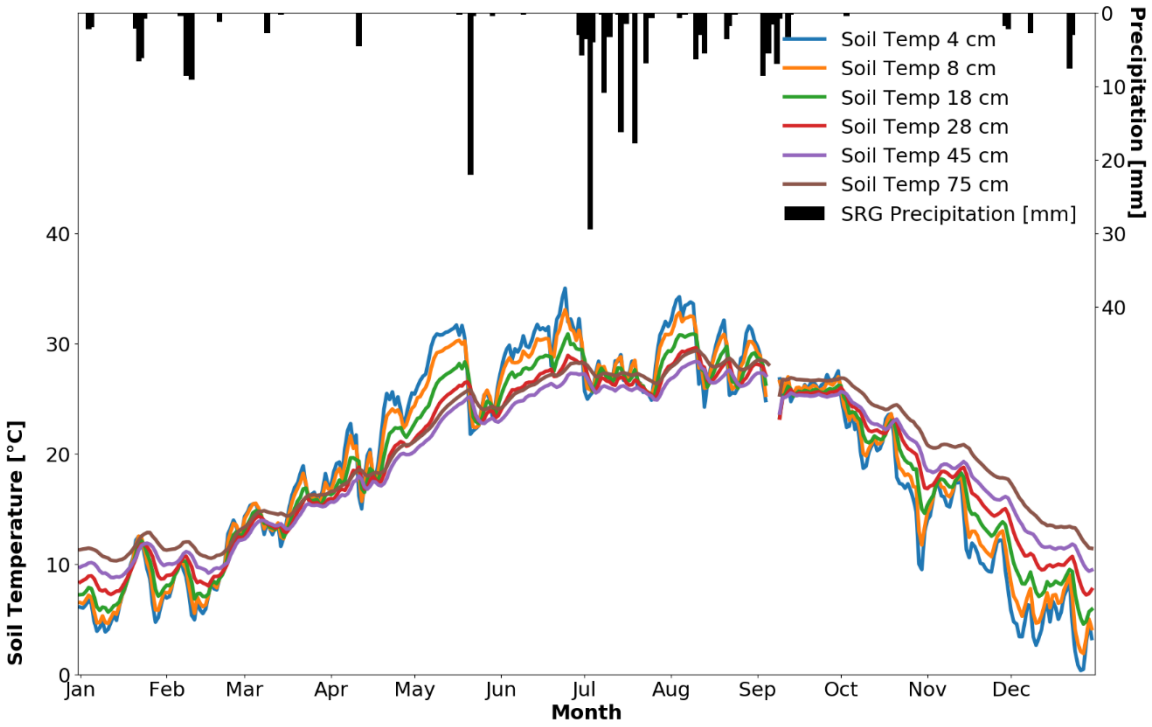

Figure 20: Time series of soil temperature at 4, 8, 18, 28, 45, and 75 cm depth at US-SRG in 2009.

Figures 21 and 22 illustrate the calculated damping depths for US-SRM and US-SRG during year 2009. Such damping depths vary significantly between mesquite and grassland cover. For US-SRM (Figure 21), February, mid-July, and mid-August were characterized by deep damping depths between 1.0 and 1.6 m. The three periods were also the times when there was high precipitation accumulation and a rapid increase in soil moisture. Shallower damping depths were concentrated from March to June and again from September to November, ranging from 0.2 to 0.8 m. For US-SRG (Figure 20), the range of damping depths was significantly lower than that of the US-SRM, varying between 5 to 60 cm. Shallow damping depths appeared mostly from mid-May to mid-July and from September to mid-October. The calculated damping depths at US-SRG also indicated that grassland attenuated heat more quickly than mesquite. The overall shallower damping

depths calculated at US-SRG could be attributed to the overall higher soil moisture near the surface which increased the thermal conductivity and thermal capacity of the soil (See Figure 16; Al-Kayssi et al., 1990, Roxy et al., 2014; Sugathan et al., 2014). The presence of a snowpack on the surface or frozen ground could render the assumption of sinusoidal wave in soil temperature invalid, which potentially explained the sudden increases in damping depths during winter months.

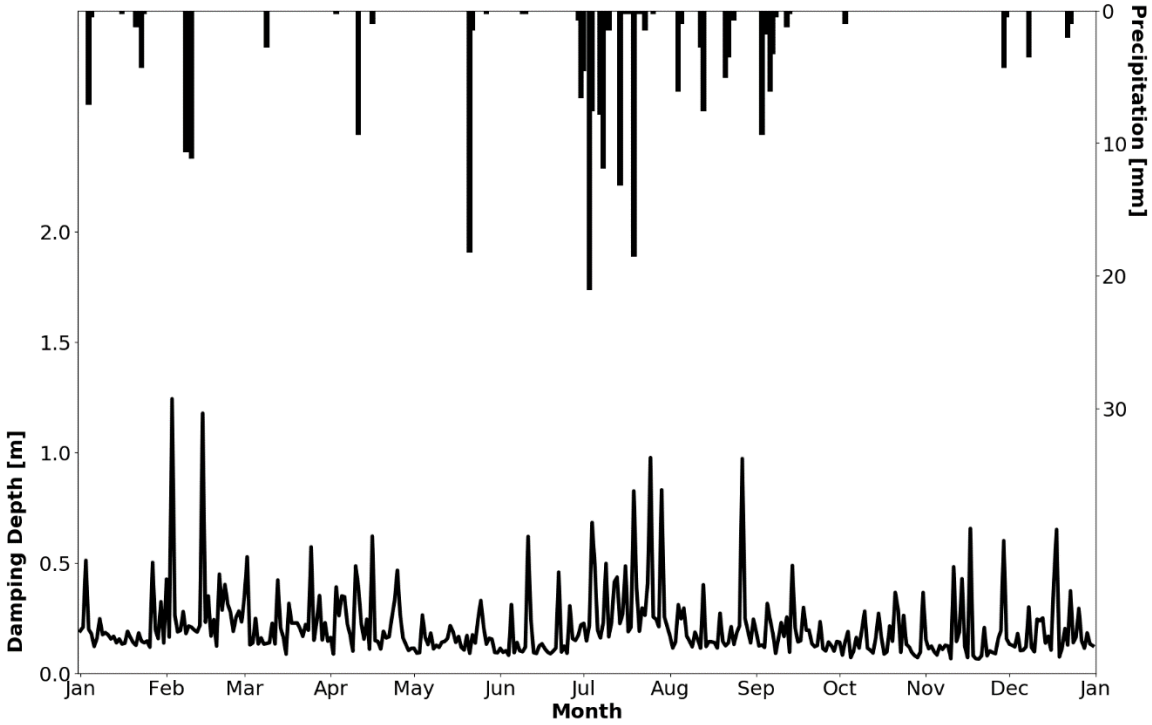

Figure 21: Time series of calculated damping depths at US-SRM for year 2009. The calculation for these damping depths used the 5 cm and 10 cm depth soil temperatures.

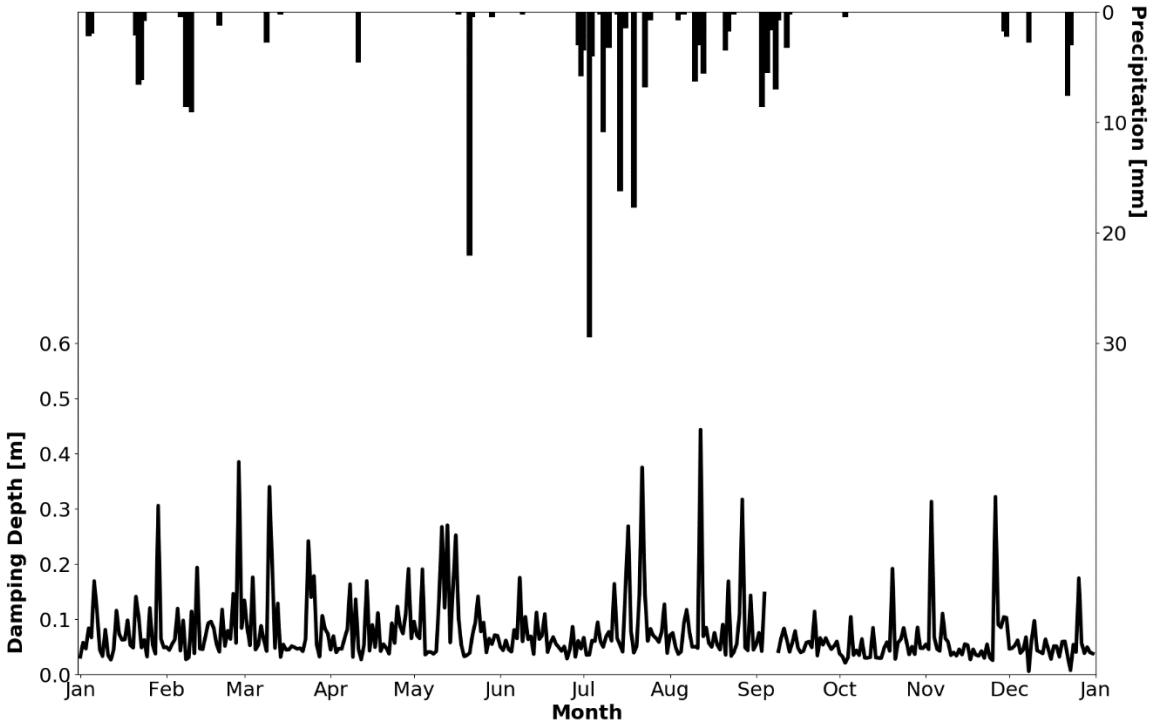

Figure 22: Time series of calculated damping depths at US-SRG for year 2009. The calculation for these damping depths used the 5 cm and 10 cm depth soil temperatures.

5.1.3. Grassland Ecosystem

Figure 23 illustrates 2-year time series of precipitation, LAI, NDVI, albedo, net radiation, the surface energy budget components and the surface soil moisture, and temperature time series at the MOISST site within the grassland ecosystem and their responses to the management operations conducted from 2014 to 2015. The vertical orange line denotes the date of 04/20/2015 when the northeastern patch was control-burned.

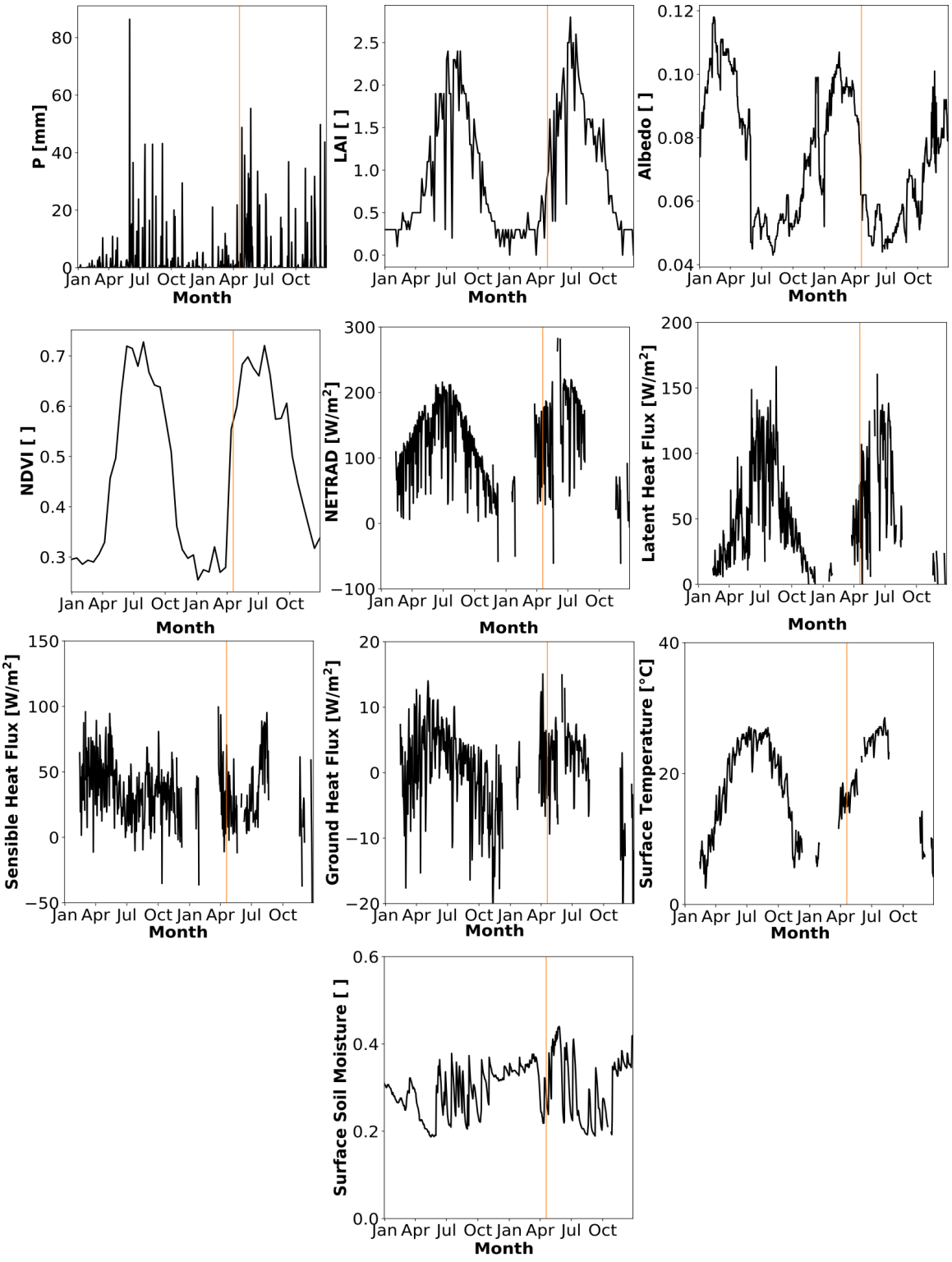

Figure 23: Time series comparison of precipitation, LAI, NDVI, albedo, net radiation, surface energy balance components, surface temperature and soil moisture at the MOISST site in Marena, OK over the period from 2014 to 2015. The vertical orange line denotes the date of the control burn.

Precipitation: From Figure 23, it is seen that for 2014, precipitation was low from January to May and from November to December. Rainfall occurred from May to September with significantly more rainfall in late May, reaching more than 80 mm in accumulation. On the other hand, from November to December 2015, there was more precipitation than during the same period in 2014, averaging 40 mm in rainfall accumulation.

LAI: The time series of LAI of 2014 and 2015 illustrate that from January to March and from November to December, LAI was generally low with some observed zero days. The rapid increase in LAI coincided with the start of the rainfall season and the increase in incoming shortwave radiation. The peak LAI in July 2015 was higher than the peak in July 2015, possibly due to higher number of days with precipitation that facilitated the growth of prairie grasses. Despite the difference in peak values in July and the thinning in April 2015, there was no abnormal change observed in LAI values between 2014 and 2015.

Albedo: Inversely correlated with LAI and NDVI, albedo was observed to be high in the winter months and remained low during summer. Its high values during the winter months showed the mixed presence of snow and prairie grass while the lower values in summer months represented the increase in surface vegetation cover and activity. Additionally, the near zero albedo in summer showed that most of the incoming solar radiation was absorbed by the ground.

NDVI: Similar to LAI, NDVI was low during the winter months from January to March and again from November to December. As precipitation increased, NDVI also increased and peaked in August. In addition, while 2014 was characterized by a gradual increase in NDVI starting in April, its counterpart in April 2015, before the thinning occurred, was characterized by a sudden increase from 0.25 to more than 0.5 while there were no

abnormal changes in either precipitation or LAI. Furthermore, despite the thinning in April 20th, 2015, observed NDVI showed no decrease post-thinning and still reached the similar peak to its 2014 counterpart. However, the 16-day temporal resolution and the 250-m spatial resolution could be the reason why the effects of thinning were not well captured during the few days subsequent to the controlled burns.

Net Radiation: Sensor malfunctioning can be seen from Figure 23 with the blank white space denotes the missing data. From the available data and common knowledge, it could be inferred that net radiation was low in the winter due to reduced amount of incoming shortwave radiation. During the post-thinning period, in June 2015, there was an abnormally high observed net radiation. However, it was not clear whether the peak was the result of sensor malfunction or other physical processes. Analysis of net radiation utilizing a shorter period is presented in the next section to assess the effects of controlled burns for vegetation thinning.

Latent Heat Flux: Similar to the measurements of net radiation, a high percentage of the data was missing due to sensor malfunction. However, precipitation is a primary factor controlling the amount of latent heat flux at MOISST with high precipitation driving higher evapotranspiration. Additionally, the increase in LAI also translated to an increase in latent heat as prairie grass transpired more water as they grew. However, the significantly high precipitation in May 2014 did not cause a significant increase in latent heat flux. A possible explanation was that the high amount of rainfall was converted to runoff at a certain threshold where the soil had reached its water holding capacity and the prairie grass could not intercept more precipitation. Additionally, despite the higher number of precipitation events and accumulation in 2015, this years' time series of latent heat flux was of similar

as that of 2014. An analysis of latent heat flux utilizing a shorter period is presented in the next section to assess the effects of vegetation thinning. Looking at the magnitude of LE over the two-year time series, it was clear that latent heat flux was the smallest component of the surface energy balance in the winter and was the largest component in the summer.

Sensible Heat Flux: Compared to latent heat flux, sensible heat flux did not exhibit strong seasonal patterns with yearly fluctuations ranging mostly between 0 and 100 $W.m^{-2}$ with a number of days below zero, showing the heat is transferred downward (See Figure 23). The slight decrease in sensible heat flux coincided with the increase in both LAI, NDVI, and precipitation as well as the decrease in albedo. Even though lower albedo allowed more radiation absorbed, energy seems to be rather be invested in evapotranspiration processes. In 2015, another problem with the sensor caused a high percentage of missing measurements. However, from the remaining data, it could be reasonable to conclude that the prescribed thinning did not affect the long-term behaviors and magnitudes of the sensible heat flux. It was also the largest component of the surface energy balance in winter and was the second largest component of the surface energy balance in summer.

Ground Heat Flux: Ground heat flux was characterized by upward direction in the winter, showing warmer subsurface during this period. It rapidly rose and peaked in April when the precipitation was at its lowest. Ground heat flux was the second largest component and the smallest component of the surface energy balance in terms of magnitude in winter and summer, respectively.

Soil Surface Temperature: The available time series of surface temperature show that temperature remained well above zero in the winter months and peaked at approximately 30°C during the June, July and August period. Surface temperature followed the pattern of

incoming solar radiation with low values in winter and high in summer. It also correlated with albedo as lower albedo allowed the surface to absorb more radiation which as a result, increased the surface temperature.

Surface Soil Moisture: The variational range of surface soil moisture was relatively stable between 0.2 and 0.4. In 2014, the moisture at MOISST decreased gradually between January and April with a sudden increase marking the start of the rainfall season. Furthermore, its time series showed a relatively well-drained soil layer with sharp changes between peaks and troughs of soil moisture. The root system of prairie grass could help to explain the sharp changes as they facilitated a well-drained soil as the roots grew and moved through the soil layer.

Due to no observable effects of vegetation thinning from the longer period of observations, the analysis was shortened to 20 days pre- and post-thinning for further exploration. A closer look to the hydro-meteorological and ground anomalies observed as a result of the prairie treatments is shown in Figure 24. Observations from the ECT at the MOISST site were limited to 20 days pre- and post-thinning to focus on the relatively quick recovery rate of tallgrass prairie that occurred after the treatment conducted in April 20th, 2015 as well as the low intensity of the thinning that was not observable from the longer time series analysis.

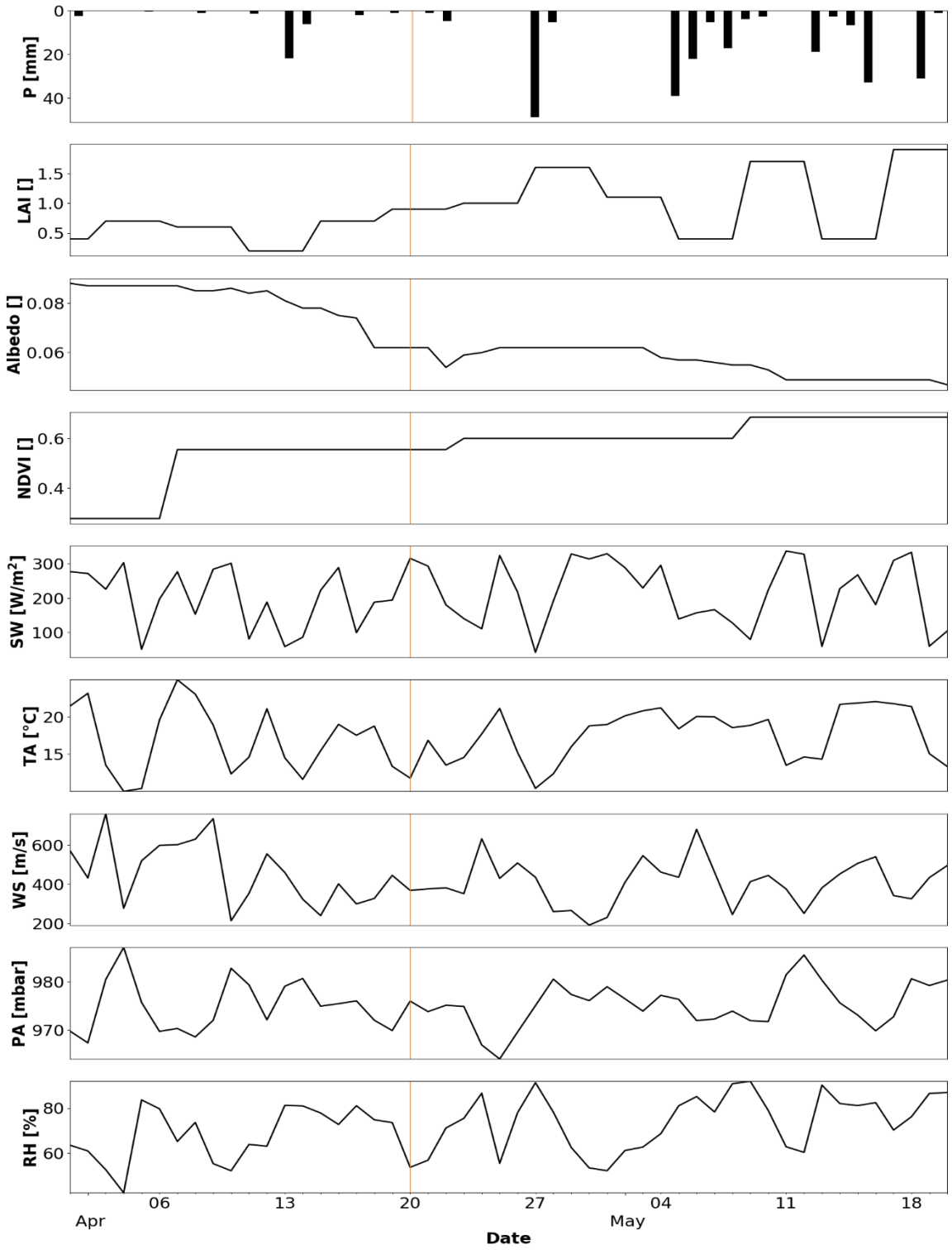

Figure 24: Hydrometeorological and ground surface conditions: Precipitation, LAI, NDVI, albedo, incoming shortwave radiation, air temperature, wind speed, atmospheric pressure and relative humidity at the MARE Mesonet station 20 days pre-thinning and 30 days post-thinning of the vegetation. The thinning date is noted with the vertical orange line.

The hydrometeorological conditions at the site were characterized by low precipitation during the month of April with an increase from May 6th onward. The average precipitation accumulation 20 days pre-thinning was 0.08 mm and 20 days post-thinning was 0.31 mm. All shortwave radiation, temperature and relative humidity illustrate the typical diurnal cycle of the spring season in the North American prairies. Daily average shortwave radiation remained consistent between 50 and 300 W.m^{-2} with some days with reduced influx rates due to clouds. Overall, pre- and post-thinning daily average shortwave radiation were at 197 W.m^{-2} and 213 W.m^{-2}, respectively. Daily average air temperature fluctuated between near 10°C and 25°C both pre- and post-thinning without any significant change. Pre-thinning the 20-day average of temperature reached 17.0°C and post-thinning such an average was 17.25°C. Relative humidity remained high in April and early May with average value of 70%. Atmospheric pressure had weather-related fluctuations during both periods.

LAI was observed to overall increase from its pre-thinning of 0.5 to over 1.6 post-thinning. However, from Figure 24, it is seen that the periods between each precipitation event were observed with reduced LAI. The lack of rainfall which caused some of the prairie grassland to wither could be the reason why LAI was reduced in these periods. A disadvantage from utilizing LAI in such short time period was that the hourly/daily change was not obtained due to the 4-day temporal resolution of the LAI product. NDVI was also observed to consistently increase from less than 0.3 pre-thinning to 0.6 right after the thinning occurred and to 0.7 about 20 days post-thinning. Low temporal resolution of 16-day and low spatial resolution of 250-m could explain why the short duration, and low intensity thinning at the northeastern patch was not captured by the satellite images. Albedo

had the highest temporal resolution among the three satellite products with images obtained every day. It is seen from Figure 24 that albedo decrease from its high of 0.1 to about 0.04 post-thinning. Noticeably, two days after the thinning occurred, albedo sharply decreased and then increased and remained stable for 11 days before gradually decreased again.

Figure 25 summarizes the responses in terms of net radiation and surface energy fluxes as well as the soil temperature and soil moisture, of the tower's footprint to the abrupt changes in vegetation cover.

Net Radiation: The averaged net radiation for the 20-day pre-thinning was 113 $W.m^{-2}$ and for 10-day and 20-day post-thinning, the same value was 129 $W.m^{-2}$ and 125 $W.m^{-2}$. The overall increases of LAI and NDVI post-thinning showed that there was either no captured disturbance to the prairie grassland or the vegetation cover recovered quickly. In conclusion, it was not clear whether the decrease in LAI in some days was due to the burning or daily fluctuation in the amount of incoming and outgoing radiation.

Latent Heat Flux: For latent heat flux, the mean value pre-thinning was 46.76 $W.m^{-2}$ and for 10-day and 20-day post-thinning, the mean was 68.26 $W.m^{-2}$ that means a 46% increase in latent heat flux post-thinning. It is also noted that even though there was more precipitation at the site post-thinning, the was only two small precipitation events during the first 10-day period post-thinning. However, even though the average LE raised post-thinning, the change in the amount of latent heat flux corresponded closely to the change in LAI and precipitation. In conclusion, there was no observable effects of the human-controlled thinning on the rate of latent heat flux.

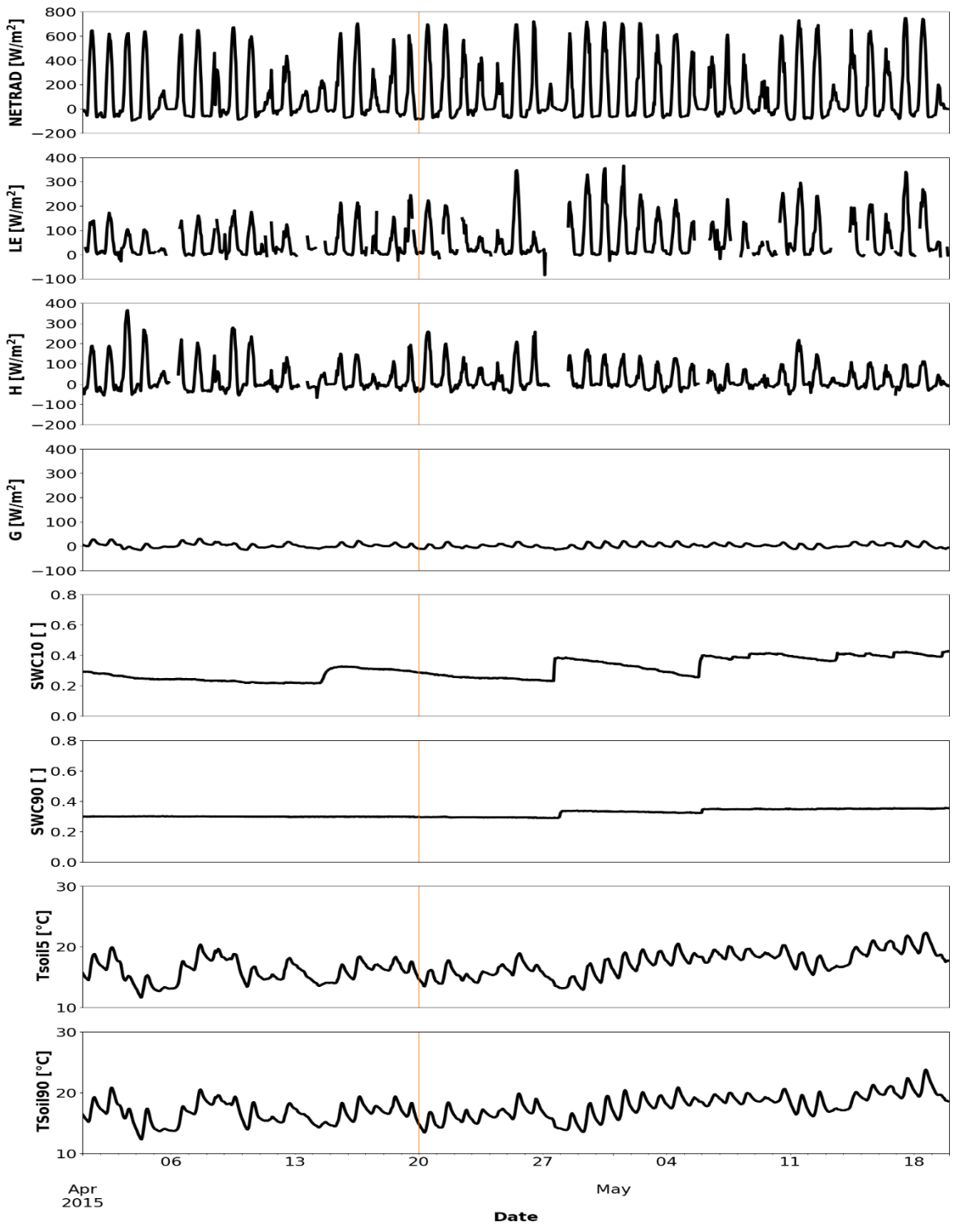

Figure 25*:* Time series of net radiation, surface energy balance components, soil moisture at 10 and 90 cm depth, and soil temperature at 10 and 90 cm depth at the MOISST site 20 days pre-thinning and 30 days post-thinning. The thinning procedure at the Northeastern Patch section of the experimental site (shown as vertical orange line).

Sensible Heat Flux: Sensible heat flux, contrastingly, increased from an average of 33.1 $W.m^{-2}$ to 36.7 $W.m^{-2}$ 10-day post-thinning and then decreased sharply to 28.09 $W.m^{-2}$ 20-day post-thinning. An explanation for this would be the heat from the thinning and the decreased albedo (dark surface) which can be seen 2 days post-thinning, increased the upward heat loss but quickly, grasses returned to their natural condition of albedo again thus reducing sensible heat flux.

Ground Heat Flux: The explanation for the behavior of sensible heat flux is supported with the time series of ground heat flux where the flux suddenly decreased from mean value of 2.7 $W.m^{-2}$ to -0.57 $W.m^{-2}$ and increased sharply back to 1.6 $W.m^{-2}$, the negative flux 10-day post-thinning illustrated the higher temperature at the subsurface that made the heat be transferred upward. Nonetheless, the change was insignificant and the available forcing variable was not sufficient to determine whether the change was due to the thinning or just typical daily fluctuations.

Surface and root-zone temperature: Surface temperature (at 10 cm depth) measurements showed a slight decrease from mean value of 16.0°C to 15.5°C 10-day post-thinning and increased to 16.7°C 20-day post-thinning, as seen in Figure 25. Rootzone temperature was only slightly higher than the surface temperature with mean of 16.7°C pre-thinning, 16.1°C 10-day post-thinning, and 17.3°C 20-day post-thinning. Similar to observed net radiation, the slight change in temperature and the available data were inconclusive in determining the cause of such change.

Surface and Root-Zone Soil Moisture: Average soil moisture at 10 cm depth was 0.26 pre-thinning and 0.28 to 0.30 post-thinning 10-day and 20-days after thinning, respectively. From the time series of surface soil moisture in Figure 25, it is seen that there was no

sudden change to the soil moisture during and post-thinning. The increase in soil moisture values post-thinning could better be associated with precipitation events that happened during the same period. Therefore, there was no concrete conclusion on the effects of vegetation thinning on soil moisture at MOISST. A similar observation was made with the rootzone soil moisture at 90-cm depth. Compared to the its counterpart at 10-cm depth, the effects of precipitation events were not as pronounced here as shown by the relatively steady soil moisture at 0.3 pre- and post-thinning.

Soil Temperature and Damping Depth: The time series of soil temperature at all available depths for the entire year of 2015 is illustrated in Figure 26. Data were missing during the first half of January, from February to late March, June, and again from September no November. From the available data, it is observed that the deeper soil layers were warmer than the shallower soil layers with the most noticeably temperature difference happened between the 20- and 50-cm layer during the summer months from June to September. On the contrary, the temperature did not vary with depth and the difference was not as pronounced from mid-January to February and from mid-November to December. The calculated damping depth for the MOISST site from the 2.5- and 10-cm depth for the year of 2015 is illustrated in Figure 27. Due to the lack of measurements during the winter months, no conclusion was reached regarding the damping depths during this period. From April to August, the damping depths fluctuated between 0.1 and 0.3 meters with shallower depths responding to the precipitation events which cooled the surface and reduced the effects of temperature wave through the soil, and as a result, decreased the damping depth. Obviously, the difference in compositions between soil layers modifies their thermal properties. As a result, he differences in the damping depths

between the surface temperature and soil temperature at distinct layers could be different. However, since the heat had to penetrate through each layer from the surface, the difference in damping depths were not substantial.

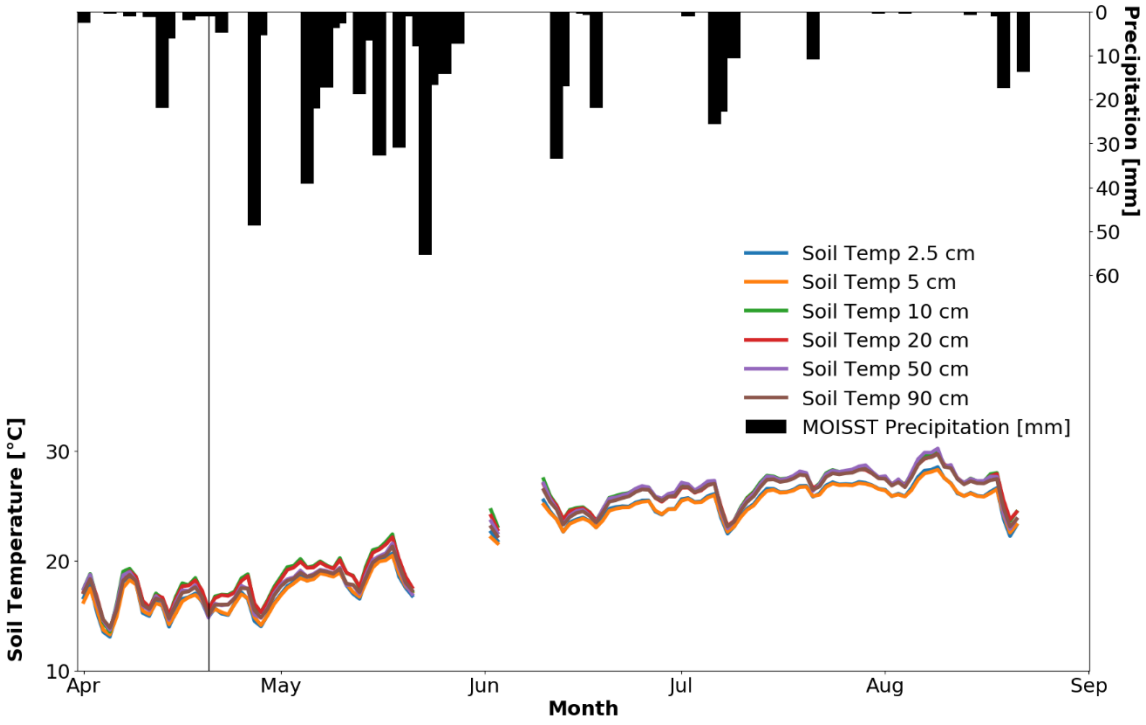

Figure 26: Time series of soil temperature at different depths at MOISST from April to September 2015, the black dashed line denotes the date the thinning occurred.

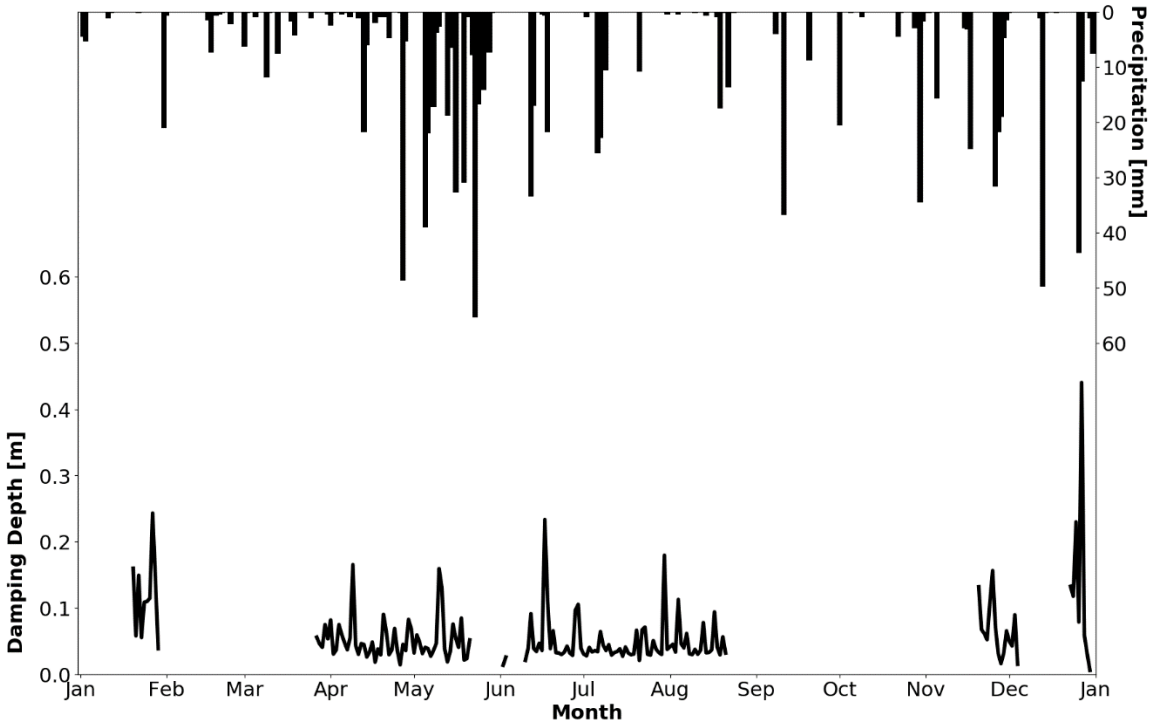

Figure 27: Time series of calculated damping depths at MOISST for year 2015, using 2 and 10 cm depth measurements, consistent with the desert and forest sites.

5.2. Model Calibration

5.2.1. Forest Ecosystem

Figures 28 through 30 illustrate the time series of hydrometeorological forcing variables for the calibration period from January 1st, 2006 to December 31st, 2006 at US-FUF, January 1st, 2007 to December 31st, 2007 for US-FWF, and January 1st, 2009 to December 31st, 2009 for US-FMF.

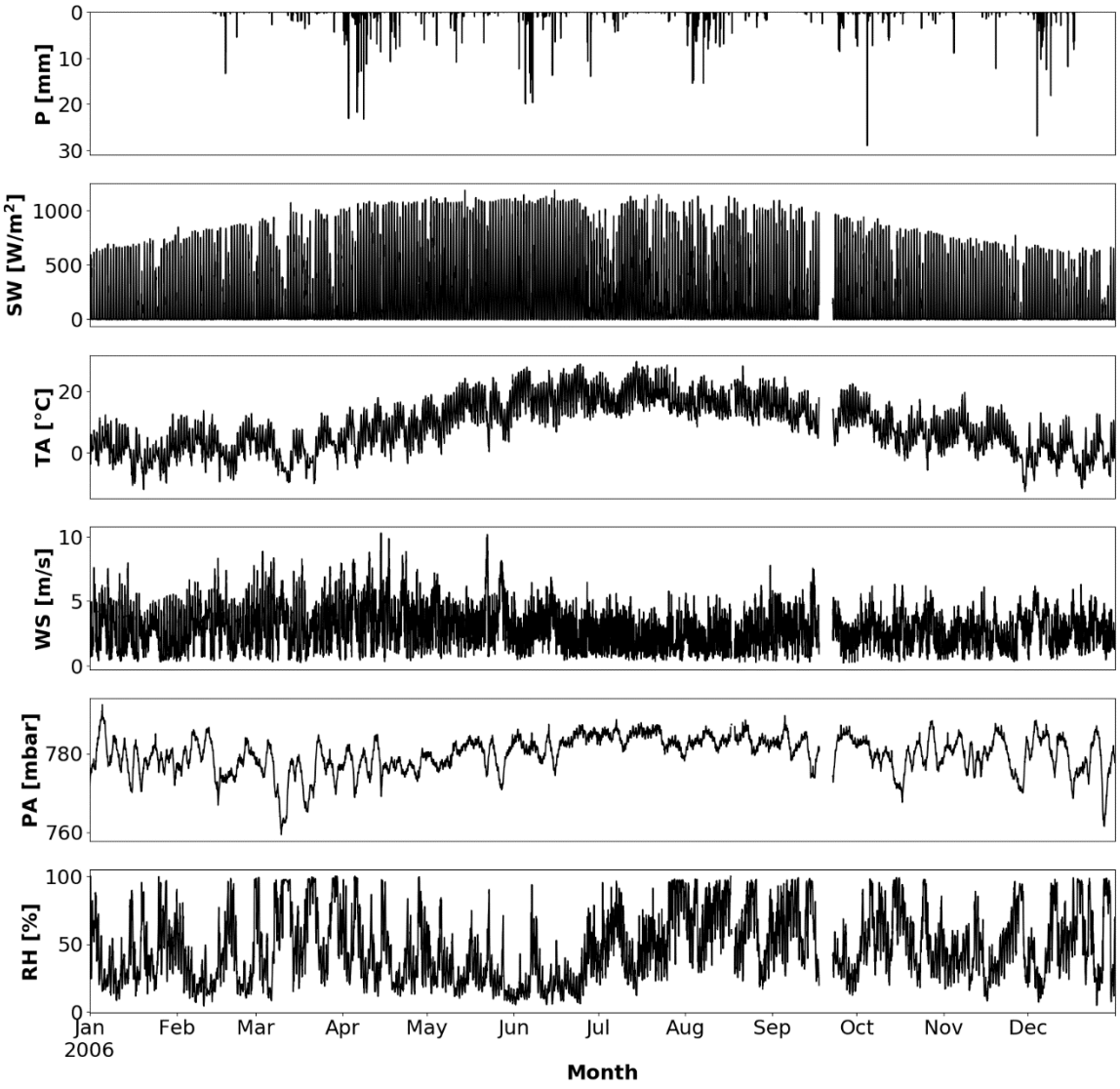

Figure 28: Hydrometeorological tRIBS model forcing variables for US-FUF from 01/01/2006 to 12/31/2006. The six forcing variables are precipitation (P, mm), incoming shortwave radiation (SW, W.m-2), air temperature (TA, °C), wind speed (WS, m.s-1), atmospheric pressure (PA, mbar), and relative humidity (RH, %).

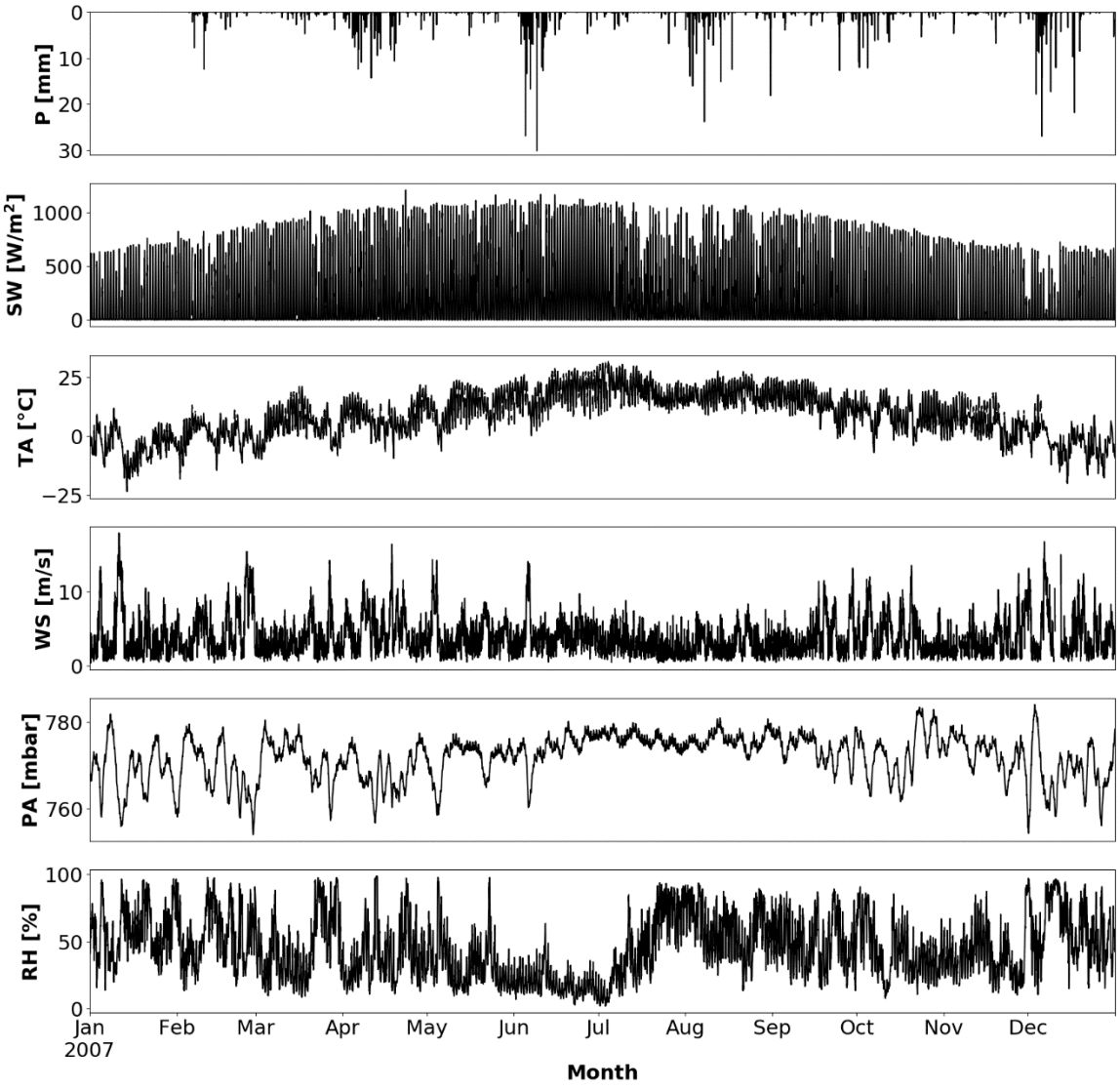

Figure 29: Hydrometeorological forcing variables for US-FWF from 01/01/2007 to 12/31/2007. The six forcing variables are precipitation (P, mm), incoming shortwave radiation (SW; W.m-2), air temperature (TA; °C), wind speed (WS; m.s-1), atmospheric pressure (PA; mbar), and relative humidity (RH; %).

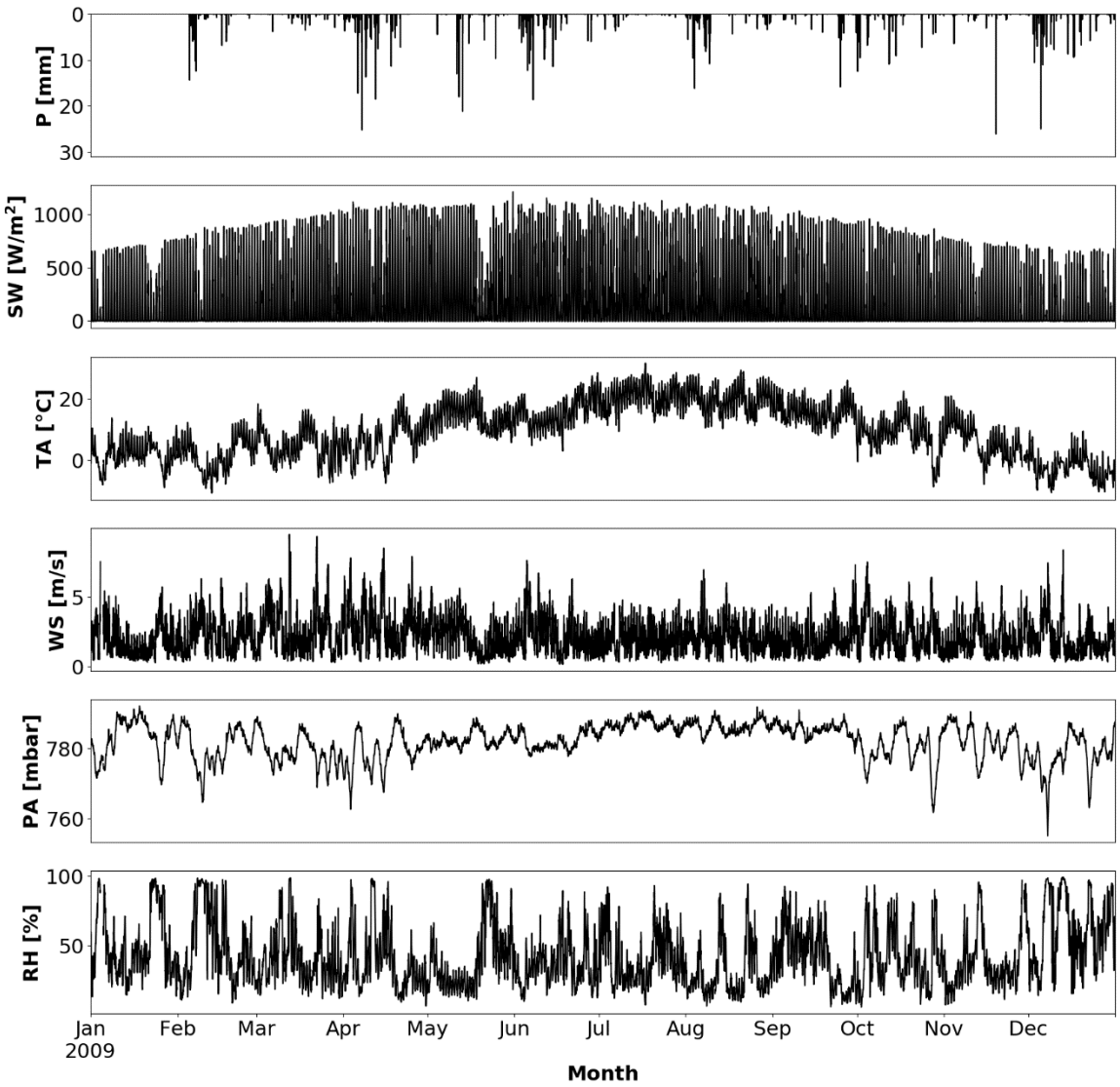

Figure 30: Hydrometeorological tRIBS model forcing variables for US-FMF from 01/01/2009 to 12/31/2009. The six forcing variables are precipitation (P, mm), incoming shortwave radiation (SW, W.m-2), air temperature (TA, °C), wind speed (WS, m.s-1), atmospheric pressure (PA, mbar), and relative humidity (RH, %).

For all stations in Flagstaff, the incoming shortwave solar radiation and air temperature expressed clear seasonal variability with low values from November to March and higher from May to September. Other forcing variables were less influenced by such a seasonal variability although atmospheric pressure had less variability from May to

October and wind speed was generally higher during the months of April and May (See Figure 28).

Figures 31 through 33 show time series of the vegetation parameters also used during the model calibration phase at US-FUF, US-FWF and US-FMF. According to Figure 31 at US-FUF vegetation fraction remained relatively constant between 0.3 and 0.4 throughout the year with an exception in December when the value decreased from 0.4 at the beginning of December to 0.2 in mid-December and returning to 0.4 at the end of December. The higher values of vegetation fraction in summer occurred in tandem with an increase in biomass activity and higher incoming solar radiation. It is also evident that there is green vegetation year-round. Albedo also remained constant most of the period with two exceptions in mid-March and late December which could be attributed to the presence of snow. Leaf Area Index (LAI), during the same period as albedo in mid-March and in late June, experienced sharp decrease before returned to its average values. For US-FWF (Figure 32), the high values of albedo from December to March evidence the presence of snow which reflected high amount of incoming solar radiation. The lower slope in albedo in March indicated snow melt while the higher slope in December represented the snow accumulation on the surface. Seasonal variability of vegetation was more pronounced at US-FWF (than US-FUF) since grassland and bush species seem to respond more thoroughly to the seasonal changes. Both LAI and vegetation fraction peaked in July and August when the incoming solar radiation was at its highest and remained low in winter time under lower solar radiation and frequent snow events. Compared to US-FUF, the stomatal resistance of the vegetation at US-FWF is twice as high in winter while these values are consistently similar for other months of the year.

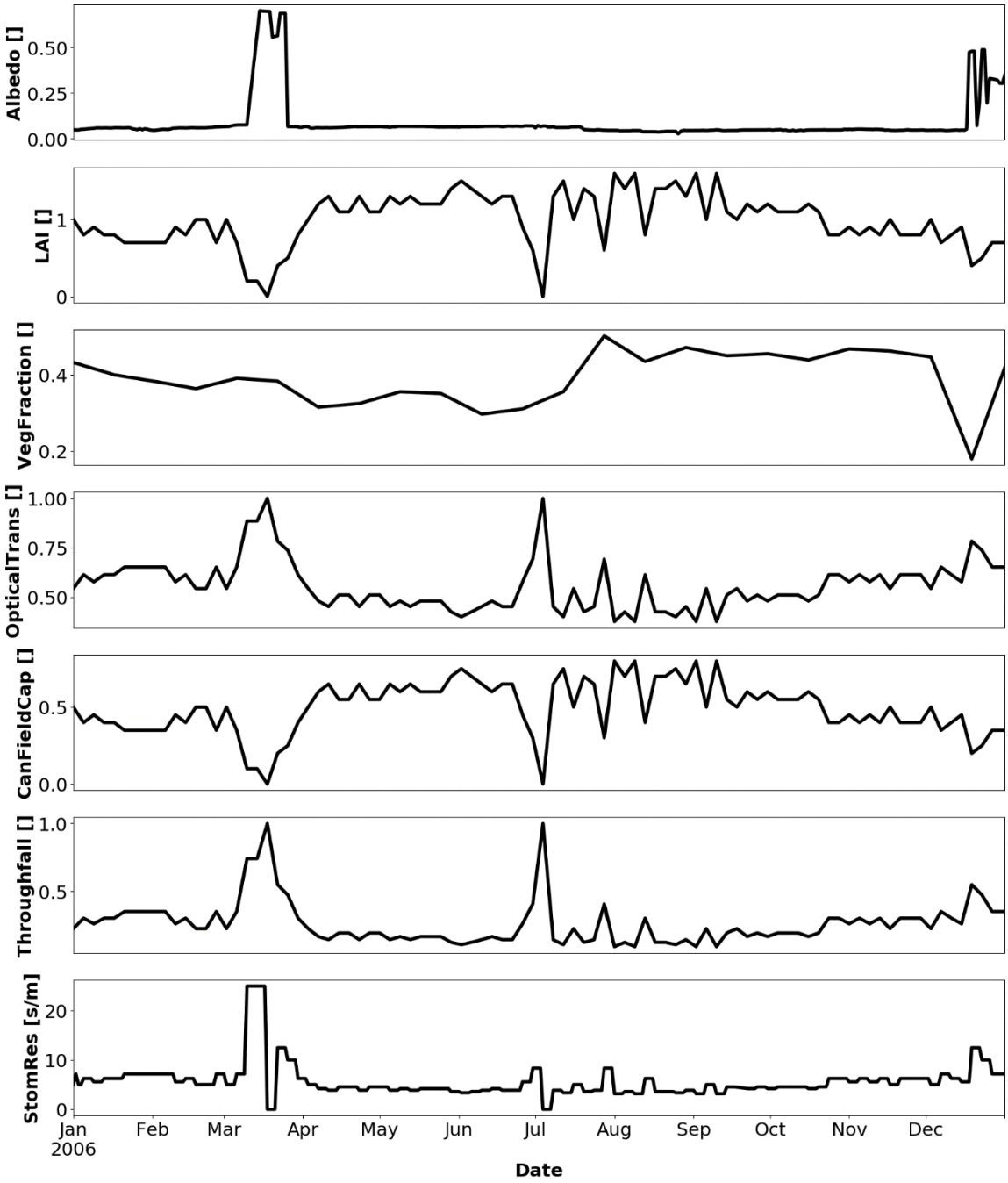

Figure 31: Dynamic vegetation parameters for US-FUF from 01/01/2006 to 12/31/2006. The six parameters are: Albedo (unitless), LAI (unitless), vegetation fraction (VegFraction; unitless), optical transmission (OpticalTrans; unitless), canopy field capacity (CanFieldCap; unitless), throughfall coefficient (unitless), and stomatal resistance (StomRes; $s.m^{-1}$).

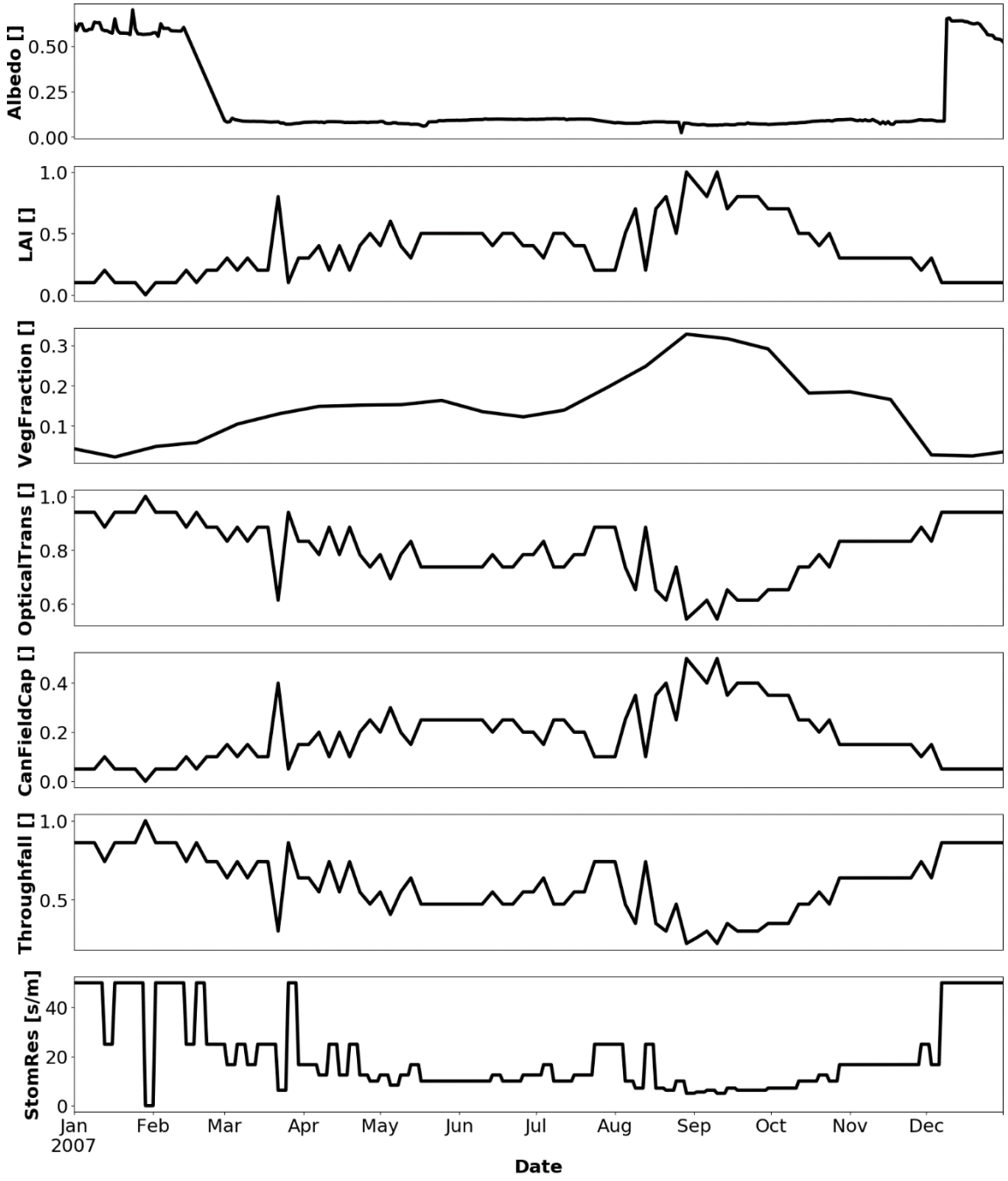

Figure 32: Dynamic vegetation parameters for US-FWF from 01/01/2007 to 12/31/2007. The six parameters are: Albedo (unitless), LAI (unitless), vegetation fraction (VegFraction; unitless), optical transmission (OpticalTrans; unitless), canopy field capacity (CanFieldCap; unitless), throughfall coefficient (unitless), and stomatal resistance (StomRes; $s.m^{-1}$).

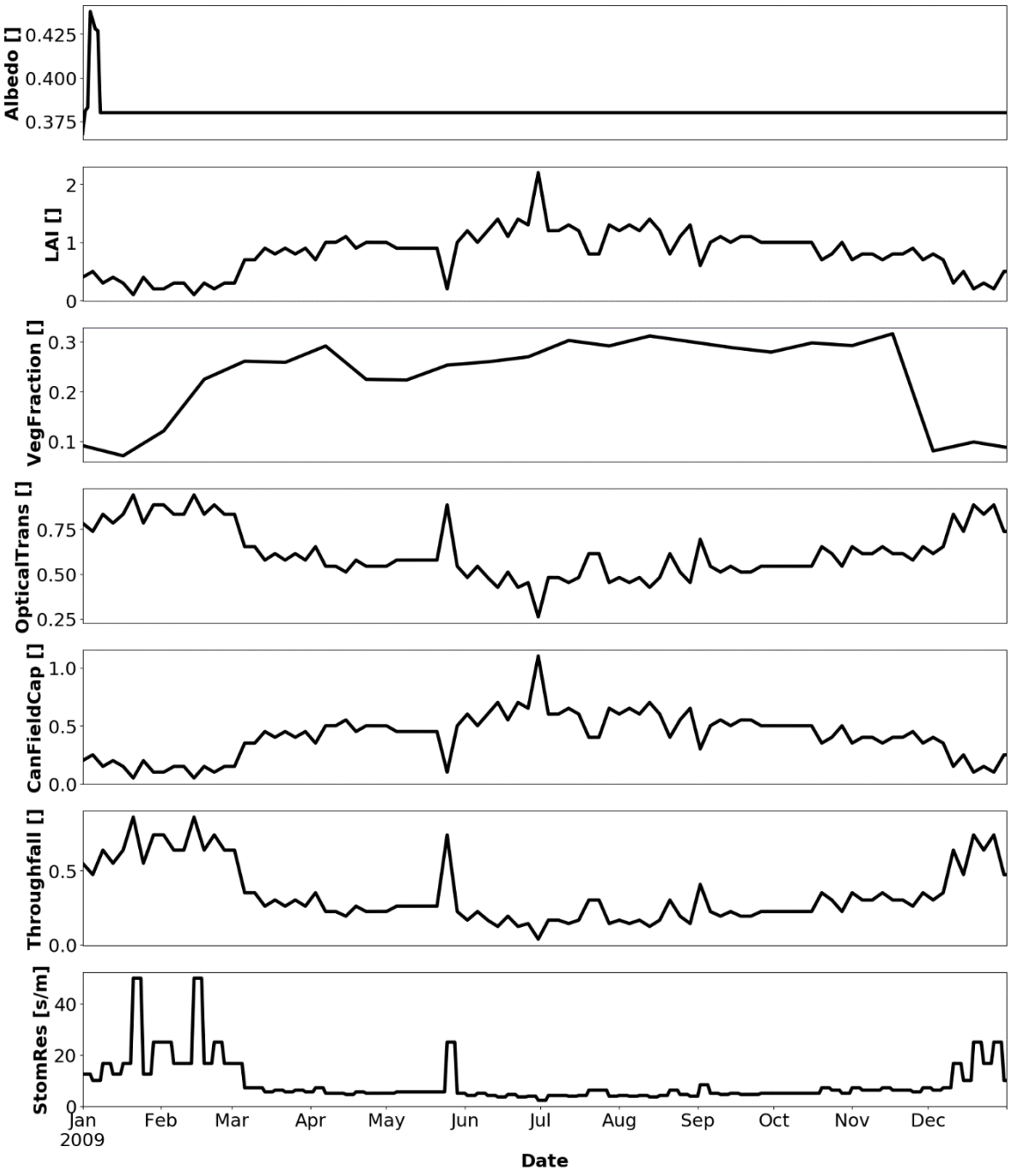

Figure 33: Dynamic vegetation parameters for US-FMF from 01/01/2009 to 12/31/2009. The six parameters are: Albedo (unitless), LAI (unitless), vegetation fraction (VegFraction; unitless), optical transmission (OpticalTrans; unitless), canopy field capacity (CanFieldCap; unitless), throughfall coefficient (unitless), and stomatal resistance (StomRes; $s.m^{-1}$).), throughfall coefficient (unitless), and stomatal resistance (StomRes; $s.m^{-1}$)

Similar to the other two stations at Flagstaff, albedo values at US-FMF remained around 0.4 most of the time with a sharp increase in January due to the presence of snow (see Figure 33). LAI was higher from June to October with a peak of 2.2 in July to an average of 0.5 during the winter months. Vegetation fraction sharply increased from mid-January to March and remained around 0.3 with a peak in August until December when it experienced a sharp decrease.

Calibrated values for static (non-time evolving) parameters at the three stations in Flagstaff are presented in Table 6. From these, both the saturated anisotropy and unsaturated anisotropy ratios did not produce any difference in results at the three simulated stations and they were kept constant. Overall, the found parameters are within the accepted literature values for the different soil and vegetation types present at each site.

5.2.1.1. US-FUF

The calibration results for the unmanaged forest at US-FUF are illustrated in Figure 34, Table 6 and Table 7. With the exception of ground heat flux (CC = 0.34, NSE = 0.11), the model captures well all other target variables with high Correlation Coefficient (CC>0.7) and Nash-Sutcliffe Efficiency Coefficient (NSE > 0.5; Figure 34 and Table 7). Overall, the model overestimated soil surface temperatures with simulated values ranging from -10°C to 50°C while observations range from -5°C to 35°C. Rootzone temperature patterns were well captured. The discrepancies in surface soil temperatures can be explained by a higher degree of dependence of the surface temperatures on remotely-sensed vegetation parameters. On the other hand, rootzone temperatures are mostly controlled by soil parameters like hydraulic conductivity, thermal conductivity, and heat

capacity. Net radiation, was underestimated at high values. The inability of the tRIBS model to simulate soil moisture in the presence of a snow layer is also reflected in the results, as shown by a vertical organization pattern, when the simulated soil moisture varied a lot while observed values remained constant during periods of frozen ground. From the calibration process it was also observed that ground heat flux, surface temperature, and rootzone temperature and sensible heat flux are sensitive to volumetric heat conductivity, soil heat capacity while latent heat flux depends on the magnitudes of vegetation and soil stress thresholds, the depth to water table as well as pore distribution index.

Table 6: Calibrated static parameters for the three ECT at Flagstaff, AZ with descriptions and their units for a simulation covering the entire year 2006.

Par	Description	Unit	US-FUF	US-FWF	US-FMF
Ks	Soil saturated hydraulic conductivity	mm/hr	20	80	85
Θs	Soil moisture at saturation	-	0.48	0.46	0.4
Θr	Residual soil moisture	-	0.035	0.045	0.053
m	Soil pore distribution index	-	1.5	1.25	2.0
ψ_B	Soil air entry bubbling pressure	mm	-240	-240	-230
f	Soil conductivity decay parameter	mm^{-1}	0.007	0.006	0.007
As	Soil saturated anisotropy ratio	-	25	25	25
Au	Soil unsaturated anisotropy ratio	-	140	140	140
n	Soil porosity	-	0.5	0.48	0.464
ks	Soil volumetric heat conductivity	J/msK	1.8	1.6	0.8
Cs	Soil heat capacity	J/m^3K	$2*10^5$	$2.2*10^5$	$1.2*10^5$
A	Vegetation canopy storage	mm	3.5	0.5	0.5
b1	Vegetation interception coefficient	-	0.65	0.25	0.65
K	Vegetation drainage coefficient	mm/hr	1.25	1.25	1.25
b2	Vegetation drainage exponential param.	mm^{-1}	6.5	2.5	6.5
H	Vegetation height	m	7	1.5	7
Θ^*_s	Stress threshold for soil evaporation	-	0.4	0.35	0.42
Θ^*_t	Stress threshold for transpiration	-	0.5	0.36	0.39
iwt	Initial groundwater table depth	mm	3000	8000	1860

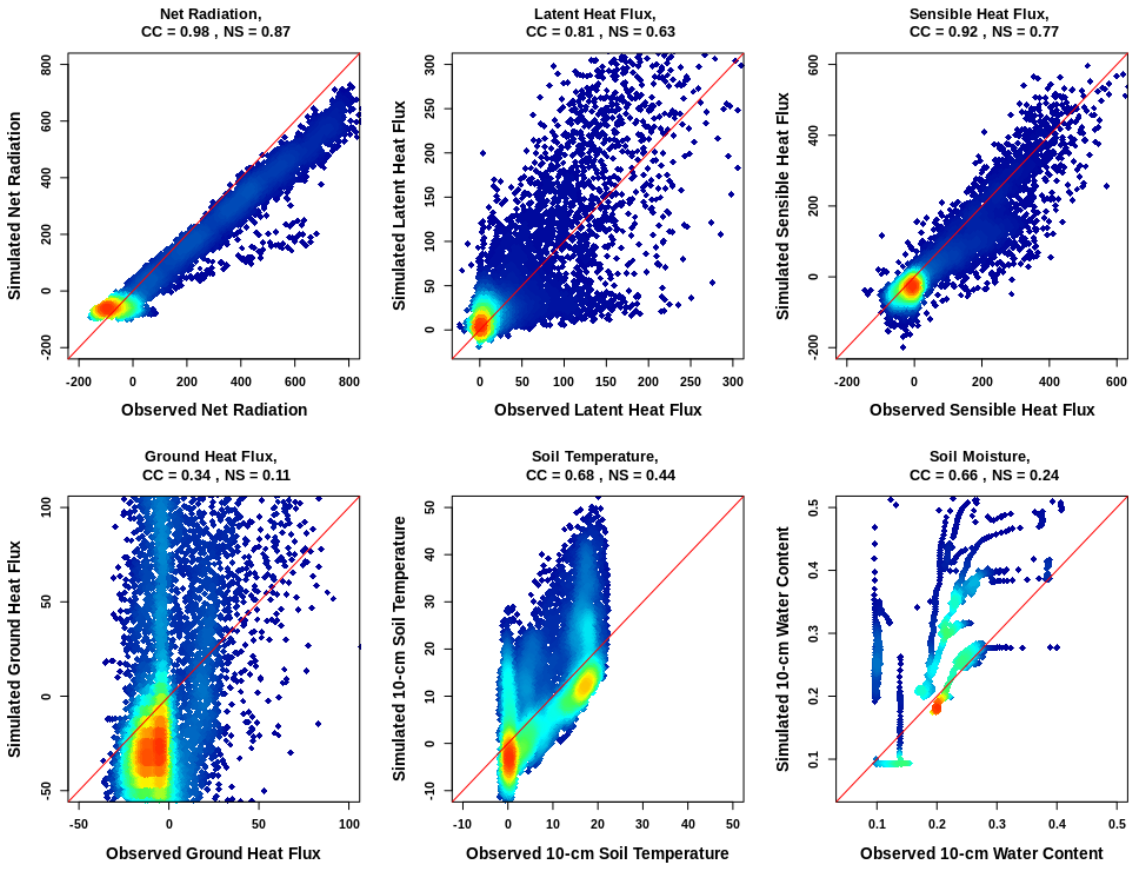

Figure 34: Density scatterplots of simulated versus observed soil and energy budget variables at US-FUF for year 2006. In all panels the x-axis represents the observations and the y-axis represents the simulated values. The diagonal red line denotes the perfect match.

Table 7: Calibration assessment metrics for US-FUF for each of the simulated variables with respect to observations for year 2006. Metrics include correlation coefficient (CC), Nash Sutcliffe coefficient (NSE), bias, and root mean squared error (RMSE)

Metrics	G ($W.m^{-2}$)	LE ($W.m^{-2}$)	H ($W.m^{-2}$)	NR ($W.m^{-2}$)	TS (°C)	Surface SWC
CC	0.34	0.81	0.92	0.98	0.68	0.66
NSE	0.11	0.63	0.77	0.87	0.44	0.24
Bias	-1.05	-9.79	26.96	24.09	-1.68	0.00
RMSE	58.12	45.79	56.87	75.00	7.54	0.058

The performance of tRIBS at capturing sub-daily variability is shown in Figure 35. The time series selected to visualize the daily variations show June and July as two example months. The diurnal responses of the net radiation, latent heat flux, sensible heat

flux were well captured with their simulated local minima and maxima matching those from the observation dataset. tRIBS was also able to capture the daily minimum of surface temperature and the diurnal trend but daily maxima were overestimated during this period. Similar behavior is observed with the ground heat flux where the diurnal cycle is simulated, but the daily local minima and maxima were overestimated across the days.

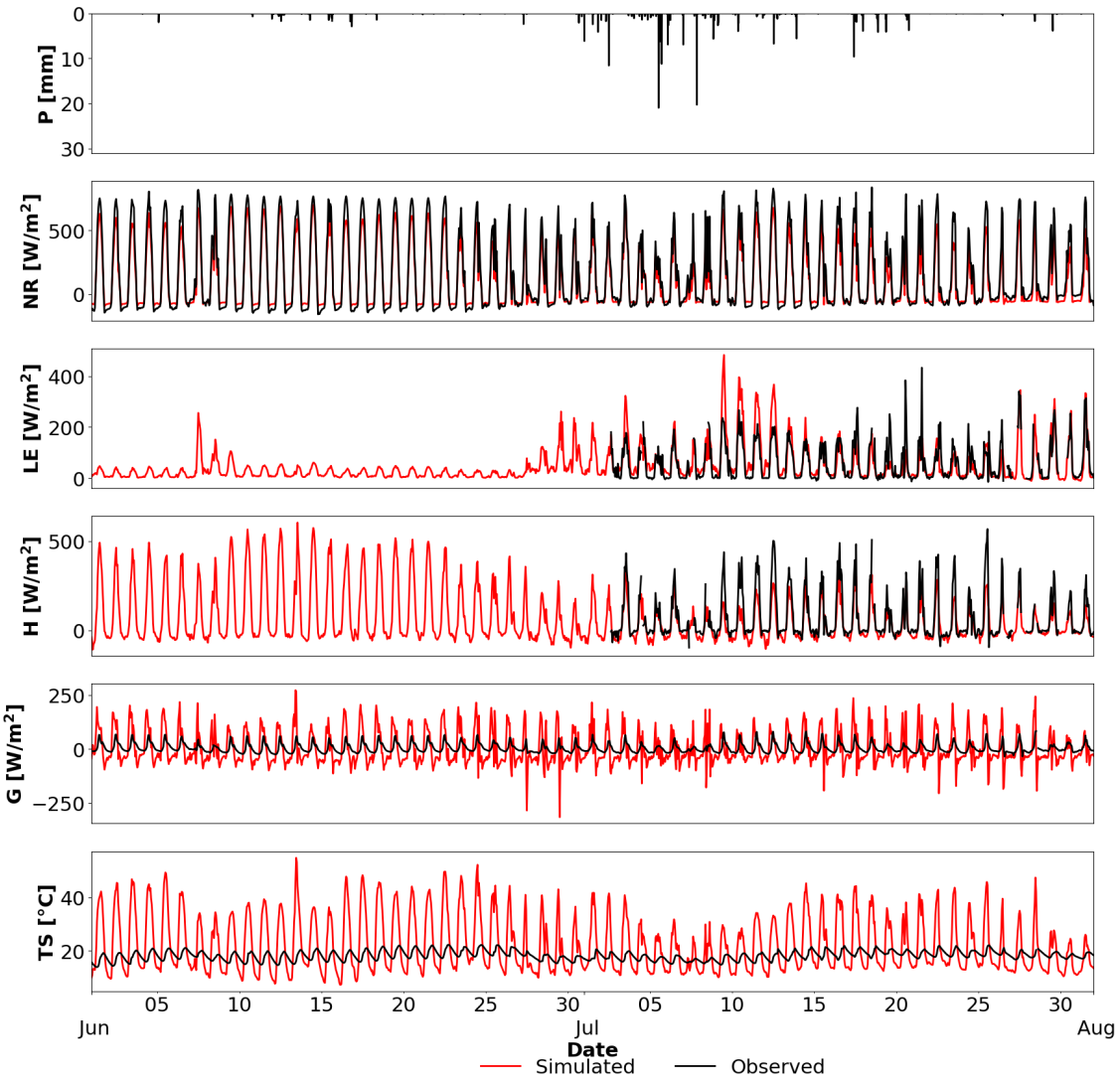

Figure 35: Time series of simulated variables (red) versus observations (black) for the months of June and July of 2006 for US-FUF. From the top down, the panels illustrate precipitation (P), net radiation (NR), latent heat flux (LE), sensible heat flux (H), gound heat flux (G) and soil temperature at 10 cm (TS).

Since surface soil moisture (at 10 cm depth) does not show a clear diurnal cycle, the entire times series of simulated versus observed values were plotted in Figure 36.

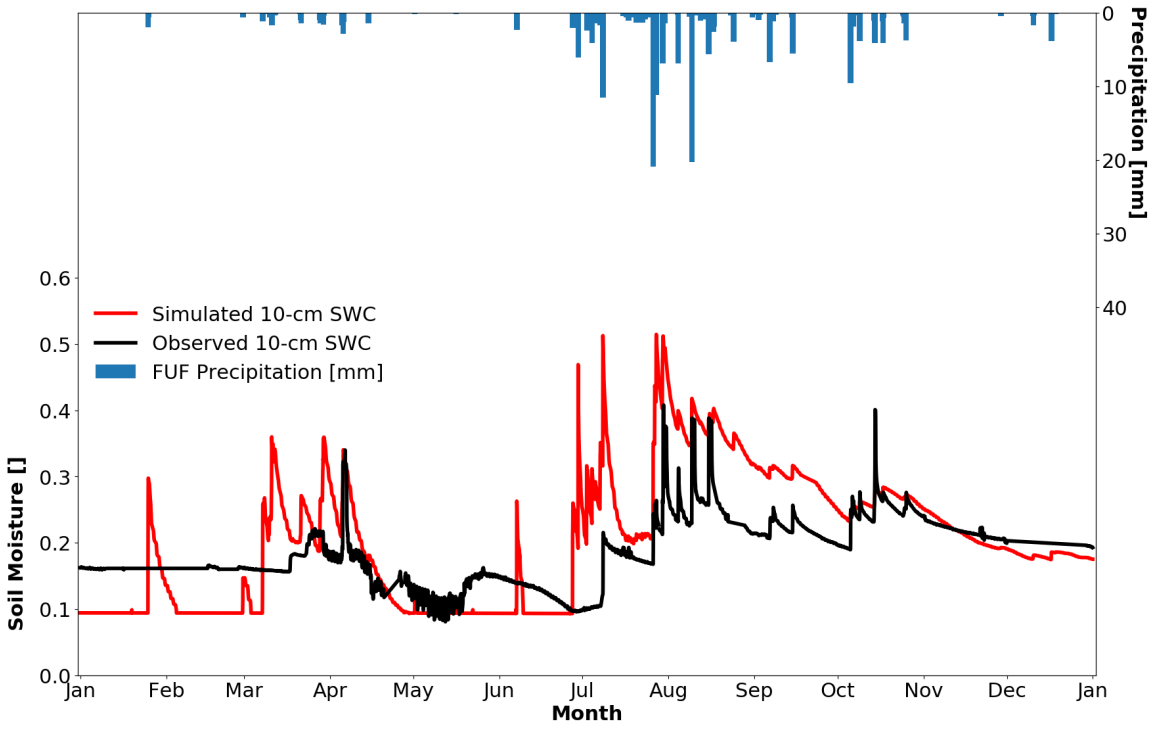

Figure 36: Time series of simulated (red) and observed (black) soil moisture at 10 cm depth for the calibration period (year 2006) at US-FUF.

Figure 36 illustrates that the model is able to reproduce the temporal variability of soil moisture including some maximum values during precipitation events and minimum during dry spells. The simulation was performed at an hourly temporal scale while the albedo was only available in daily temporal scale, LAI was available every 4 days and NDVI every 16 days. With soil moisture dependence on the surface vegetation, low temporal resolution severely reduced the accuracy and the ability of tRIBS to perform well. Furthermore, the model was not able to simulate well the presence of a snow layer on the surface, which amplified the errors during the winter months. The effects of low resolution

from satellite-derived forcing variables could also be seen in the forthcoming simulations across the three ecosystems.

5.2.1.2. US-FWF

The calibration results for US-FWF are illustrated in Figure 37 and Table 8.

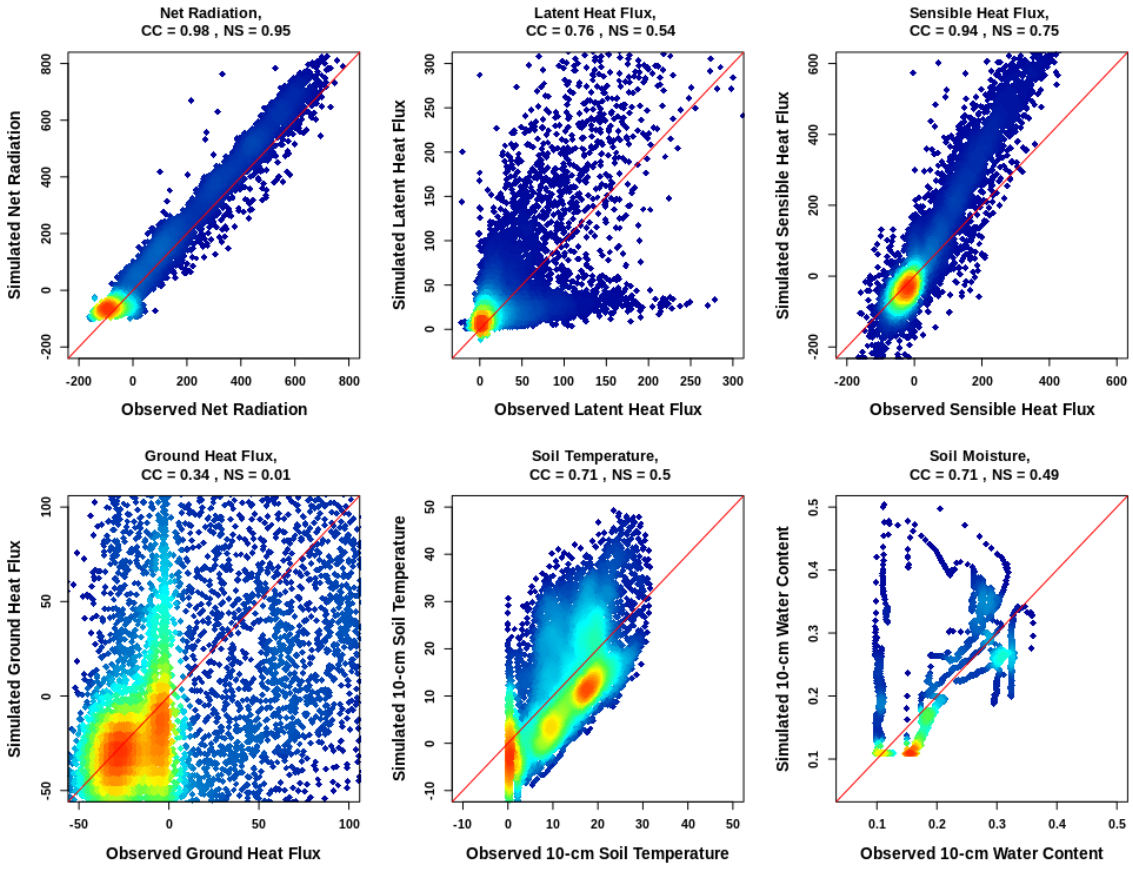

Figure 37: Density scatterplots of simulated variables at US-FWF for year 2007. In all panel the x-axis represents the observations and the y-axis represents the simulated values. The diagonal red line denotes the perfect match between observations and simulations.

Similar to US-FUF, the model shows ability in simulating net radiation (CC = 0.98, NS = 0.95) sensible heat flux (CC = 0.94, NS = 0.75) and 10-cm depth temperature (CC = 0.71, NS = 0.5). Due to freezing temperatures during the winter time, the model had trouble

simulating soil moisture during this period. However, tRIBS produced reasonable results during the remaining period of the year with adequate results for the soil moisture variable, shown with high correlation (0.71) and high Nash-Sutcliffe Coefficients (0.49). Similar to the simulation at US-FUF, the model was also able to capture the historic mean of the ground heat flux (NS = 0.01) but it was not able to capture the daily local minima and maxima. Simulated latent heat flux at US-FWF expressed comparable behaviors to US-FUF with two significant patterns of underestimation and overestimation in winter and summer respectively. Compared to calibrated parameters at US-FUF, the saturated hydraulic conductivity is the most affected parameter post-fire where its value at US-FWF is 4 times higher than that of US-FUF. Soil moisture at saturation and porosity were smaller than those at US-FUF albeit at a smaller difference. Heat conductivity increased while heat capacity decreased at US-FWF. Soil moisture variable depended on multiple parameters but there are 9 most important parameters that controlled their behaviors which are the stress thresholds for soil evaporation and plant transpiration, the pore distribution index, and air entry bubbling pressure and saturated hydraulic conductivity, soil moisture at saturation, residual soil moisture, and porosity. The last three parameters control the range of the simulated soil moisture.

Table 8: Calibration metrics for US-FWF for each of the simulated variables with respect to the observations. Metrics include CC, NS, bias, and RMSE.

Metrics	G ($W.m^{-2}$)	LE ($W.m^{-2}$)	H ($W.m^{-2}$)	NR ($W.m^{-2}$)	TS (°C)	Surface SWC
CC	0.34	0.76	0.94	0.98	0.71	0.71
NS	0.01	0.54	0.75	0.95	0.50	0.49
Bias	3.14	-12.18	-24.26	-29.65	1.10	0.04
RMSE	59.63	57.71	86.13	53.25	6.75	0.08

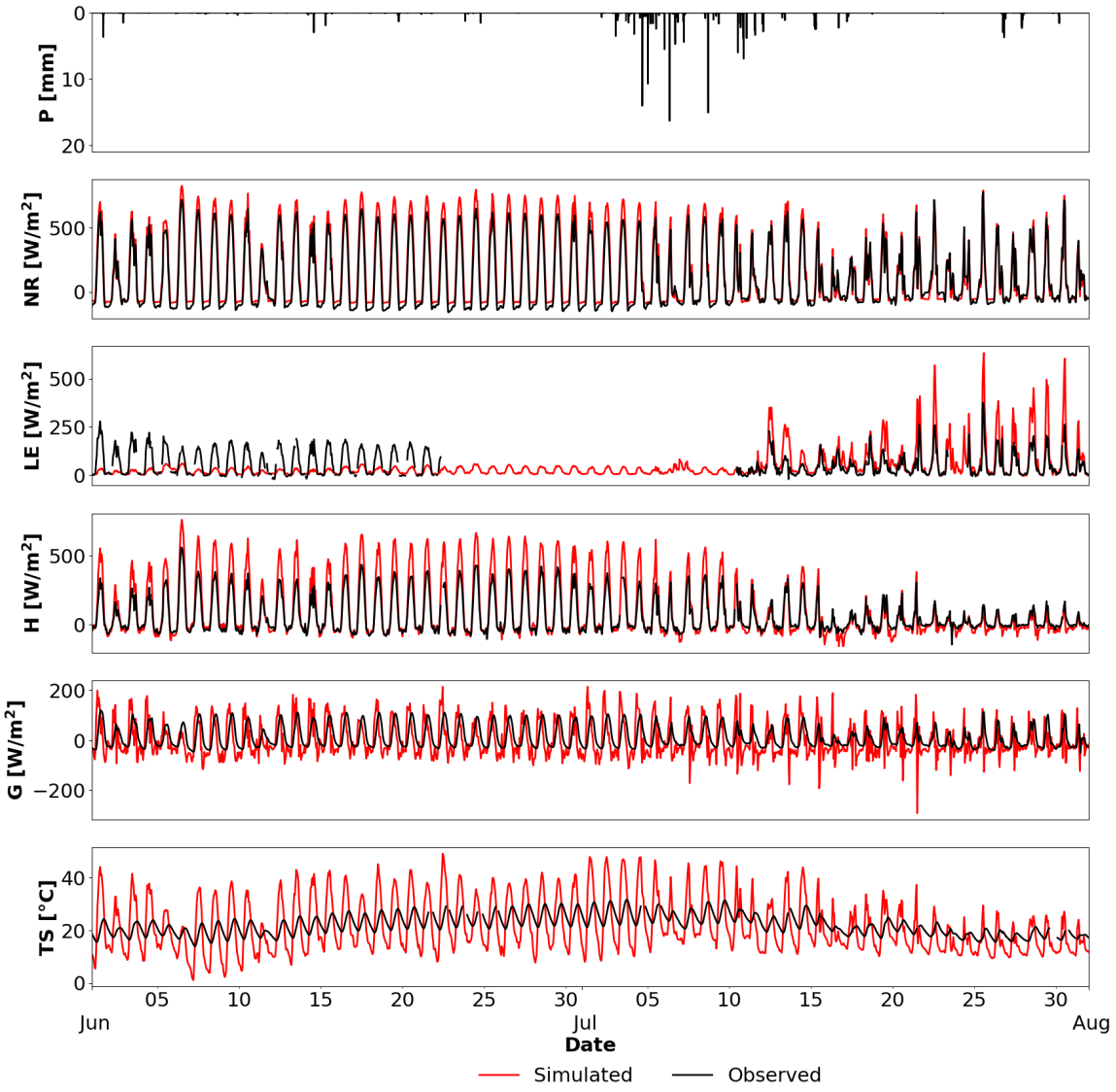

Figure 38: Time series of simulated (red) versus observed (black) values for the months of June and July (Year 2007) for US-FWF. From the top down, the panels illustrate precipitation (P), net radiation (NR), latent heat flux (LE), sensible heat flux (H), gound heat flux (G) and soil temperature at 10 cm (TS).

Similar to the results of soil moisture at 10 cm for US-FUF, the model did not capture the

effects of the winter snow layer as seen in Figure 39 where the observed moisture remained relatively high from January to May despite relatively low precipitation depths.

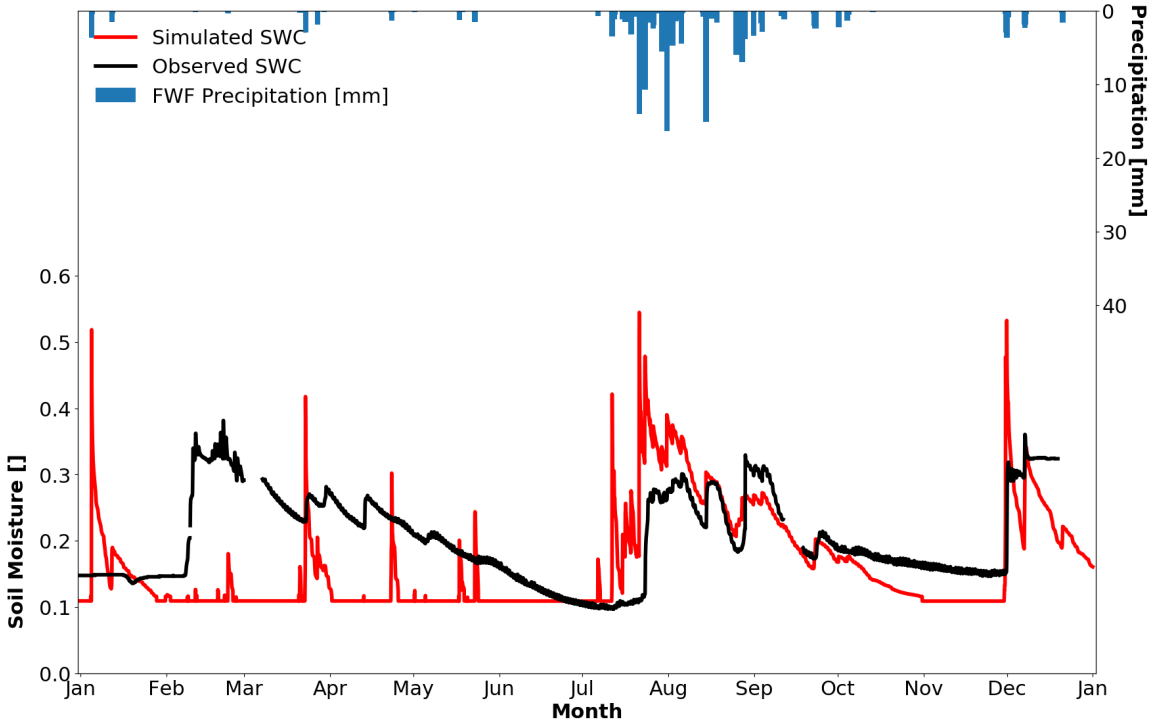

Figure 39: Time series of simulated (red) and observed (black) soil moisture at 10 cm for the calibration period at US-FWF.

5.2.1.3. US-FMF

The calibration results for US-FMF are illustrated in Figures 40, 41 and 42 and Table 9. Simulated ground heat flux expressed similar behaviors as those in US-FUF and US-FWF where the model was able to capture the historic mean but failed to capture the minima and maxima of the variables. The model performed reasonably on surface soil moisture with correlation coefficient of 0.86 and Nash-Sutcliffe coefficient of 0.52. However, the simulation performed poorly in winter where frozen ground present. Sensible heat flux was also well simulated with a correlation coefficient of 0.94 and Nash-Sutcliffe coefficient of 0.62. Surprisingly, despite the high correlation between simulation and observations, the model underestimated the net radiation as shown with a near zero NS of

0.14. Surface temperature was reasonably simulated and its diurnal variability is also captured. Similar to US-FWF, the model did not simulate soil moisture well in the winter, as seen in both Figure 40 and Figure 42. Soil moisture was also not well-captured during the summer months at US-FMF, as seen in Figure 42 where it consistently underestimated the actual soil moisture.

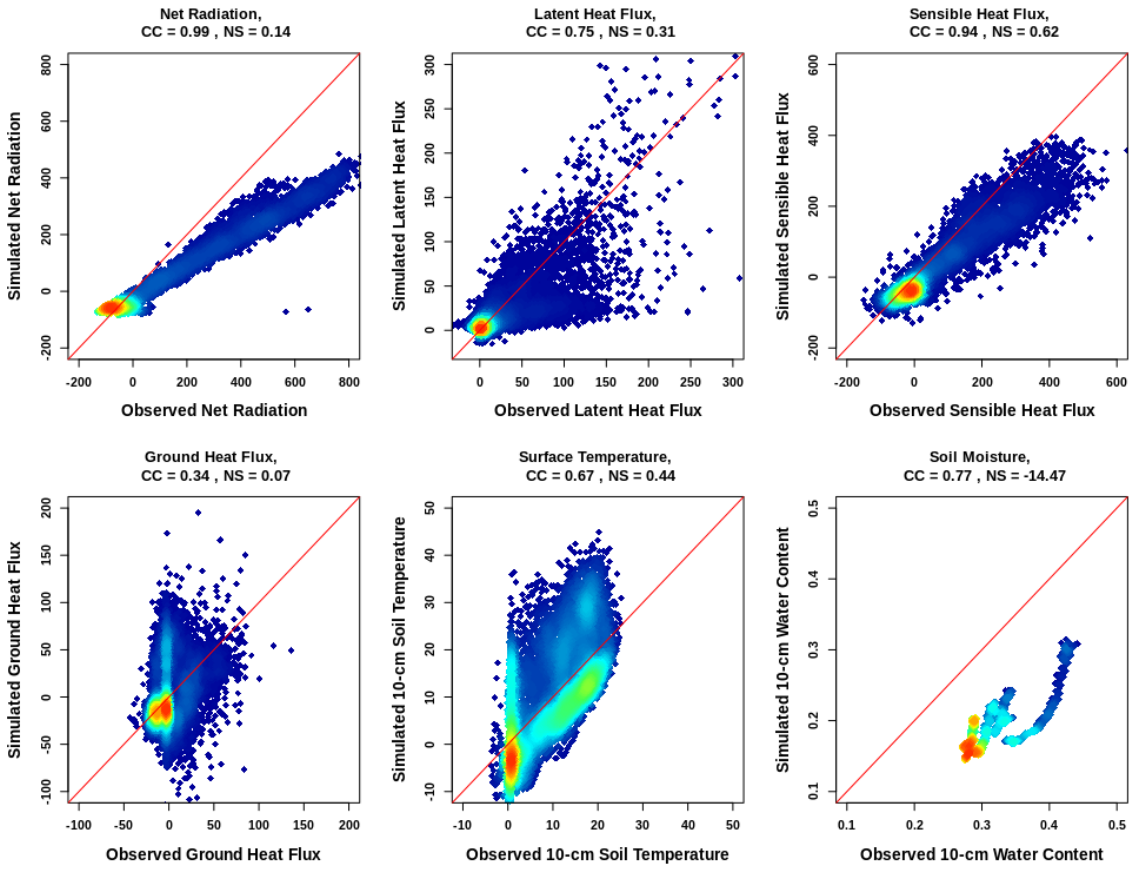

Figure 40: Density scatterplots of the simulated variables at US-FMF. In all panels the x-axis represents the observations and the y-axis represents the simulated values. The diagonal red line denotes perfect match between observations and simulations.

In comparison with undisturbed forest (US-FUF) and severely disturbed forest due to wildfire (US-FWF), human-controlled thinning at US-FMF had noticeable effects on the parameterization of the model for three parameters: saturated hydraulic conductivity, pore distribution index, and air entry bubbling pressure. As dynamic vegetation parameters were

obtained directly from satellite images, the three mentioned parameters, along with soil heat capacity, were the main controlling parameters on the behaviors of surface temperature (10-cm), soil moisture, and surface energy budget.

Table 9: Calibration metrics for US-FMF for each of the simulated variables with respect to the observations. Metrics include CC, NS, bias, and RMSE.

Metrics	G ($W.m^{-2}$)	LE ($W.m^{-2}$)	H ($W.m^{-2}$)	NR ($W.m^{-2}$)	TS (°C)	Surface SWC
CC	0.34	0.75	0.94	0.99	0.67	0.77
NS	0.07	0.31	0.62	0.14	0.44	-14.47
Bias	0.69	7.45	37.13	66.98	-0.56	0.13
RMSE	30.94	30.73	63.43	134.51	8.45	0.13

From Figure 41 and Figure 42, the simulation at US-FMF captured well the diurnal cycles of the latent heat and sensible heat flux while overestimated the ground heat flux and underestimated the resulting net radiation. The diurnal behaviors of soil temperature are also overestimated despite being able to capture the daily cycles. A similar problem was encountered at US-FMF regarding soil moisture simulations during the winter months. However, the period of June to December was characterized by well simulated soil moisture with both the trend and the magnitude of the soil moisture captured by the model.

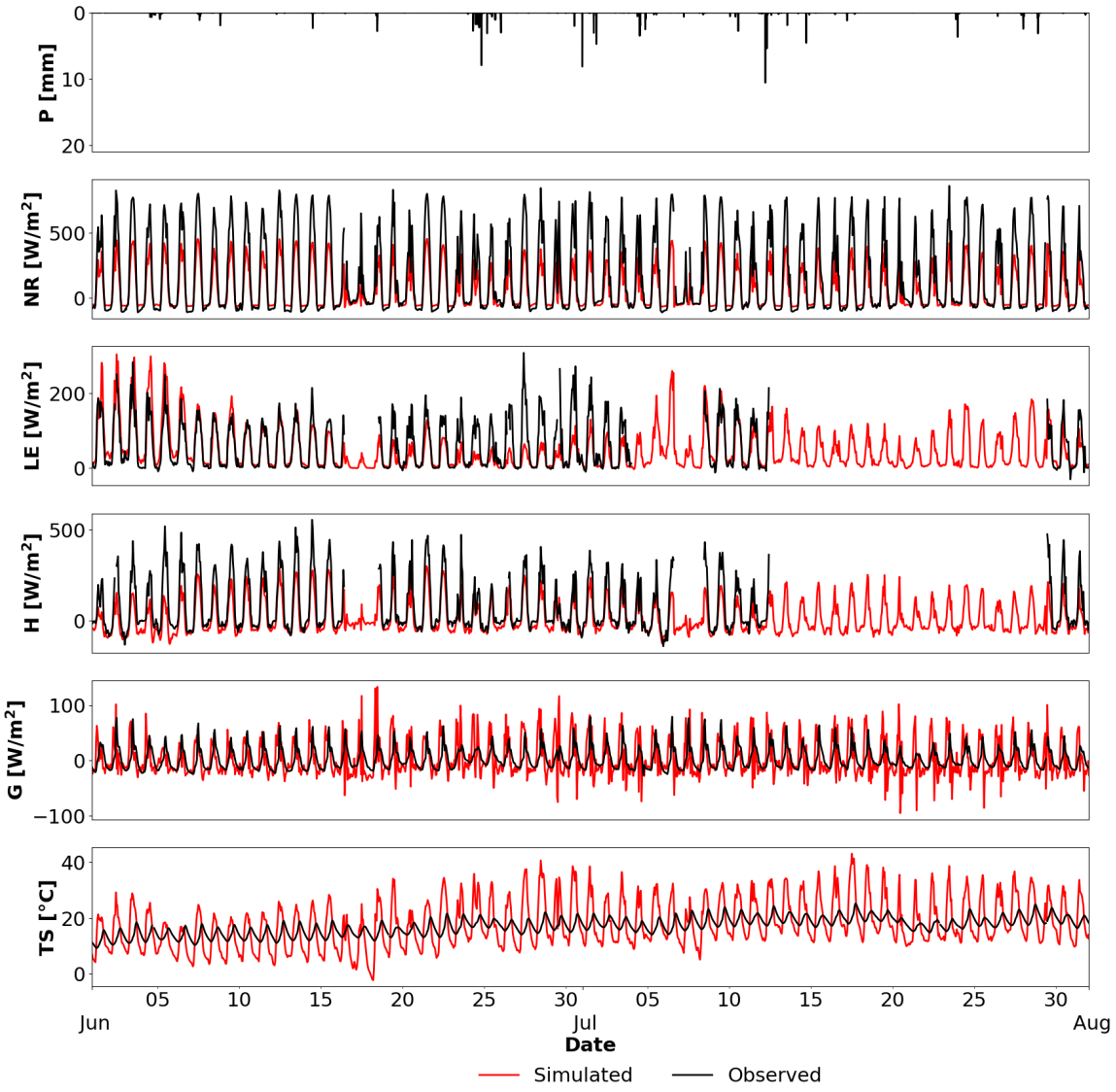

Figure 41: Time series of simulated variables (red) versus the observations (black) for the months of June and July (Year 2009) for US-FMF. From the top down, the panels illustrate precipitation (P), net radiation (NR), latent heat flux (LE), sensible heat flux (H), gound heat flux (G) and soil temperature at 10 cm (TS).

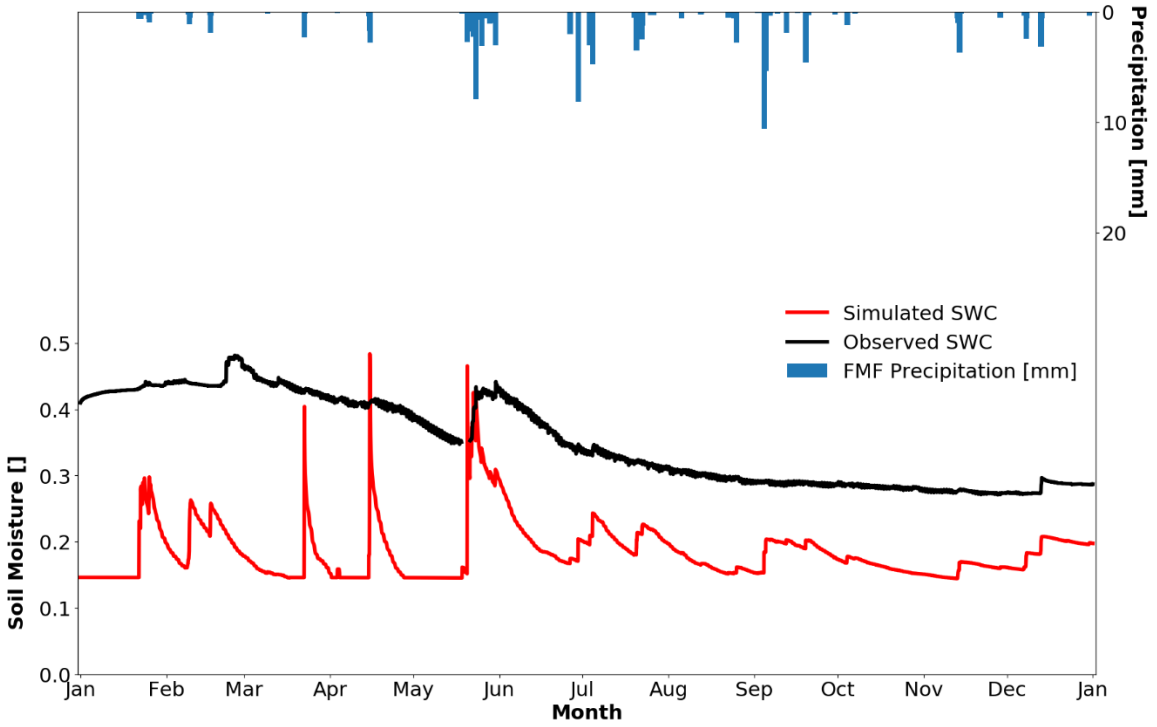

Figure 42: Time series of simulated (red) and observed (black) soil moisture at 10 cm for the calibration period at US-FMF.

5.2.2. Desert Ecosystem

Figures 43, 44 and 45 illustrate the time series of hydrometeorological forcing variables, for the calibration period from January 1st, 2009 to December 31st, 2009 at US-SRC, US-SRM, and US-SRG. It could be seen that the precipitation patterns between the three stations were quite similar, although precipitation magnitudes are observed to be higher at US-SRG and US-SRM. In addition, due to the proximity between the three stations, patterns and magnitudes of the remaining forcing parameters were also similar. This eliminates the influences of hydrometeorological spatial variability when conducting comparisons of the effects of vegetation on water and energy budgets.

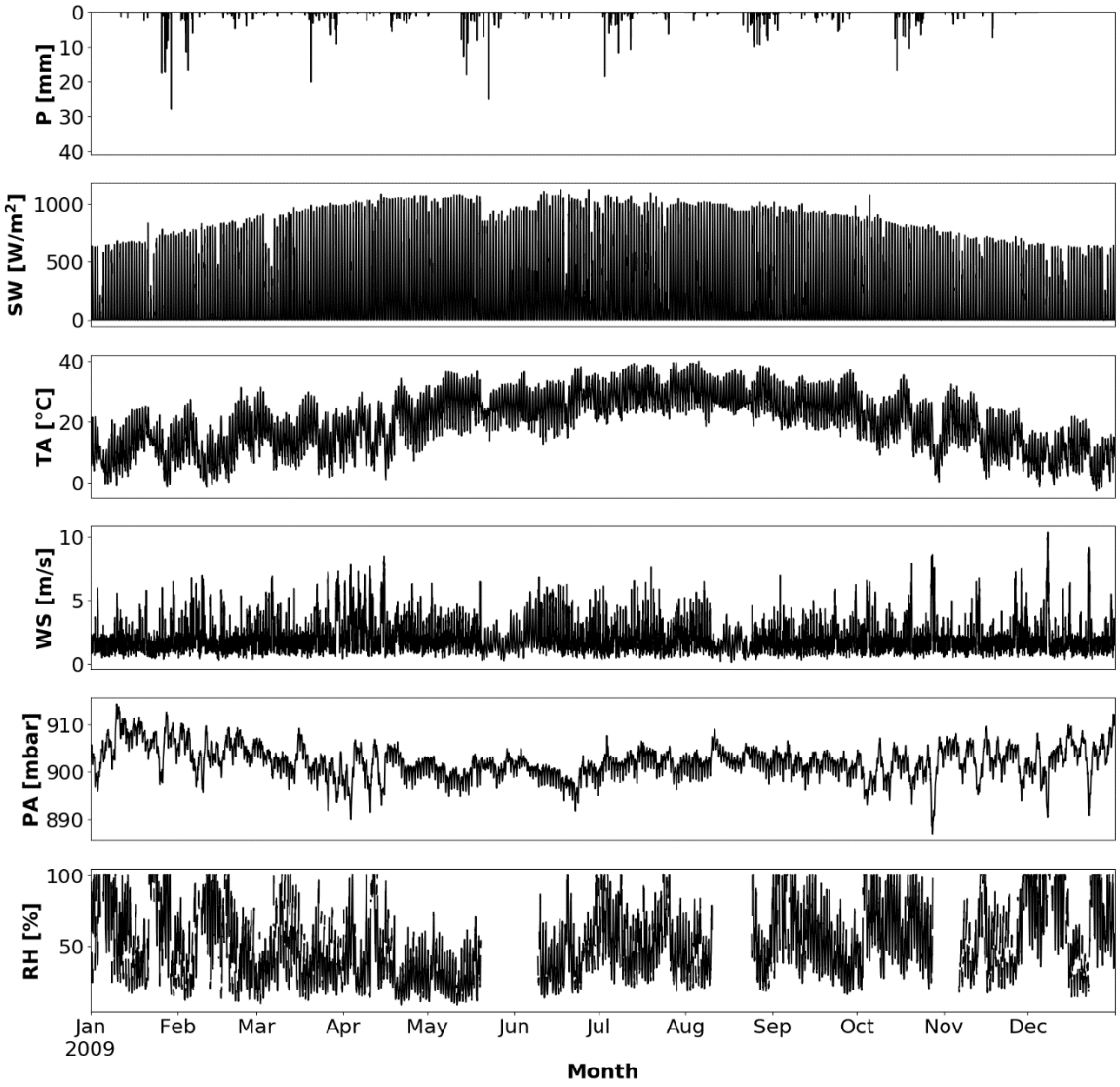

Figure 43: Hydrometeorological forcing variables for US-SRC from 01/01/2009 to 12/31/2009. The six forcing variables are precipitation (mm), incoming shortwave radiation ($W.m^{-2}$), air temperature (°C), wind speed ($m.s^{-1}$), atmospheric pressure (mbar), and relative humidity (%).

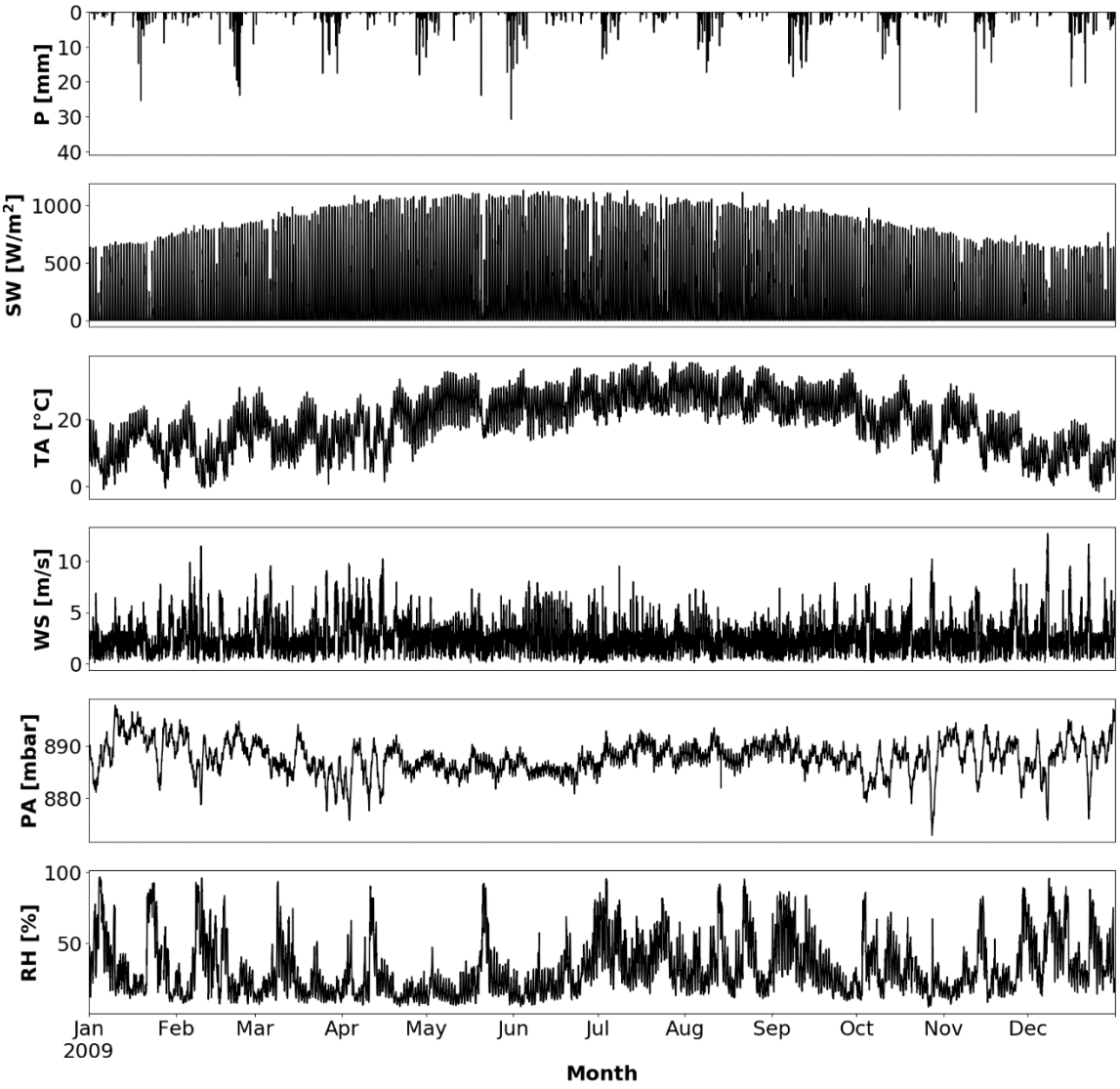

Figure 44: Hydrometeorological forcing variables for US-SRM from 01/01/2009 to 12/31/2009. The six forcing variables are precipitation (mm), incoming shortwave radiation ($W.m^{-2}$), air temperature (°C), wind speed ($m.s^{-1}$), atmospheric pressure (mbar), and relative humidity (%).

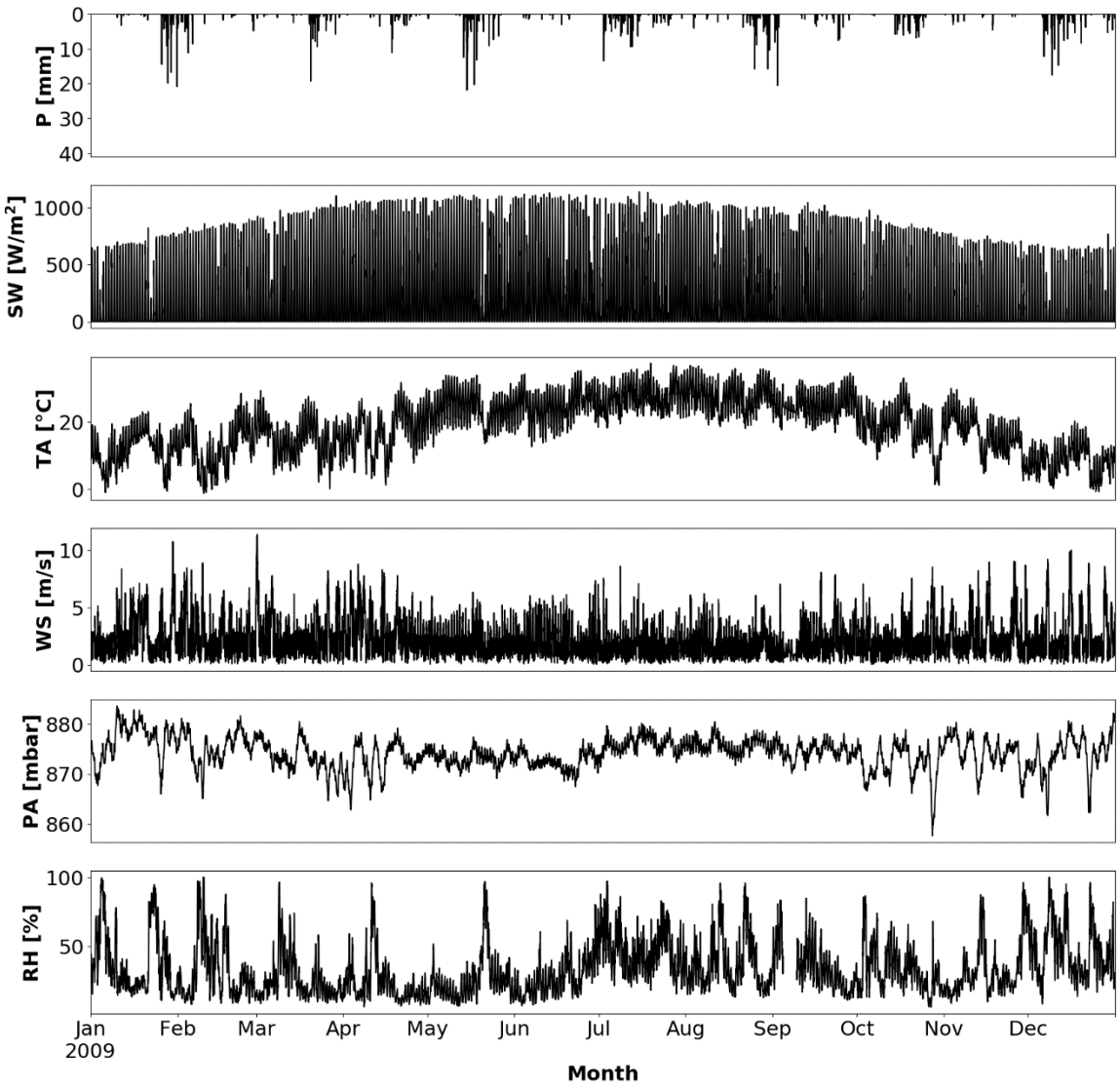

Figure 45: Hydrometeorological forcing variables for US-SRG from 01/01/2009 to 12/31/2009. The six forcing variables are precipitation (mm), incoming shortwave radiation ($W.m^{-2}$), air temperature (°C), wind speed ($m.s^{-1}$), atmospheric pressure (mbar), and relative humidity (%).

Satellite-derived vegetation parameters are presented in Figure 46, 47, and 48.

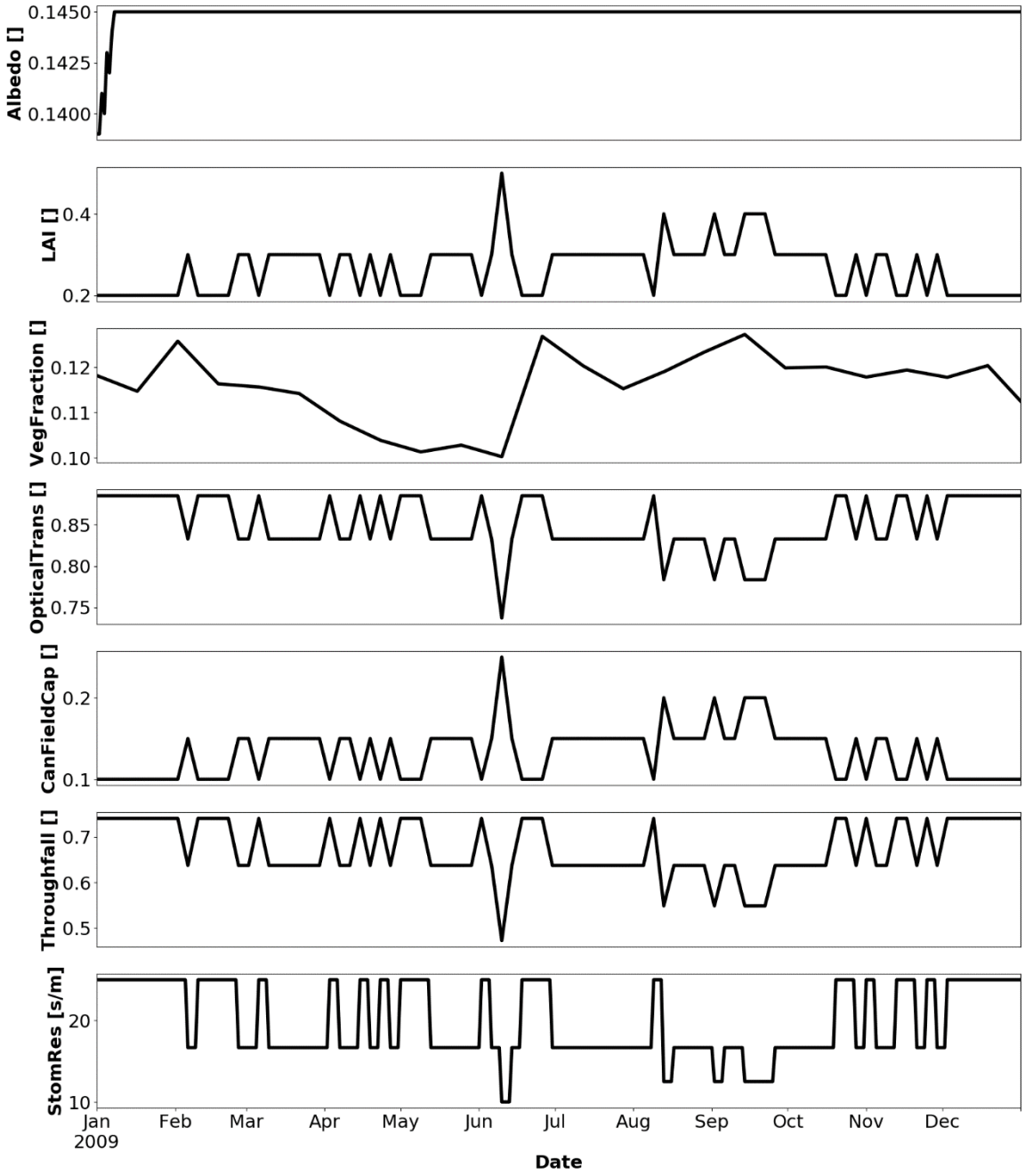

Figure 46: Dynamic vegetation parameters for US-SRC from 01/01/2009 to 12/31/2009. The six parameters are: Albedo (unitless), LAI (unitless), vegetation fraction (unitless), optical transmission (unitless), canopy field capacity (unitless), throughfall coefficient (unitless), and stomatal resistance ($s.m^{-1}$).

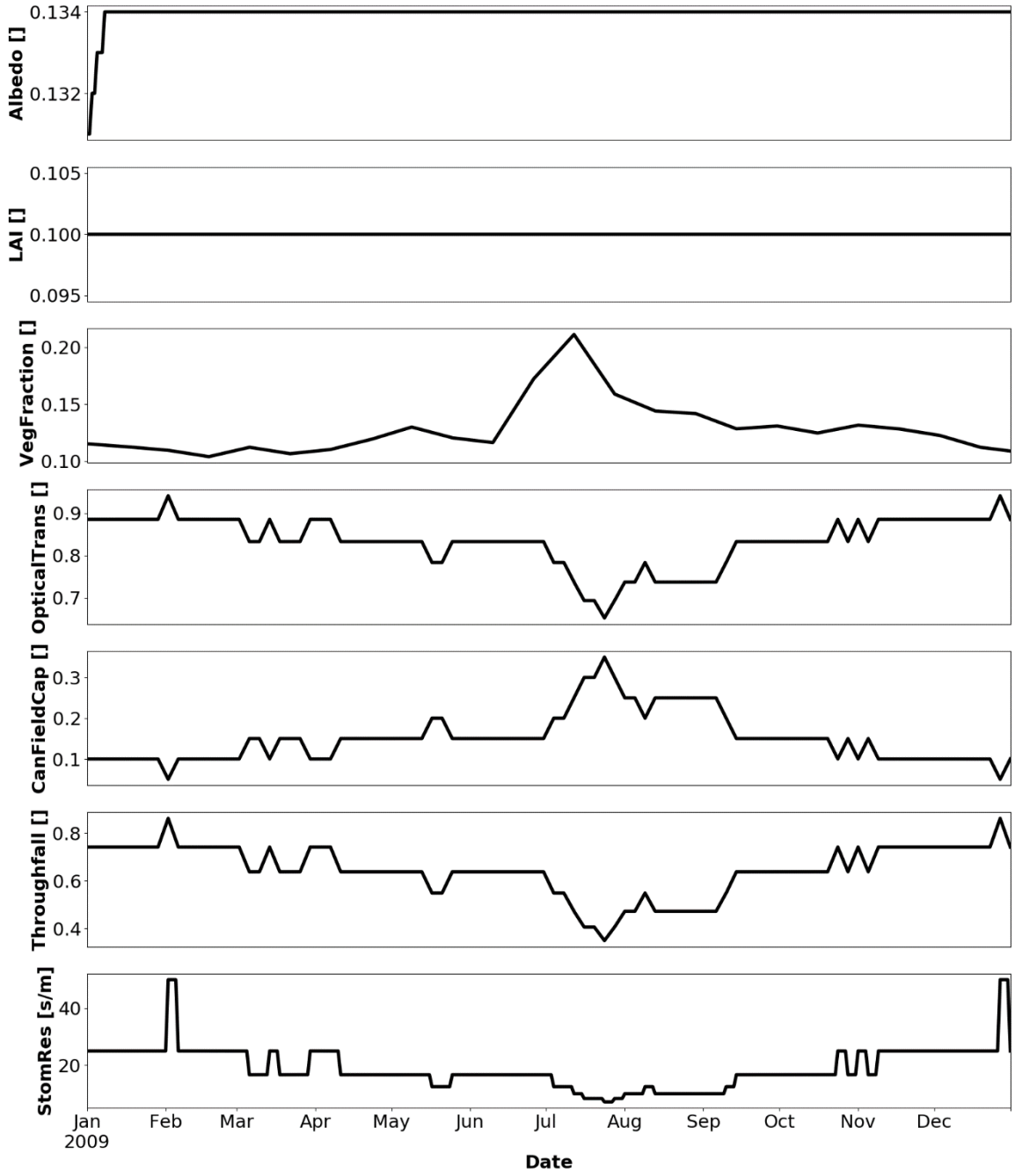

Figure 47: Dynamic vegetation parameters for US-SRM from 01/01/2009 to 12/31/2009. The six parameters are: Albedo (unitless), LAI (unitless), vegetation fraction (unitless), optical transmission (unitless), canopy field capacity (unitless), throughfall coefficient (unitless), and stomatal resistance ($s.m^{-1}$).

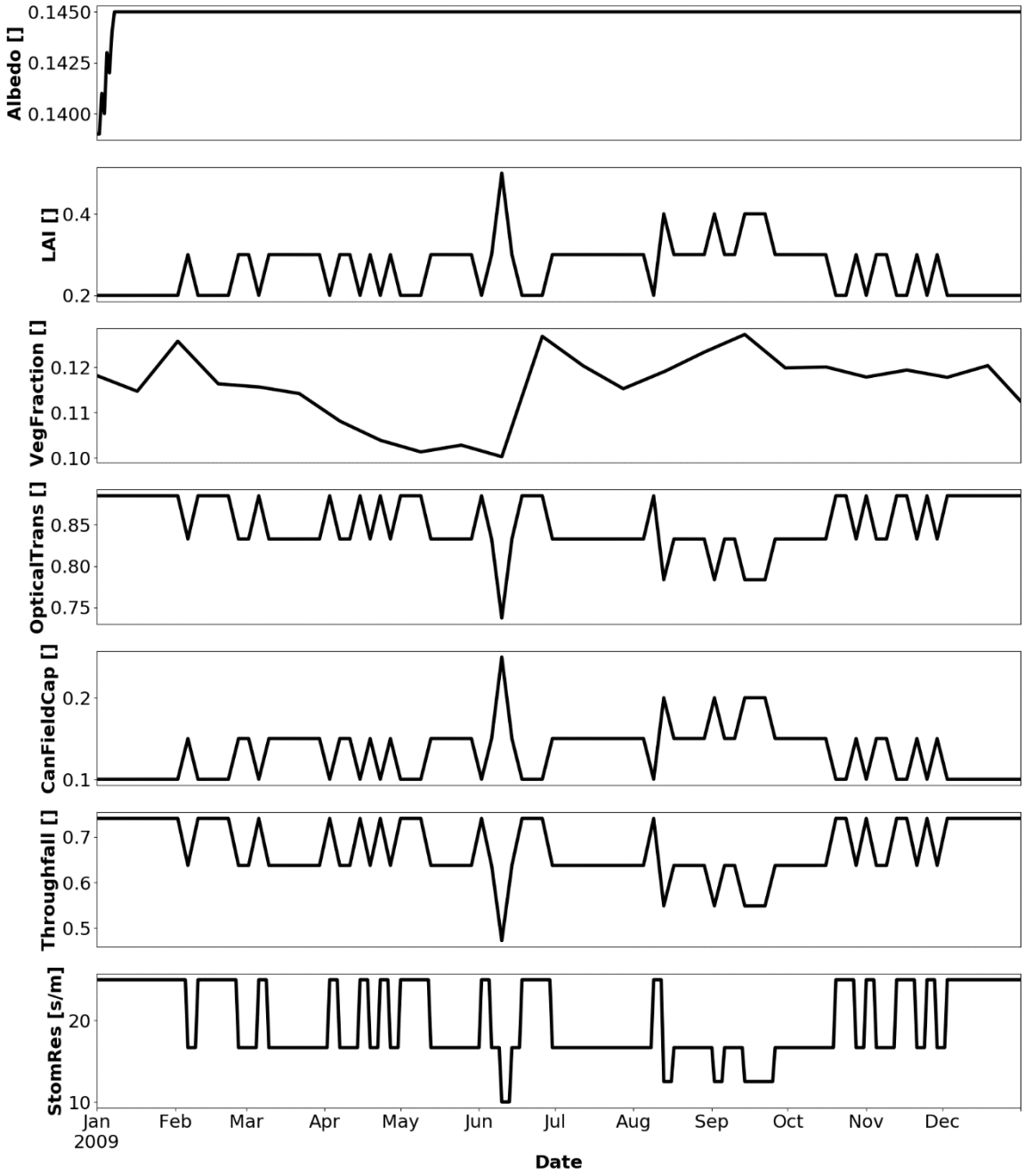

Figure 48: Dynamic vegetation parameters for US-SRG from 01/01/2009 to 12/31/2009. The six parameters are: Albedo (unitless), LAI (unitless), vegetation fraction (unitless), optical transmission (unitless), canopy field capacity (unitless), throughfall coefficient (unitless), and stomatal resistance ($s.m^{-1}$).

Compared to US-SRC, vegetation covers at US-SRG and US-SRM displayed clearer seasonal variability as seen with the vegetation fraction sharply increased from June

to August 2009 and remained low for the rest of the calibration period. LAI displayed clear seasonal trends at US-SRG while remaining relative constant at US-SRC with a decrease from March to June and did not vary throughout the year at US-SRM. Albedo time series were identical between creosote and mesquite with low values in early January and quickly increasing in mid-January. The calibrated soil characteristics and static vegetation parameters for all three stations at Santa Rita are summarized in Table 10.

Table 10: Calibrated parameters for the three ECT at Santa Rita, AZ with descriptions and their units.

Parameter	**Description**	**Unit**	**US-Src**	**US-Srm**	**US-Srg**
Ks	Saturated Hydraulic Conductivity	mm/hr	120	30	80
Θs	Soil Moisture at Saturation	-	0.41	0.32	0.31
Θr	Residual Soil Moisture	-	0.019	0.007	0.008
m	Pore Distribution Index	-	2.2	6.5	5.0
ψ_B	Air Entry Bubbling Pressure	mm	-200	-120	-100
f	Decay Parameter	mm^{-1}	0.02	0.002	0.002
As	Saturated Anisotropy Ratio	-	25	50	25
Au	Unsaturated Anisotropy Ratio	-	140	140	240
n	Porosity	-	0.43	0.43	0.463
ks	Volumetric Heat Conductivity	J/msK	2.2	0.7	0.8
Cs	Soil Heat Capacity	J/m^3K	$2.2*10^6$	$1.8*10^6$	$1.9*10^6$
A	Canopy Storage	mm	0.1	0.1	0.1
b1	Interception Coefficient	-	0.5	0.2	0.2
K	Drainage Coefficient	mm/hr	0.1	2.2	0.1
b2	Drainage Exponential Parameter	mm^{-1}	5.5	3.5	1.5
H	Vegetation Height	m	2.4	5.0	0.5
Θ^*_s	Stress Threshold for Soil Evaporation	-	0.35	0.37	0.3
Θ^*_t	Stress Threshold for Transpiration	-	0.2	0.37	0.1
iwt	Groundwater Table Depth	mm	3150	3000	8120

Surface soil moisture seemed to depend on the saturated hydraulic conductivity, porosity, pore distribution index, and air entry bubbling pressure as well as the limits for water content in soil including soil moisture at saturation, residual soil moisture, stress

threshold for plant transpiration and for soil evaporation. Rootzone soil moisture also depended on the same parameters, along with groundwater table depth. Sensible heat flux, ground heat flux, surface temperature, and rootzone temperature depended on soil heat capacity, and volumetric heat conductivity.

5.2.2.1. US-SRC

Figure 49 illustrates density scatterplots comparing observed and simulated values at US-SRC.

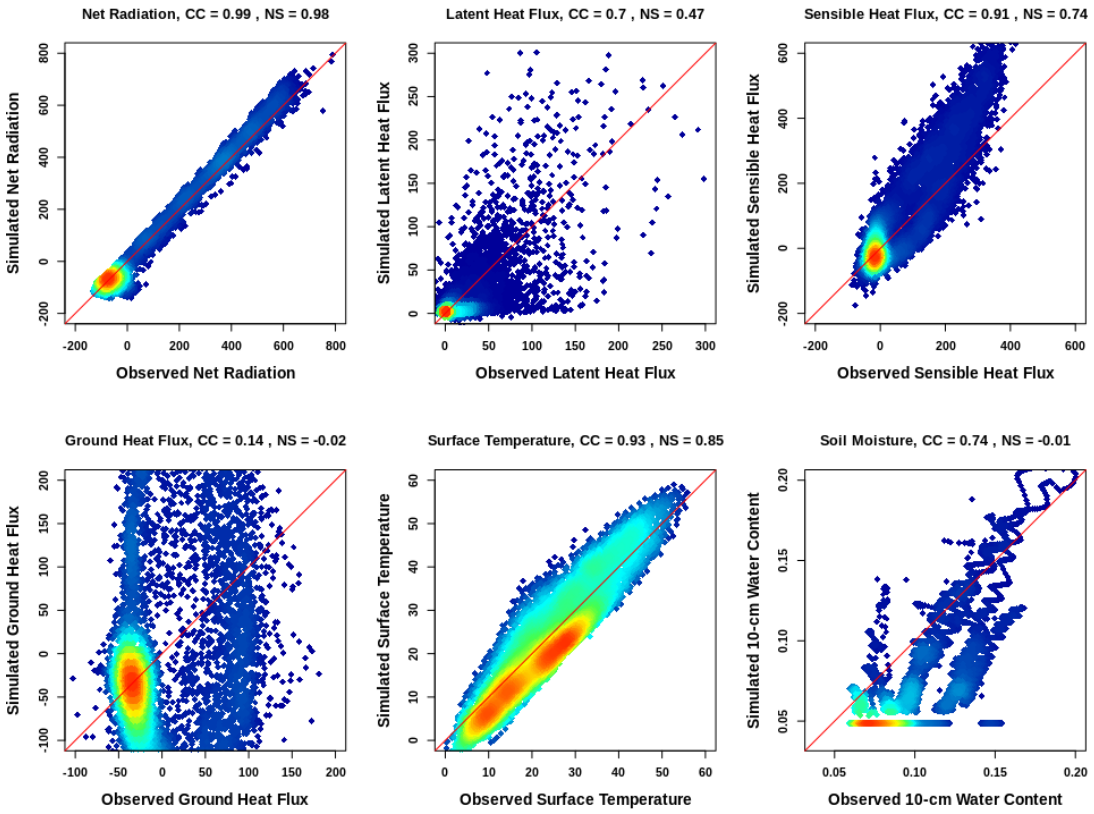

Figure 49: Density scatterplots of simulated versus observed variables at US-SRC. In all panels the x-axis represents the observations and the y-axis represents the simulated values. The diagonal red line denotes the perfect match. Surface simulations of temperature and soil moisture are all for 10 cm depth, while observations of the same variables are at 5 cm and 12.5 cm depth.

Figure 49 shows that the calibrated parameters adequately represent the physical processes that control soil moisture, surface temperature, and surface energy budgets (latent heat flux, sensible heat flux, and net radiation) in this creosote-dominated environment. Nonetheless, the model had issues capturing the maxima and minima as well as the diurnal variations in ground heat flux. Errors in simulating this variable could come from the subsurface heterogeneity that the model parameterization currently cannot capture and the instrument calibration error. tRIBS captured well the surface temperature and net radiation, as shown by the very high NS of 0.93 and 0.98, respectively. The model also predicted reasonably well sensible heat flux (NS = 0.76) and latent heat flux (NS = 0.55) with the highest accuracy occurred when the observations for both variables are low. As the magnitude of the two variables increased, the model tended to overestimate sensible heat flux while underestimating latent heat flux. Soil moisture at 10 cm depth (Figure 50) was reasonably captured by the model with historic mean captured (NS = -0.01); however, the model also overestimated the rate of moisture recession limb that makes simulated soil moisture drain faster than the observation, as seen in Figure 50. Unlike the simulations at Flagstaff, AZ, the simulation at US-SRC was able to capture the behavior of soil moisture during the winter months from January to March. In order to assess the model's ability to capture the diurnal cycles of surface temperature and surface energy balance components, the time series for these variables are plotted for the month of June and July in Figure 51. The results show that the model is able to capture well the diurnal variability for all of the simulated variables, especially net radiation, soil temperature at 5 cm, and sensible heat flux. The model does capture the trend and the variability in ground heat flux, however, it fails to capture the local maxima and minima.

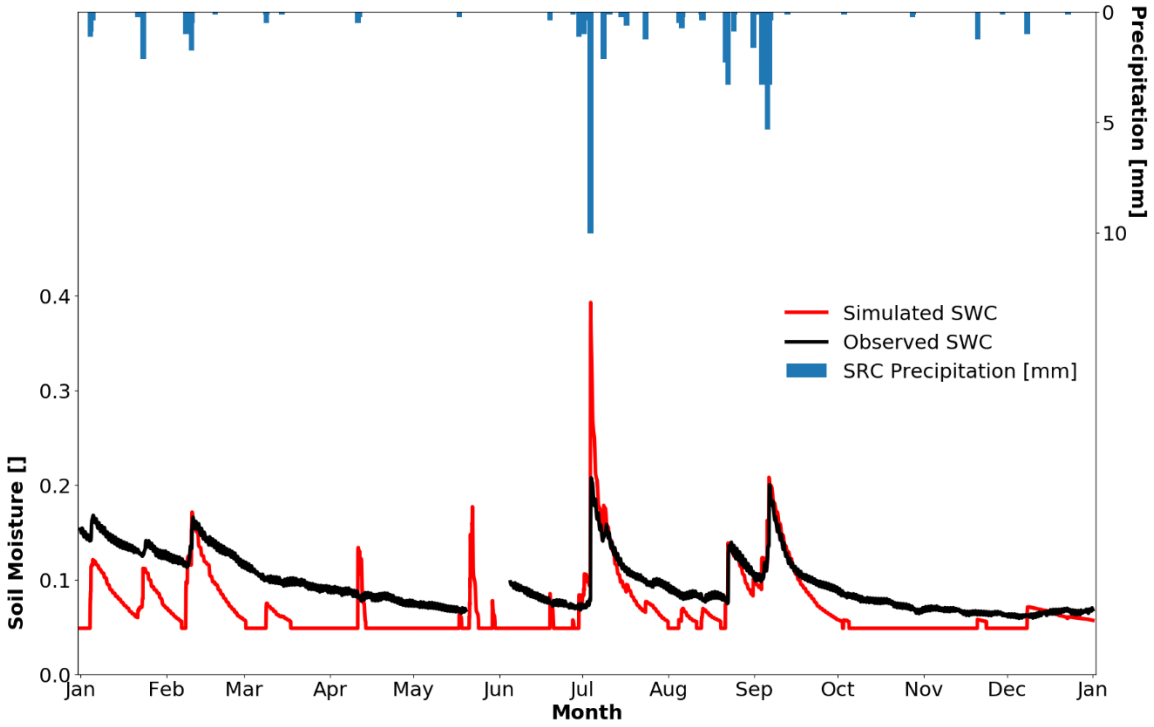

Figure 50: Time series of simulated (red) and observed (black) soil moisture at 10 cm depth for the calibration period at US-SRC.

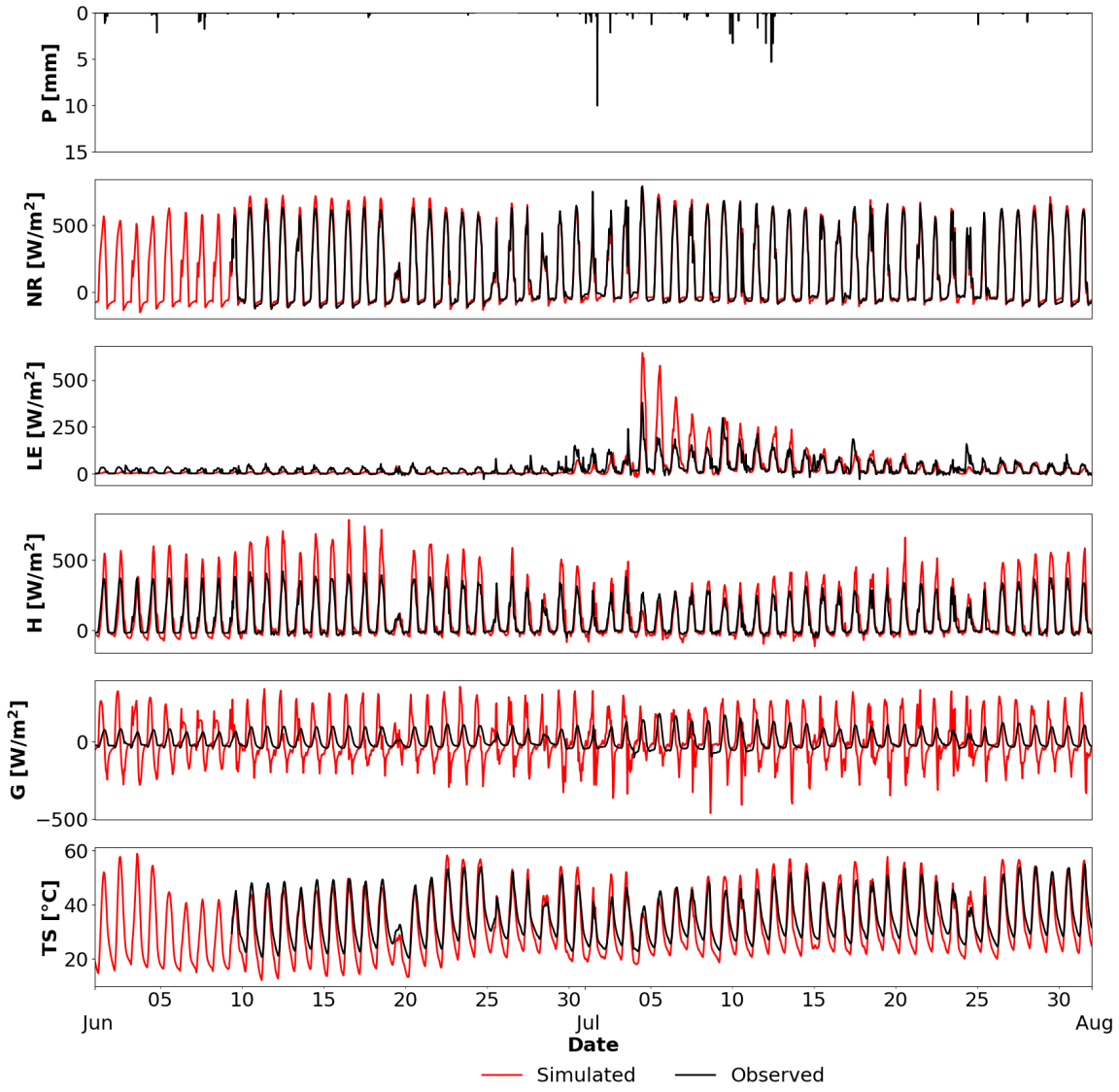

Figure 51: Time series of simulated variables (red) versus the observations (black) for the months of June and July for US-SRC. From the top down, the panels illustrate precipitation (P), net radiation (NR), latent heat flux (LE), sensible heat flux (H), ground heat flux (G) and soil temperature at 10 cm (TS).

5.2.2.2. US-SRG

The scatter density plots for calibration results at US-SRG are illustrated in Figure 52. With the exception of latent heat flux (NS = 0.40), all simulated variables show high NS and CC values. NS of 0.71, 0.71, 0.96, 0.57, 0.88, 0.54, and 0.8 fare obtained for ground heat flux, sensible heat flux, net radiation, surface temperature, rootzone temperature,

surface soil moisture, and rootzone moisture, respectively. The model overestimated the values of sensible heat flux for magnitudes above 300 $W.m^{-2}$. tRIBS also overestimated the magnitude of ground heat flux at high values.

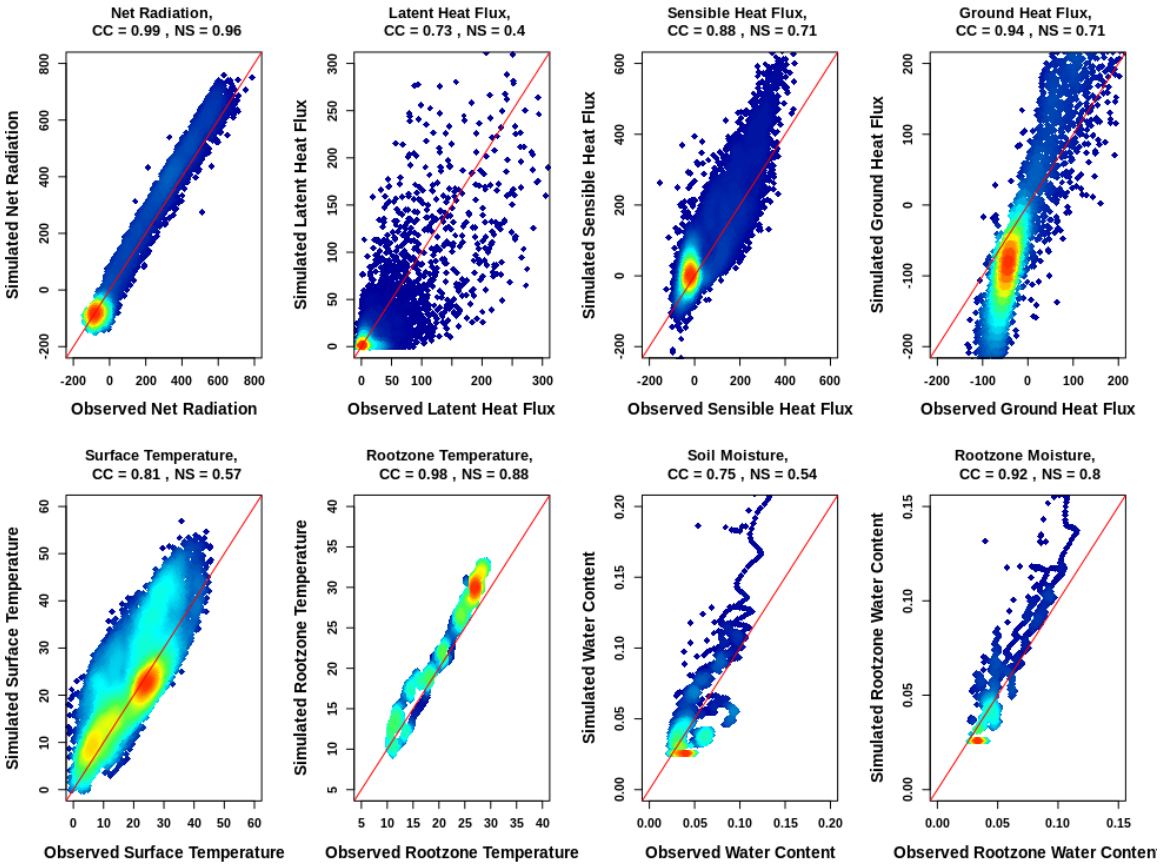

Figure 52: Density scatterplots of the simulated variables at US-SRG. In all panels the x-axis represents observations and the y-axis, the simulated values. The diagonal red line denotes the perfect match between observed and simulated values. Surface simulations of temperature and soil moisture are all for 10 cm depth, while observations of the same variables are at 4 cm and 10 cm depth. Root-zone simulations of soil temperature and moisture were all for 1 m, while observations correspond to 75 cm depth.

A daily time series comparison between simulated and observed surface soil moisture is illustrated in Figure 53. The model performed well during the summer months from May to October. Even though the model was able to capture the maximum soil moisture from January to April, the moisture trend was unsatisfactory as the simulated

moisture dried out too fast compared to the observation. The frozen soil condition at the site during the same period and the model inability to simulate in snow condition led to the low quality results during the winter months.

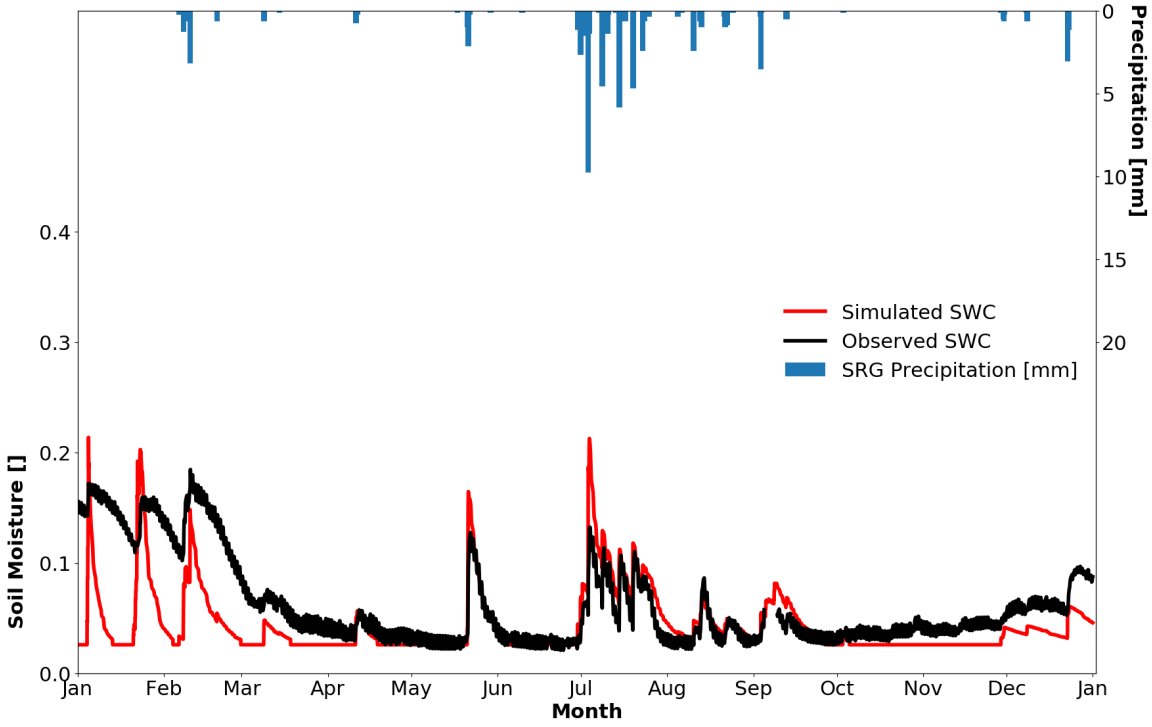

Figure 53: Time series of simulated surface soil moisture (red) and observations (black) for the calibration period at US-SRG using 10-cm soil moisture measurement.

Similar to simulation results at US-SRC, the soil moisture variability at US-SRG depended on the amount of precipitation. The highest discrepancies between the model results and field observations occurred during the winter months, where frozen soil layers led to slower decrease in the observed soil moisture. Diurnal behaviors of surface energy fluxes and temperature, in addition to the local minima and maxima for each variable, were well captured by tRIBS as illustrated in Figure 54, with the exception of some model underestimations of latent heat flux in June and overestimations in July.

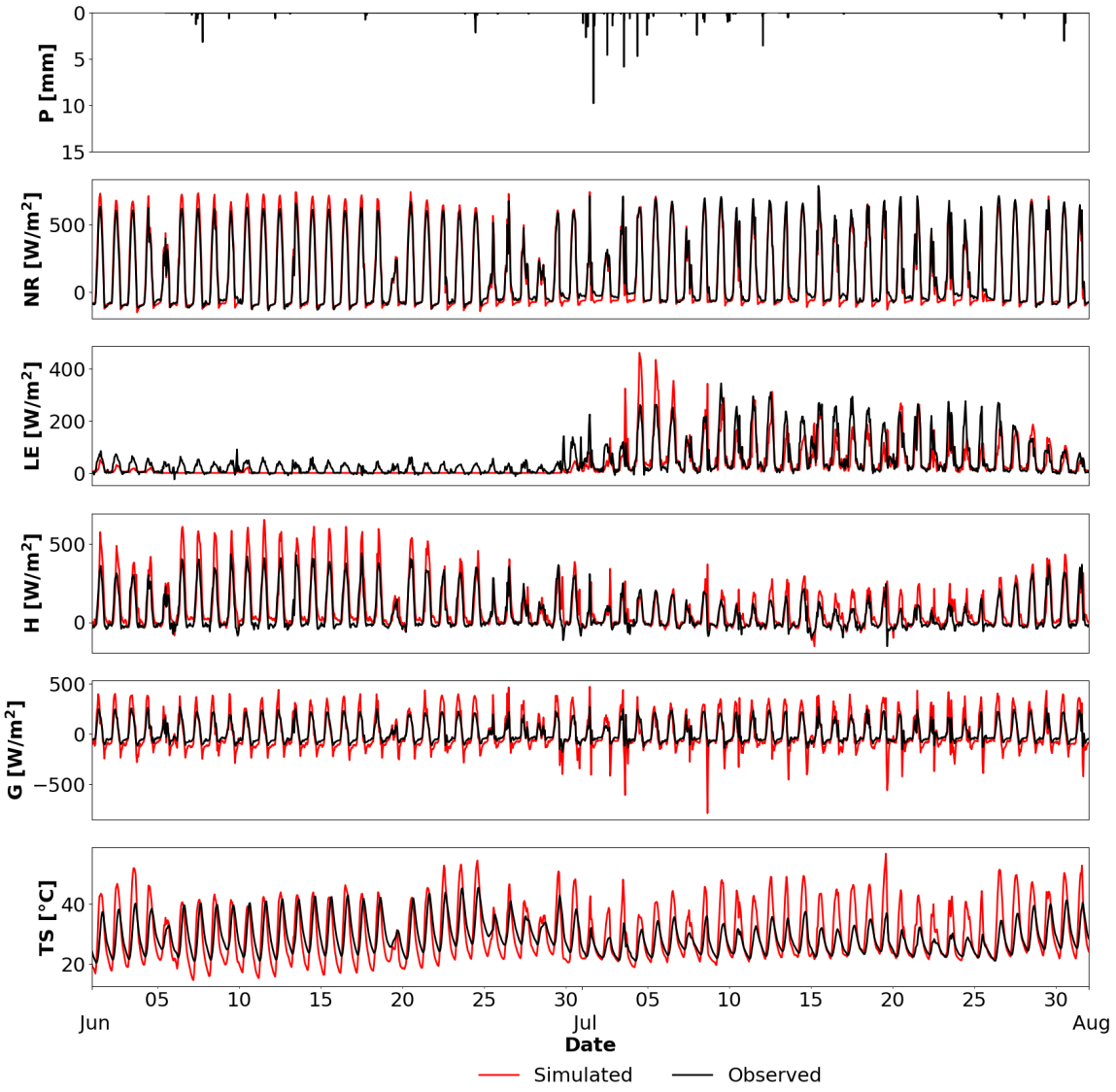

Figure 54*:* Time series of simulated variables (red) versus the observations (black) for the months of June and July for US-SRG.

Table 11: Calibration metrics for US-SRG for each of the simulated variables with respect to the observations. Metrics include CC, NS, bias, and RMSE.

Metrics	G ($W.m^{-2}$)	LE ($W.m^{-2}$)	H ($W.m^{-2}$)	NR ($W.m^{-2}$)	TS (°C)	Rootzone TS (°C)	Surface SWC	Rootzone SWC
CC	0.94	0.73	0.88	0.98	0.81	0.98	0.75	0.92
NS	0.71	0.40	0.71	0.96	0.57	0.88	0.54	0.80
Bias	9.21	6.37	-33.26	-14.52	-3.21	-1.86	0.004	0.0001
RMSE	83.74	27.75	73.27	48.35	7.43	2.46	0.02	0.01

5.2.2.3. US-SRM

Figure 55 illustrate density scatterplots as a result of the calibration for US-SRM in 2009. Similar to US-SRG, the model simulated and captured the variability of ground heat flux, sensible heat flux, net radiation, and temperatures at two different depths with high accuracy, as shown by the high CC (> 0.7) and NS (> 0.5). Latent heat flux, surface soil moisture, and rootzone moisture show lower performances. Despite the shortcomings, the general trends in both soil moisture and latent heat flux were captured.

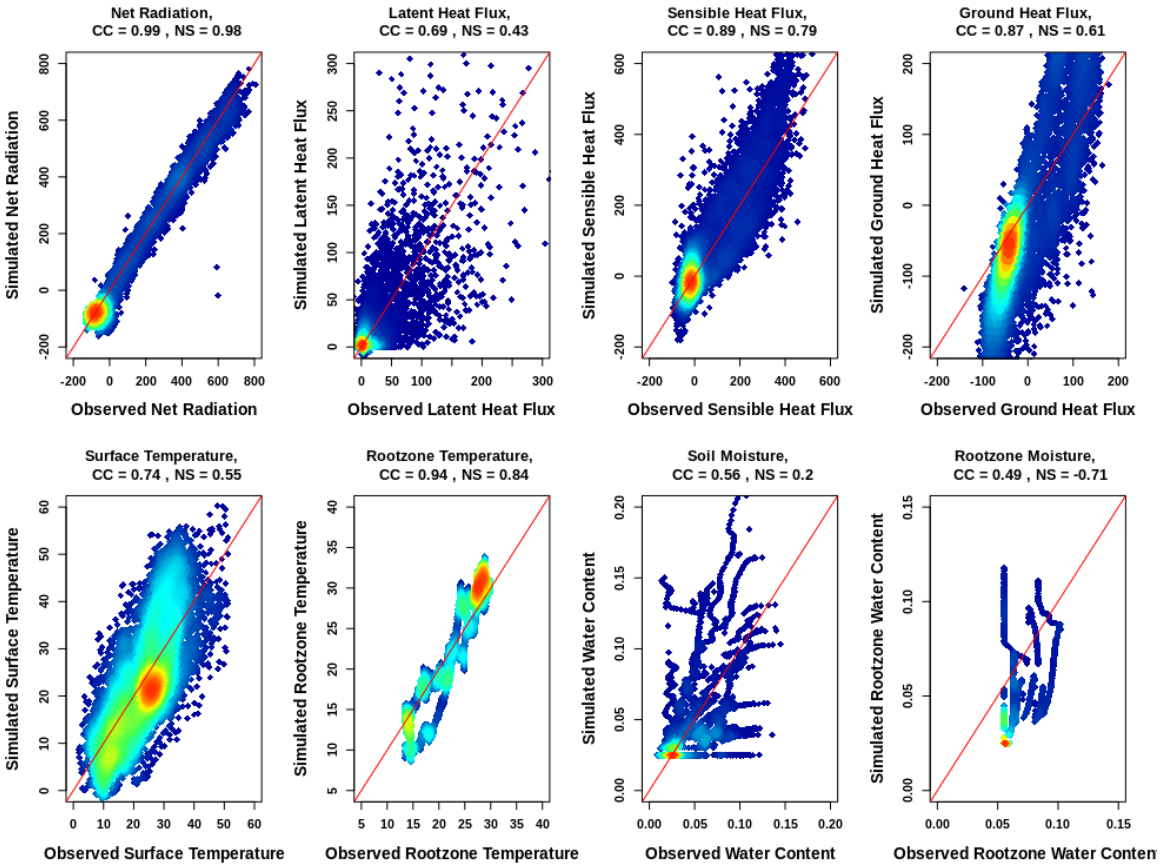

Figure 55: Density scatterplots of the simulated variables at US-SRM. In all panels the x-axis represents the observations and the y-axis the simulated values. The diagonal red line denotes the perfect match. Surface simulations of temperature and soil moisture are all for 10 cm depth, while observations of the same variables are at 5 cm and 10 cm depth. Root-zone simulations of soil temperature and moisture were all for 1 m, while observations where only available at 70 cm depth.

From the diurnal variability plot (Figure 56), latent heat flux is observed to be overestimated by tRIBS in June while adequately captured in July. This can be attributed to the constant values of stress thresholds throughout the simulated period or the errors from estimating the stomatal resistance from satellite products. The model also failed to capture any evapotranspiration from June as seen in Figure 56. The surface temperature diurnal variations were captured by tRIBS. However, the model underestimated the temperature in June while overestimated its upper threshold during the day and accurately captures the lower temperatures at night in July.

Table 12: Calibration metrics for US-SRM for each of the simulated variables with respect to the observations. Metrics include CC, NS, bias, and RMSE.

Metrics	G ($W.m^{-2}$)	LE ($W.m^{-2}$)	H ($W.m^{-2}$)	NR ($W.m^{-2}$)	TS (°C)	Rootzone TS (°C)	Surface SWC	Rootzone SWC
CC	0.92	0.67	0.87	0.99	0.77	0.95	0.56	0.49
NS	0.62	0.34	0.75	0.98	0.59	0.85	0.20	-0.71
Bias	1.80	1.84	-10.49	4.30	0.45	0.06	0.00	0.02
RMSE	98.97	28.01	67.94	33.45	7.30	2.77	0.03	0.03

The time series comparison of simulated and observed soil moisture for US-SRM is presented in Figure 56. Among the six calibration simulation across Santa Rita, AZ and Flagstaff, AZ, the simulated soil moisture had the worst score in CC and NSE. It can be seen that there was a lag in simulated soil moisture compared to the observation in which the simulated moisture reacted quicker to the observed precipitation events in the winter months while the reverse is true for the summer months where simulated soil moisture reacted slower compared to the observations.

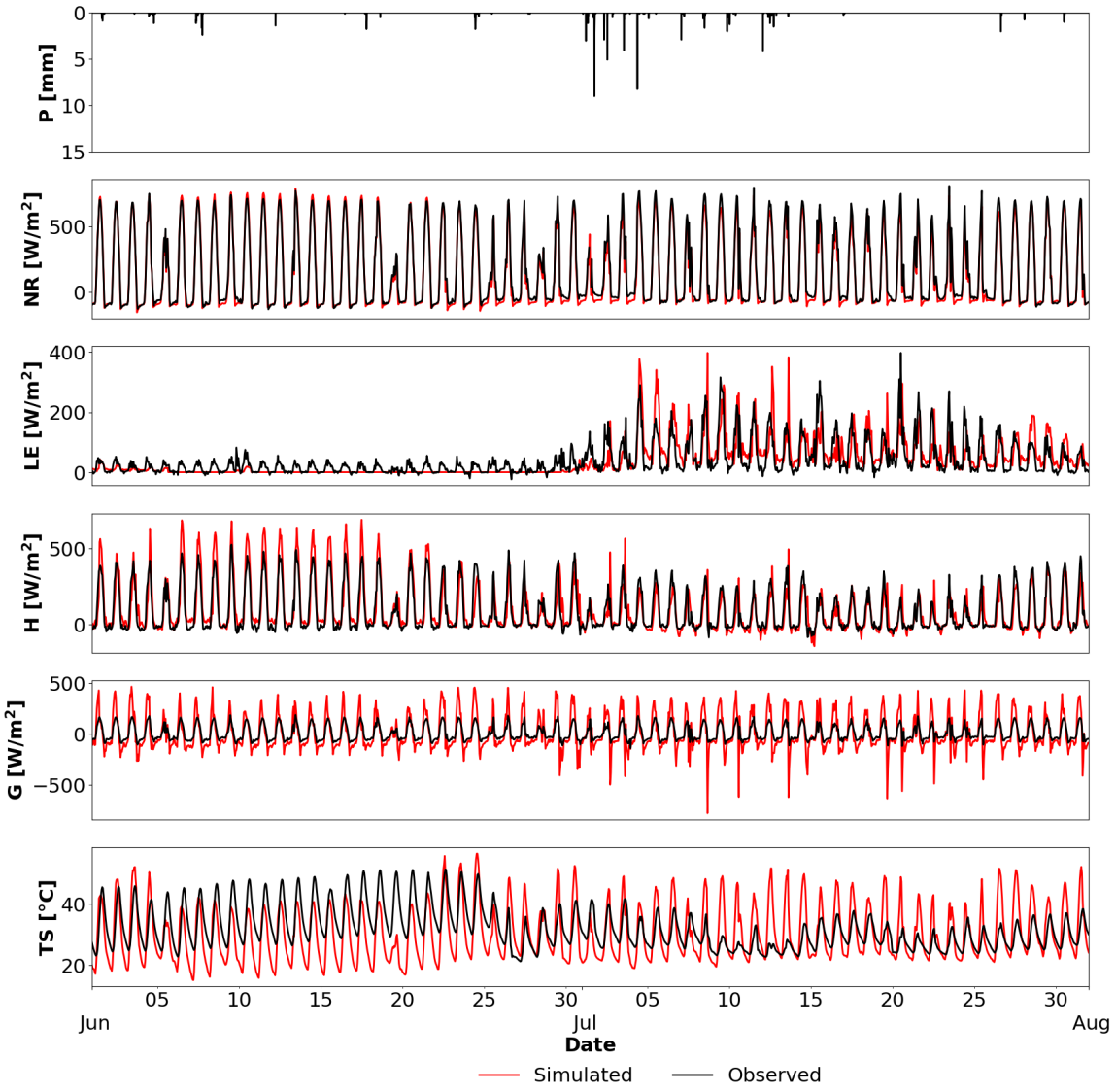

Figure 56: Time series of simulated variables (red) versus the observations (black) for the months of June and July for US-SRM.

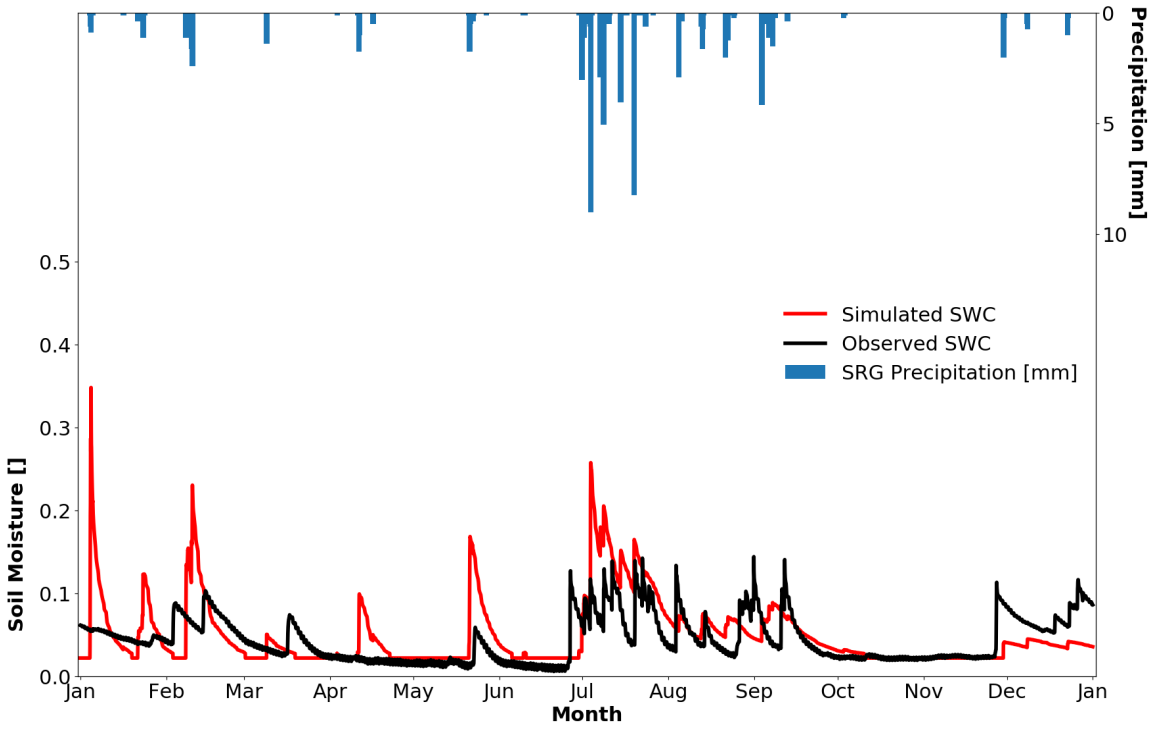

Figure 57: Time series of simulated (red) and observed (black) surface soil moisture for the calibration period at US-SRM.

5.2.3. Grassland Ecosystem

Figure 58 illustrates the time series of hydrometeorological forcing variables for the calibration period from January 1st, 2016 to December 31st, 2016 at the MOISST station in Marena, OK. Seasonality is clearly marked through the time series of precipitation, incoming shortwave radiation, air temperature and atmospheric pressure. Precipitation was concentrated from May to October with high a maximum hourly value of 30 mm. The months of November through February were mostly dry with few isolated events. Incoming shortwave radiation and air temperature increased gradually from their lows in January and February to their highs from May to October and gradually decreased again from November onward. Air pressure fluctuated greatly for most of the time with an exception

from June to September where it stayed relatively stable around 980 mb. Wind speed and relative humidity did not exhibit clear seasonal trends although relative humidity remained high year round.

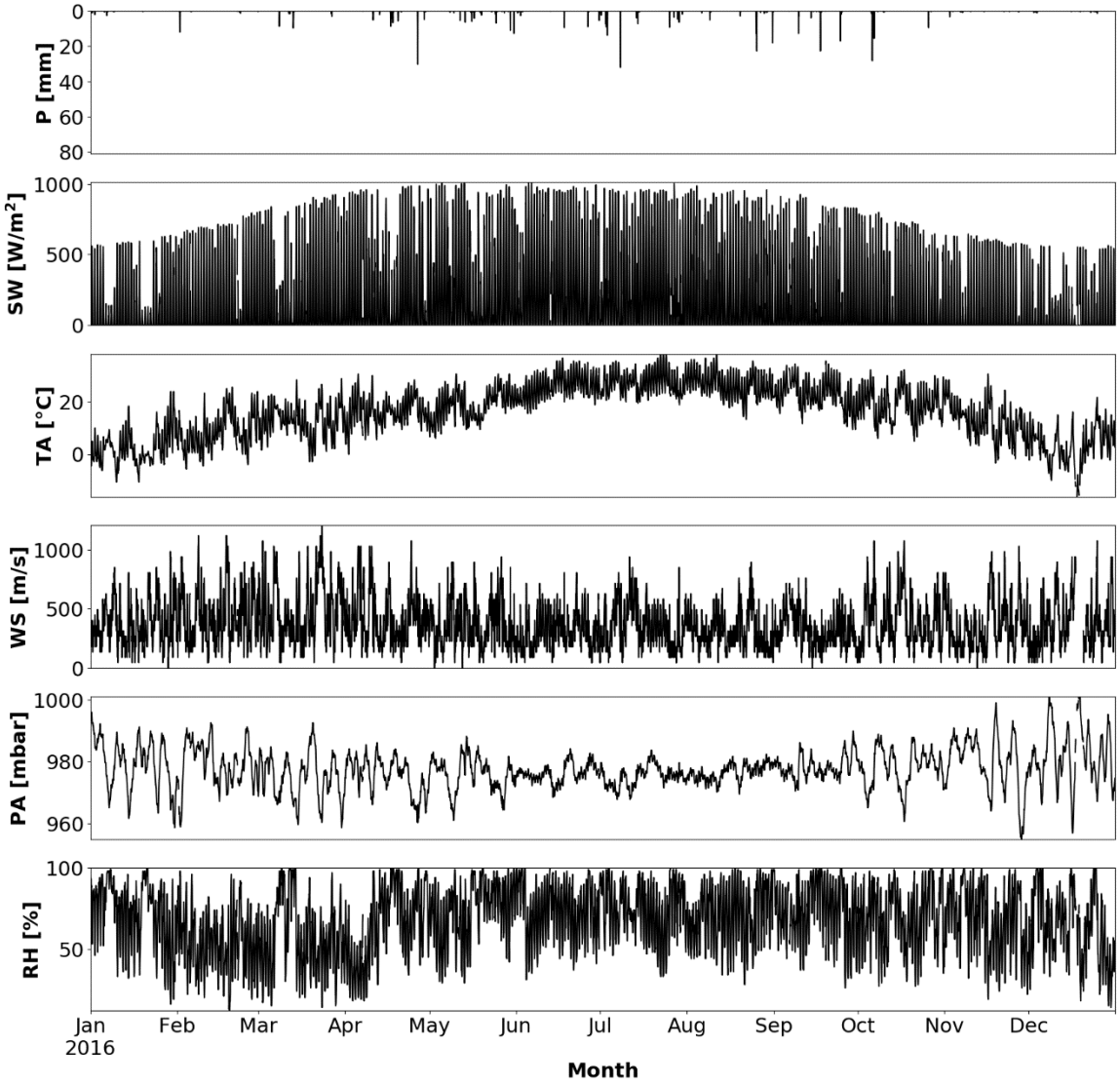

Figure 58: Hydrometeorological forcing variables at MOISST from 01/01/2016 to 12/31/2016. The six forcing variables are precipitation (mm), incoming shortwave radiation ($W.m^{-2}$), air temperature (°C), wind speed ($m.s^{-1}$), atmospheric pressure (mbar), and relative humidity (%).

Dynamic vegetation forcing parameters are presented in Figure 59 for the calibration period of 2016. These parameters also displayed clear seasonal variability.

Vegetation fraction and LAI both increased from mid-April to October (0.2 to 0.6 and 0.2 to 3), while albedo decreased (0.15 to < 0.05) during the same period which shows the vegetation at the site absorbs most of the incoming radiation. Two sudden decreases in LAI values in July and mid-September were observed due to unknown reasons.

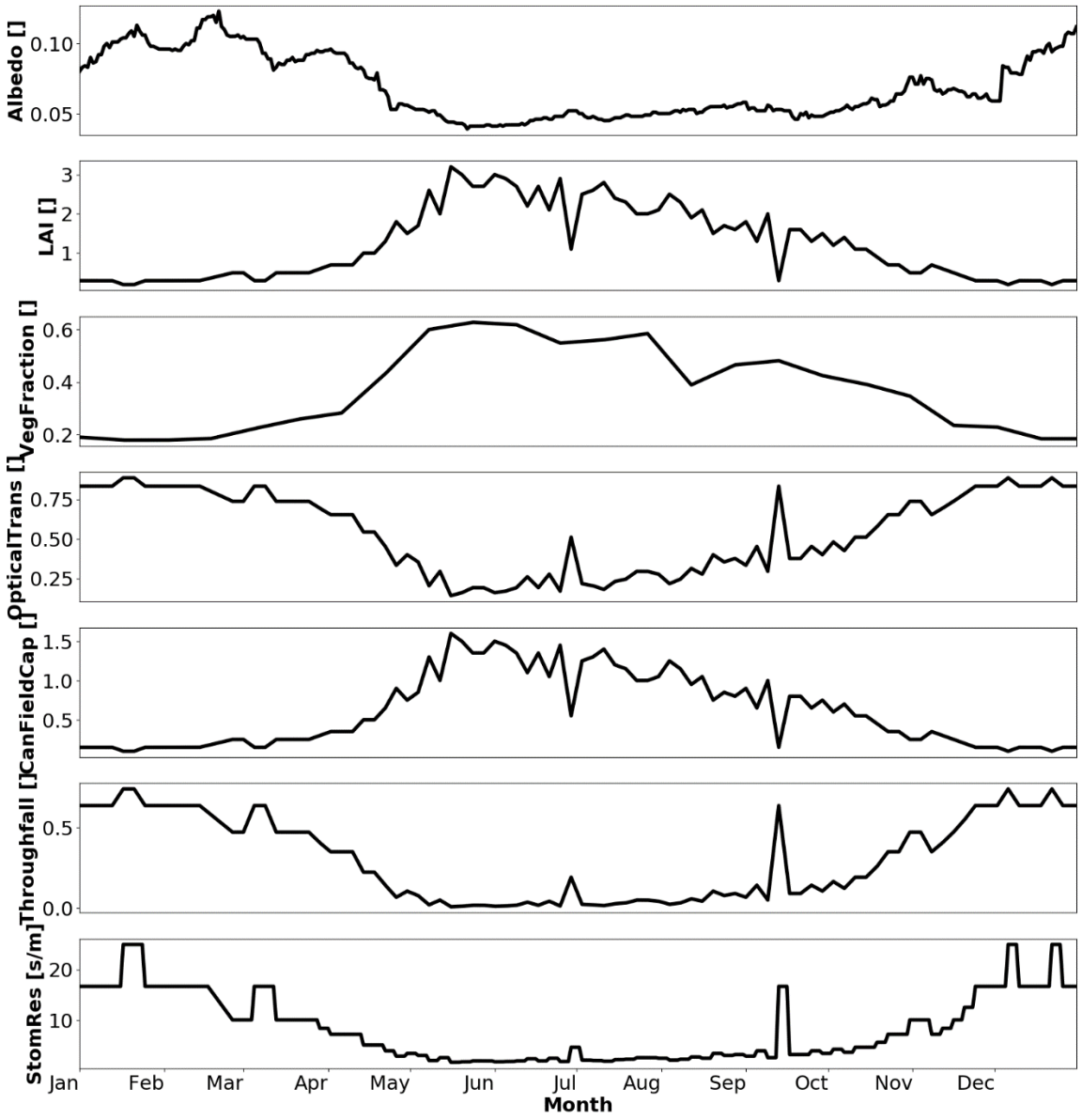

Figure 59: Dynamic vegetation parameters for US-SRC from 01/01/2016 to 12/31/2016. The six parameters are: Albedo (unitless), LAI (unitless), vegetation fraction (unitless), optical transmission (unitless), canopy field capacity (unitless), throughfall coefficient (unitless), and stomatal resistance ($s.m^{-1}$).

Results of the calibration process are shown in Figure 60. With the exception of ground heat flux (CC = 0, NS = -0.04) and rootzone moisture (CC = 0.46, NS = -0.15), the model captured the magnitude and temporal variability of all other variables reasonably, as shown with high CC near and above 0.8 and NS higher than 0.5 for most variables.

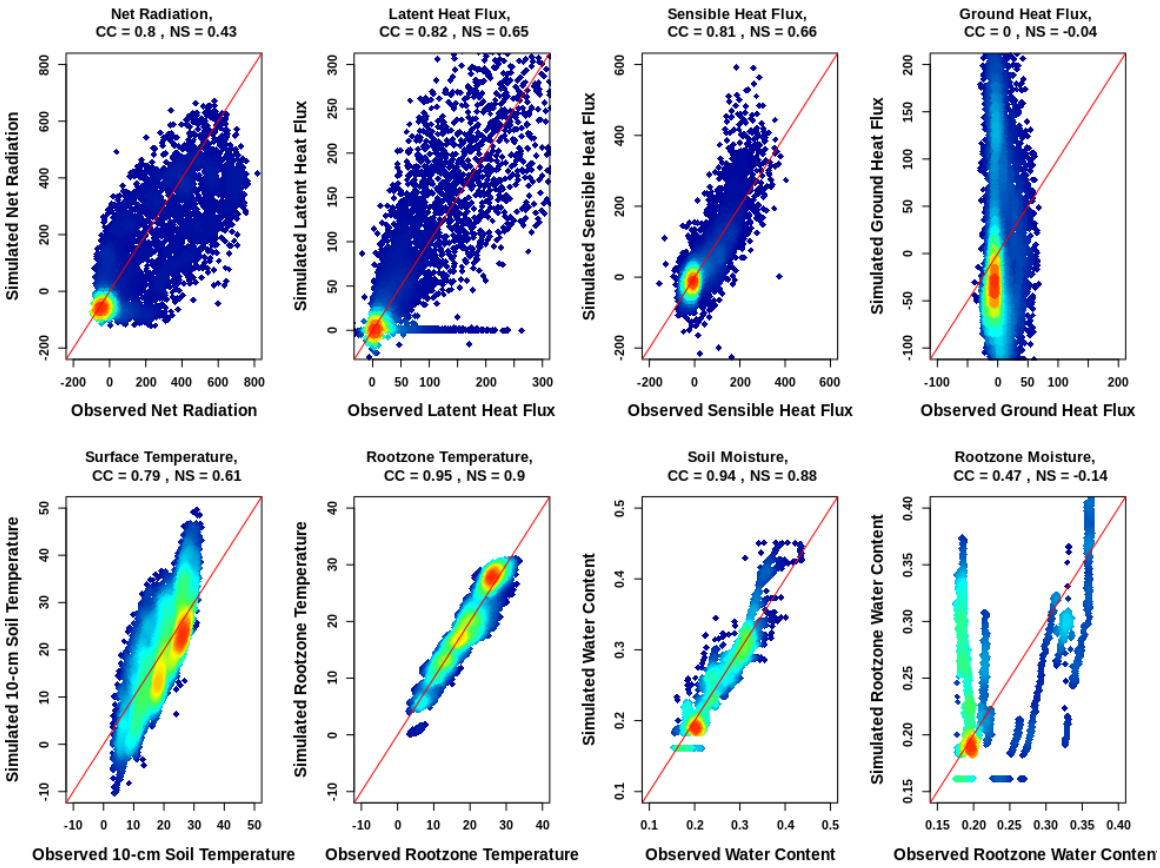

Figure 60: Density scatter plot of the simulated variables at MOISST for the complete 2016 year. In all panel the x-axis represents the observations and the y-axis represents the simulated values. The diagonal red line denotes the ideal match. Surface simulations of temperature and soil moisture are all for 10 cm depth, while observations of the same variables are at 5 cm and 10 cm depth. Root-zone simulations of soil temperature and moisture were all for 1 m, while observations where only available at 90 cm depth.

Table 13: Calibration metrics for MOISST for each of the simulated variables with respect to the observations. Metrics include CC, NS, bias, and RMSE.

Metrics	G ($W.m^{-2}$)	LE ($W.m^{-2}$)	H ($W.m^{-2}$)	NR ($W.m^{-2}$)	TS (°C)	Rootzone TS (°C)	Surface SWC	Rootzone SWC
CC	0.0	0.82	0.81	0.80	0.79	0.95	0.94	0.47
NS	-0.04	0.65	0.66	0.43	0.61	0.90	0.88	-0.14
Bias	2.72	5.38	1.57	48.20	-0.19	-0.09	0.00	-0.02
RMSE	93.96	47.00	55.09	145.17	6.24	2.22	0.02	0.07

Compared to previous simulations at Flagstaff and Santa Rita, simulated net radiation at MOISST is observed to be worse. The inability to simulate ground heat flux and the rootzone moisture at the site can be attributed to both the parameterization of subsurface soil characteristics and the type and accuracy of field instruments. The diurnal behaviors (Figure 61) of latent heat flux and sensible heat were well captured with the model being able to estimate the daily local minima and maxima. For net radiation, tRIBS was able to gauge the daily local minima but failed to reach the daily maxima. As expected from previous simulations at Flagstaff and Santa Rita, the model did not perform well in the winter months for soil moisture, as seen in Figure 62. However, the soil moisture behaviors were well captured from mid-April to December with simulated peaks and troughs near identical to the observations.

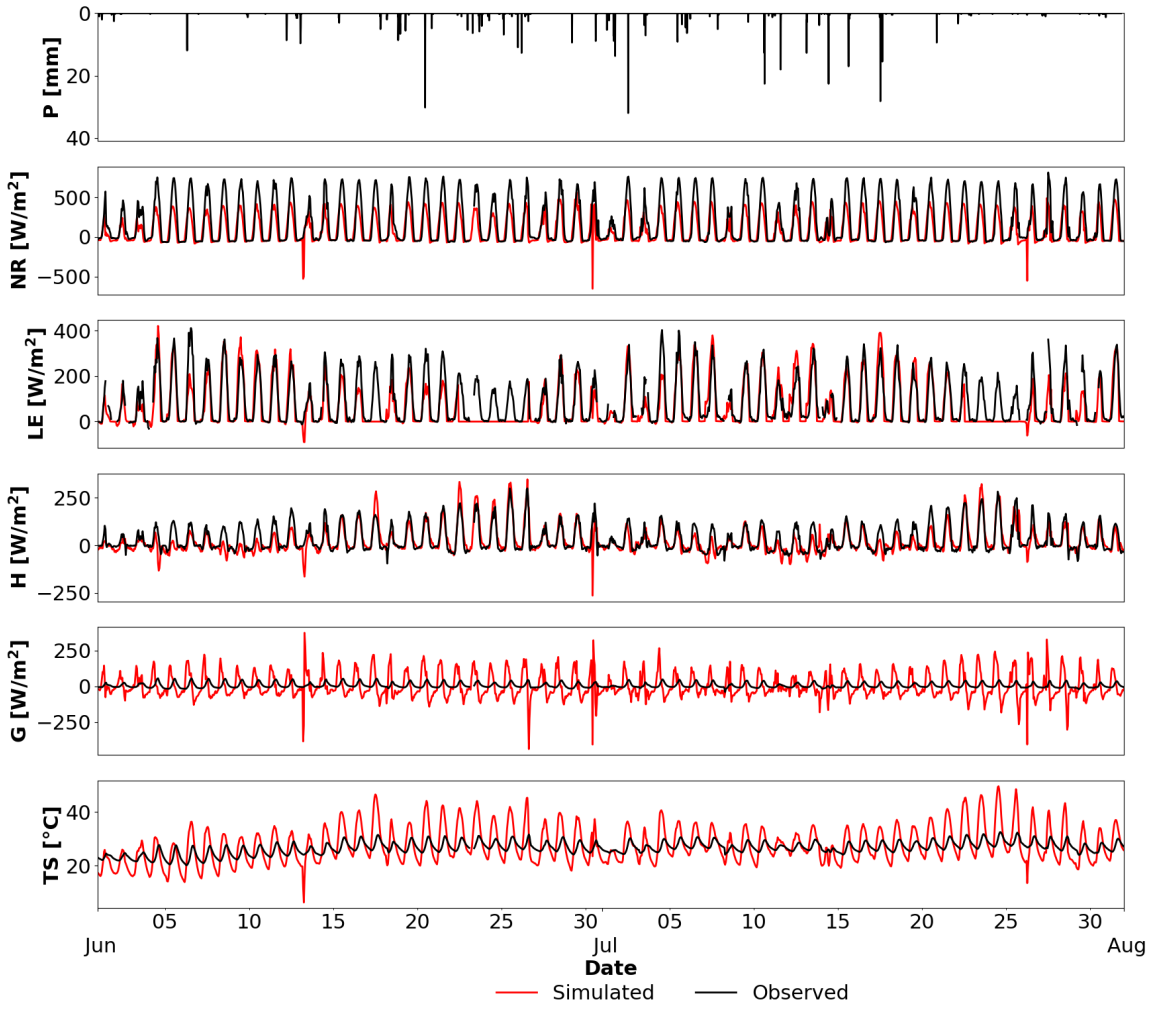

Figure 61: Time series of simulated variables (red) versus the observations (black) for the months of June and July in 2016 at MOISST.

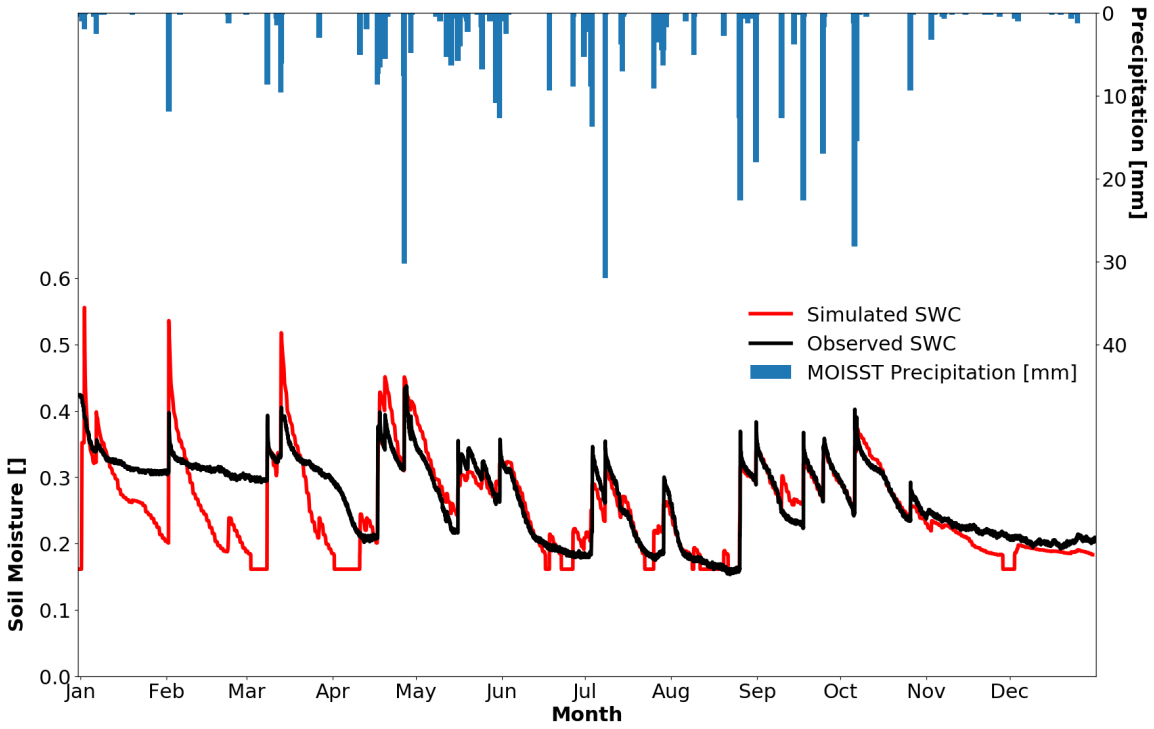

Figure 62: Time series of simulated soil moisture (red) and observations (black) for the calibration period (i.e. 2016) at MOISST.

5.3. Model Validation

To prevent repetition, Figures illustrating the forcing functions for each of the validation simulation are not shown here. The model validation used the corresponding weather forcing and dynamic vegetation variables and parameters for the test year in a similar way to the calibration simulations.

5.3.1. Forest Ecosystem

5.3.1.1. US-FUF

Validation of calibrated model parameters for US-FUF was conducted for year 2007 and the results compiled in Figures 63, 64 and 65 and Table 14. Verification metrics from the outputs demonstrated that the model was able to sustain satisfactory performance using a different set of forcing variables and dynamic vegetation parameters. Ground heat flux remained the worst of the six simulated variables with low CC and NSE. The

performance of the surface soil moisture simulations decreased from a NSE value of 0.24 to -0.32. This was possibly due to the presence of excess snow during the winter period. Furthermore, it can be seen the simulated 10-cm soil moisture was underestimated. Nonetheless, this value still shows the model's ability to capture the seasonal variability of soil moisture at this forested site during snow-free months. Net radiation and sensible heat flux remained the best simulated variables at US-FUF with high CC and NSE. In case of net radiation, the model also underestimated the variable at high magnitude of net radiation. Ground heat flux was not well simulated, as expected from the calibration. There was a wide range of values in the simulated latent heat flux where the model captured well the lower range of LE but as observed latent heat increased, the estimation became diverged from the actual 1:1 line. Overall, these LE estimations were still close to the actual observations as seen with NSE of 0.48.

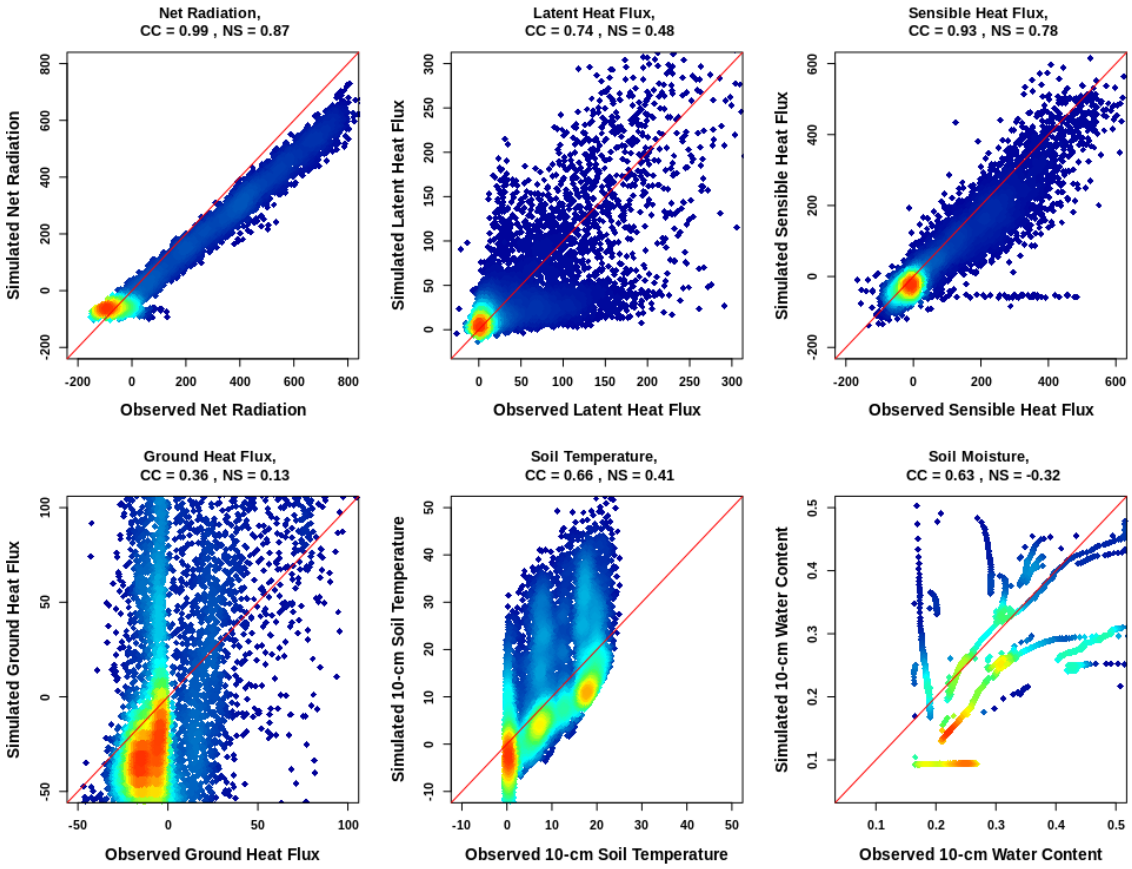

Figure 63: Density scatterplots of simulated versus observed values at US-FUF for the variables of interest during the validation period (year 2007). In all panels the x-axis represents the observations and the y-axis, the simulated values. The diagonal red line denotes the perfect match.

Table 14: Validation metrics for US-FUF for each of the simulated variables with respect to the observations. Metrics include correlation coefficient (CC), Nash Sutcliffe coefficient (NSE), bias, and root mean squared errors (RMSE).

Metrics	G ($W.m^{-2}$)	LE ($W.m^{-2}$)	H ($W.m^{-2}$)	NR ($W.m^{-2}$)	TS (°C)	Surface SWC
CC	0.36	0.74	0.93	0.99	0.66	0.79
NS	0.13	0.48	0.78	0.87	0.41	-0.32
Bias	-0.20	3.17	25.27	27.50	-1.52	-0.04
RMSE	62.23	43.83	58.52	73.71	8.92	0.08

Figure 62 illustrates the model capability to capture the diurnal variability of the simulated variables. The effects of missing forcing variables in mid-July can be observed where all simulated variables remained zero during the same period. Other than this, the

model proved to be stable and could continue the simulations while ensuring the quality as the forcing variables became available again.

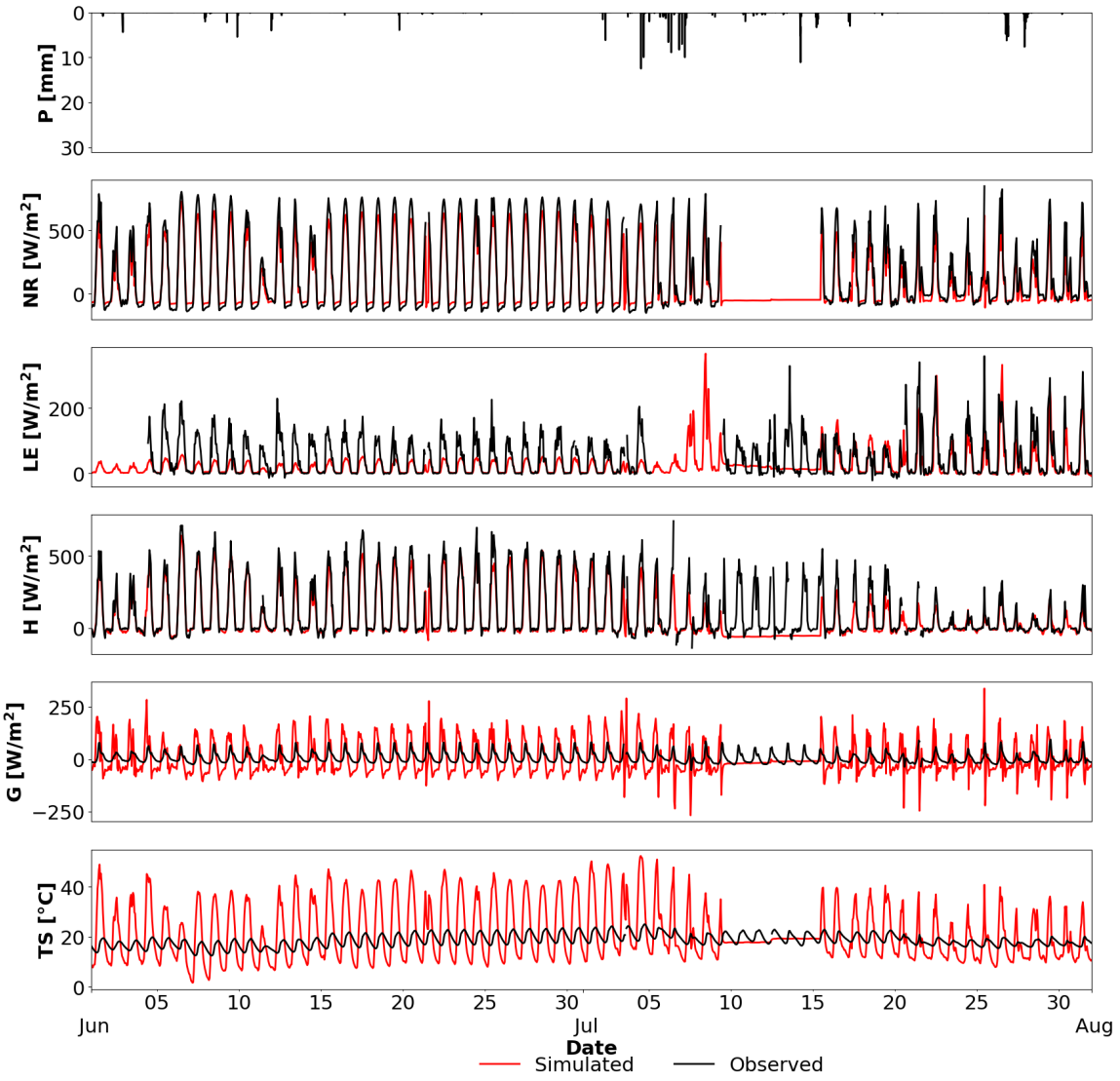

Figure 64: Validation time series of simulated variables (red) versus observations (black) for the months of June and July of 2007 for US-FUF.

A closer view to surface soil moisture validation (Figure 63), illustrates some underestimations during the winter and spring seasons possible due to the snow-related processes at this site, similar to those observed during the calibrations. However, the

model seemed to respond well to precipitation variability starting from July The behaviors of soil moisture was well simulated from July to September. From October to December, tRIBS was able to mimics the trend of soil moisture but it tended to underestimate the actual amount of moisture at the site. This observation was also made with the first six months from January to June where the model both failed to capture the peaks and troughs of the soil moisture as well as its temporal fluctuations.

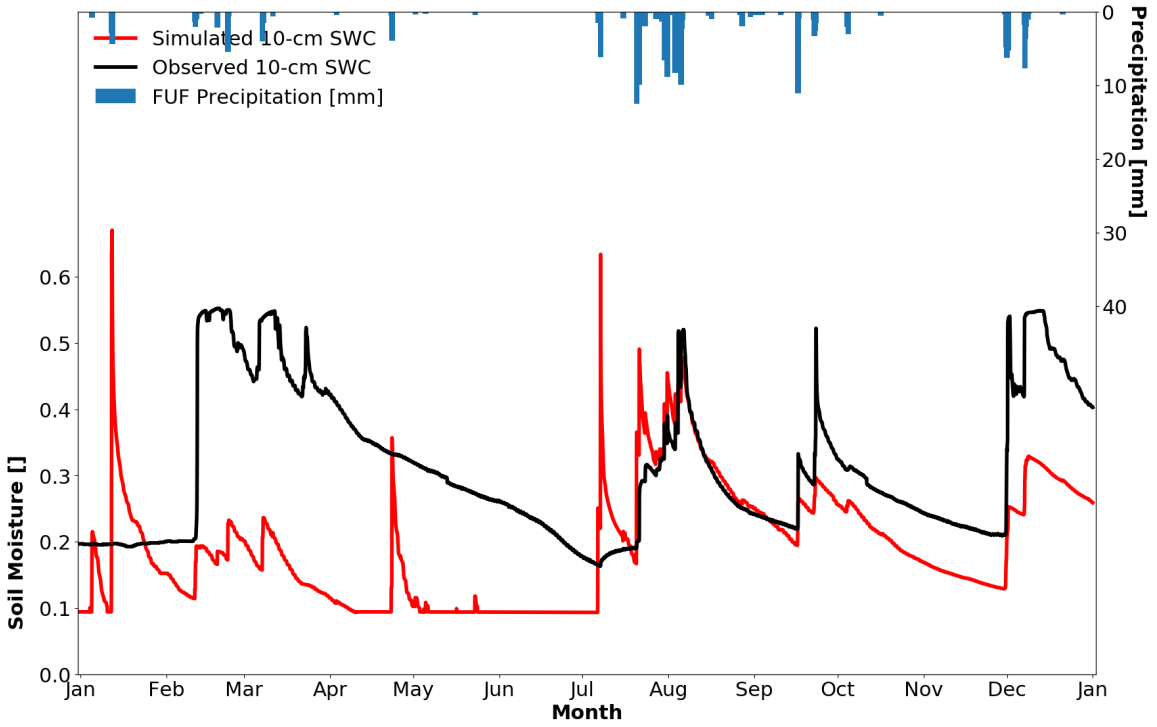

Figure 65: Validation time series of simulated soil moisture (red) and observations (black) for the calibration period (year 2007) at US-FUF.

5.3.1.2. US-FWF

The validation results for US-FWF shown by Figures 66, 67 and 68 and Table 15 reach similar scores to the calibration that indicate the appropriateness of the calibrated parameter values.. The presence of snow in the area might have been the main reason for this as the model performance during summer months was exceptional with both peaks and

troughs in magnitude of soil moisture correctly captured. Net radiation was well captured and the model sufficiently estimated the higher range of net radiation without under- or overestimate the variable. On the other hand, the sensible heat flux was seen to be overestimated at the upper range. Simulated latent heat flux still exhibited the diverging behaviors observed during the calibration where the lower values were captured while the mid-range LE was underestimated and upper range LE was overestimated. Both the soil temperature and soil moisture metrics were worse, however, the model was still able to capture the diurnal variations of these two variables.

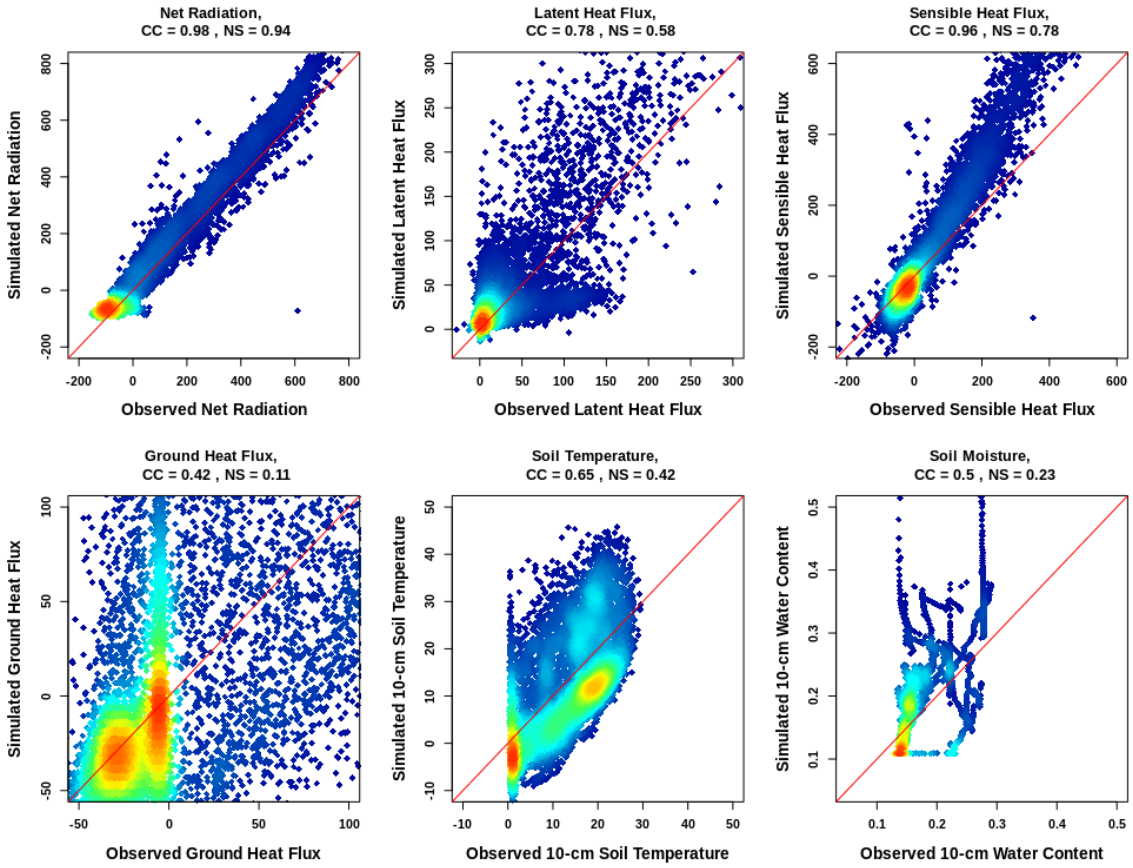

Figure 66: Validation density scatter plot of the simulated versus observed values at US-FWF. In all panels the x-axis represents the observations and the y-axis represents the simulated values. The diagonal red line denotes a perfect match.

Table 15: Validation metrics for US-FWF for each of the simulated variables with respect to the observations. Metrics include correlation coefficient (CC), Nash Sutcliffe coefficient (NSE), bias, and root mean squared error (RMSE).

Metrics	G ($W.m^{-2}$)	LE ($W.m^{-2}$)	H ($W.m^{-2}$)	NR ($W.m^{-2}$)	TS (°C)	Surface SWC
CC	0.42	0.78	0.96	0.98	0.65	0.50
NS	0.11	0.58	0.78	0.94	0.42	0.23
Bias	1.42	-10.18	-29.78	-31.06	0.60	-0.01
RMSE	56.06	45.08	87.17	56.72	8.81	0.06

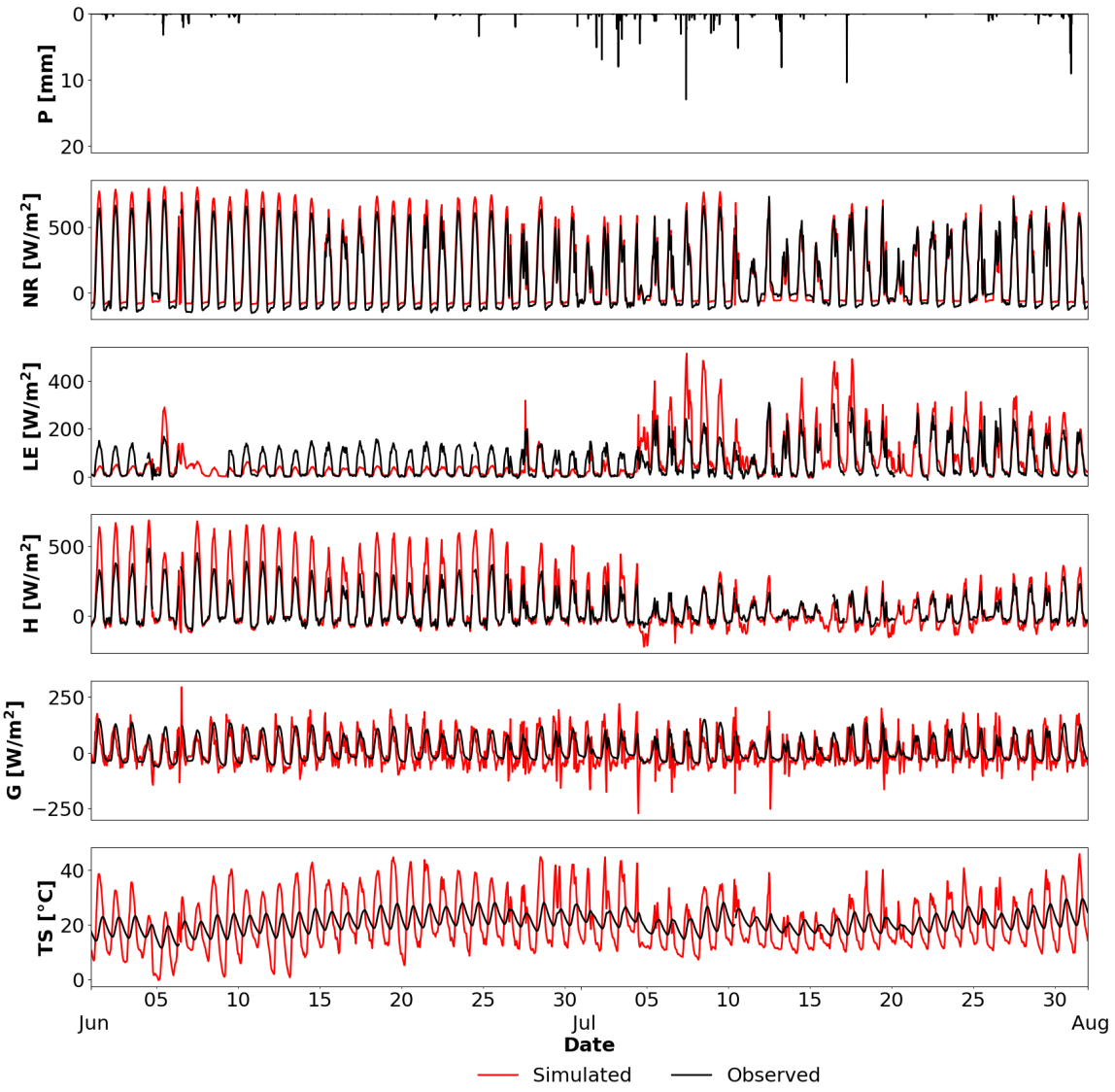

Figure 67: Validation time series of simulated variables (red) versus the observations (black) for the months of June and July at US-FWF.

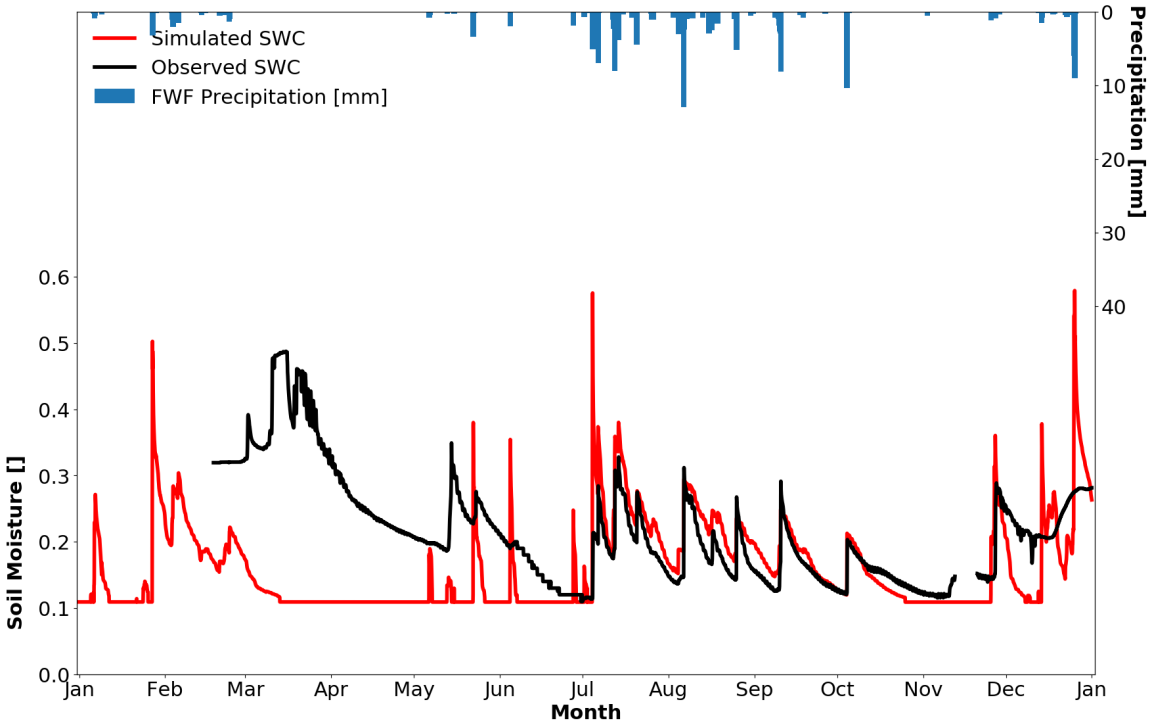

Figure 68: Validation time series of simulated surface soil moisture (red) and observations (black) at US-FWF.

5.3.1.2. US-FMF

The validation results for US-FMF shown by Figures 69, 70 and 71 and Table 16 reach satisfactory scores except by ground heat flux. Net radiation was systematically underestimated by tRIBS, particularly for large values. Soil moisture was not well simulated and the model severely underestimated the actual soil moisture at US-FMF with negative NSE. 10-cm soil temperature was both underestimated and overestimated at the same time. However, for most of the simulation period, the estimation of soil temperature was concentrated around the 1:1 line which showed despite there were some divergence from the actual observation, the model generally was able to simulate the soil temperature (NSE = 0.46).

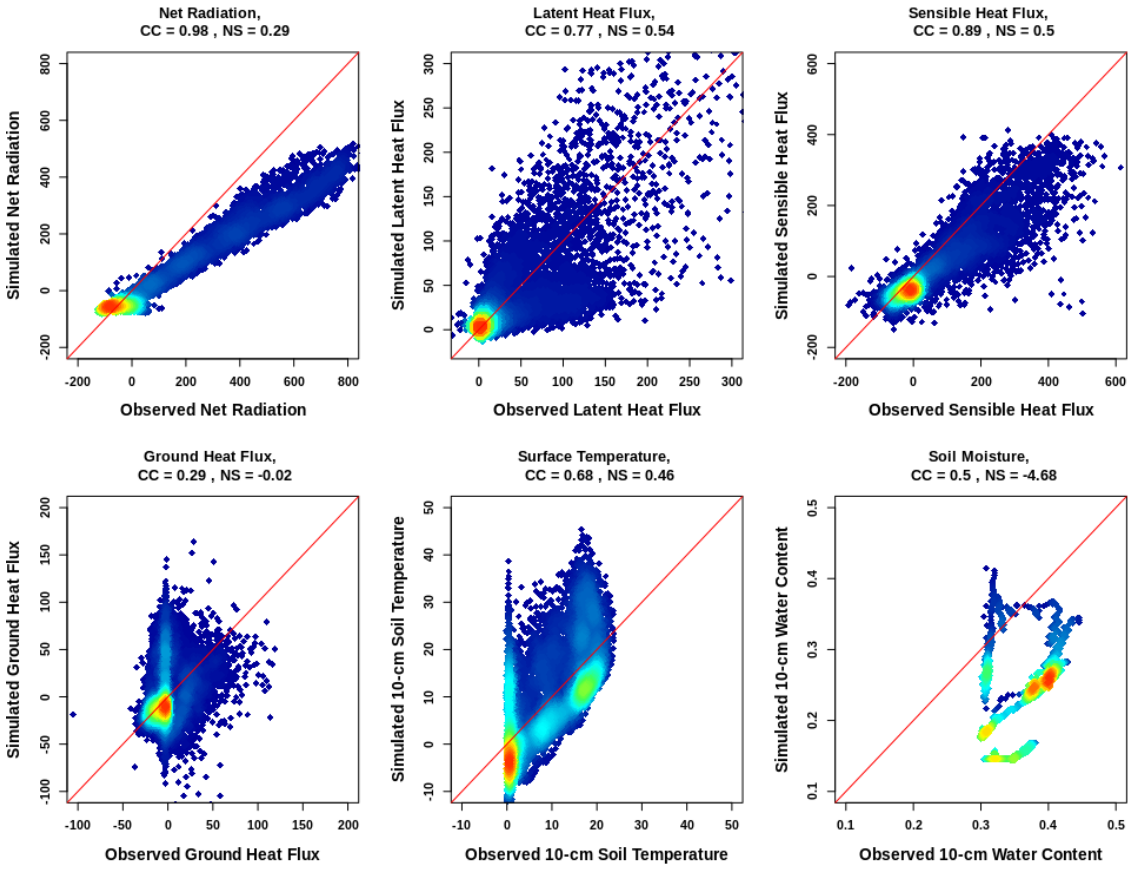

Figure 69: Validation density scatter plots of the simulated versus observed values at US-FMF in year 2010. In all panel the x-axis represents the observations and the y-axis represents the simulated values. The diagonal red line denotes the perfect match.

Table 16: Validation metrics for US-FMF for each of the simulated variables with respect to the observations. Metrics include correlation coefficient (CC), Nash Sutcliffe coefficient (NSE), bias, and root mean squared error (RMSE).

Metrics	G ($W.m^{-2}$)	LE ($W.m^{-2}$)	H ($W.m^{-2}$)	NR ($W.m^{-2}$)	TS (°C)	Surface SWC
CC	0.29	0.77	0.89	0.98	0.68	0.50
NS	-0.02	0.54	0.5	0.29	0.46	-4.68
Bias	-0.06	2.91	40.20	65.67	-0.24	0.01
RMSE	30.55	40.92	70.75	129.85	8.19	0.14

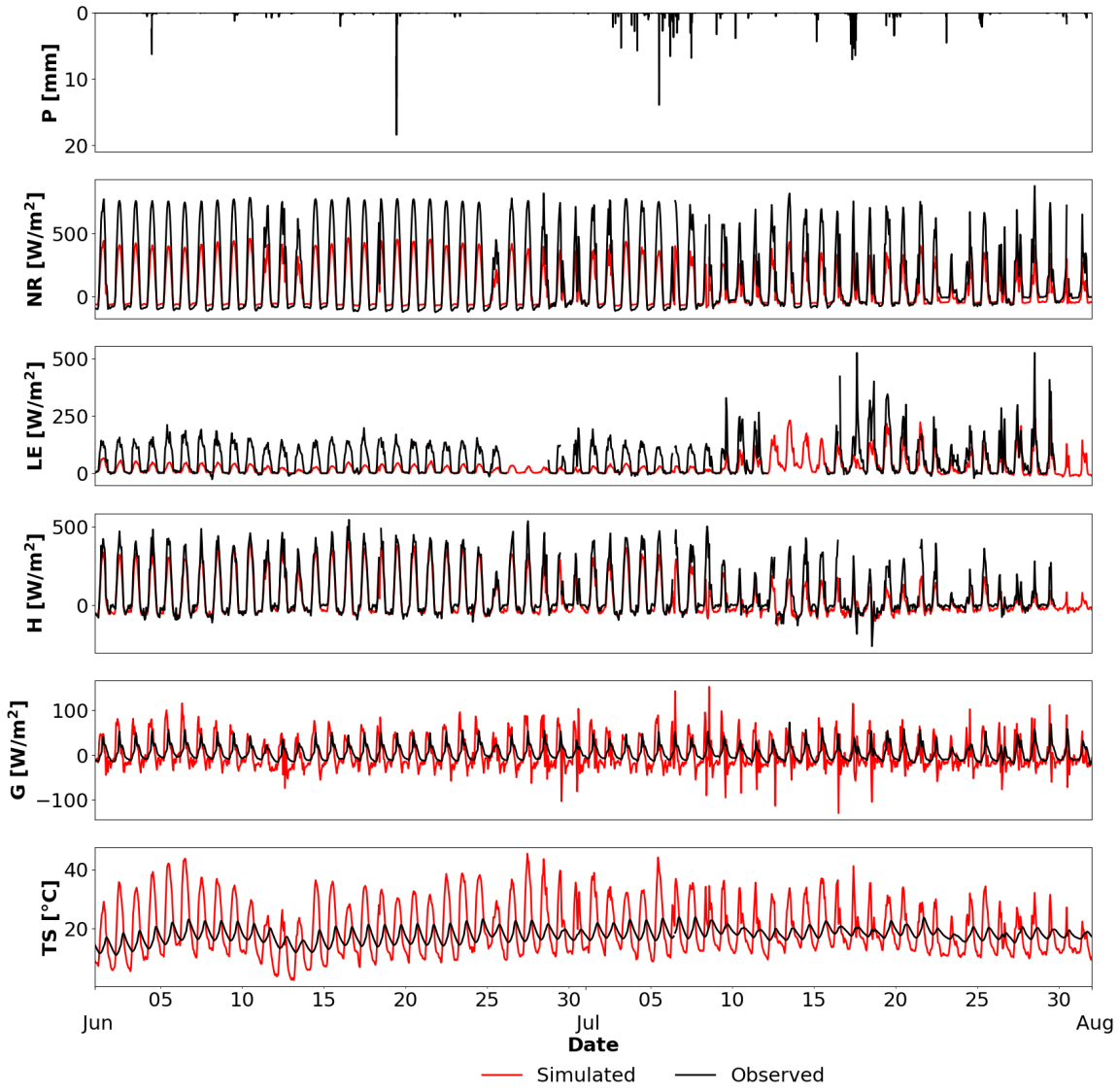

Figure 70: Validation time series of simulated variables (red) versus the observations (black) for the months of June and July at US-FMF.

The time series of 10-cm soil moisture at US-FMF is illustrated in Figure 70 shows that tRIBS overestimated the soil moisture year-round at US-FMF. Unlike the simulation at US-FUF and US-FWF where summer moisture was well captured, the simulated summer months' moisture at US-FMF was not good even though the simulated moisture trend mimicked those of observations.

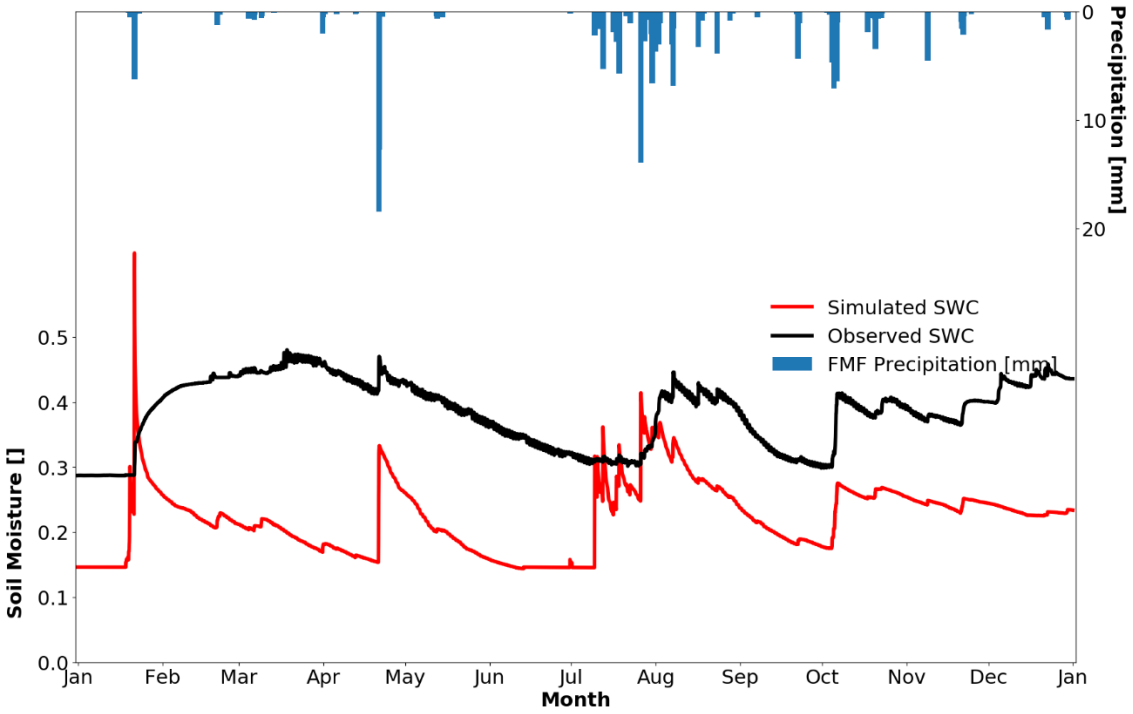

Figure 71: Validation time series of simulated soil moisture (red) and observations (blue) at US-FMF.

5.3.2. Desert Ecosystem

5.3.2.1. US-SRC

The results of the model validation at US-SRC are presented in Figures 72, 73 and 74 and Table 17. It can be seen that during the validation period, the model produces similar results for all variables using the calibrated parameters. With the exception of ground heat flux, the model performed well and was able to capture the temporal variability of the simulated variables with high CC (CC>0.80) and NSE (NSE>0.5). Without the presence of snow for most of the simulation period, the model was able to capture the behaviors of soil moisture with most of the peaks and troughs.

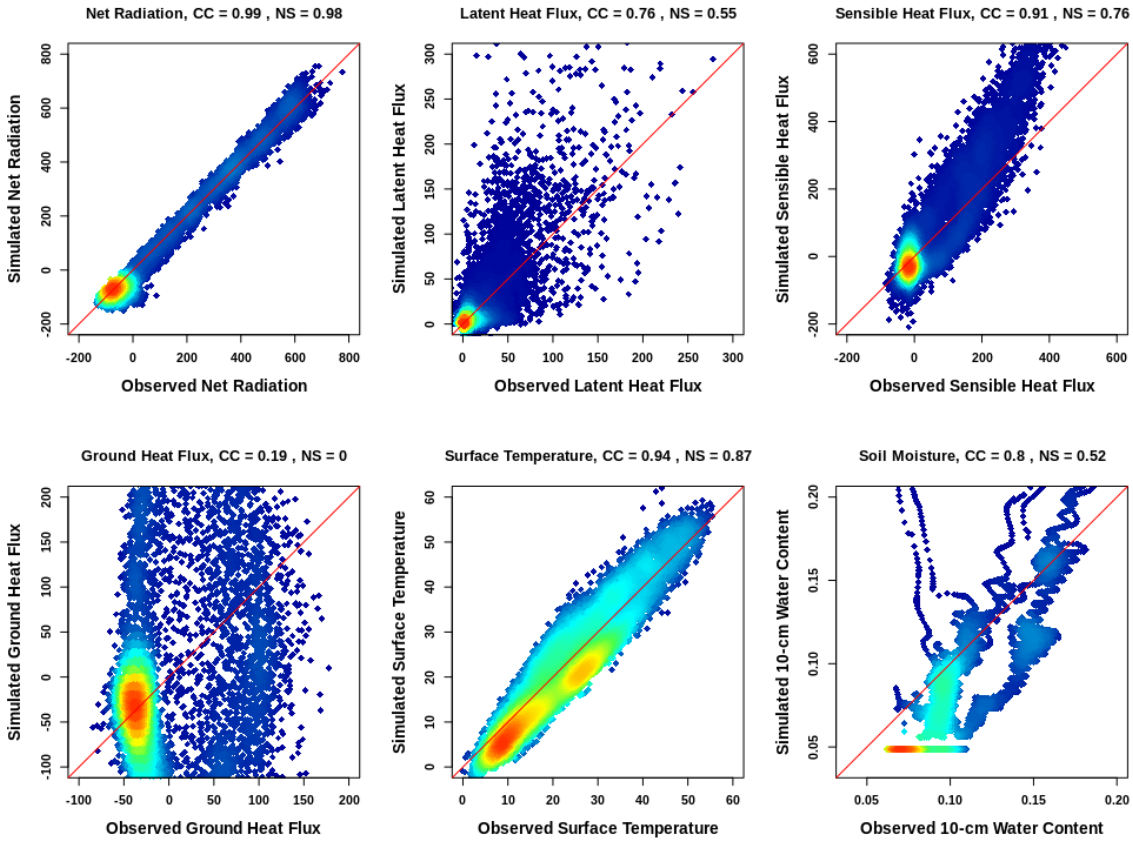

Figure 72: Validation density scatter plots of the simulated variables at US-SRC. In all panels the x-axis represents the observations and the y-axis represents the simulated values. The diagonal red line denotes a perfect match.

Table 17: Validation metrics for US-FMF for each of the simulated variables with respect to the observations. Metrics include correlation coefficient (CC), Nash Sutcliffe coefficient (NSE), bias, and root mean squared error (RMSE).

Metrics	G ($W.m^{-2}$)	LE ($W.m^{-2}$)	H ($W.m^{-2}$)	NR ($W.m^{-2}$)	TS (°C)	Surface SWC
CC	0.19	0.76	0.91	0.94	0.99	0.80
NSE	0.0	0.55	0.76	0.87	0.98	0.52
Bias	1.92	-3.90	-19.27	0.17	1.23	0.02
RMSE	133.65	31.99	81.43	30.46	4.94	0.04

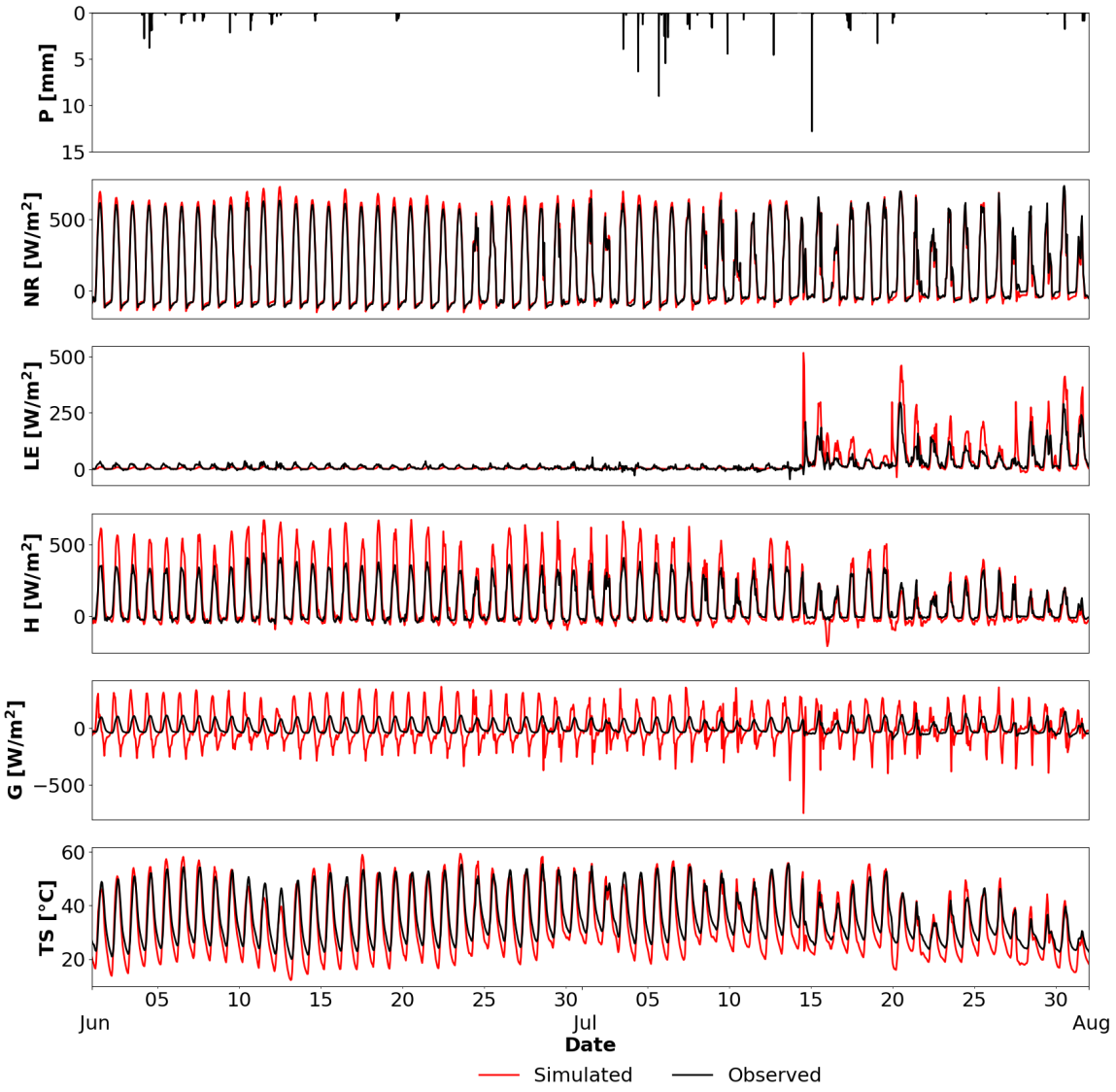

Figure 73: Validation time series of simulated variables (red) versus the observations (black) for the months of June and July for US-SRC.

The time series of simulated soil moisture illustrated in Figure 74 shows that even though tRIBS could not capture the peaks and troughs of the observed soil moisture at the site, it was able to mimic the moisture trend reasonably. July to October was characterized by well simulated moisture with peak soil moisture captured. However, due to inadequate parameterization of the tRIBS's parameters, water was seen to drain at higher rate than the observations.

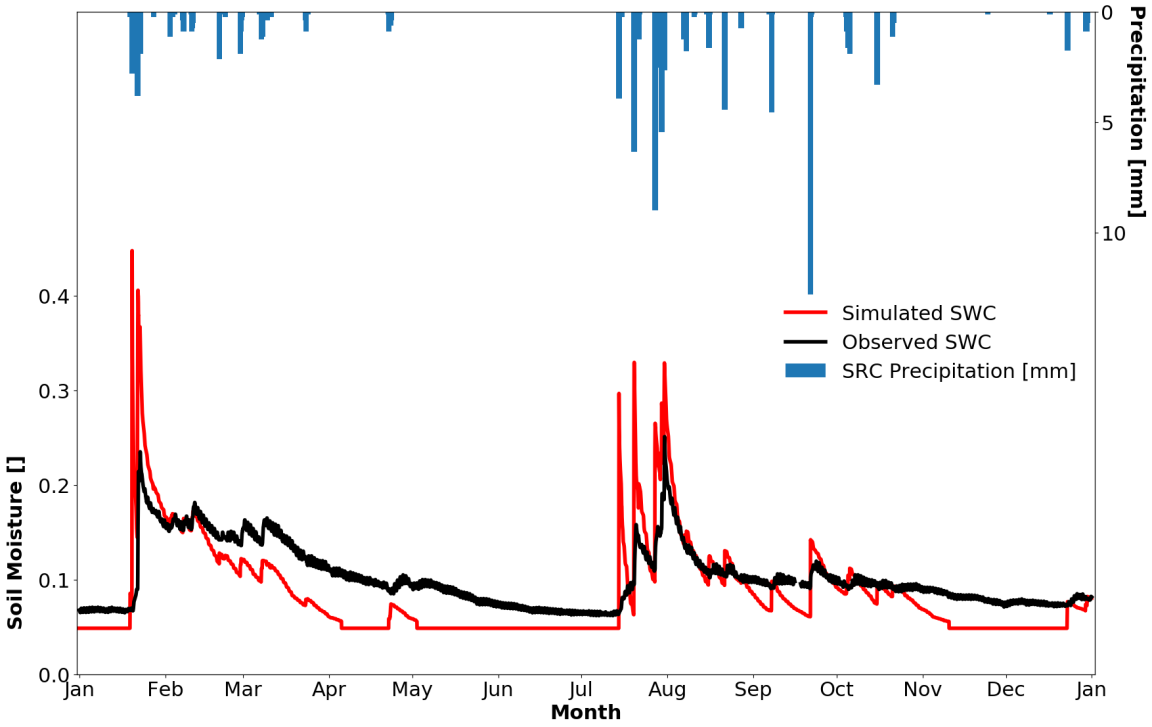

Figure 74: Validation time series of simulated soil moisture (red) and observations (black) at US-SRC.

5.3.2.2. US-SRG

The results of the model validation at US-SRG are presented in Figures 75, 76 and 77 and Table 18. All of the simulated variables show high CC (CC>0.75) and NSE (NSE>0.49). These results show the capability of tRIBS to adequately capture the seasonal behaviors of the variables of interests as well as their daily diurnal fluctuations in the absence of snow. Time series plots for the surface soil moisture revealed some discrepancies that will have to be investigated in depth in future studies.

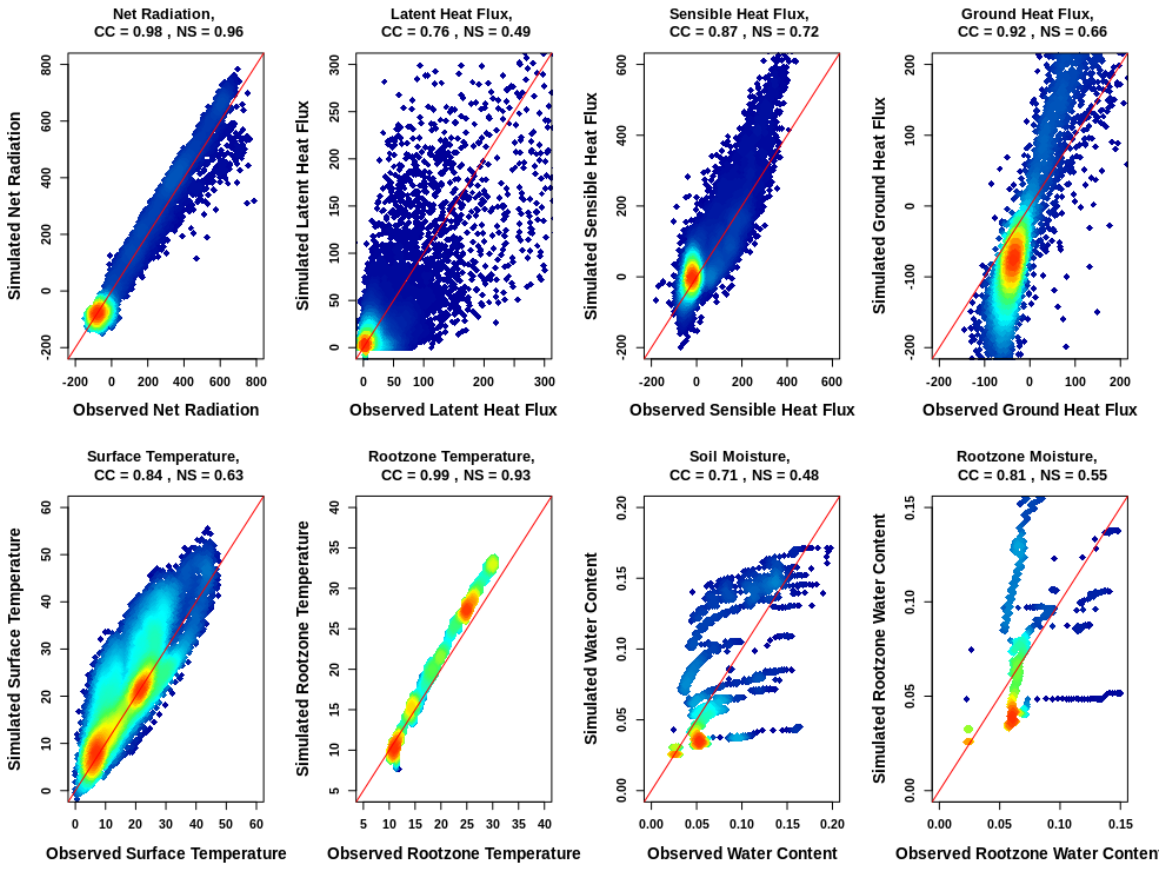

Figure 75: Validation density scatter plots of simulated versus observed values at US-SRG. In all panels the x-axis represents the observations and the y-axis represents the simulated values. The diagonal red line denotes a perfect match.

Table 18: Validation metrics for US-SRG for each of the simulated variables with respect to the observations. Metrics include correlation coefficient (CC), Nash Sutcliffe coefficient (NSE), bias, and root mean squared error (RMSE).

Metrics	G ($W.m^{-2}$)	LE ($W.m^{-2}$)	H ($W.m^{-2}$)	NR ($W.m^{-2}$)	TS (°C)	Rootzone TS (°C)	Surface SWC	Rootzone SWC
CC	0.92	0.76	0.87	0.98	0.84	0.99	0.71	0.81
NS	0.66	0.49	0.72	0.96	0.63	0.93	0.48	0.55
Bias	8.31	3.93	-22.08	-1.68	-3.13	-1.40	0.00	-0.01
RMSE	86.13	39.29	67.87	50.06	6.91	2.03	0.03	0.04

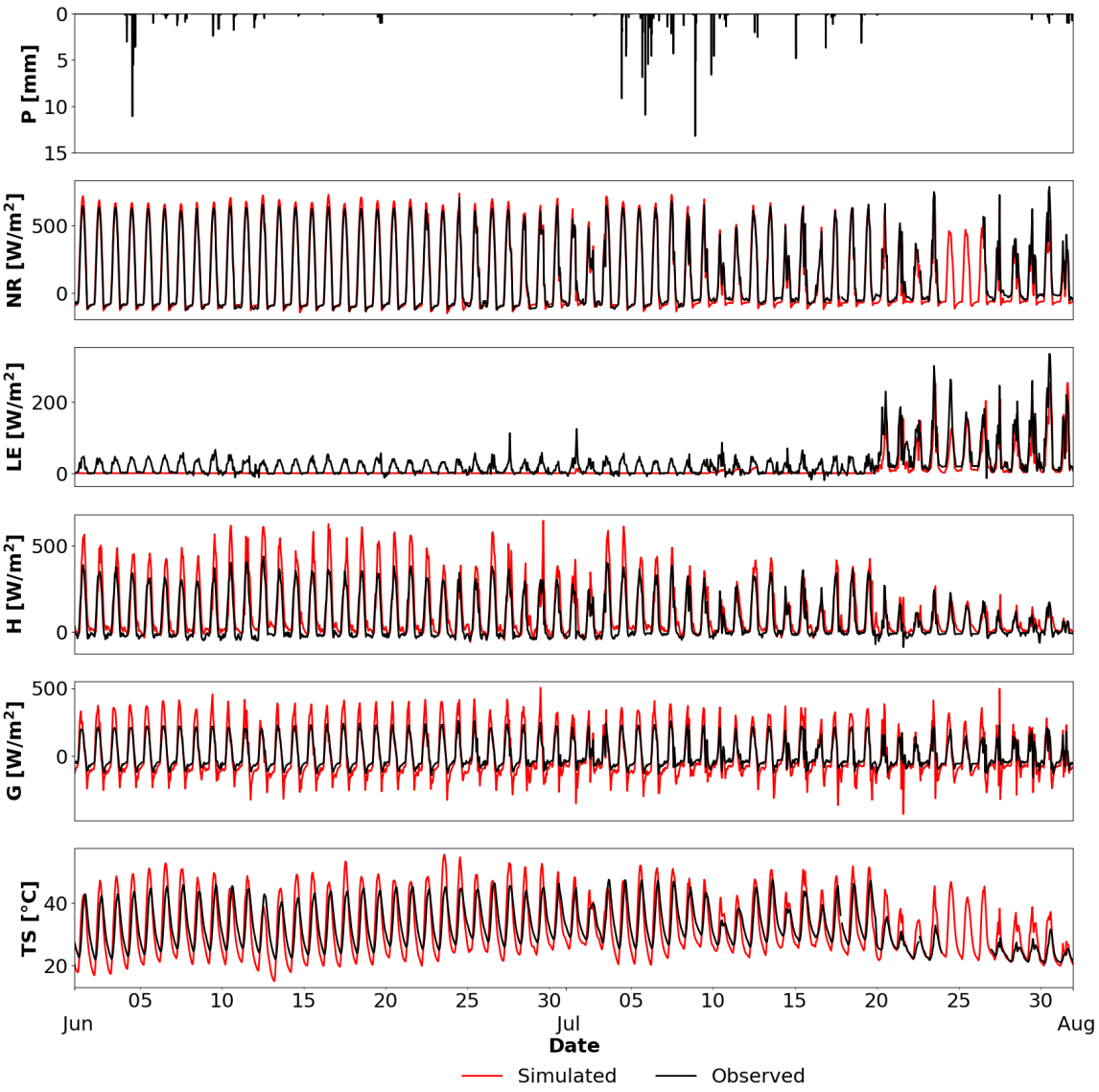

Figure 76: Validation time series of simulated variables (red) versus the observations (black) for the months of June and July for US-SRG.

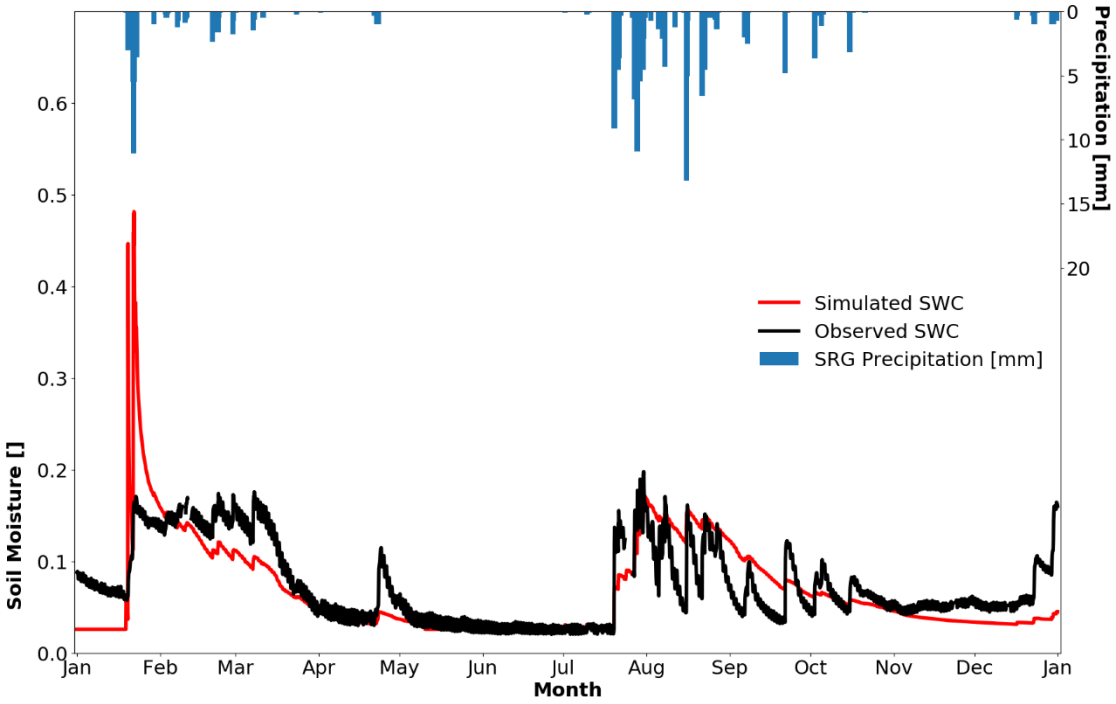

Figure 77: Time series of simulated soil moisture (red) and observations (black) for the validation period at US-SRG.

5.3.2.3. US-SRM

The results of the model validation at US-SRM are presented in Figures 78, 79 and 80 and Table 19. Compared to the calibration, ground heat flux, latent heat flux, sensible heat flux, net radiation, and surface temperature remained well simulated with high CC (CC>0.64) and NSE (NSE>0.32) values. Soil moisture time series (Figure 66) show that the validation runs could capture the trends of soil moisture but not its local maxima and minima.

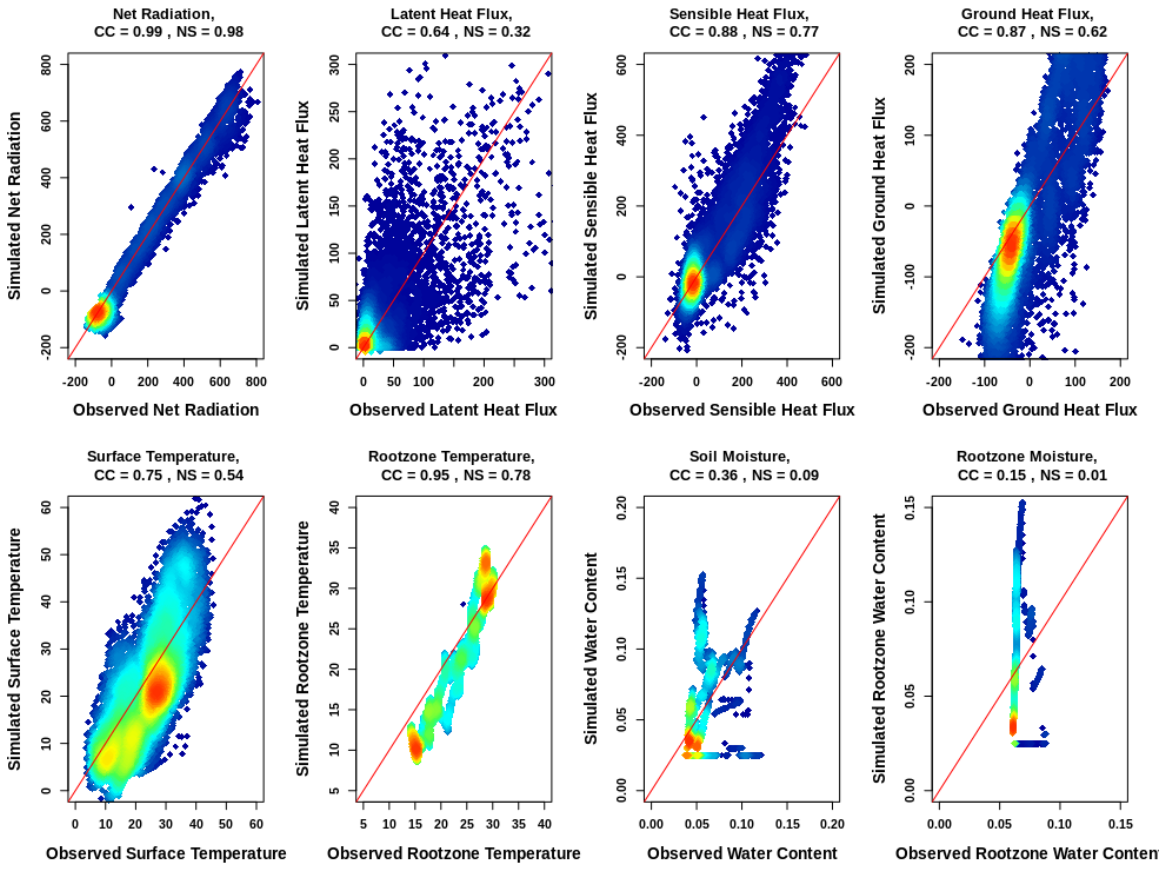

Figure 78: Density scatter plot of the simulated variables at US-SRM. In all panel the x-axis represents the observations and the y-axis represents the simulated values. The diagonal red line denotes 1:1 line.

Table 19: Validation metrics for US-SRM for each of the simulated variables with respect to the observations. Metrics include correlation coefficient (CC), Nash Sutcliffe coefficient (NSE), bias, and root mean squared error (RMSE).

Metrics	G ($W.m^{-2}$)	LE ($W.m^{-2}$)	H ($W.m^{-2}$)	NR ($W.m^{-2}$)	TS (°C)	Rootzone TS (°C)	Surface SWC	Rootzone SWC
CC	0.87	0.64	0.88	0.99	0.75	0.95	0.36	0.15
NS	0.62	0.32	0.77	0.98	0.54	0.78	0.09	0.01
Bias	1.07	-1.83	-10.00	4.61	1.97	1.71	0.00	0.00
RMSE	88.67	39.61	73.36	34.94	8.43	3.73	0.03	0.03

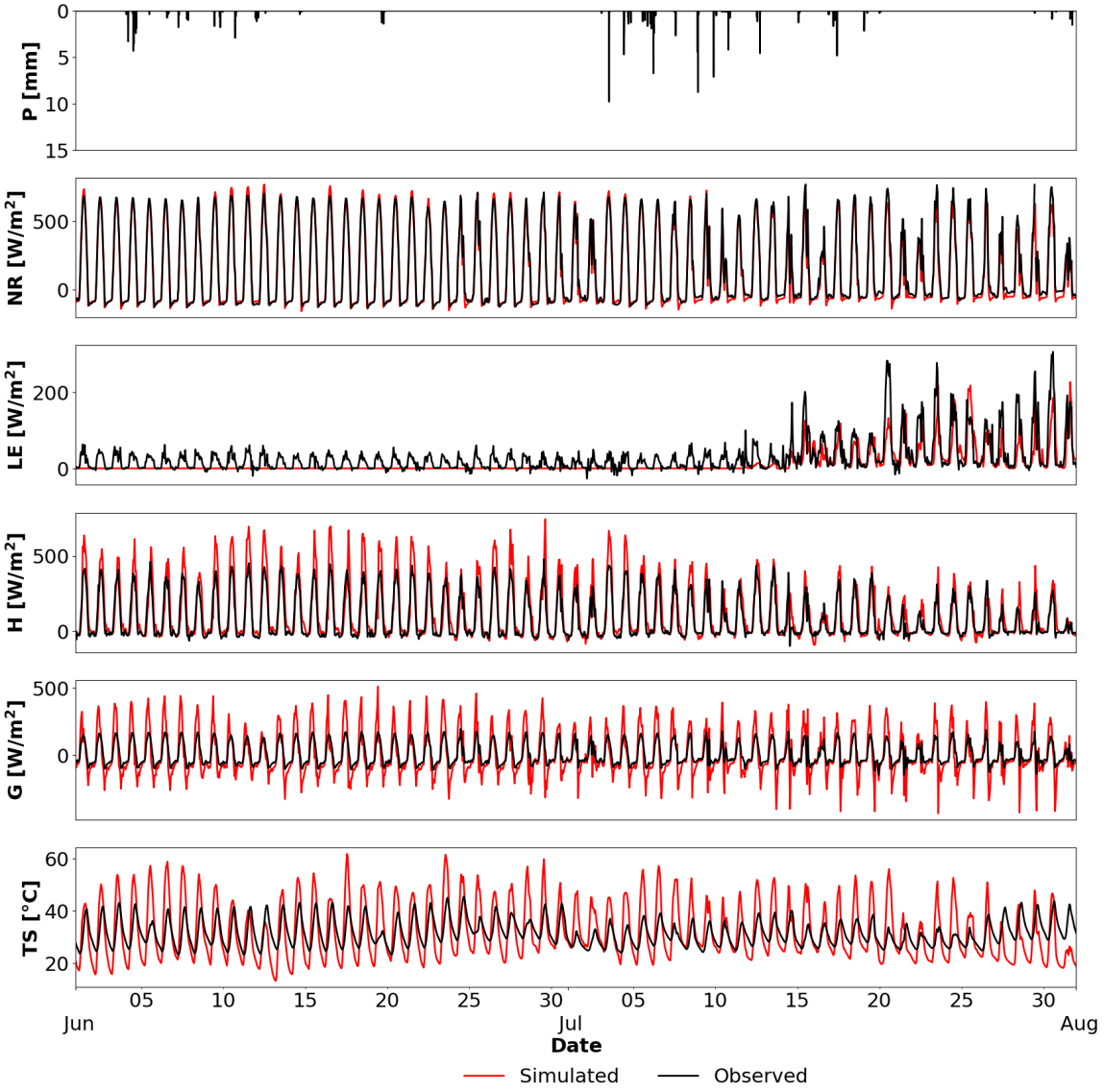

Figure 79: Validation time series of simulated variables (red) versus the observations (black) for the months of June and July for US-SRM.

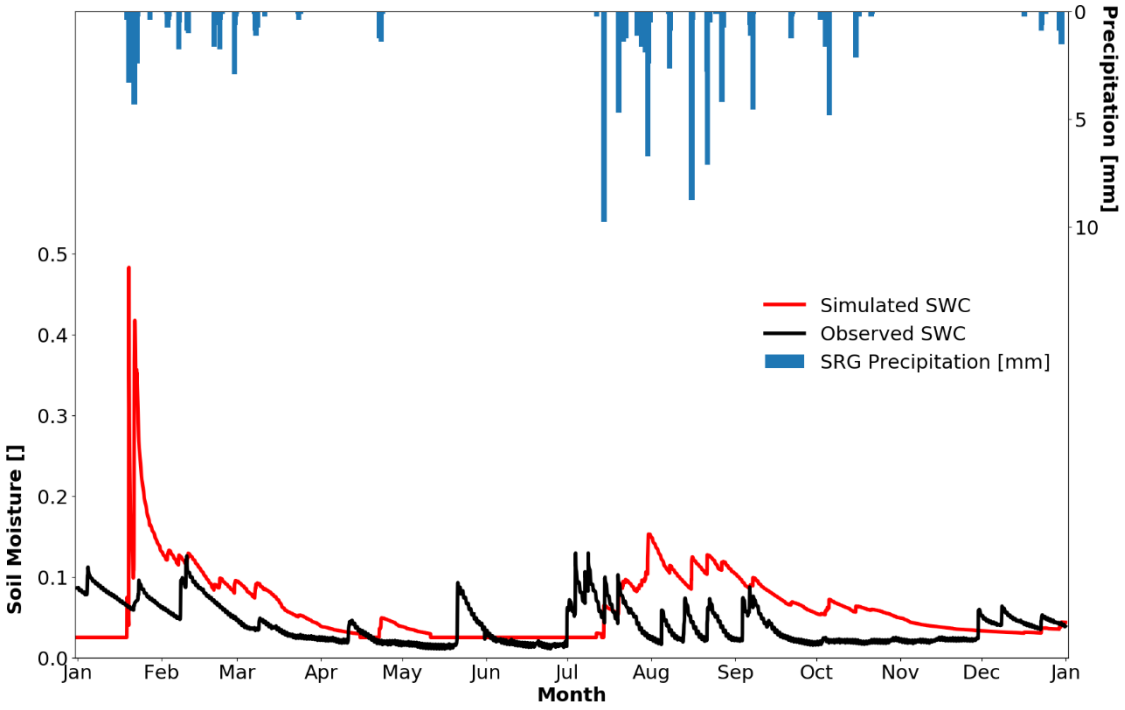

Figure 80: Validation time series of simulated soil moisture (red) and observations (black) at US-SRM.

5.3.3. Grassland Ecosystem

The results of the model validation at US-SRM are presented in Figures 81, 82 and 83 and Table 20. Simulated latent heat flux, sensible heat flux, net radiation, and temperatures at two depths are similar to those from the calibration results with high NSE (NSE>0.48), showing that the calibrated parameters are adequate. However, the 10-cm soil moisture results were slightly worse than during the calibration stage with CC=0.70 and NSE= 0.37 while rootzone moisture greatly improved with CC= 0.80 and NSE=0.59. Ground heat flux remained as the worst simulated variable with the model unable to capture its temporal behavior. In addition, while tRIBS was able to capture the annual trend of surface soil moisture, it failed to capture the peaks and troughs during precipitation events. Overall for this variable (precipitation) the NSE suggests the model still performs better than the historic mean.

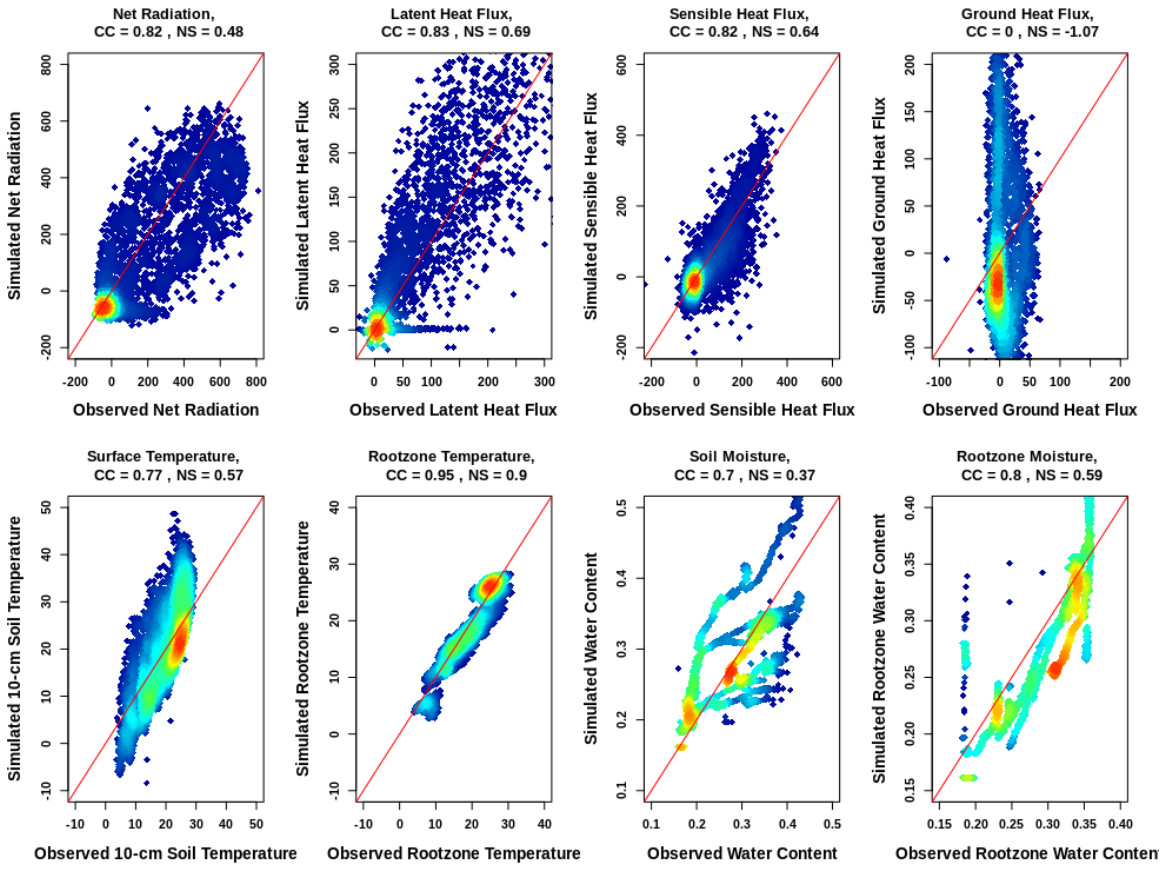

Figure 81: Validation density scatter plots of the simulated versus observed values at MOISST. In all panels the x-axis represents the observations and the y-axis represents the simulated values. The diagonal red line denotes the perfect match.

Table 20: Validation metrics for MOISST for each of the simulated variables with respect to the observations. Metrics include correlation coefficient (CC), Nash Sutcliffe model efficiency coefficient (NSE), bias, and root mean squared error (RMSE).

Metrics	G ($W.m^{-2}$)	LE ($W.m^{-2}$)	H ($W.m^{-2}$)	NR ($W.m^{-2}$)	TS (°C)	Rootzone TS (°C)	Surface SWC	Rootzone SWC
CC	0.0	0.83	0.82	0.82	0.77	0.95	0.70	0.80
NSE	-1.07	0.69	0.64	0.48	0.57	0.90	0.37	0.59
Bias	-12.11	-5.54	10.58	48.69	-0.58	0.46	-0.01	0.02
RMSE	121.67	50.79	53.57	144.55	6.26	2.17	0.05	0.04

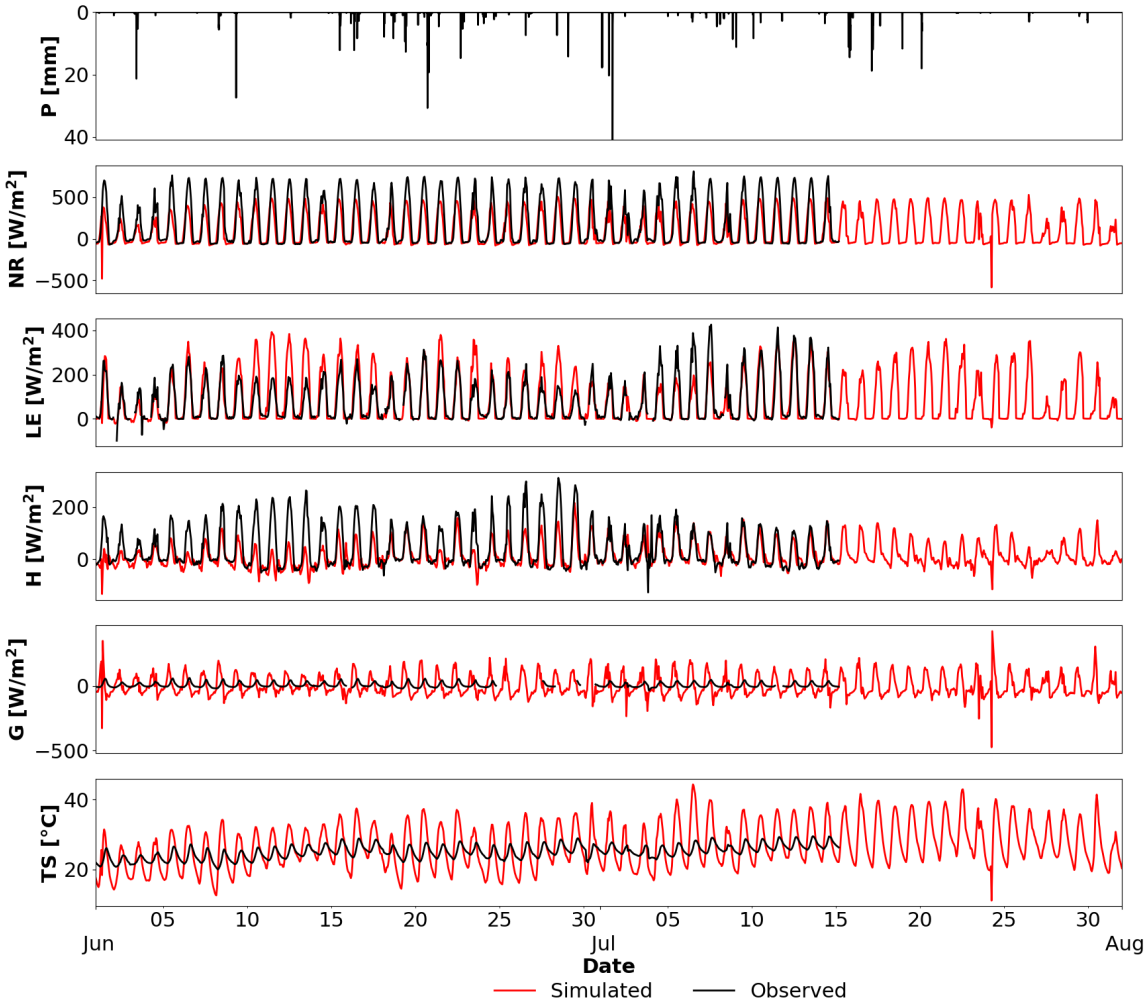

Figure 82: Validation time series of simulated variables (red) versus the observations (black) for the months of June and July for MOISST.

From Figure 82, it is seen that the diurnal variations in net radiation, latent heat flux, and sensible heat flux was well simulated. With some of the missing measurements at MOISST during the same period, these results could potentially be used to fill the gap of the missing data. From Figure 83, compared to both Flagstaff and Santa Rita simulation, tRIBS simulated well the soil moisture from September to December with most of the peaks and troughs as well as the trend captured. From January to July, the simulated moisture followed the trend of the observed soil moisture but the magnitude of the simulated moisture was not well captured.

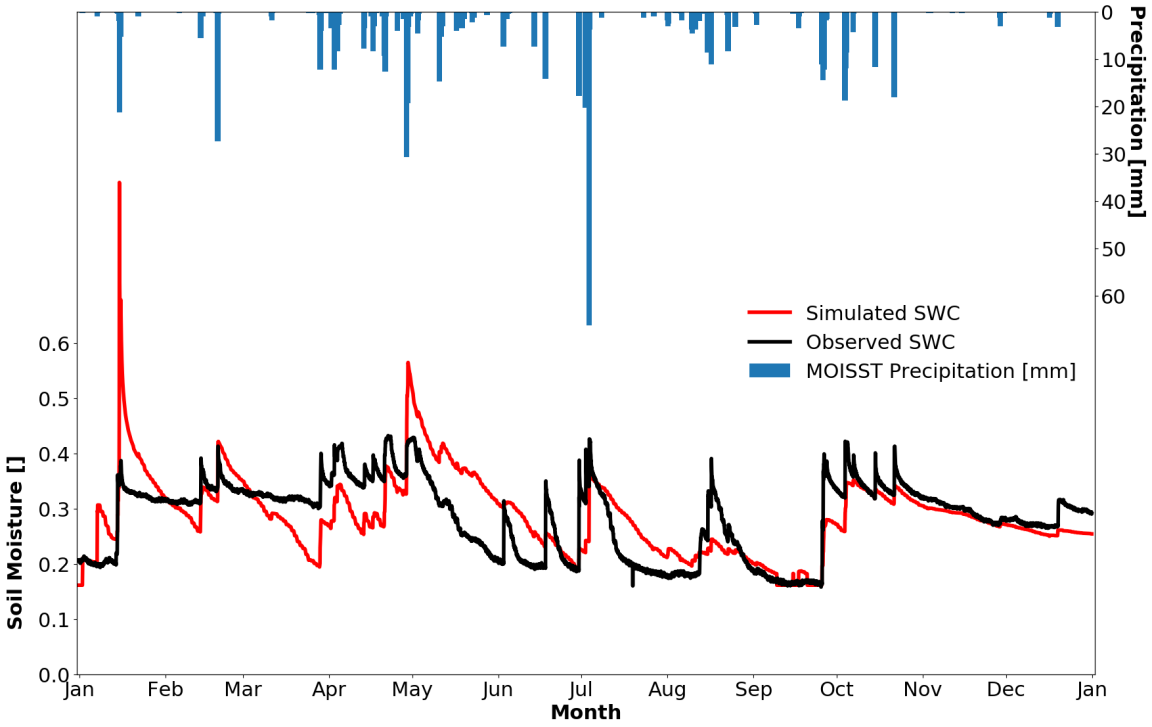

Figure 83: Time series of simulated soil moisture (red) and observations (black) for the validation period at MOISST.

5.4. Quantifying the Effects of Precipitation Inputs and Vegetation Change on the Partitioning of Evapotranspiration

5.4.1. Desert Ecosystem

From Figures 84 through 86 and Table 21 it can be seen that both tRIBS and the data-intensive models predict similar amounts of ET, evaporation (E) and transpiration (T) across the year with the highest values during the Monsoon season for the three stations with high CC and NS. In general, tRIBS seems to provide lower values of ET during the first half of the year (January through June) but higher T values during the second semester with the exception of October to November where the estimation was near-zero for both models.

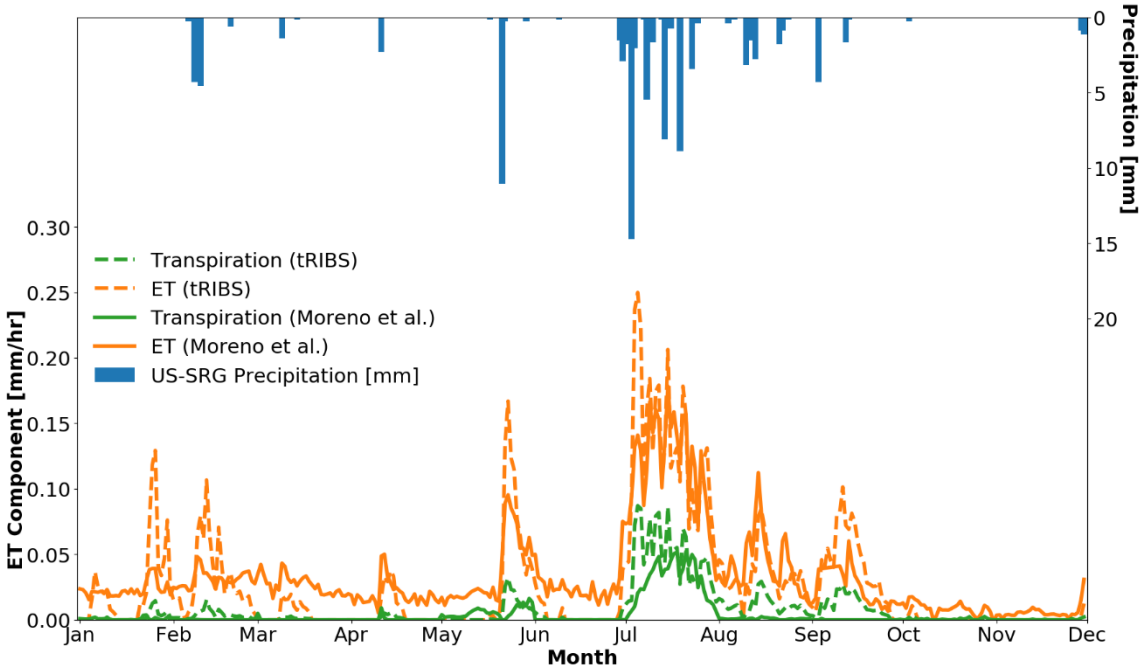

Figure 84: Daily time series comparison of total ET and T at US-SRG from 01/01/2009 to 11/30/2009 (the tRIBS calibration year) between the tRIBS outputs and Moreno et al. (2020) model.

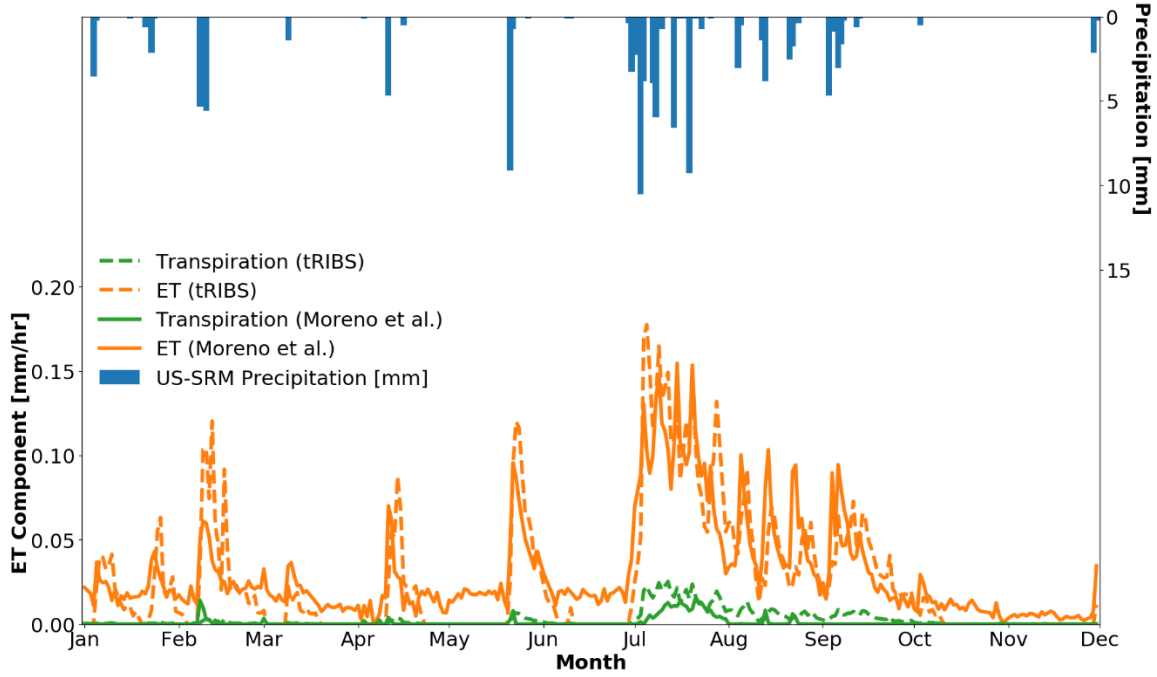

Figure 85: Daily time series comparison of total ET and T at US-SRM from 01/01/2009 to 11/30/2009 (the tRIBS calibration year) between tRIBS and Moreno et al. (2020) model.

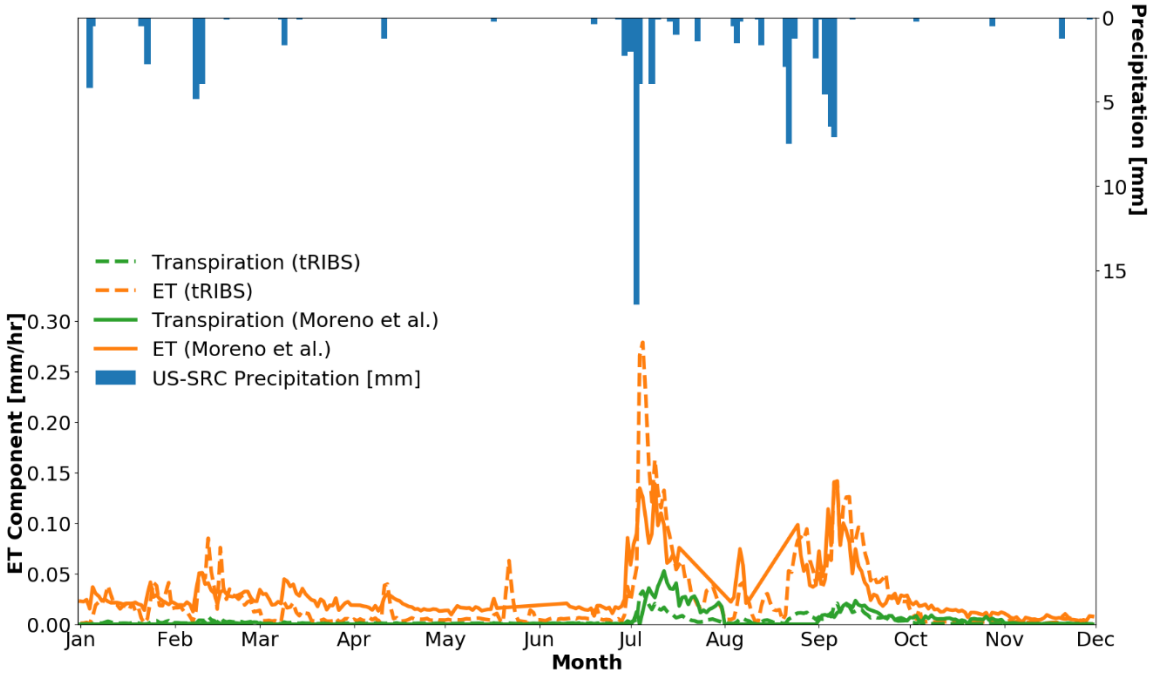

Figure 85: Daily time series comparison of total ET and T at US-SRC from 01/01/2009 to 11/30/2009 (the tRIBS calibration year) between tRIBS and Moreno et al. (2020) model.

Table 21: Evaluation metrics between tRIBS and the data-intensive model outputs regarding ET and its partitioning components for three stations at Santa Rita, AZ

Metrics	US-SRG	US-SRM	US-SRC
CC -Transpiration	0.80	0.69	0.62
CC - ET	0.88	0.85	0.82
NSE - Transpiration	0.54	0.33	-1.01
NSE - ET	0.73	0.71	0.62

The partitioning of ET into evaporation from soil and wet canopy (E_{soil} and E_{wet} due to intercepted precipitation) and transpiration (T) is illustrated in Figures 87 through 95 for the three desert ECTs. For all three stations (US-SRC, US-SRG, US-SRM), the dominant component contributing to the total ET was E_{soil}, followed by T, and E_{wet}. The following paragraphs summarize the model outputs by station.

5.4.1.1. US-SRC

The partitioning of ET at US-SRC is shown in Figures 87 and 88 in absolute and relative terms. Such Figures 87 and 88 illustrate that ET, Esoil, and T rates experienced a sudden increase in July as the monsoon season brought high amounts of precipitation at the station. The antecedent wet condition from high rainfall in July, combined with continuous precipitation, high air temperature, and incoming shortwave radiation values in July made the total evapotranspiration the highest in August at a rate of 70 mm/month. The lowest rate of ET is observed in June as a result of a long period without precipitation at the rate of less than 5 mm/month.

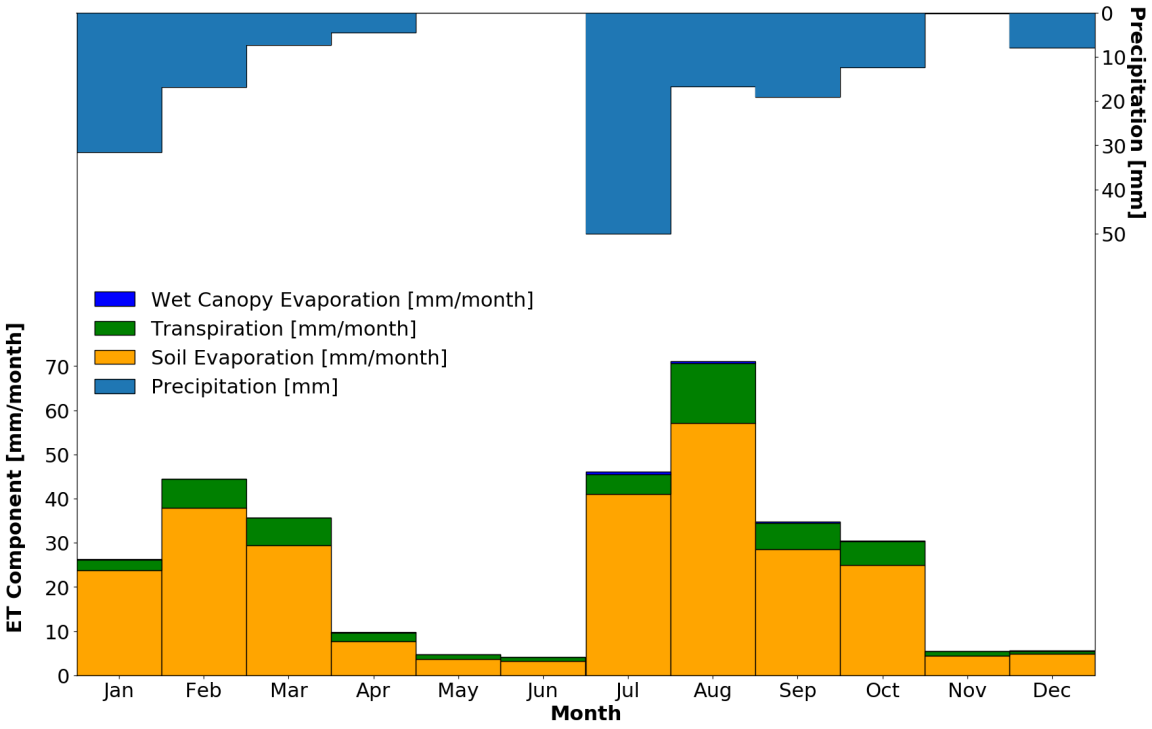

Figure 86: Partitioning of ET into soil evaporation (Esoil), wet canopy evaporation (Ewet), and transpiration (T) at US-SRC in 2010. Hourly partitioning values were aggregated to monthly values with corresponding precipitation accumulation.

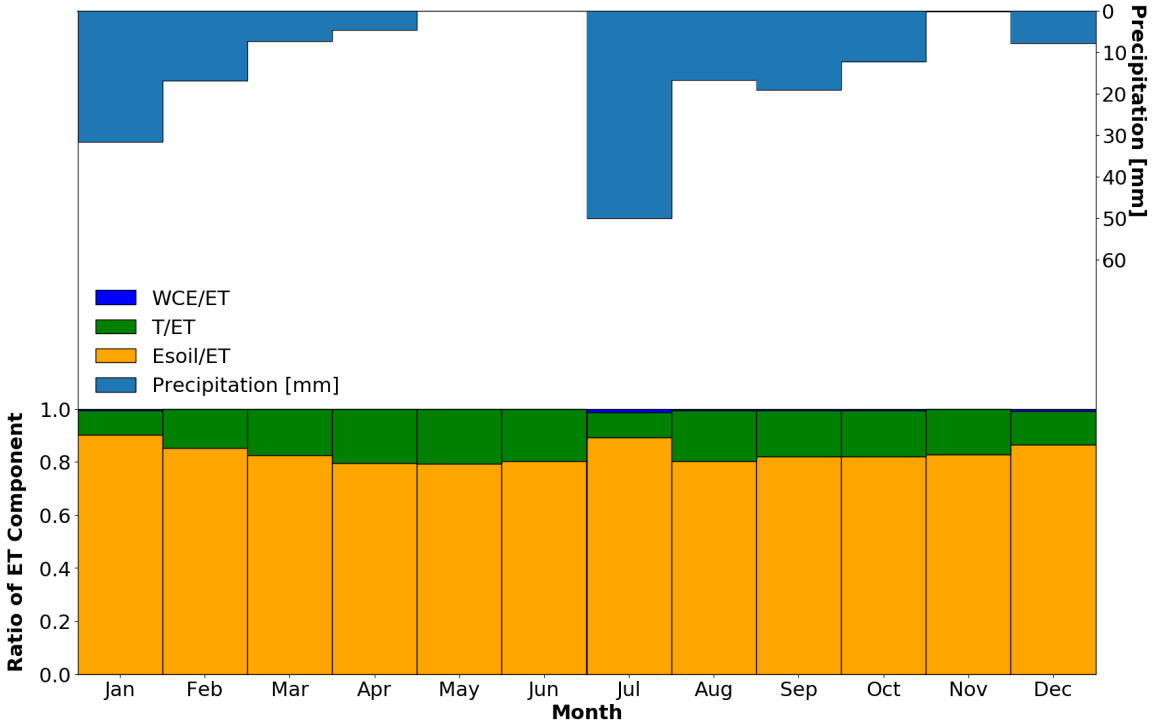

Figure 87: Relative Partitioning of ET into soil evaporation (Esoil), wet canopy evaporation (Ewet), and transpiration (T) at US-SRC in 2010. Hourly partitioning values were aggregated to monthly values with corresponding precipitation accumulation.

Annually, as seen in Figure 88, evaporation from soil accounted for 80 to 90% of the total evapotranspiration at the US-SRC site while transpiration accounted for the 10 to 20% of ET. The distribution between soil evaporation and transpiration made up the bulk of ET. On the other hand, evaporation from wet canopy was insignificant at the site at about 0.5 to 0.7% and concentrated mostly from July to October. In order to study the time lags between precipitation and ET processes, the hourly time series of the components of ET have been plotted from June to August for the same 2010 year in Figure 89. Precipitation can be seen to influence the response and partitioning of ET. The lack of precipitation from June 1st to July 13th translated to near zero ET. As soon as precipitation started, ET increased with soil evaporation as the dominant component. It is also noted that transpiration, in absolute terms, was not as prominent at the beginning of the monsoon

season and it only reached the highest rates in August. This was due to the lower LAI values in July that represented lower phenological activity of creosote which was mentioned in the analysis in section 5.1.2. Furthermore, as evapotranspiration directly relates to the latent heat flux, ET also exhibited diurnal behavior and obviously, daily soil evaporation reached the maximum at noon, similar to transpiration while wet canopy did not exhibit such behavior due to its dependence on intercepted precipitation. Evaporation from soil was also at its highest of 0.7 mm/hr at the start of the monsoon rainfall and sharply decreased afterward as a result of dry antecedent soil condition. However, as rainfall became more prominent in August, the rate decreased gradually as the wet soil condition had been established.

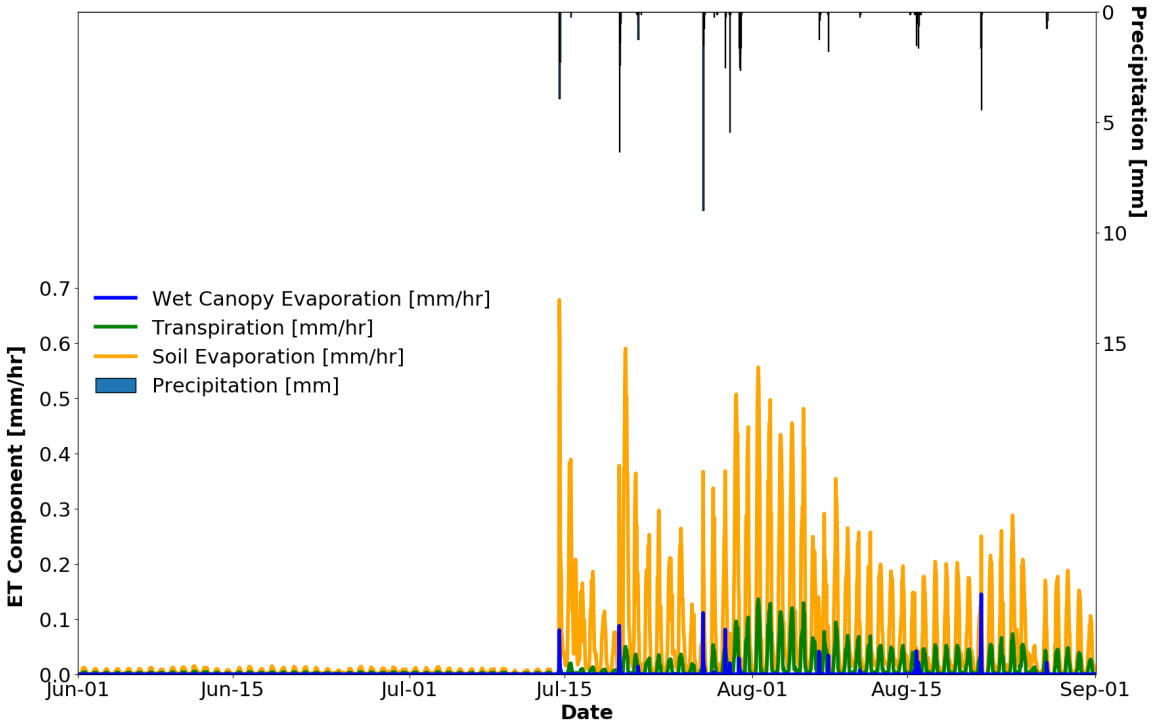

Figure 88: June to September partitioning of ET into soil evaporation (Esoil), wet canopy evaporation (Ewet), and transpiration (T) at US-SRC at an hourly temporal scale.

5.4.1.2. US-SRG

The partitioning of ET at US-SRG is shown in Figures 90 and 91 in absolute and relative terms. Similar to the ET partitioning at US-SRC, soil evaporation, transpiration, and wet canopy evaporation all experienced a sudden increase in July as the monsoon season brought high amounts of precipitation to the region. In absolute terms, ET was highest in August at a total rate of 120 mm/month and June had the lowest with virtually no ET activity. Different from US-SRC, the contribution from wet canopy evaporation was higher as can be seen in Figure 91 at US-SRG due to ta higher vegetative cover with mixture of both mesquite and grassland during the monsoon season.

Compared to US-SRC, at US-SRG there was more variability in contribution from the partition of ET between transpiration and soil evaporation. With the exception of July, August, and September, soil evaporation was the dominant contributor to total ET, accounting from 60% to 90% total ET. August saw the overtake of transpiration as the largest contributor at 50% total ET while wet canopy evaporation contributed 10% and soil evaporation at 40%. Other than that, transpiration generally contributed between 10% and 40% total ET. The high vegetation fraction, precipitation, and incoming shortwave radiation provided favorable conditions for more transpiration to occur during the summer monsoon months. Both transpiration and evaporation from soil were near zero in May and June due to the absence of precipitation during this period in 2010.

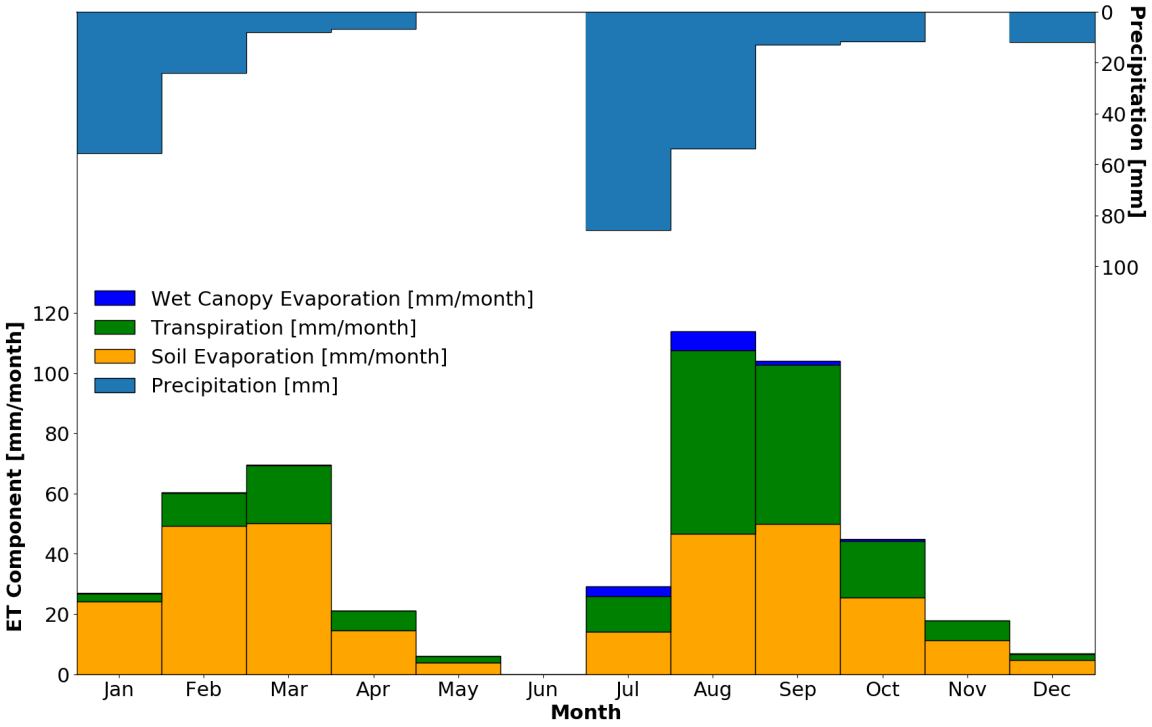

Figure 89: Partitioning of ET into soil evaporation, wet canopy evaporation, and transpiration at US-SRG in 2010. Hourly partitioning terms and precipitation were aggregated to monthly values.

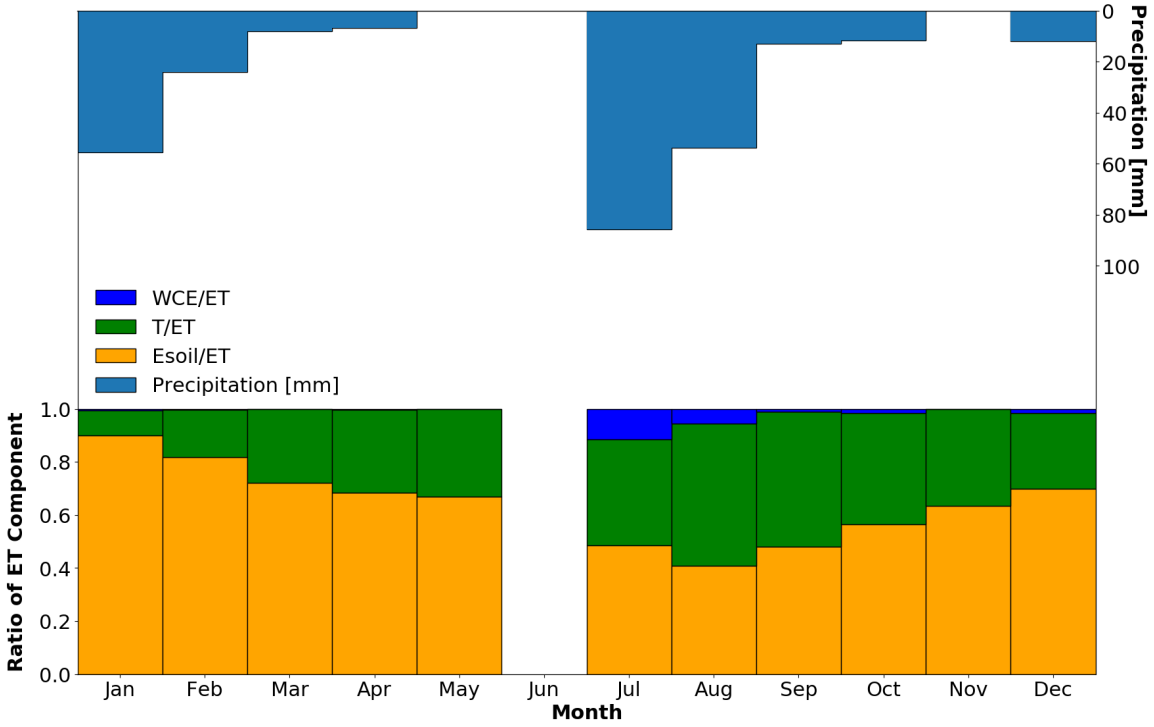

Figure 90: Relative partitioning of ET into soil evaporation, wet canopy evaporation, and transpiration at US-SRG in 2010. Hourly partitioning terms and precipitation were aggregated to monthly values.

Hourly time series of the ET components are presented in Figure 92. While June and the first half of July were characterized by virtually no evapotranspiration, later half of July until August saw the rapid increase in transpiration that overtake soil evaporation as well as an increase in the rate of wet canopy evaporation. Similar to US-SRC, both soil evaporation and transpiration exhibited diurnal variations where the maximum rate occurred at noon when the incoming solar radiation reached its peak. Transpiration also overtook soil evaporation in August with peak at 0.5 mm/hr due to high vegetation fraction and LAI from the dominant grassland vegetation, compared to the sparsely populated creosote.

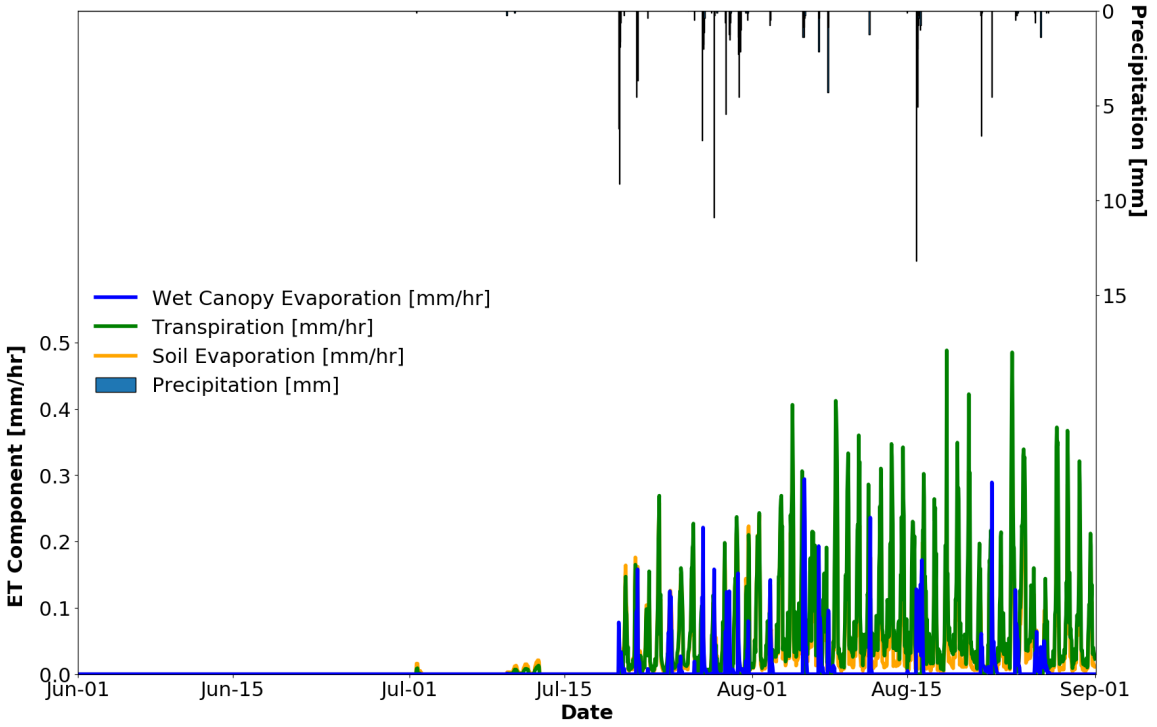

Figure 91: Partitioning of ET into soil evaporation (Esoil), wet canopy evaporation (Ewet), and transpiration (T) at US-SRG in from June to August at hourly temporal scale.

5.4.1.3. US-SRM

The partitioning of ET at US-SRM is shown in Figures 93 and 94 in absolute and relative terms. Similar to both US-SRC and US-SRG, ET rates experienced a sudden increase in July as the monsoon season brought high amounts of precipitation to the region. The antecedent wet condition from high rainfall in July, combined with continuous precipitation, high air temperature, and incoming shortwave radiation values in July made the total evapotranspiration the highest in August at nearly 100 mm/month. The lowest rate of ET is observed in June as a result of long period without precipitation and was near zero. Soil evaporation still remained the highest contributor to the total rate of evapotranspiration, ranging from the lowest of 75% in August and September to 95% in January and December. Transpiration accounted for the remaining 5% to 25% with the

highest contribution in August, coinciding with the highest observed LAI and NDVI at the site, as seen in section 5.1.2. Wet canopy evaporation was very low at US-SRM with less than 1% observed in August.

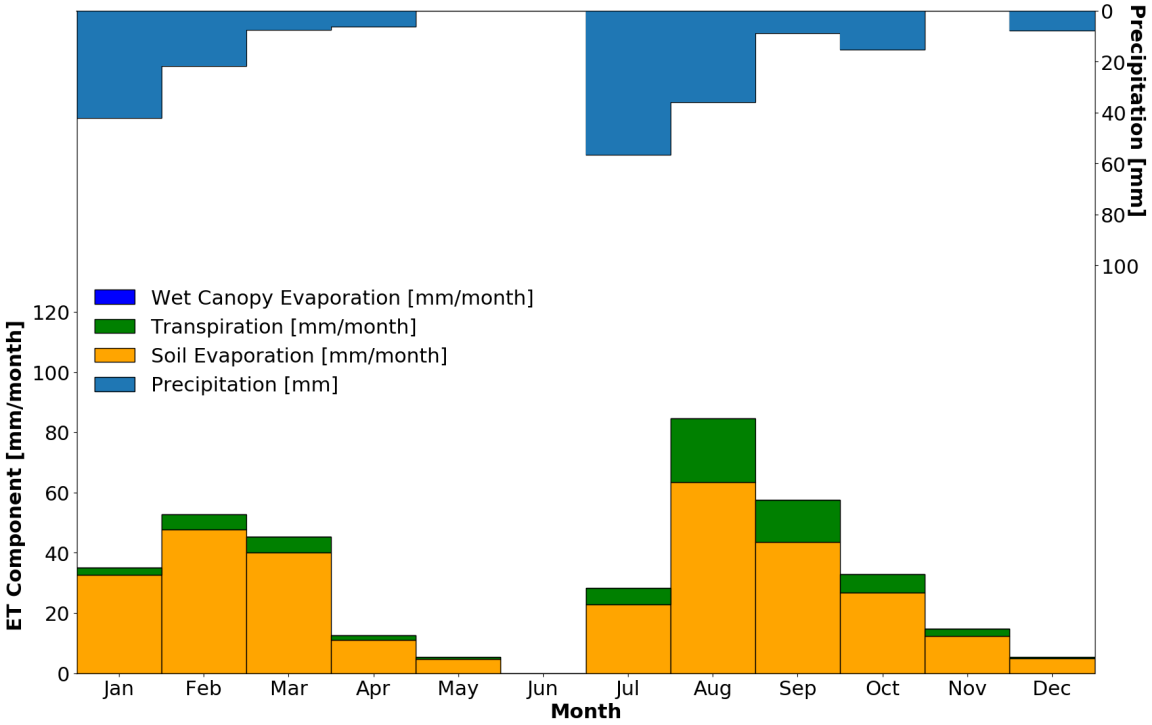

Figure 92: Partitioning of ET into soil evaporation, wet canopy evaporation, and transpiration at US-SRM in 2009. Hourly partitioning terms and precipitation were aggregated to monthly values.

As shown by Figure 95, the hourly time series of the ET components were nearly zero in June with the lack of precipitation. With the start of the monsoon season in mid-July, soil evaporation and transpiration started to increase and reached their peaks in early August as a result of high incoming solar radiation and number of days with precipitation. Values occurred at a rate of 0.5 and 0.2 mm/hr for soil evaporation and transpiration, respectively. No substantial wet canopy evaporation occurred with most below 0.1 mm/hr as a result of relatively lower NDVI at the site which resulted in lower vegetation fraction. The diurnal

variations in both soil evaporation and transpiration followed the diurnal cycle of latent heat flux, which depended on the amount of incoming solar radiation that was low at night and early morning and peaked at noon. The peak transpiration and peak soil evaporation in early August were the result of high number of rainfall days in late July.

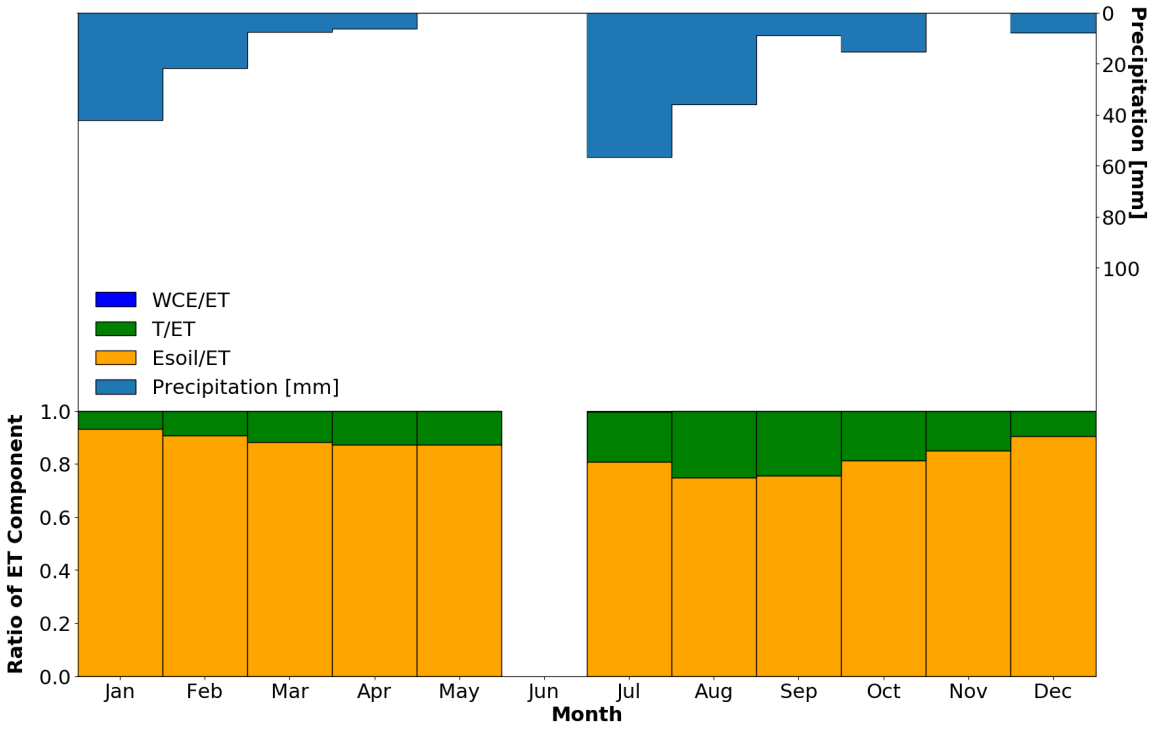

Figure 93: Relative partitioning of ET into soil evaporation, wet canopy evaporation, and transpiration at US-SRM in 2010. Hourly partitioning terms and precipitation were aggregated to monthly values.

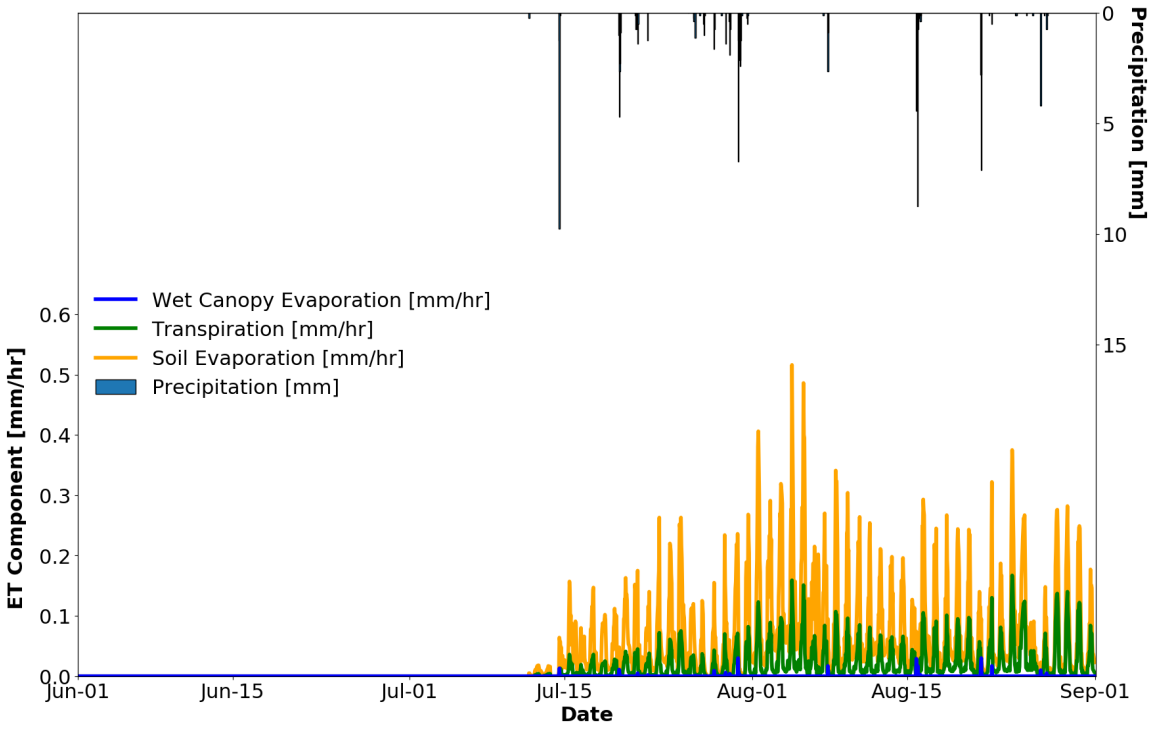

Figure 94: Partitioning of ET into soil evaporation (Esoil), wet canopy evaporation (Ewet), and transpiration (T) at US-SRM from June to August 2010 at hourly temporal scale.

5.4.2. Forest Ecosystem

5.4.2.1. US-FUF

The partitioning of ET at US-FUF is shown in Figures 96 and 97 in absolute and relative terms. Relative to Santa Rita, the partitioning had differences particularly in relation to a larger wet canopy evaporation and a delayed high-transpiration season in October. The highest soil evaporation and wet canopy evaporation were observed in August at the rate of 60 mm/month and 50 mm/month respectively while the transpiration was not as significant at only 5 mm/month. The maximum transpiration rates were observed in October at 20 mm/month. The lowest wet canopy evaporation was seen in June and November at the rate of near zero while lowest transpiration was observed in January, February, and December as a result of cold weather and shredded needles of ponderosa

pines. Due to higher LAI in the forest ecosystem, more rainfall was intercepted by the canopy and made wet canopy evaporation a significant contributor at US-FUF, compared to the three stations in a desert ecosystem at Santa Rita, AZ.

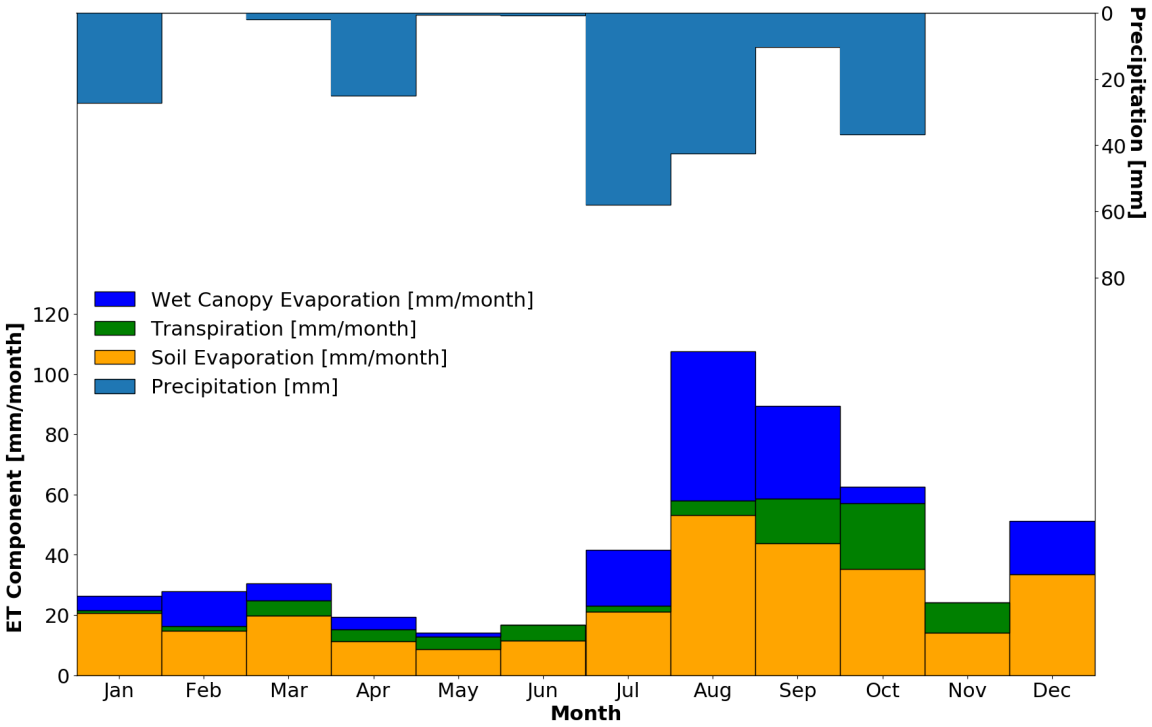

Figure 95: Partitioning of ET into soil evaporation, wet canopy evaporation, and transpiration at US-FUF in 2007. Hourly partitioning terms and precipitation were aggregated to monthly values.

In the relative terms (Figure 97), the first half of 2007 from January to June was dominated by evaporation from bare soil, ranging from 50% in February to 80% in January. Transpiration was low during January, February, July, August, and December, ranging between 0 and 5% and its contribution increased drastically between March and June and between September and November with peak of 41% in November (despite the largest absolute rate in October). Evaporation from wet canopy is highly correlated with the precipitation accumulation. It accounted for 18 to 41% of total evapotranspiration from

January to April and again 34 to 46% from July to September where there was a high concentration of precipitation.

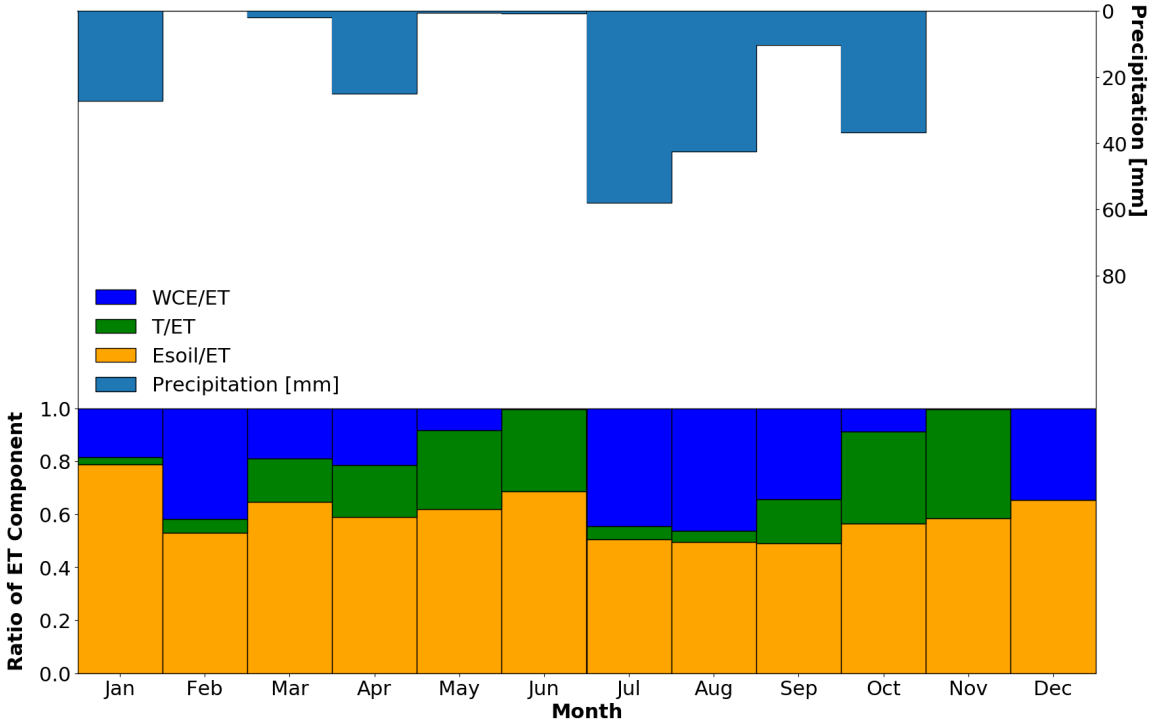

Figure 96: Relative partitioning of ET into soil evaporation, wet canopy evaporation, and transpiration at US-FUF in 2007. Hourly partitioning terms and precipitation were aggregated to monthly values.

The hourly time series from June to September for the ET partitioning are illustrated in Figure 98. Unlike the observations at Santa Rita for all three stations, transpiration and evaporation still occurred in forest ecosystem, at a lower rate, during the month of June under no precipitation condition. The mean transpiration in June was at 0.01 to 0.02 mm/hr while the rate for soil evaporation during the same period was 0.03 to 0.05 mm/hr. Obviously, wet canopy evaporation remained zero without intercepted rainfall. As soon as precipitation increased in early July, the rate of all three components increased sharply with wet canopy evaporation overtaking soil evaporation as the main contributor to total ET.

High LAI and high NDVI at the site which translated to higher percentage of intercepted water and higher vegetation fraction were the main reasons for this pattern. Another difference between Santa Rita and US-FUF is that the wet canopy evaporation also displayed diurnal cycle behaviors at US-FUF along transpiration and soil evaporation. Transpiration was also significant in the latter half of August due to the water transported from the deep rooting system.

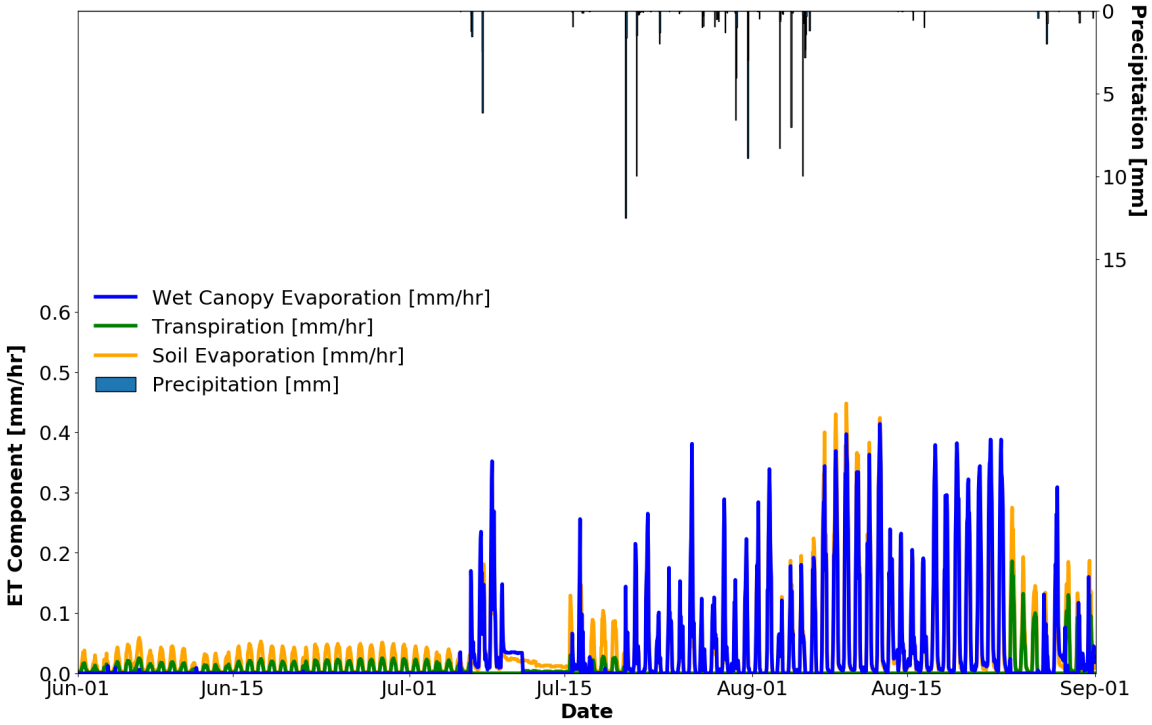

Figure 97: Partitioning of ET into soil evaporation (Esoil), wet canopy evaporation (Ewet), and transpiration (T) at US-FUF from June to August 2007 at hourly temporal scale.

5.4.2.2. US-FWF

The partitioning of ET at US-FWF is shown in Figures 99 and 100 in absolute and relative terms. For US-FWF where surface vegetation cover was mix of ponderosa pine forest, shrubs, and grassland, wet canopy evaporation was not as pronounced as at the US-

FUF, even though it was still higher than simulations at Santa Rita. It was at its peak in August at the rate of 30 mm/month and at the lowest in June due to the absence of precipitation. Soil evaporation was again the largest contributor with peak of 120 mm/month in August and was lowest in February, possibly due to the snow layer on surface and low temperature. Transpiration was low during the winter months, similar to US-FUF and gradually increased from its low of 2 mm/month in April to its peak in September of 30 mm/month as both NDVI and LAI and incoming solar radiation increased.

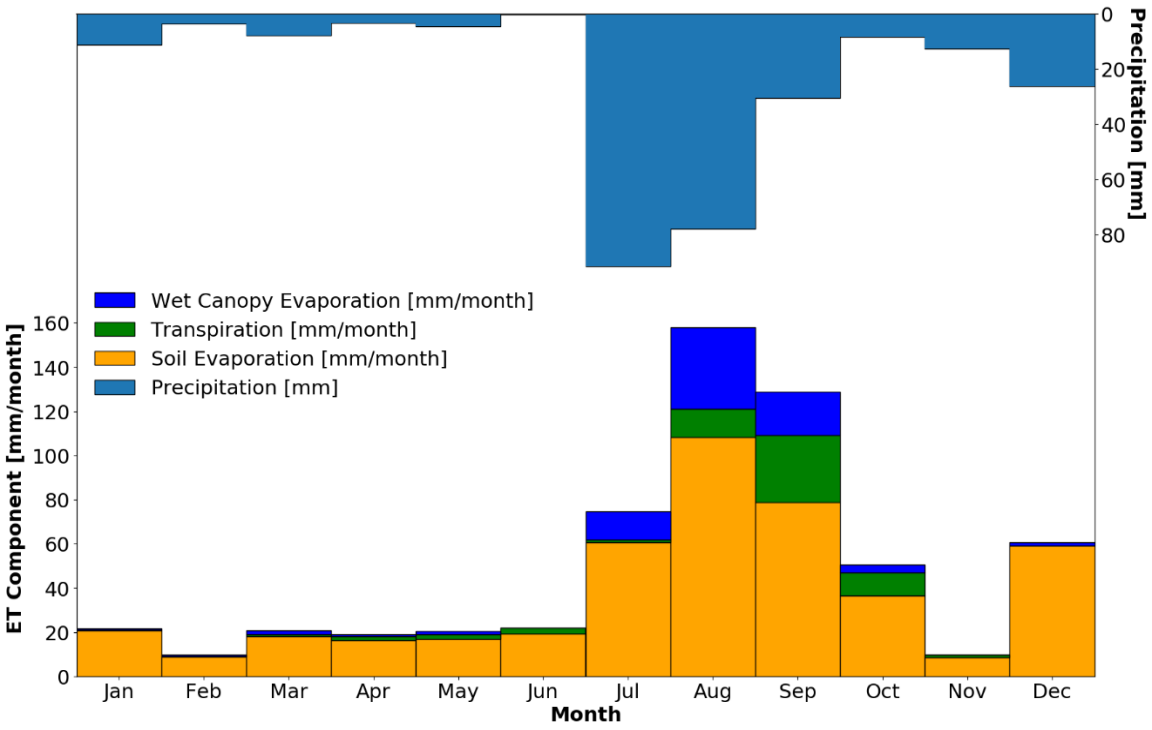

Figure 98: Partitioning of ET into soil evaporation, wet canopy evaporation, and transpiration at US-FWF in 2007. Hourly partitioning was averaged to monthly values with corresponding precipitation accumulation.

In relative terms (Figure 100), soil evaporation accounted between 60 and 98% of ET, wet canopy evaporation between 2 and 20%, and transpiration between 0 and 20%. The reason why transpiration was low in winter despite the presence of precipitation and wet canopy evaporation was due to the closure of stomata to prevent heat loss during the cold months. In June, when there was no precipitation, water was withdrawn from the root-zone which explained why transpiration still occurred. The loss of ponderosa pines due to the 1996 wildfire and the replacement by shrubs and grass also decreased the percent contribution by transpiration at US-FWF and made the contribution from soil evaporation the highest, similar to all stations at Santa Rita.

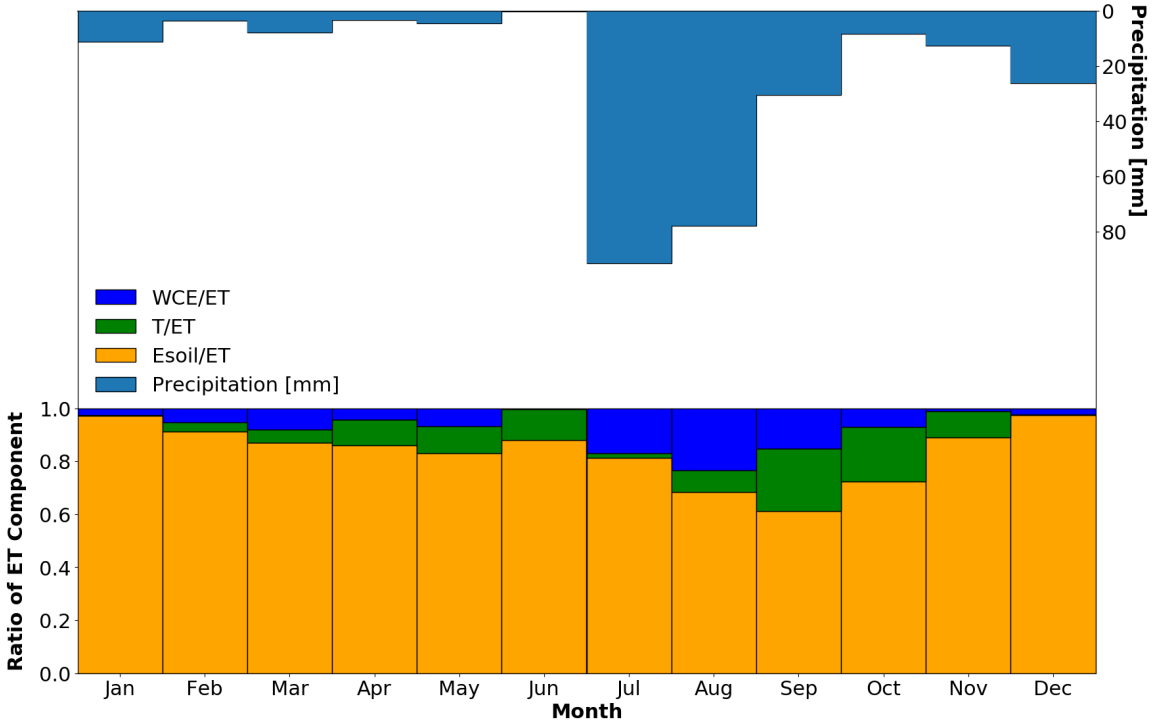

Figure 99: Relative partitioning of ET into soil evaporation, wet canopy evaporation, and transpiration at US-FWF in 2007. Hourly partitioning was aggregated to monthly values.

June, July and August hourly time series of the partitioning of ET at US-FWF are illustrated in Figure 101. Similar to US-FUF, June was dominated by soil evaporation at a rate

between 0.05 and 0.1 mm/hr. The increase in rainfall by mid-July caused a sharp increase in soil evaporation which reached 0.5 mm/hr during the second rainfall event in early July. Wet canopy evaporation remained between 0.05 and 0.4 mm/hr on rainy days and transpiration increased from 0.02 mm/hr in early July to 0.3 mm/hr mid-August.

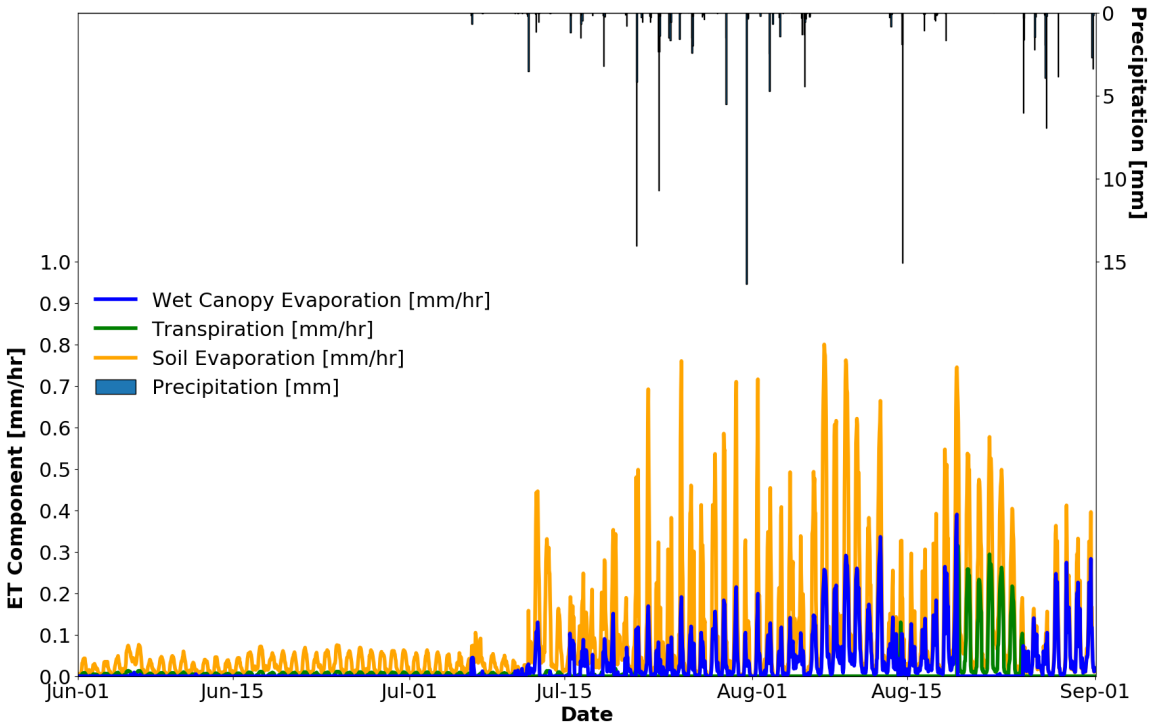

Figure 100: Partitioning of ET into soil evaporation (Esoil), wet canopy evaporation (Ewet), and transpiration (T) at US-FWF from June to August at hourly temporal scale.

5.4.3. Grassland Ecosystem

The partitioning of ET at MOISST is shown in Figures 102 and 103 in absolute and relative terms. This is the only station among the 7 stations in this study with transpiration as the dominant contributor of ET. Transpiration increased from its low of 5 mm/month in January and December to approximately 100 mm/month in July. The second largest component was soil evaporation, ranging from 2.5 mm/month in January and December to

40 mm/month in September, and the smallest component was wet canopy evaporation mostly from May to October at a rate between 1 to 10 mm/month. Unlike Santa Rita where there was a clear distinction between dry and wet seasons in terms of precipitation, at MOISST, the precipitation existed year-round and in higher accumulations. In case of 2016, there was two rainfall peaks in April and July. While the July peak in rainfall coincided with high transpiration and high wet canopy evaporation due to the high LAI, and NDVI of the same month, the high precipitation in April did not cause significant change to the rate of ET, as seen in Figure 102. A potential explanation for this may rely on the fact that prairie grassland just started to grow in April so the effect of rainfall was not as pronounced as it transitioned from winter to spring, which led to higher overall runoff.

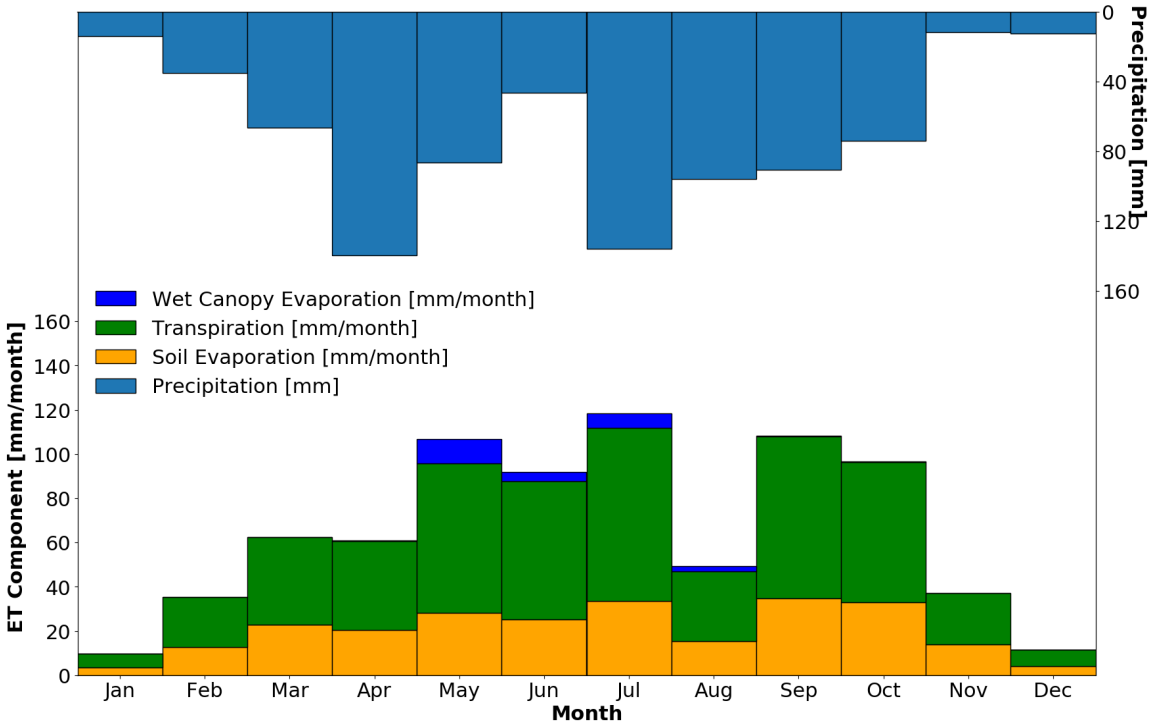

Figure 101: Partitioning of ET into soil evaporation, wet canopy evaporation, and transpiration at MOISST in 2016. Hourly partitioning components and precipitation were aggregated to monthly values.

In terms of relative contribution (Figure 103), transpiration accounted for 60 to 70% ET at the grassland ecosystem while soil evaporation accounted for 30 to 40% ET and wet canopy evaporation accounted for 2 to 10% ET that concentrated in 4 months from May to August. The wet canopy evaporation was negligible for the remaining months of 2016. The reason why transpiration was dominant is the prairie grassland with low overall canopy cover but entrenched and multi-level rooting system.

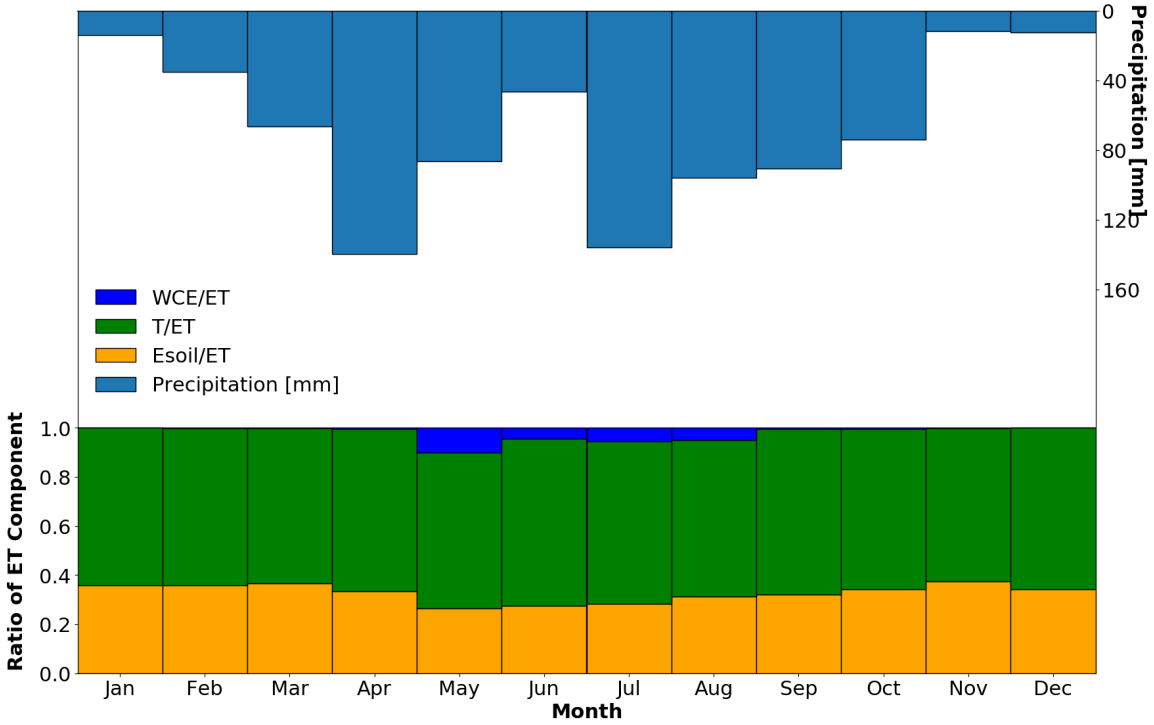

Figure 102: Relative partitioning of ET into soil evaporation, wet canopy evaporation, and transpiration at US-FWF in 2007. Hourly partitioning was averaged to monthly value with corresponding precipitation accumulation.

Figure 104 illustrates the hourly time series of the partitioning of ET at MOISST in 2016. Unlike Flagstaff and Santa Rita, ET rates were high during June with soil evaporation at 0.2 mm/hr and transpiration at 0.1 to 0.6 mm/hr during the day. There were also some irregularities in the behavior of ET. between June 1st and June 15th, there was little rainfall

but both transpiration and soil evaporation remained high while in the period around August 15th, there was no observed ET. The reason for this was potentially due to higher amount of incoming shortwave radiation in August that caused the grassland to close its stomata to prevent water to deplete.

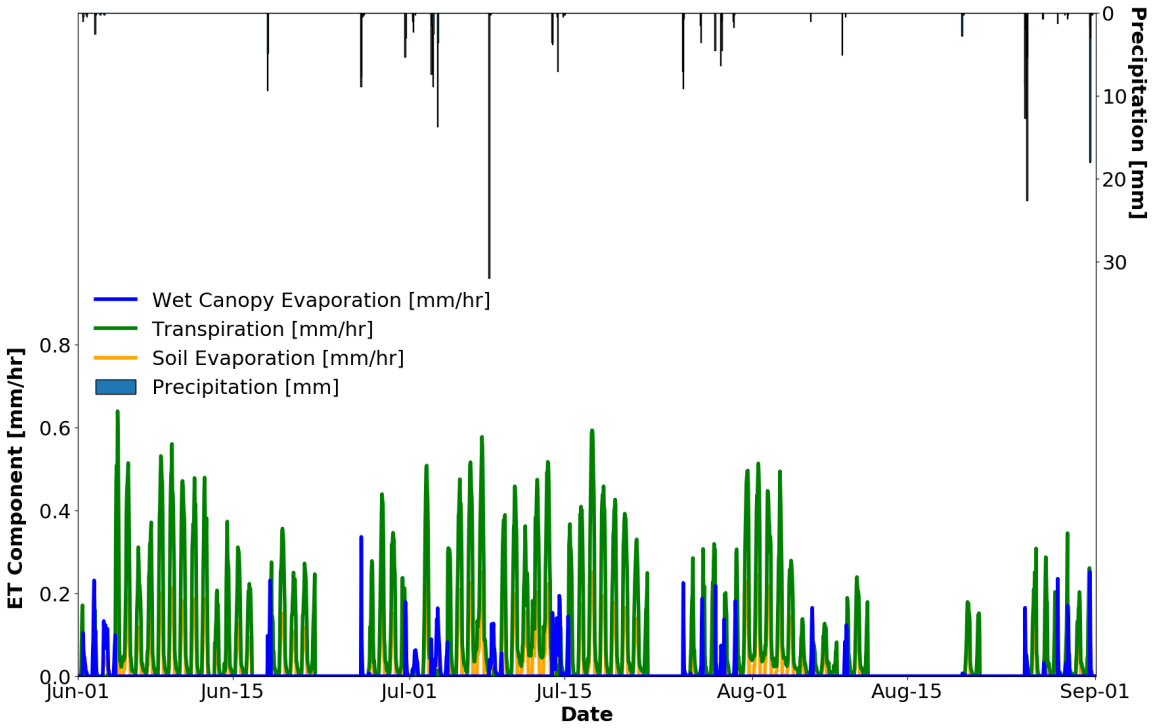

Figure 103: Partitioning of ET into soil evaporation (Esoil), wet canopy evaporation (Ewet), and transpiration (T) at MOISST from June to August 2007 at hourly temporal scale.

5.5. Quantifying the Effects of Vegetation and Soil Moisture on the Soil Damping Depth

5.5.1. Forest Ecosystem

5.5.1.1. US-FUF

Figure 105 (left and right panels) illustrate density scatterplots between damping depth calculated from the simulated surface (at 10 cm) and root zone (at 1 m) soil

temperature versus the observed LAI (left panel) and surface soil moisture (right panel). Hourly values were aggregated to daily scale.

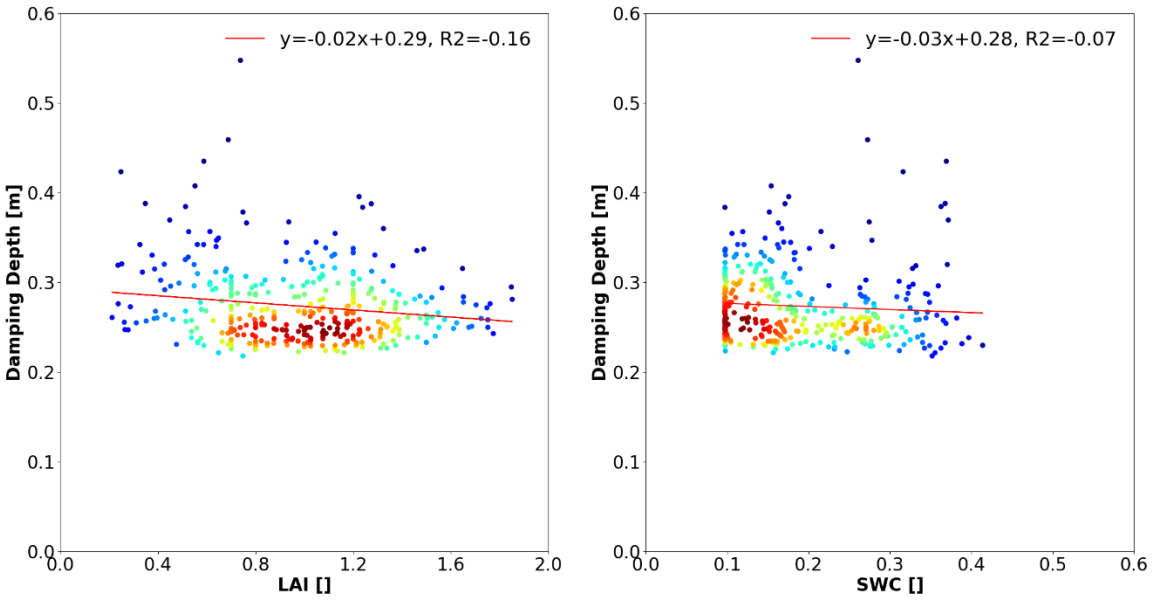

Figure 104: Daily Damping Depth from simulated surface temperature and root zone temperature versus LAI (left) and daily average moisture between the simulated 10-cm and 100-cm soil moisture (right) for US-FUF in 2007.

It can be seen that there were no observable relationships between either LAI or the average soil moisture and calculated damping depths at US-FUF. The correlation coefficient between damping depth and LAI was -0.16 which showed that they were slightly negatively correlated. The CC was -0.07 for the calculated damping depth and average soil moisture. Calculated damping depth was seen to fluctuate between 0.2 and 0.55 m while LAI fluctuated between 0.3 and 2.0. The density scatterplots show a high number of points situated between 0.25 meters for the damping depth and between 0.8 and 1.2 for LAI. A possible explanation on why there was no observed relationship between calculated damping depths and LAI is that the low temporal resolution of LAI (4 days) and the propagation of errors from the simulated surface temperature and rootzone temperatures.

Similarly, errors in both the simulated 10- and 100-cm depth soil moisture led to unobservable relationships between damping depth and soil moisture utilizing tRIBS.

5.5.1.2. US-FWF

Figure 106 illustrates density scatterplots between damping depth calculated from the simulated surface soil and root zone soil temperatures versus the observed LAI (left panel) and the daily average between the simulated 10- and 100-cm depth soil moisture (right panel). The correlation coefficient between LAI and calculated damping depths was -0.35 which slowed they were negatively correlated. As LAI increase, less incoming shortwave radiation could reach and heated the surface as well as penetrated into deeper soil layer, which decreased the amplitude at which surface temperature varied and made subsurface temperature non-dependence on the incoming radiation. Negative correlation coefficient was also observed for average soil moisture and calculated damping depth with value of -0.11 which meant they were also negatively correlated. However, due to the simulation error in both temperature and soil moisture, it was inconclusive on the relationship between damping depth and soil moisture at US-FWF.

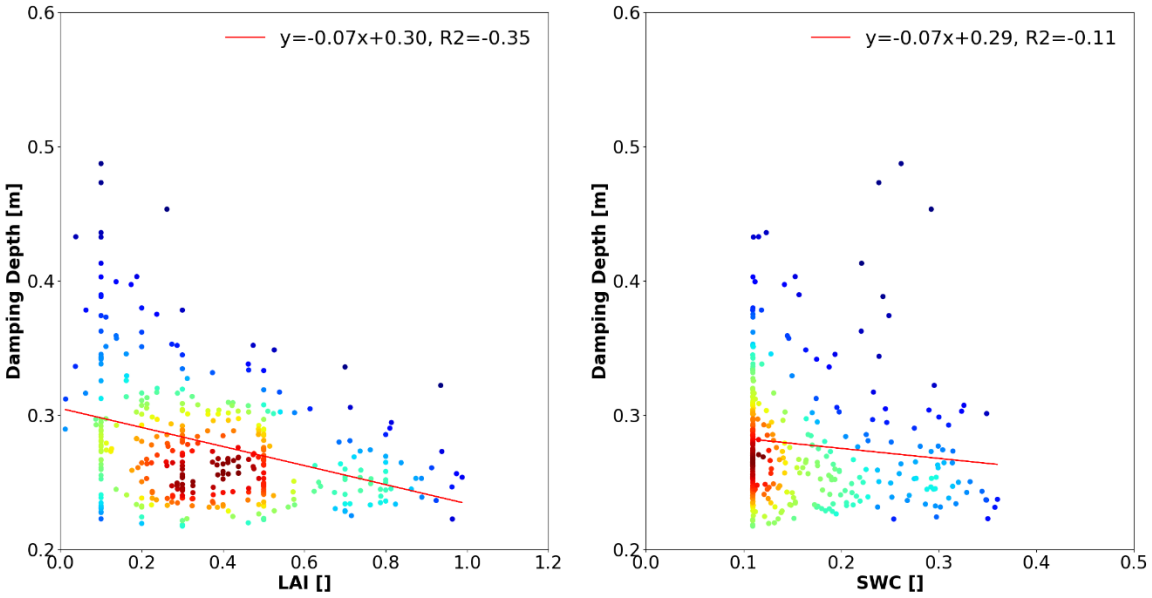

Figure 105: Daily Damping Depth from simulated surface temperature and root zone temperature versus LAI (left) and daily average moisture between the simulated 10-cm and 100-cm soil moisture (right) for US-FWF in 2007.

5.5.1.3. US-FMF

Figure 104 illustrates the density scatter plot between damping depth calculated from the simulated surface soil temperature and root zone soil temperature versus the observed LAI (left panel) and the daily average between the simulated 10- and 100-cm depth soil moisture at US-FMF in 2010. The correlation coefficient between LAI and calculated damping depth was also negative with value of -0.18. The negative CC showed that at US-FMF, as LAI increased, the corresponding damping depth decreased which could be explained by the same analogy at US-FWF. However, due to low temporal resolution of LAI as well as errors from soil temperature simulation, no conclusion was reached for the relationship of LAI and damping depths using tRIBS model. The correlation coefficient for average soil moisture and calculated damping depth, on the contrary, was nearly zero at 0.02 which showed there was no relationship between the two

variables. However, similar to the other two stations, the errors from both simulations of soil temperatures and soil moisture prevents reasonable conclusion on their relationship.

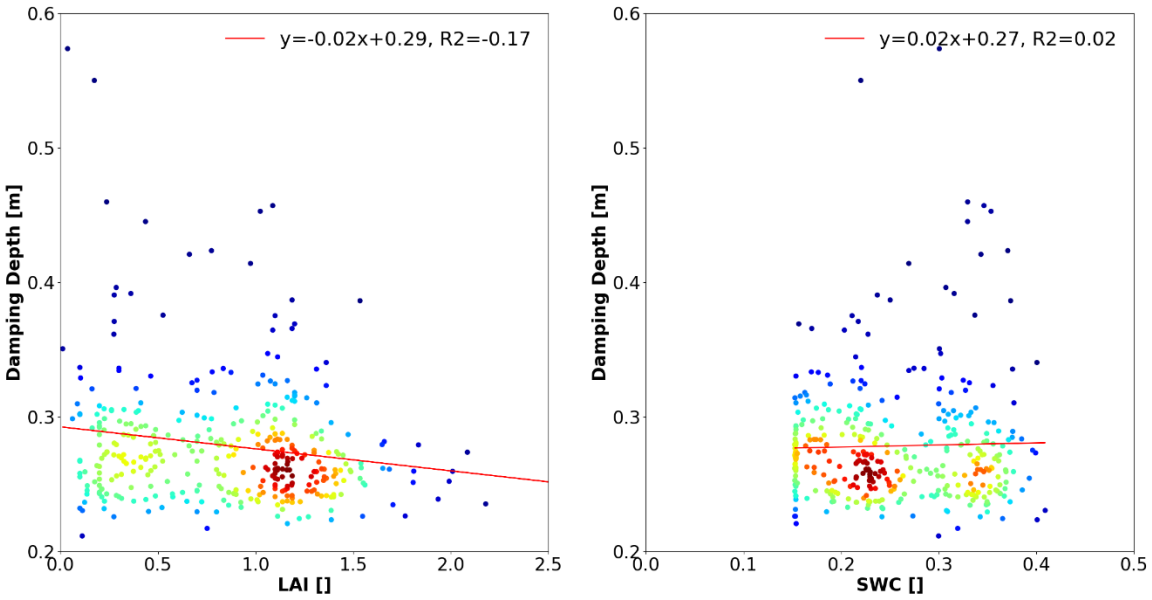

Figure 106: Daily Damping Depth from simulated surface temperature and root zone temperature versus LAI (left) and daily average moisture between the simulated 10-cm and 100-cm soil moisture (right) for US-FMF in 2010.

5.5.2. Desert Ecosystem

5.5.2.1. US-SRC

Figure 108 illustrates the density scatter plot between damping depth calculated from the simulated surface soil temperature and root zone soil temperature versus the observed LAI (left panel) and the daily average between the simulated 10- and 100-cm depth soil moisture at US-SRC in 2010. With the correlation coefficient between LAI and calculated damping depth of -0.001, it showed that the two variables were not correlated. However, as seen in section 5.1, the deeper soil temperature sensor at US-SRC malfunctioned for the whole period of measurements, thus, the simulated rootzone temperature was not verified against any field measurements. Additionally, 4-day LAI

observations also prevent sound conclusion regarding their relationship. The same observation was also made between average soil moisture and calculated damping depth at US-SRC where their correlation coefficient was also slightly negative at -0.04.

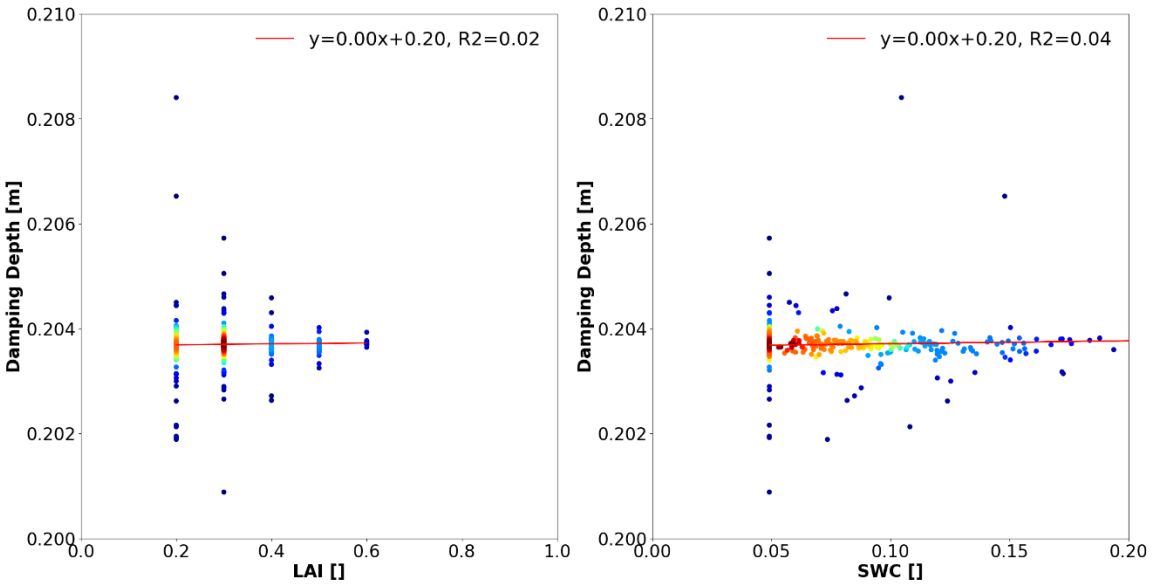

Figure 107: Daily Damping Depth from simulated surface temperature and root zone temperature versus LAI (left) and daily average moisture between the simulated 10-cm and 100-cm soil moisture (right) for US-SRC in 2010.

5.5.2.2. US-SRG

Figure 109 illustrates the density scatter plot between damping depth calculated from the simulated surface soil temperature and root zone soil temperature versus the observed LAI (left panel) and the daily average between the simulated 10- and 100-cm depth soil moisture at US-SRG in 2009. One again, both the correlation coefficients showed slight negative value with -0.03 for LAI and -0.02 for average soil moisture. They both showed that these variables were not correlated.

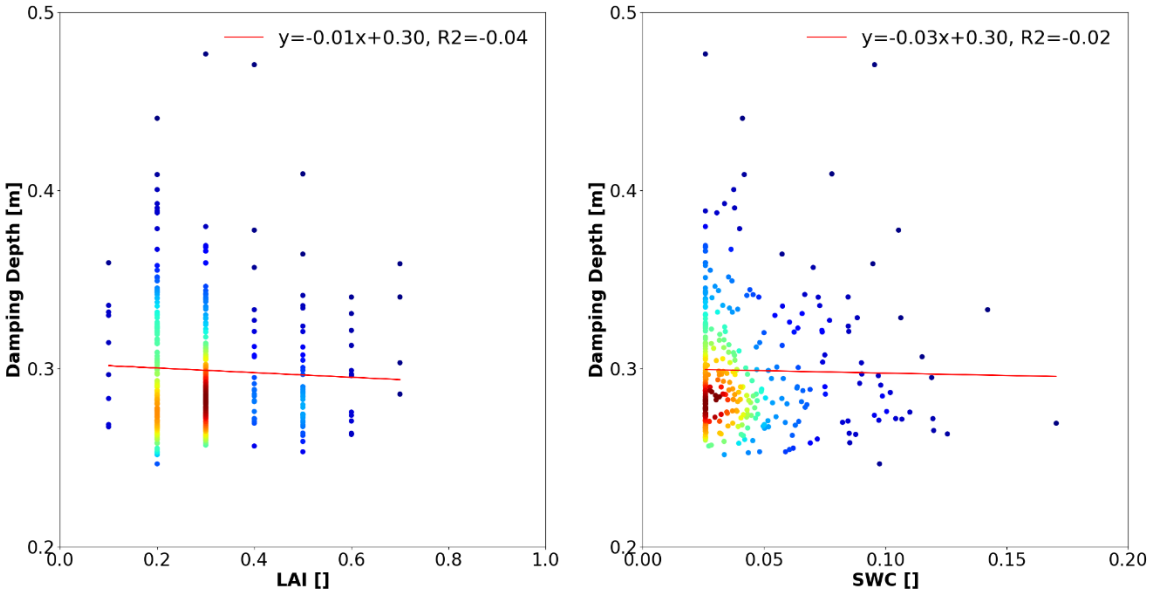

Figure 108: Daily Damping Depth from simulated surface temperature and root zone temperature versus LAI (left) and daily average moisture between the simulated 10-cm and 100-cm soil moisture (right) for US-SRG in 2009.

5.5.2.3. US-SRM

Figure 110 illustrates the density scatter plot between damping depth calculated from the simulated surface soil temperature and root zone soil temperature versus the observed LAI (left panel) and the daily average between the simulated 10- and 100-cm

depth soil moisture at US-SRM in 2009. With both correlation coefficients near zero, there was no conclusion reached regarding the relationship of these variables.

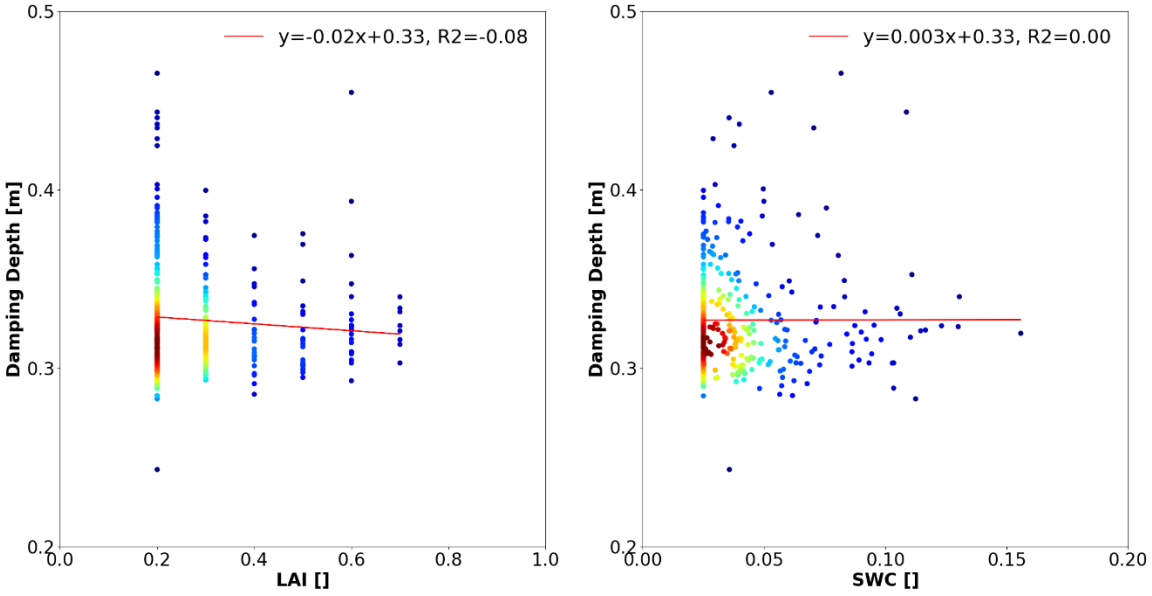

Figure 109: Daily Damping Depth from simulated surface temperature and root zone temperature versus LAI (left) and daily average moisture between the simulated 10-cm and 100-cm soil moisture (right) for US-SRM in 2009.

5.5.3. Grassland Ecosystem

Figure 111 illustrates the density scatter plot between damping depth calculated from the simulated surface soil temperature and root zone soil temperature versus the observed LAI (left panel) and the daily average between the simulated 10- and 100-cm depth soil moisture at MOISST in 2016. Similar to stations at Flagstaff, AZ, and Santa Rita, AZ. Both correlation coefficients showed negative values with the CC between calculated damping depth and LAI was -0.08 and CC between calculated damping depth and average soil moisture of -0.1, which again, showed that there was no relationship between these variables. In conclusion, it was not possible to assess the relationship of soil moisture or LAI with the damping depths calculated from the simulated surface and

rootzone temperatures and gain any meaningful conclusion. There are two reasons for this. The first reason why was due to the low resolution of LAI that was obtained every 4 days that reduced its usefulness when being assessed again the damping depth that was calculated at hourly temporal scale and averaged to daily values. The second reason was due to the error propagation from both the simulated soil moisture and soil temperatures.

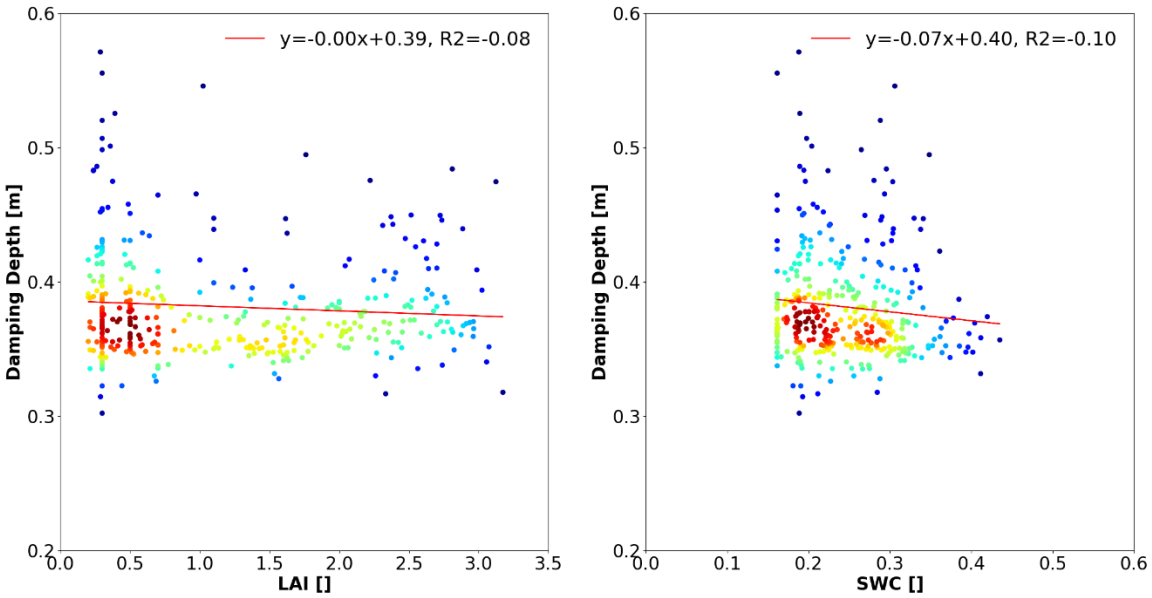

Figure 110: Daily Damping Depth from simulated surface temperature and root zone temperature versus LAI (left) and daily average moisture between the simulated 10-cm and 100-cm soil moisture (right) for MOISST in 2016.

5.6. VisualTribs

VisualTribs is developed utilizing Python and tested using benchmark simulations on the model website (http://vivoni.asu.edu/tribs/benchmarkExamples.html). The current version of the software has the capability to visualize all the model outputs and export the figures to user-desired format from serial simulations while parallel simulation outputs were not implemented. Source code and a pre-compiled version of the software are hosted on GitHub and the University of Oklahoma website (http://moreno.oucreate.com) for

public access. Examples from the program are illustrated in Figure 111 of the simulation in 1998 for latent heat flux at Peacheater Creek, a tributary to the Illinois River in northeastern Oklahoma. The Appendix one illustrates a user manual of this tool.

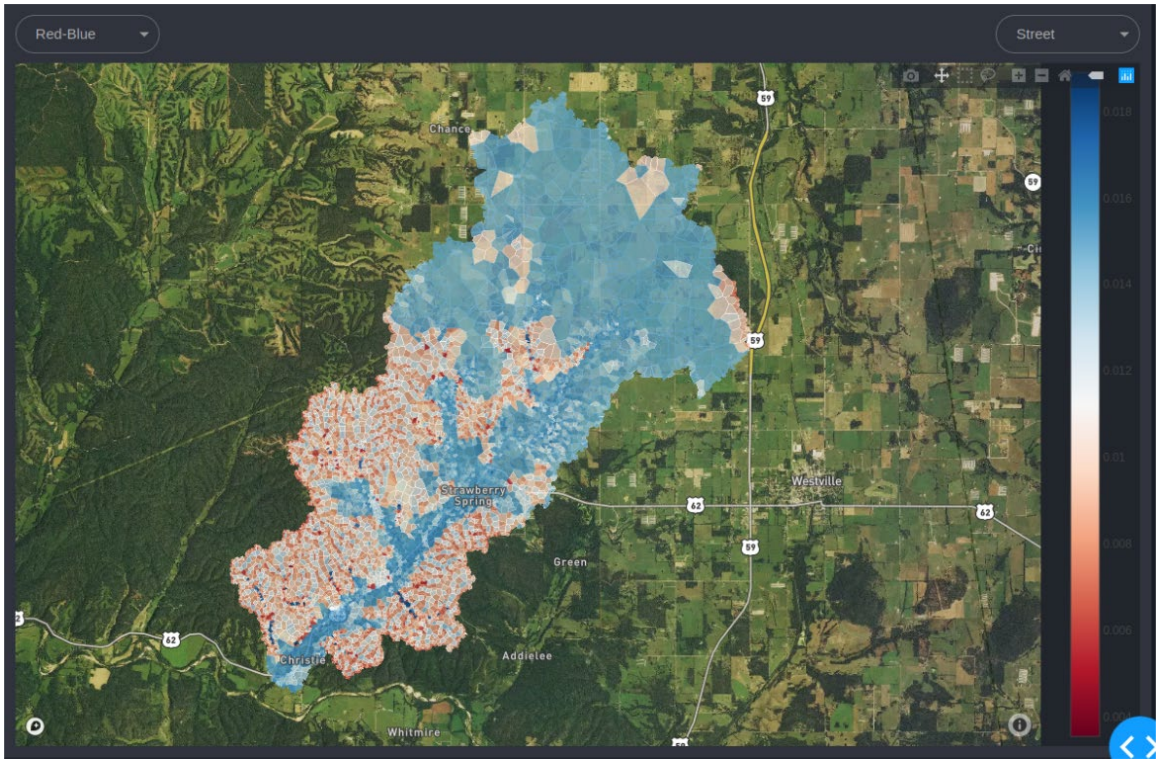

Figure 111: VisualtRIBS user interface with example of spatially varied latent heat flux at Peacheater Creek.

5.7. Limitations of the Study

There are still limitations in this study with respect to the eddy covariance measurements, the satellite remote sensing data, and the parameterization of the models. The uncertainties in eddy flux measurements have been extensively examined in multiple studies. Hollinger and Richardson (2005) found that the increase in the magnitudes of measured fluxes caused the uncertainties to increase, especially with latent heat flux and sensible heat flux during the vegetation growing season. In addition, the non-orthogonal sonic anemometer (CSAT3) used in measuring the wind speed, wind direction and sensible

heat flux at more than 30% of the eddy covariance stations also underestimated these variables by 6 to 10% (Frank et al., 2013). These uncertainties in flux measurements was one of the factors that potentially affected the quality of the simulation as well as the partitioning of evapotranspiration into three components. Missing measurements of the hydrometeorological forcing variables was another limitation in simulating the fluxes, soil moisture and soil temperature. Even though the model was able to continue the simulation with some missing measurements, hydrometeorological forcing variables were essential and important in determining the conditions of the atmosphere that directly influenced the partitioning of surface energy fluxes, soil moisture and temperature through a variety of physical equations. The periods of missing data affected the quality of the outputs, especially with the surface energy balance.

With respect to the errors of the physically based model, tRIBS utilized 26 parameters for the characterization of soil properties and surface vegetation conditions. With the exception of the 7 dynamic vegetation variables mentioned in section 4.2.2, the remaining parameters remained constant throughout the simulation duration and could not be changed when the simulation was in progress. As many studies have shown, soil thermal properties exhibited seasonal changes and vary with the soil water content (Farouki, 1981; Alvalá et al., 2002; Malmedal et al., 2014). By constraining the thermal properties into constant values for simulation period of one year, in addition to the uncertainties in flux measurements, the errors propagated and affected the quality of the simulation at the seven stations.

The third limitation of this study was the resolution of the satellite data for the surface condition (albedo) and the dynamic vegetation variables (LAI, NDVI). The highest

temporal resolution product was albedo at daily time scale, while the resolution for LAI and NDVI was 4 and 16 days, respectively. The current model capability did not interpolate the observed LAI and NDVI values and assumed that they remained constant between the date of measurement, e.g. the LAI values remained the same for 4 days and NDVI values remained the same for 16 days. However, during the vegetation growing season in spring and summer, both LAI and NDVI could change quickly day to day. With the simulation conducted at hourly time scale for all three ecosystems, the low resolution of the satellite products was another source of limitation in assessing the effects of vegetation on latent heat flux and sensible heat flux, soil moisture and soil temperature, and the diurnal behaviors of these variables.

Chapter 6: Summary and Conclusions

This master's thesis studied the effects of gradual and abrupt vegetation changes on the surface and root-zone temperature and soil moisture, evapotranspiration and the surface energy budget components and their partitions through the utilization of eddy covariance measurements, satellite images, and a physically-based, distributed hydrological model across three distinct ecosystems of the United States. Analyses of measured fluxes at the forest ecosystem in Flagstaff showed the long-term consequences of severe wildfire on the partitioning of surface energy budget, especially with latent heat flux, sensible heat flux, and net radiation. Both human-induced thinning and natural wildfire sites experienced a decrease in both latent heat flux and sensible heat flux. In addition, ground heat flux drastically increased from March to September for wildfire site, but the same occurrence was not observed at the human-induced thinning site. Furthermore, net radiation was reduced by half, compared to the undisturbed site and its soil temperature increased by 2

to 3°C during summer months from June to August. For soil moisture, its magnitude decreased with the severity of the disturbance, with highest average soil moisture at the control site, followed by human-induced thinning site, and finally the severe wildfire site.

The intensity of the disturbance was also an important factor to assess the changes post-disturbance, this conclusion is proved with the human-controlled thinning site where post-thinning measurements showed little effects on the partitions of surface energy balance. Partitioning of evapotranspiration also demonstrated the importance of LAI and vegetation fraction on the rate of evaporation from wet canopy and transpiration between ponderosa pine forest-dominated site and disturbed site with mixture of pine, shrubs, and bushes. Partitioning of evapotranspiration revealed a higher percentage of contribution by wet canopy evaporation and transpiration at ponderosa pine forest which was directly correlated to higher LAI and vegetation fraction. Disturbance due to wildfire reduced the contributions by both wet canopy evaporation and transpiration and increased evaporation from bare soil and the overall evapotranspiration.

The differences in vegetation cover types is also assessed with analyses of three eddy covariance sites in Santa Rita, AZ. Despite the higher monthly average soil moisture surrounding the creosote-dominated site, its latent heat flux was significantly less than the observations at mesquite- and grassland-dominated sites. With higher percentage of coverage on the surface, sensible heat flux as well as soil temperature were the lowest with grassland surface landcover among three study sites. Partitioning of surface energy fluxes was seasonally dependent where latent heat flux was highest from July to September while for both ground heat flux and sensible heat flux, April to June were their highest. Partitioning of evapotranspiration at Santa Rita revealed low contribution by evaporation

from wet canopy due to lower LAI while similar to Flagstaff, evaporation from bare soil remained the highest contributor. Furthermore, transpiration at grassland-dominated site was observed to be at higher rate than at creosote- and mesquite-dominated sites because of the higher vegetation fraction on the surface. Overall, the changes in the partitioning of surface energy balance fluxes, soil moisture, and soil temperature at Santa Rita was advanced by the amount of precipitation accumulation, the surface vegetation types which directly related to the amount of water demand, and the percentage of surface vegetation cover which intercepted not only the incoming solar radiation, but also the wind speed, wind direction, the porosity and the interconnectability of subsurface media, thus directly influenced the responses of surface fluxes, temperature, and soil moisture.

Calibration and validation simulations of seven research sites illustrates utilizing tRIBS showed the model has the capability to capture the temporal variability and the diurnal cycle of soil temperature, soil moisture, and surface energy balance components at high resolution (1-hour) and the quality of outputs can be sustained for simulation longer than one year. Quality of simulations was verified with metrics such as the Nash-Sutcliffe coefficient and correlation coefficient and showed satisfactory results for the simulated variables. However, soil moisture and ground heat flux results are less consistent due to the characterization of complex subsurface soil characteristics, especially in the vertical soil compositions, the coarse resolution of satellite images, and the uncertainties in field measurements. Finally, the current model does not have the capability to account for partitioning of the surface energy balance with presence of snow or frozen soil. Completing the snow layer module for tRIBS is another crucial step to understand the partitioning in wintertime.

The high correlation coefficient and the Nash-Sutcliffe efficiency coefficient between the observed and simulated latent heat flux proved valuable in partitioning the evapotranspiration into the three components: soil evaporation, transpiration, and wet canopy evaporation from intercepted precipitation. The partitioning at the three eddy covariance stations of the desert ecosystem at Santa Rita was compared against Moreno et al.'s model (2020) and displayed similar behaviors and high agreements between the two methods. Additionally, the transpiration at creosote station (US-SRC) in Moreno et al.'s method was directly obtained from the sap flow measurement which proved the physically-based model partitioning of ET adequate and reasonable. This conclusion has positive implication in which future studies can utilize the simulation of latent heat flux to study the partitioning of evapotranspiration across different ecosystems without the need for expensive instruments and fieldwork.

The simulation outputs also have the potential to be use as gap-filling data in the missing eddy covariance measurements. As shown in section 5.2., model calibration, and section 5.3, model validation, high correlation coefficients and Nash-Sutcliffe coefficient between observed measurements and simulation proved that tRIBS's estimations were representative of the actual flux magnitudes and the underlying physical processes. Furthermore, the strong agreement between the simulation and measurements shown in the diurnal variability figures illustrated that tRIBS was able to capture the diurnal cycle of these fluxes. In addition to utilizing the readily available inputs, the three reasons facilitate the conclusion that tRIBS is a low cost with high accuracy method in filling the gap of the missing turbulent flux measurements.

The process of conducting simulation provided invaluable insights on the controlling parameters and forcing functions that determine the quality of the outputs. Missing measurements from hydrometeorological forcing variables severely affected the simulated variables during the missing period although the quality of simulation directly after the missing period was not affected. Precipitation, incoming shortwave radiation, and relative humidity are the most important forcing functions that drive the outputs. Satellite-derived vegetation parameters also have strong influence on the outputs of surface energy balance fluxes and soil moisture. Calibrated parameters reveal the importance of saturated hydraulic conductivity, porosity, soil moisture at saturation, residual soil moisture, pore distribution index, air entry bubbling pressure, stress threshold for plant transpiration and for evaporation on the simulated soil moisture at 10- and 100-centimeter depth. The behaviors of ground heat flux and soil temperature highly depended on four parameters in tRIBS, the heat conductivity, heat capacity of the soil, saturated soil conductivity, and porosity. Both latent heat flux and sensible heat flux varied with changes in air entry bubbling pressure and the stress thresholds. Overall, the model performed well with net radiation without the need to calibrate any parameter.

The combination of the time-series analysis of the surface-energy fluxes, soil moisture, soil temperature and the simulation of these variables using a physically-based hydrologic model, tRIBS, will be beneficial to the U.S. Army Research Office in future mission planning. The knowledge of the effects of vegetation cover changes and its phenological responses will provide the army with the estimations of soil moisture that can be used for transporting heavy equipment and the surface heat responses through ground-heat flux, sensible-heat flux, and soil temperature that potentially be applied in landmine

detection. Understanding the effects of vegetation on surface-energy balance can also be applied through hypothetical scenarios through the simulation with assumptive dynamic vegetation variables which can then be applied in other water demand and weather prediction models.

The final goal of developing a toolkit to assist scientists and engineers was completed with the development of VisualtRIBS and a folder of R scripts. The former software allows users to quickly visually the time series of the output variables at either pixel-scale or basin-scale while the latter allows users to quickly process satellite images from NASA to calculate the dynamic vegetation parameters, extract and aggregate eddy covariance measurements to create hydrometeorological forcing files, simulation definition files, and automatic calibration for 26 parameters using the SCE-UA global optimization algorithm (Duan et al., 1994).

Having high temporal- and spatial-resolution data is crucial to produce high quality estimations. Furthermore, the model capability in simulating soil moisture and ground heat flux was affected in case of the presence of snow layer of frozen ground. Other than the quality of the data, the most important factor to ensure the simulation results is the data management. tRIBS is a complex model that employs multiple file formats. One simulation requires thousands of different files and the timestamps for spatially dynamic files are especially important to produce accurate estimations. For this reason, organizing the files into groups and put them in different folders is strategic for management and backtracking, should errors or problem arises. Finally, making use of programming to automate data acquisition, data extraction, and model setup is invaluable to reduce time required to setup the simulation, reduce human errors and ensure consistent qualities of data processing.

Chapter 7: Future Work

The future work of the project would be to expand the simulations from pixel scale (utilizing eddy covariance measurements at one location and extracted pixel values from satellite images) to basin scale (multiple eddy covariance measurements and full utilization of satellite images at finer resolution) using the calibrated parameters and assessment of tRIBS's performance at regional scale. In addition, furthering the capability of VisualtRIBS in combining the parallel simulation outputs for visualization is required as more complex, data-demanding simulations at basin scale will require parallelization to reduce running time. Finally, developing better, modern user interface for VisualtRIBS as well as inserting additional options for mapping coloring would allow users to better view the results in different conditions. These steps will allow the model to be readily utilized by military personnel, weather forecasters, and other engineers, scientists to quickly run the simulations and visualize the results with high accuracy.

Appendix 1

I. Installation

VisualtRIBS utilizes Python 3.7 which can be downloaded from:

https://www.python.org/downloads/

a. Using Virtual Environment

1. Navigate to the project folder using command:

```
cd path/to/project/folder
```

2. Create a virtual environment using command:

```
virtualenv venv
```

3. Activate the virtual environment:

```
source venv/bin/activate
```

4. Install the required packages:

```
pip install -r requirements.txt
```

b. Using Web-Based Version

The web-based version of VisualtRIBS is hosted on Heroku at:

https://visualtribs.herokuapp.com/

No further installation is required.

II. User Guide

1. Start the program

To start VisualtRIBS, navigate to the folder using command:

```
cd path/to/project/folder
```

Start the program with command:

```
python index.py
```

Open an internet browser (Chrome, FireFox) and type the address below in the search bar and hit enter:

```
127.0.0.1:8050/
```

2. Program Layout

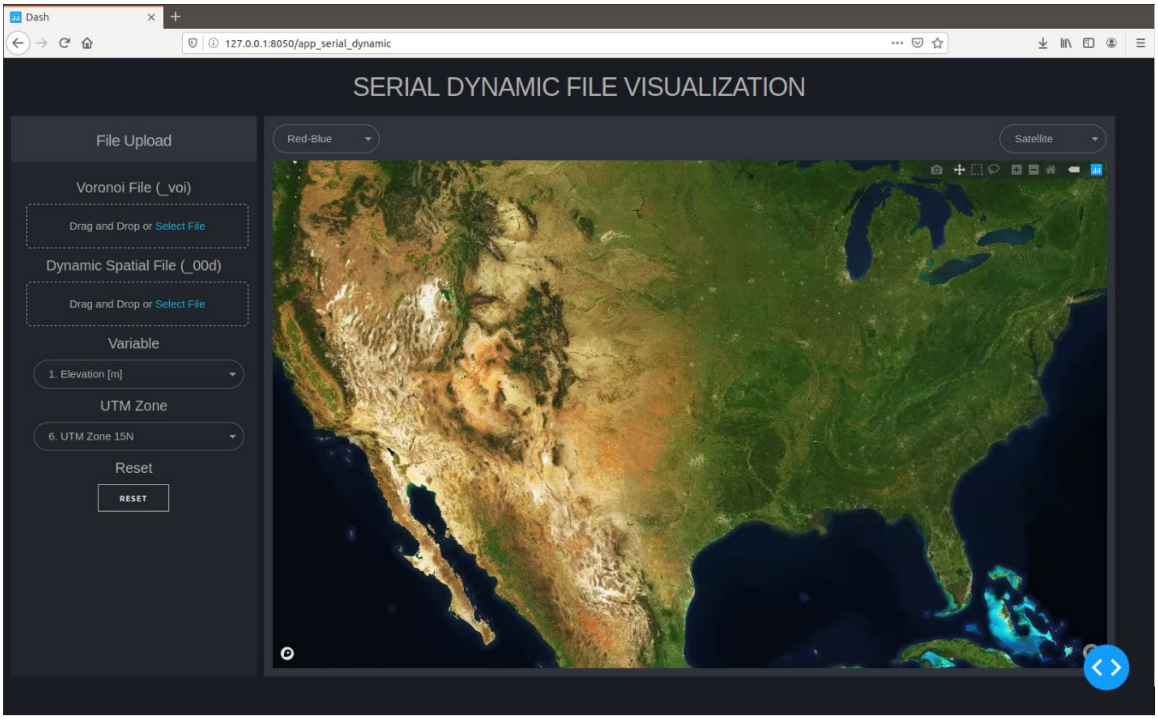

Figure 1.1: VisualtRIBS Layout

The layout of VisualtRIBS is illustrated in Figure 1.1. The left panel shows the file upload options, variable to visualize, and the corresponding UTM zone of the simulated basin. The right panel shows the high-resolution map with color scheme option (top left) and the type of basemap (top right).

3. Select the Voronoi Polygon file (_voi, _voi.#)

To upload the voronoi polygon file, click the box below Voronoi File (_voi) on the left panel, a pop-up box will open and the selected _voi file will be uploaded.

To upload the voronoi polygon file from parallel simulation, select all the applicable voronoi polygon files (_voi.#) for the basin and upload them. It is necessary that the order of the uploaded voronoi polygon files be the same as the spatial files (_00d.#)

4. Select the Spatial Dynamic file (_00d)

To upload the spatial dynamic file, click the box below Spatial Dynamic (_00d) on the left panel, a pop-up box will open and the selected _00d file will be uploaded.

To upload the vo spatial dynamic file from parallel simulation, select all the applicable spatial dynamic files (_00d.#) for the basin and upload them. It is necessary that the order of the uploaded spatial dynamic files be the same as the voronoi polygon files (_00d.#)

Note: *The order of the uploaded voronoi files must be the same as the order of the uploaded spatial file in parallel visualization, e.g: if you upload* ***_voi.1, _voi.2, _voi.3*** *or* ***_voi.2, _voi.3, _voi.1*** *for polygon files then the correct order for spatial files is* ***_00d.1, _00d.2, _00d.3*** *or* ***_00d.2, _00d.3, _00d.1****, respectively.*

5. Select the variable to visualize

To visualize a variable, click on the box below the Variable on the left panel, there are 54 variable options for the spatial dynamic file (_00d) and 55 variable options for the time-integrated spatial file (_00i).

6. Select Projection:

Since tRIBs utilizes Easting/Northing convention for projection, it is necessary to convert the coordinates to the Universal Transverse Mercator Coordinate System (UTM) to project the simulated basins onto the world map. To select corresponding UTM zone of the simulated watershed, click the UTM Zone option on the left panel.

7. Select Color Scheme

To select a color scheme, click the bar on the top left of the map.

8. Select Basemap

To select base map, click the bar on the top right of the map. There currently are 4 options for the basemap:

- Outdoor: Basemap with street names and elevation contour lines (Figure 1.2)

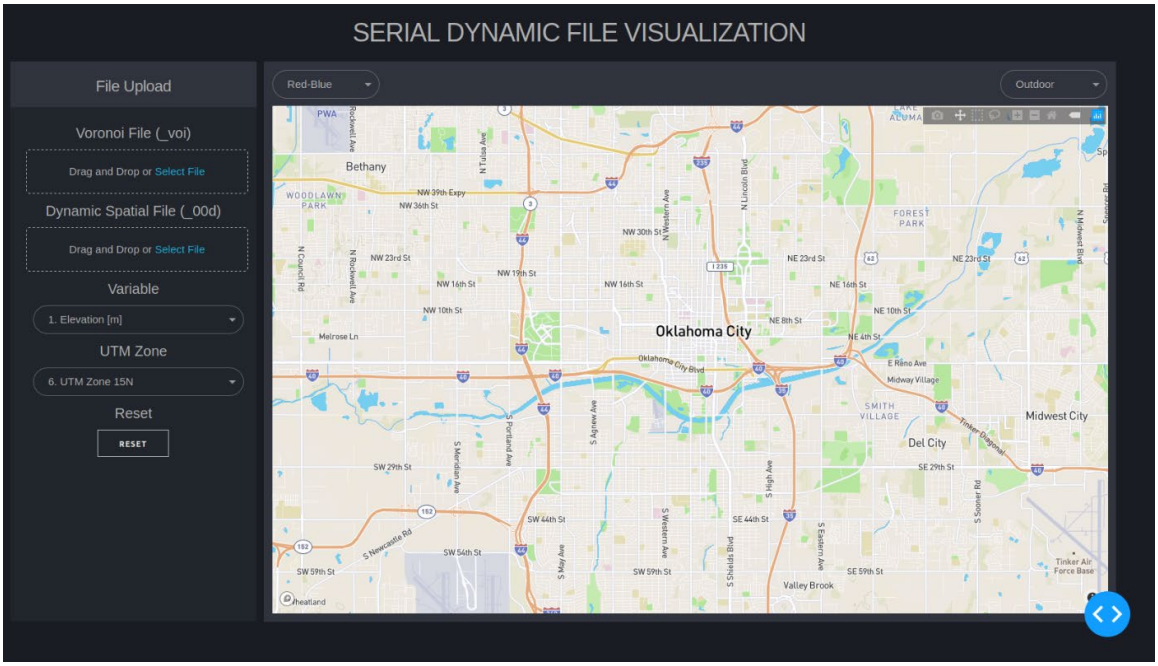

Figure 1.2: Outdoor Basemap

- Satellite: Basemap with high-resolution satellite images without street names (Figure 1.3)

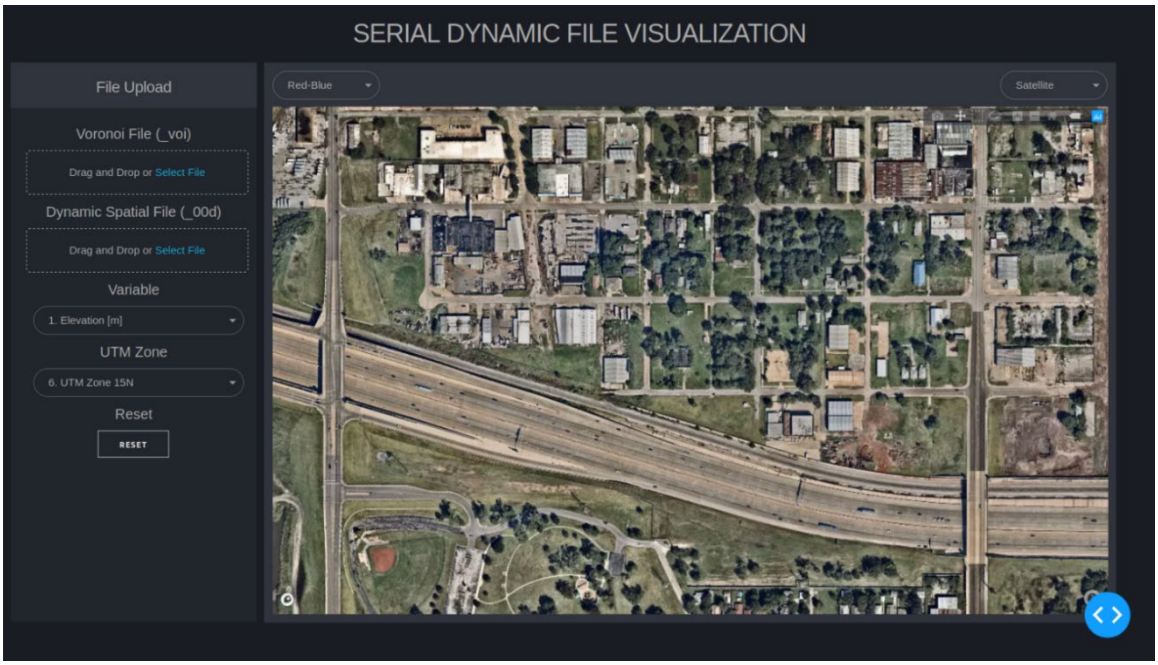

Figure 1.3: Satellite Basemap

- Open-Street: Basemap with detailed street names without elevation contour lines (Figure 1.4)

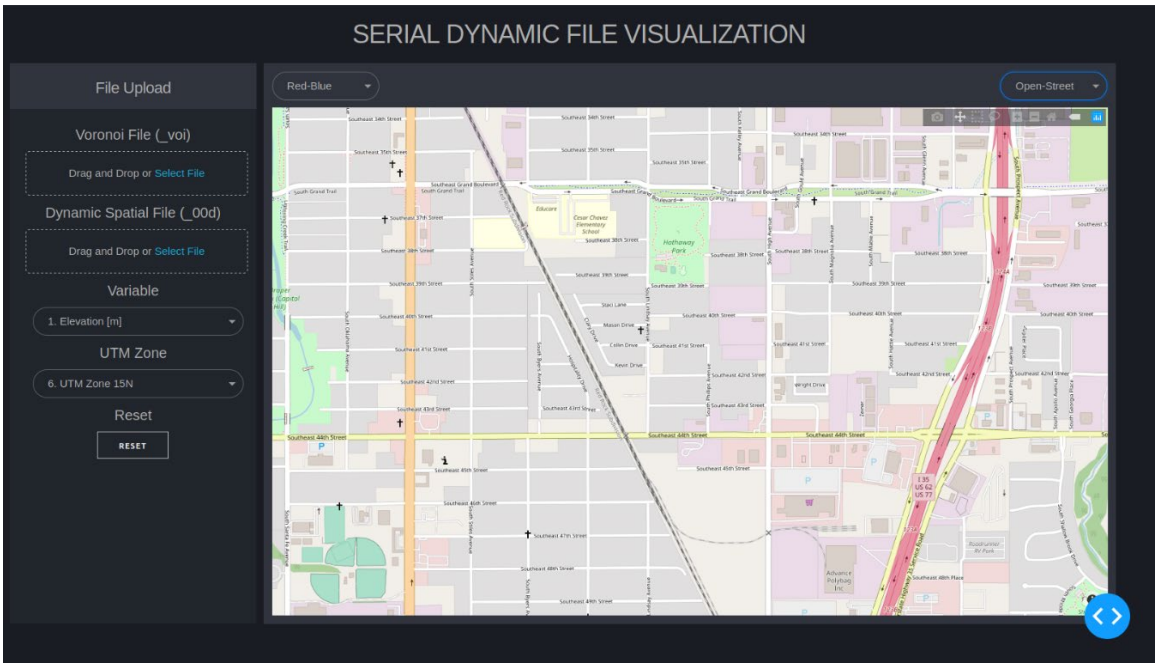

Figure 1.4: Open-Street Basemap

- Street: Basemap with high-resolution satellite images and street names (Figure 1.5)

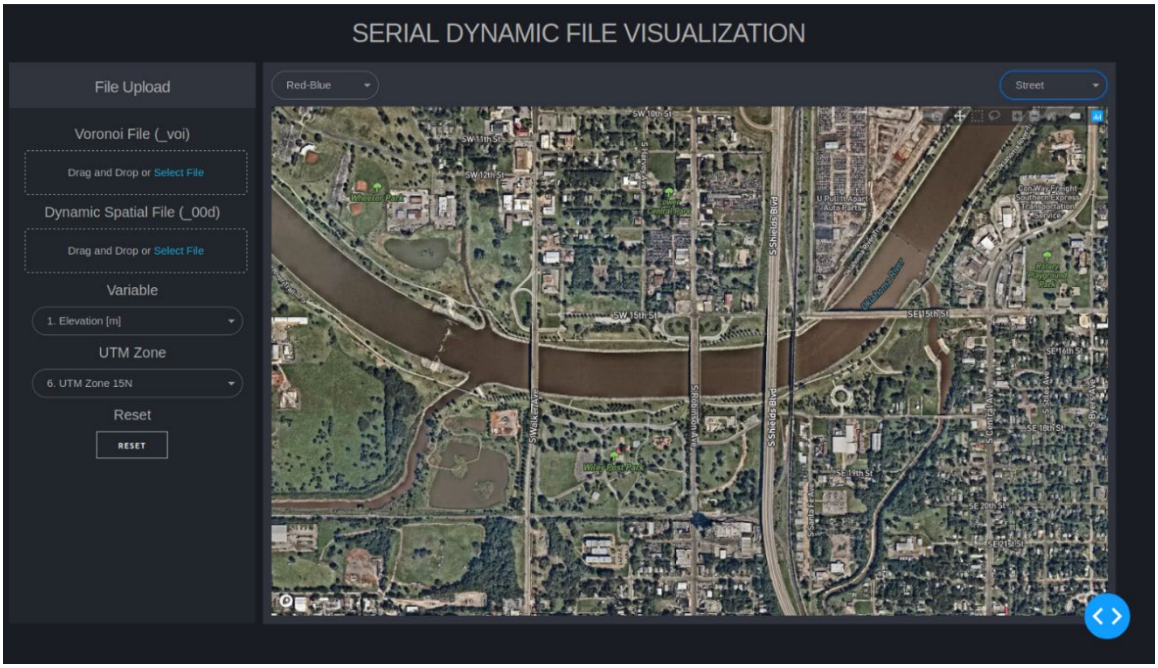

Figure 1.5: Street Basemap

9. Visualize the Variable

After all the options have been set, the tool will automatically read both the voronoi polygon files and the spatial output files, create a corresponding geojson in the background and project the results onto the basemap. To download the result, click on the camera icon at the top right of the basemap.

Note: *Depend on the number of voronoi cells in the simulation basin, the visualization tool can take from 5 seconds (Peachcheater Creek) to 30 seconds (Redondo Creek) to complete the task, if you see VisualtRIBS shows "updating …", it means the tool is still running and please do not reload the page or uploaded data will be resetting.*

III. Visualization Example

1. Actual Evaporation at Peachcheater Creek, OK

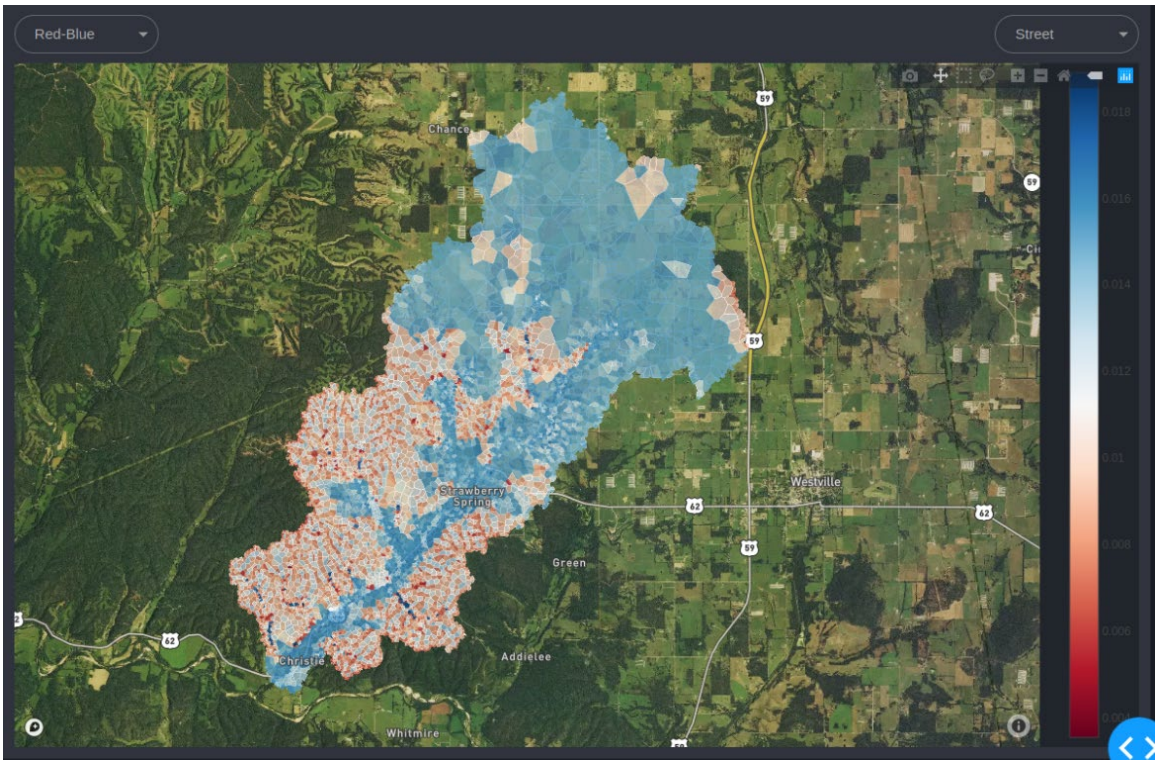

Figure 1.6: Actual Evaporation at Peacheater Creek, OK with Red-Blue color scheme

2. Sensible Heat Flux at Redondo Creek, NM

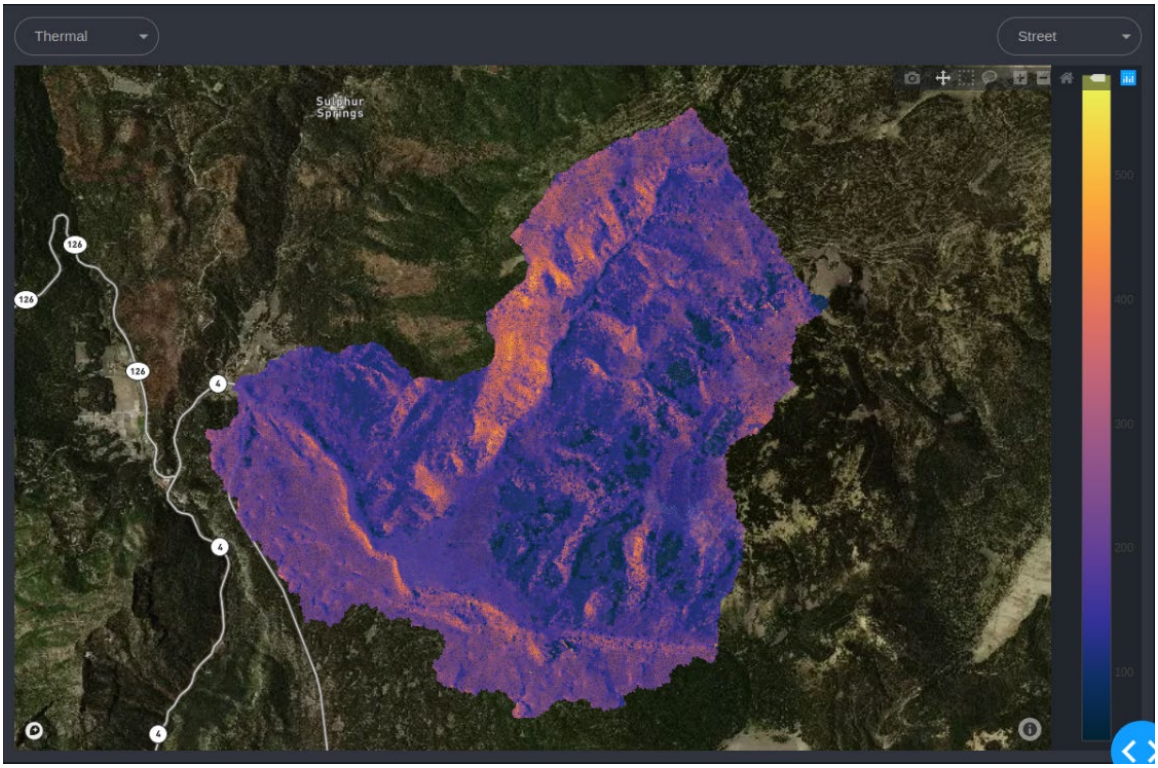

Figure 1.7: Sensible Heat Flux at Redondo Creek, NM with Thermal color scheme

References

Abella, Scott R, Charles W Denton, Rory W Steinke, and David G Brewer. "Soil Development in Vegetation Patches of Pinus Ponderosa Forests: Interface with Restoration Thinning and Carbon Storage." *Forest Ecology and Management* 310, no. C (2013): 632-42.

Al-Kayssi, A.W, A.A Al-Karaghouli, A.M Hasson, and S.A Beker. "Influence of Soil Moisture Content on Soil Temperature and Heat Storage under Greenhouse Conditions." Journal of Agricultural Engineering Research 45, no. 4 (1990): 241-52.

Algimantas Sirvydas, Vidmantas Kučinskas, Paulius Kerpauskas, Jūratė Nadzeikienė, and Albinas Kusta. "Solar Radiation Energy Pulsations in a Plant Leaf." *Journal of Environmental Engineering and Landscape Management* 18, no. 3 (2010): 188-195.

Allen, Richard G., Tasumi, Masahiro, and Trezza, Ricardo. "Satellite-based Energy Balance for Mapping Evapotranspiration with Internalized Calibration (METRIC)--model. (Report)." Journal of Irrigation and Drainage Engineering 133, no. 4 (2007): 380-394.

Alvalá, R. C. S., R. Gielow, H. R. Da Rocha, H. C. Freitas, J. M. Lopes, A. O. Manzi, C. Von Randow, M. A. F. S. Dias, O. M. R. Cabral, and M. J. Waterloo. "Intradiurnal and Seasonal Variability of Soil Temperature, Heat Flux, Soil Moisture Content, and Thermal Properties under Forest and Pasture in Rondônia." Journal of Geophysical Research: Atmospheres 107, no. D20 (2002): LBA 10-1-BA 10-20.

Amiro, B. D., Barr, A. G., Barr, J. G., Black, T. A., Bracho, R., Brown, M., Chen, J., Clark, K. L., Davis, K. J., Desai, A. R., Dore, S., Engel, V., Fuentes, J. D., Goldstein, A. H., Goulden, M. L., Kolb, T. E., Lavigne, M. B., Law, B. E., Margolis, H. A., Martin, T., Mccaughey, J. H., Misson, L., Montes-Helu, M., Noormets, A., Randerson, J. T., Starr, G., and Xiao, J. "Ecosystem Carbon Dioxide Fluxes after Disturbance in Forests of North America." *Journal of Geophysical Research: Biogeosciences* 115, no. G4 (2010): N/a.

Amiro, Orchansky, Barr, Black, Chambers, Chapin III, Goulden, Litvak, Liu, Mccaughey, Mcmillan, and Randerson. "The Effect of Post-fire Stand Age on the Boreal Forest Energy Balance." Agricultural and Forest Meteorology 140, no. 1 (2006): 41-50.

Aubinet, Marc, Vesala, Timo, and Papale, Dario. Eddy Covariance: A Practical Guide to Measurement and Data Analysis. 2012 ed. Springer Atmospheric Sciences. Dordrecht: Springer Netherlands, 2012.

Auld, Tony D., and Ross A. Bradstock. "Soil Temperatures after the Passage of a Fire: Do They Influence the Germination of Buried Seeds?" Australian Journal of Ecology 21, no. 1 (1996): 106-09.

Bakker, Mark, and John L. Nieber. "Damping of Sinusoidal Surface Flux Fluctuations with Soil Depth." Vadose Zone Journal 8, no. 1 (2009): 119-26.

Bardsley, Earl. "Goodness of Fit Indices for Discharge Forecasts in Real Time." Journal of Hydrology (New Zealand) 54, no. 1 (2015): 63.

Beringer, Jason, F. Stuart Chapin, Catharine C Thompson, and A. David Mcguire. "Surface Energy Exchanges along a Tundra-forest Transition and Feedbacks to Climate." Agricultural and Forest Meteorology 131, no. 3-4 (2005): 143-61.

Bliss, L. C., and Ross W. Wein. "Plant Community Responses to Disturbances in the Western Canadian Arctic." Canadian Journal of Botany 50, no. 5 (1972): 1097-109.

Boisramé, Thompson, and Stephens. "Hydrologic Responses to Restored Wildfire Regimes Revealed by Soil Moisture-vegetation Relationships." Advances in Water Resources 112 (2018): 124-46.

Brooks, R. H. and Corey, A. T. “Hydraulic properties of porous media.” Hydrology Paper, no. 3 (1964).

Bruin, H., A. Kohsiek, and R. Hurk. "A Verification of Some Methods to Determine the Fluxes of Momentum, Sensible Heat, and Water Vapour Using Standard Deviation and Structure Parameter of Scalar Meteorological Quantities." Boundary-Layer Meteorology 63, no. 3 (1993): 231-57.

Carlyle-Moses, D. E., A. G. Price, Martz, Lawrence, and Buttle, Jim. "Modelling Canopy Interception Loss from a Madrean Pine-oak Stand, Northeastern Mexico." Hydrological Processes 21, no. 19 (2007): 2572-580.

Carlson, and Ripley. "On the Relation between NDVI, Fractional Vegetation Cover, and Leaf Area Index." Remote Sensing of Environment 62, no. 3 (1997): 241-52.

Cavanaugh, Michelle L., Shirley A. Kurc, and Russell L. Scott. "Evapotranspiration Partitioning in Semiarid Shrubland Ecosystems: A Two-site Evaluation of Soil Moisture Control on Transpiration." *Ecohydrology* 4, no. 5 (2011): 671-81.

Chapin, F. Stuart, and Gaius R. Shaver. "Changes in Soil Properties and Vegetation Following Disturbance of Alaskan Arctic Tundra." Journal of Applied Ecology 18, no. 2 (1981): 605-17.

Corona, Claudia R, Jason J Gurdak, Jesse E Dickinson, T.P.A Ferré, and Edwin P Maurer. "Climate Variability and Vadose Zone Controls on Damping of Transient Recharge." Journal of Hydrology 561 (2018): 1094-104.

Cosh, Michael H., Ochsner, Tyson E., McKee, Lynn, Dong, Jingnuo, Basara, Jeffrey B., Evett, Steven R., Hatch, Christine E., Small, Eric E., Steele-Dunne, S.C., Zreda, Marek, and Sayde, Chadi. "The Soil Moisture Active Passive Marena, Oklahoma, in Situ Sensor Testbed (SMAP-MOISST): Testbed Design and Evaluation of in Situ Sensors." Vadose Zone Journal 15, no. 4 (2016): Urn:issn:1539-1663. Dore, Sabina, and Kolb, Thomas. Fri. 2016. "AmeriFlux US-Fuf Flagstaff – Unmanaged Forest". United States. doi:10.17190/AMF/1246051. https://www.osti.gov/servlets/purl/1246051.

Dan, Li, and Ji Jinjun. "The Surface Energy, Water, Carbon Flux and Their Intercorrelated Seasonality in a Global Climate-vegetation Coupled Model." Tellus B: Chemical and Physical Meteorology 59, no. 3 (2007): 425-38.

Dore, Sabina, and Kolb, Thomas. Fri. 2016. "AmeriFlux US-Fmf Flagstaff - Managed Forest". United States. doi:10.17190/AMF/1246050. https://www.osti.gov/servlets/purl/1246050.

Dore, Sabina, and Kolb, Thomas. 2016. "AmeriFlux US-Fwf Flagstaff - Wildfire". United States. doi:10.17190/AMF/1246052. https://www.osti.gov/servlets/purl/1246052.

Dore, Sabina, Mario Montes-Helu, Stephen C. Hart, Bruce A. Hungate, George W. Koch, John B. Moon, Alex J. Finkral, and Thomas E. Kolb. "Recovery of Ponderosa Pine Ecosystem Carbon and Water Fluxes from Thinning and Stand-replacing Fire." Global Change Biology 18, no. 10 (2012): 3171-185.

Dore, S., T. E. Kolb, M. Montes-Helu, S. E. Eckert, B. W. Sullivan, B. A. Hungate, J. P. Kaye, S. C. Hart, G. W. Koch, and A. Finkral. "Carbon and Water Fluxes from Ponderosa Pine Forests Disturbed by Wildfire and Thinning." Ecological Applications 20, no. 3 (2010): 663-83.

Duan, Qingyun, Soroosh Sorooshian, and Vijai K Gupta. "Optimal Use of the SCE-UA Global Optimization Method for Calibrating Watershed Models." Journal of Hydrology 158, no. 3-4 (1994): 265-84.

Durán Zuazo, V., H. Martínez, J. Pleguezuelo, R. Martínez Raya, and Francia Rodríguez. "Soil-erosion and Runoff Prevention by Plant Covers in a Mountainous Area (se Spain): Implications for Sustainable Agriculture." *Environmentalist* 26, no. 4 (2006): 309-19.

Duveiller, Gregory, Josh Hooker, and Alessandro Cescatti. "The Mark of Vegetation Change on Earth's Surface Energy Balance." *Nat Commun* 9, no. 1 (2018): 679.

E. R. Vivoni, D. Entekhabi, R. L. Bras, and V. Y. Ivanov. "Controls on Runoff Generation and Scale-dependence in a Distributed Hydrologic Model." Hydrology and Earth System Sciences 11, no. 5 (2007): 1683-701.

E. Perra, M. Piras, R. Deidda, C. Paniconi, G. Mascaro, E. R. Vivoni, P. Cau, P. A. Marras, R. Ludwig, and S. Meyer. "Multimodel Assessment of Climate Change-induced Hydrologic Impacts for a Mediterranean Catchment." *Hydrology and Earth System Sciences* 22, no. 7 (2018): 4125-143.Ershadi, Mccabe, Evans, and Wood. "Impact of Model Structure and Parameterization on Penman–Monteith Type Evaporation Models." Journal of Hydrology 525, no. C (2015): 521-35.

Farouki, O., and Cold Regions Research Engineering Lab Hanover Nh. Thermal Properties of Soils, 1981.

Feagin, R.A., Lozada-Bernard, S.M., Ravens, T.M., Moller, I., Yeager, K.M., and Baird, A.H. "Does Vegetation Prevent Wave Erosion of Salt Marsh Edges? (GEOLOGY)(Author Abstract)(Report)." *Proceedings of the National Academy of Sciences of the United States* 106, no. 25 (2009): 10109-10113.

Frank, John M, William J Massman, and Brent E Ewers. "Underestimates of Sensible Heat Flux Due to Vertical Velocity Measurement Errors in Non-orthogonal Sonic Anemometers." Agricultural and Forest Meteorology 171-172, no. C (2013): 72-81.

Friedl, M., Mciver, Hodges, Zhang, Muchoney, Strahler, Woodcock, Gopal, Schneider, Cooper, Baccini, Gao, and Schaaf. "Global Land Cover Mapping from MODIS:

Algorithms and Early Results." Remote Sensing of Environment 83, no. 1-2 (2002): 287-302.

Frouz, Jan. "Effects of Soil Development Time and Litter Quality on Soil Carbon Sequestration: Assessing Soil Carbon Saturation with a Field Transplant Experiment along a Post-mining Chronosequence." *Land Degradation & Development* 28, no. 2 (2017): 664-72.

Guan, Xiaodan, Jianping Huang, Ni Guo, Jianrong Bi, and Guoyin Wang. "Variability of Soil Moisture and Its Relationship with Surface Albedo and Soil Thermal Parameters over the Loess Plateau." *Advances in Atmospheric Sciences* 26, no. 4 (2009): 692-700.

H. A. Moreno, H. V. Gupta, D. D. White, and D. A. Sampson. "Modeling the Distributed Effects of Forest Thinning on the Long-term Water Balance and Streamflow Extremes for a Semi-arid Basin in the Southwestern US." Hydrology and Earth System Sciences 20, no. 3 (2016): 1241-267.

Harden, Jennifer W., Kristen L. Manies, Merritt R. Turetsky, and Jason C. Neff. "Effects of Wildfire and Permafrost on Soil Organic Matter and Soil Climate in Interior Alaska." Global Change Biology 12, no. 12 (2006): 2391-403.

He, Ivanov, Bohrer, Maurer, Vogel, and Moghaddam. "Effects of Fine-scale Soil Moisture and Canopy Heterogeneity on Energy and Water Fluxes in a Northern Temperate Mixed Forest." Agricultural and Forest Meteorology 184 (2014): 243-56. Ivanov, Valeriy Y., Enrique R. Vivoni, Rafael L. Bras, and Dara Entekhabi. "Catchment

Hydrologic Response with a Fully Distributed Triangulated Irregular Network Model." Water Resources Research 40, no. 11 (2004): N/a.

He, Lingli, Valeriy Y Ivanov, Gil Bohrer, Julia E Thomsen, Christoph S Vogel, and Mahta Moghaddam. "Temporal Dynamics of Soil Moisture in a Northern Temperate Mixed Successional Forest after a Prescribed Intermediate Disturbance." Agricultural and Forest Meteorology 180 (2013): 22-33.

Hernandez, Helios. "Natural Plant Recolonization of Surficial Disturbances, Tuktoyaktuk Peninsula Region, Northwest Territories." Canadian Journal of Botany 51, no. 11 (1973): 2177-196.

Holden, Berhe, and Treseder. "Decreases in Soil Moisture and Organic Matter Quality Suppress Microbial Decomposition following a Boreal Forest Fire." Soil Biology and Biochemistry 87 (2015): 1-9.

Hollinger, D. Y., and A. D. Richardson. "Uncertainty in Eddy Covariance Measurements and Its Application to Physiological Models." Tree Physiology 25, no. 7 (2005): 873-85.

Holmes, T. R. H., M. Owe, R. A. M. De Jeu, and H. Kooi. "Estimating the Soil Temperature Profile from a Single Depth Observation: A Simple Empirical Heatflow Solution." Water Resources Research 44, no. 2 (2008): N/a.

I. Mammarella, O. Peltola, A. Nordbo, L. Järvi, and Ü. Rannik. "Quantifying the Uncertainty of Eddy Covariance Fluxes Due to the Use of Different Software Packages and Combinations of Processing Steps in Two Contrasting Ecosystems." Atmospheric Measurement Techniques 9, no. 10 (2016): 4915-933.

Ivanov, Valeriy Y., Rafael L. Bras, and Enrique R. Vivoni. "Vegetation-hydrology Dynamics in Complex Terrain of Semiarid Areas: 2. Energy-water Controls of Vegetation Spatiotemporal Dynamics and Topographic Niches of Favorability." Water Resources Research 44, no. 3 (2008): N/a.

Ivanov, Vivoni, Bras, and Entekhabi. "Preserving High-resolution Surface and Rainfall Data in Operational-scale Basin Hydrology: A Fully-distributed Physically-based Approach." Journal of Hydrology 298, no. 1 (2004): 80-111.

Jacobs, Adrie F.G, Bert G Heusinkveld, and Albert A.M Holtslag. "Long-term Record and Analysis of Soil Temperatures and Soil Heat Fluxes in a Grassland Area, The Netherlands." Agricultural and Forest Meteorology 151, no. 7 (2011): 774-80.

José Alexandre Varanda Andrade, Francisco Manuel Gonçalves De Abreu, and Manuel Armando Valeriano Madeira. "Influence of Litter Layer Removal on the Soil Thermal Regime of a Pine Forest in a Mediterranean Climate Influência Da Manta Morta No Regime Térmico De Um Solo Sob Pinus Num Clima Do Tipo Mediterrâneo." *Revista Brasileira De Ciência Do Solo* 34, no. 5 (2010): 1481-490.

Jury, William A., Gardner, Wilford R, and Gardner, Walter H. Soil Physics / William A. Jury, Wilford R. Gardner, Walter H. Gardner. 5th ed. New York: J. Wiley, 1991.

Kim, Jongho, April Warnock, Valeriy Y Ivanov, and Nikolaos D Katopodes. "Coupled Modeling of Hydrologic and Hydrodynamic Processes including Overland and Channel Flow." *Advances in Water Resources* 37 (2012): 104-26.Kimball, B. A., R. D. Jackson, F. S. Nakayama, S. B. Idso, and R. J. Reginato. “Soil-heat Flux

Determination: Temperature Gradient Method with Computed Thermal Conductivities". Soil Science Society of America. Journal. (1976): 40:25-28.

Klemmedson, James O. "Effect of Mesquite Trees on Vegetation and Soils in the Desert Grassland." Journal of Range Management 30, no. 5 (1977): 361-67.

Kljun, Natascha, Calanca, P., Rotach, M.W., and Schmid, Hans Peter. "A Simple Two-dimensional Parameterisation for Flux Footprint Prediction (FFP)." Geoscientific Model Development 8, no. 11 (2015): 3695-713.

Kurc, Shirley. 2016. "AmeriFlux US-SRC Santa Rita Creosote". United States. doi:10.17190/AMF/1246127. https://www.osti.gov/servlets/purl/1246127.

Kurc, Shirley A., and Eric E. Small. "Dynamics of Evapotranspiration in Semiarid Grassland and Shrubland Ecosystems during the Summer Monsoon Season, Central New Mexico." Water Resources Research 40, no. 9 (2004): N/a.

Lawrence, D., and M. Slingo. "An Annual Cycle of Vegetation in a GCM. Part II: Global Impacts on Climate and Hydrology." Climate Dynamics 22, no. 2-3 (2004): 107-22.Li, Fang, David M Lawrence, and Ben Bond-Lamberty. "Impact of Fire on Global Land Surface Air Temperature and Energy Budget for the 20th Century Due to Changes within Ecosystems." Environmental Research Letters 12, no. 4 (2017): 10.

Lin, J. D. 1980. On the force-restore method for prediction of ground surface temperature, *J. Geophys. Res.*, 85(C6), 3251–3254

Liuzzo, Lorena, Leonardo V. Noto, Enrique R. Vivoni, and Goffredo La Loggia. "Basin-Scale Water Resources Assessment in Oklahoma under Synthetic Climate Change Scenarios Using a Fully Distributed Hydrologic Model." Journal of Hydrologic Engineering 15, no. 2 (2010): 107-22.

Lu, Nan, Chen, Shiping, Wilske, Burkhard, Sun, Ge, and Chen, Jiquan. "Evapotranspiration and Soil Water Relationships in a Range of Disturbed and Undisturbed Ecosystems in the Semi-arid Inner Mongolia, China." Journal of Plant Ecology 4, no. 1-2 (2011): 49-60.

Mahan, Hayden R. In-situ Measurements and Remotely Sensed Estimations of Surface Fluxes over the Southern Great Plains of the United States / by Hayden Mahan., 2016.

Mahmood, Taufique H., and Enrique R. Vivoni. "A Climate-induced Threshold in Hydrologic Response in a Semiarid Ponderosa Pine Hillslope." *Water Resources Research* 47, no. 9 (2011): N/a.

Malmedal, Keith, Carson Bates, and David Cain. "The Measurement of Soil Thermal Stability, Thermal Resistivity, and Underground Cable Ampacity." 2014 IEEE Rural Electric Power Conference (REPC), 2014, C5-1-5-12.

Mark D. Schwartz & Todd M. Crawford. “DETECTING ENERGY-BALANCE MODIFICATIONS AT THE ONSET OF SPRING.” Physical Geography 22:5, 394-409 (2001), DOI: 10.1080/02723646.2001.10642751Mckay, Christopher P, Jamie L Molaro, and Margarita M Marinova. "High-frequency Rock Temperature Data from Hyper-arid Desert Environments in the Atacama and the Antarctic Dry

Valleys and Implications for Rock Weathering." Geomorphology 110, no. 3 (2009): 182-87.

Méndez-Barroso, Luis A., Enrique R. Vivoni, Agustin Robles-Morua, Giuseppe Mascaro, Enrico A. Yépez, Julio C. Rodríguez, Christopher J. Watts, Jaime Garatuza-Payán, and Juan A. Saíz-Hernández. "A Modeling Approach Reveals Differences in Evapotranspiration and Its Partitioning in Two Semiarid Ecosystems in Northwest Mexico." Water Resources Research 50, no. 4 (2014): 3229-252.

Montes-Helu, M.C., T. Kolb, S. Dore, B. Sullivan, S.C. Hart, G. Koch, and B.A. Hungate. "Persistent Effects of Fire-induced Vegetation Change on Energy Partitioning and Evapotranspiration in Ponderosa Pine Forests." *Agricultural and Forest Meteorology* 149, no. 3-4 (2009): 491-500.

Montes-Helu, S. E. Eckert, B. W. Sullivan, B. A. Hungate, J. P. Kaye, S. C. Hart, G. W. Koch, and A. Finkral. "Carbon and Water Fluxes from Ponderosa Pine Forests Disturbed by Wildfire and Thinning." Ecological Applications 20, no. 3 (2010): 663-83.

Nassar, Ibrahim, and Horton, Robert. Soil Thermal Diffusivity and Water Transport in Unsaturated, Nonisothermal, Salty Soil, 1988, ProQuest Dissertations and Theses.

Panferov, O., Y. Knyazikhin, R.B Myneni, J. Szarzynski, S. Engwald, K.G Schnitzler, and G. Gravenhorst. "The Role of Canopy Structure in the Spectral Variation of Transmission and Absorption of Solar Radiation in Vegetation Canopies." *IEEE Transactions on Geoscience and Remote Sensing* 39, no. 2 (2001): 241-53.Peng, X., J. Heitman, R. Horton, and T. Ren. “Determining Near-Surface Soil Heat Flux

Density Using the Gradient Method: A Thermal Conductivity Model–Based Approach.” Journal of Hydrometeoryno. 18 (2017): 2285–2295

Penman, H. L. "Natural Evaporation from Open Water, Bare Soil and Grass." Proceedings of the Royal Society of London. Series A, Mathematical and Physical Sciences (1934-1990) 193, no. 1032 (1948): 120-45.

Pitman, John Iain. "Rainfall Interception by Bracken Litter — Relationship between Biomass, Storage and Drainage Rate." Journal of Hydrology 111, no. 1 (1989): 281-91.

Ren, Diandong, and Ming Xue. "A Revised Force-Restore Model for Land Surface Modeling." Journal of Applied Meteorology 43, no. 11 (2004): 1768-782.

Robson, R. "Elementary Calculation of Soil Damping Depth." American Journal of Physics 57, no. 7 (1989): 632-634.

Román, Schaaf, Woodcock, Strahler, Yang, Braswell, Curtis, Davis, Dragoni, Goulden, Gu, Hollinger, Kolb, Meyers, Munger, Privette, Richardson, Wilson, and Wofsy. "The MODIS (Collection V005) BRDF/albedo Product: Assessment of Spatial Representativeness over Forested Landscapes." *Remote Sensing of Environment* 113, no. 11 (2009): 2476-498.

Roxy, M., S. Sumithranand, and V. Renuka. "Estimation of Soil Moisture and Its Effect on Soil Thermal Characteristics at Astronomical Observatory, Thiruvananthapuram, South Kerala." Journal of Earth System Science 123, no. 8 (2014): 1793-807.

Santos, A. j. b., Silva, G. t. d. a., Miranda, H. s., Miranda, A. c., and Lloyd, J. "Effects of Fire on Surface Carbon, Energy and Water Vapour Fluxes over Campo Sujo Savanna in Central Brazil." Functional Ecology 17, no. 6 (2003): 711-19.

Schulze, E.-D., R. Leuning, and F. Kelliher. "Environmental Regulation of Surface Conductance for Evaporation from Vegetation." Vegetatio 121, no. 1 (1995): 79-87.

Scott, Russell L., Joel A. Biederman, Erik P. Hamerlynck, and Greg A. Barron-Gafford. "The Carbon Balance Pivot Point of Southwestern U.S. Semiarid Ecosystems: Insights from the 21st Century Drought." Journal of Geophysical Research: Biogeosciences 120, no. 12 (2015): 2612-624.

Shunlin Liang, Xiaowen Li, and Jindi Wang. Advanced Remote Sensing: Terrestrial Information Extraction and Applications. 1st ed. Academic Press, 2012.

Silverman, S. M., and Air Force Cambridge Research Center. Geophysics Research Directorate. Some Notes on the Correlation Coefficient S.M. Silverman. GRD

Sugathan, Neena, V. Biju, and G. Renuka. "Influence of Soil Moisture Content on Surface Albedo and Soil Thermal Parameters at a Tropical Station." Journal of Earth System Science 123, no. 5 (2014): 1115-128. Research Notes; No. 13. 1959.

Thompson, S. E., C. J. Harman, P. Heine, and G. G. Katul. "Vegetation-infiltration Relationships across Climatic and Soil Type Gradients." *Journal of Geophysical Research: Biogeosciences* 115, no. G2 (2010): N/a.Dore, S., T. E. Kolb, M.

Tiegang, Zhang, Li, Peng, Li, Zhanbin, and Guo, Xiaoding. "Effects of Perennial Vegetation on Runoff and Erosion for Field Plots on Loess Plateau in

China." *Nature Environment and Pollution Technology* 12, no. 1 (2013): 63-68.Van Wijk, W. Physics of Plant Environment. Amsterdam: North-Holland Pub, 1963.

Vivoni, E., Ivanov, V., Bras, R., & Entekhabi, D. (2005). On the effects of triangulated terrain resolution on distributed hydrologic model response. *Hydrological Processes, 19*(11), 2101-2122.

Vivoni, Enrique R., Julio C. Rodríguez, and Christopher J. Watts. "On the Spatiotemporal Variability of Soil Moisture and Evapotranspiration in a Mountainous Basin within the North American Monsoon Region." Water Resources Research 46, no. 2 (2010): N/a.

Xiang, Tiantian, Enrique R. Vivoni, and David J. Gochis. "Seasonal Evolution of Ecohydrological Controls on Land Surface Temperature over Complex Terrain." Water Resources Research 50, no. 5 (2014): 3852-874.

Zehetgruber, Bernhard, Johannes Kobler, Thomas Dirnböck, Robert Jandl, Rupert Seidl, and Andreas Schindlbacher. "Intensive Ground Vegetation Growth Mitigates the Carbon Loss after Forest Disturbance." Plant and Soil 420, no. 1 (2017): 239-52.

Zhang, Yuanchong & B. Rossow, W & Lacis, Andrew"Calculation of surface and top of atmosphere radiative fluxes from physical quantities based on ISCCP data sets. 1: Method and sensitivity to input data uncertainties." Journal of Geophysical Research (1995). 100. 10.1029/94JD02747.

Zhu, Dan, Philippe Ciais, Gerhard Krinner, Fabienne Maignan, Albert Jornet Puig, and Gustaf Hugelius. "Controls of Soil Organic Matter on Soil Thermal Dynamics in the Northern High Latitudes." Nature Communications 10, no. 1 (2019): 3172.